UNIVERSITA' DELLA CALABRIA

Dipartimento di Fisica

Dottorato di Ricerca in

Scienze e Tecnologie Fisiche, Chimiche e dei Materiali

Con il contributo di (Regione Calabria)

Borsa POR Calabria FSE/FESR 2014-2020

CICLO

XXXIV

Raman spectroscopic characterization of thin films to be used in Electrochromic Devices

Settore Scientifico Disciplinare FIS 07

Coordinatore: Ch.ma Prof.ssa Gabriella Cipparrone

Firma ___ Firma oscurata in base alle linee guida del Garante della privacy

Supervisore: Dr. Marco Castriota

Firma ___ Firma oscurata in base alle linee guida del Garante della privacy

Dottorando: Dr. Antonello Nucera

Firma ___ Firma oscurata in base alle linee guida del Garante della privacy

“La borsa di dottorato è stata cofinanziata con risorse del Programma Operativo Regionale Calabria FSE/FESR 2014 – 2020 (CCI 2014IT16M2OP006)”

Alla mia famiglia

To my family

TABLE OF CONTENTS

Abstract

L'elettrocromismo è una proprietà peculiare di alcuni materiali quando soggetti ad un potenziale elettrico. Tale proprietà viene sfruttata in appositi dispositivi elettrocromici formati da questi materiali e da altri che insieme provvedono alla loro realizzazione ed al loro funzionamento. In questi ultimi anni, le performance globali di tali dispositivi sono aumentate parecchio anche se ulteriori miglioramenti sono attualmente oggetto di studio da parte della comunità scientifica.

Lo scopo di questo lavoro di tesi è stato lo studio di materiali per potenziale uso in dispositivi elettrocromici, la realizzazione di un dispositivo elettrocromico in grado di modulare l'irraggiamento solare nonché una parte del calore ad esso associato e la sua completa caratterizzazione.

Le analisi strumentali impiegate per la caratterizzazione dei vari materiali e dei dispositivi realizzati sono state la Spettroscopia Raman, la Voltammetria Ciclica e la Spettroscopia UV-visibile.

La spettroscopia Raman è una tecnica d'indagine formidabile poiché non-distruttiva in grado di rivelare molte informazioni chimico fisiche strutturali dei campioni analizzati. Negli ultimi anni ha acquisito grande rilevanza nell'analisi di campioni biologici dato lo sviluppo della tecnica Raman SERS (*Surface Enhanced Raman Spectroscopy*).

I risultati della tesi sono esposti in differenti capitoli che trattano i concetti teorici connessi all'elettrocromismo (capitoli 1 e 2) e quelli relativi alle tecniche d'indagine impiegate durante il percorso (capitolo 3). I risultati delle analisi condotte sono esposti nel capitolo 4. Il capitolo 5 presenta le conclusioni e le prospettive future.

Nella prima parte del capitolo 4, sono state condotte delle analisi Raman su differenti materiali polimerici quali polimetilmetacrilati (PMMA) e ossido di polietilene (PEO) nonché polimeri naturali come il chitosano per i potenziali benefici operativi (i primi) ed ambientali (il secondo) che questi possono apportare nella realizzazione di un dispositivo elettrocromico. Materiali polielettrolitici possono essere impiegati come strato elettrolita in dispositivo elettrocromico, in questo lavoro di tesi è stato osservato l'effetto SERS di strati di polielettrolita sullo spettro Raman dell'acido acetico. Film di chitosano drogati con complesso di zinco sono stati analizzati mediante spettroscopia Raman. L'interpretazione dei risultati ottenuti ha permesso di stabilire che l'interazione tra il polimero naturale ed il complesso di zinco avviene al livello dei gruppi N-H ed O-H. I

leganti bipiridinici sono spesso impiegati nella formazione di molecole di metallopolimero con proprietà elettrocromiche. In questa tesi, è stato studiato l'effetto SERS di una placca d'oro sugli spettri Raman di campioni di bipiridina, mostrando un interessante miglioramento dei segnali Raman relativi alla bipiridina. La grafite ed il grafene possono migliorare la conducibilità dei dispositivi elettrocromici migliorandone le prestazioni. In questo lavoro di tesi, mediante l'uso della spettroscopia Raman sono state mostrate le caratteristiche strutturali di grafite funzionalizzata e di nano-placche di grafene.

È stato dimostrato l'effetto SERS dello strato sottile di Ag sugli spettri Raman della rodamina 6G depositata. È stata mostrata la caratterizzazione Raman di film di TiO2.

Nella seconda parte del capitolo 4, sono stati realizzati dispositivi elettrocromici formati da una soluzione elettrocromica di viologeno e ferrocene alla quale è stata aggiunto in determinate proporzioni il bisfenolo A glicerolato. Le proprietà ottiche dei dispositivi realizzati sono state studiate con la spettroscopia UV-vis-NIR prima e dopo la polimerizzazione indotta da esposizione alla luce UV. In particolare, è stata mostrata l'analisi delle proprietà di trasmissione dei dispositivi negli stati colorato e trasparente (rispettivamente lo stato ON e OFF). Inoltre, le proprietà elettrochimiche dei dispositivi sono state studiate mediante misure di voltammetria ciclica che mostrano le differenze tra lo stato ON e OFF dei dispositivi.

Osservazioni conclusive sono state fatte nell'ultimo capitolo della tesi, con la ricerca sulla tecnologia elettrocromica che sta proseguendo con ulteriori analisi strutturali dei materiali.

Abstract

Electrochromism is related to the optical properties of some materials when subject to an electric potential. These properties are exploited in special electrochromic devices formed by these materials and others that together provide for their implementation and operation. In recent years, the overall performance of these devices has increased considerably, although further improvements are currently being studied by the scientific community.

The aim of this thesis work has been the study of materials for potential use in electrochromic devices, the creation of an electrochromic device capable of modulating solar radiation as well as a part of the heat associated with it and its complete characterization.

The instrumental analyses used for the characterization of the various materials and devices were Raman spectroscopy, Cyclic Voltammetry and UV-visible spectroscopy.

Raman spectroscopy is a formidable investigation technique because it is non-destructive and it can reveal a lot of structural chemical and physical information from the samples analysed. In recent years it has gained great importance in the analysis of biological samples because of the development of the Raman technique named as SERS (Surface Enhanced Raman Spectroscopy).

The results of the thesis are presented in different chapters that deal with the theoretical concepts related to electrochromism (chapters 1 and 2) and those related to the investigation techniques used during the course (chapter 3). The results of the analyses are set out in Chapter 4. Chapter 5 presents the conclusions and future perspectives.

In the first part of Chapter 4, Raman analyses have been conducted on different polymeric materials such as polymethylmethacrylates (PMMA) and polyethylene oxide (PEO) as well as natural polymers such as chitosan for potential operational (the former) and environmental benefits (the second) that these can bring in the realization of an electrochromic device. Polyelectrolyte materials can be used as an electrolyte layer in electrochromic device, in this thesis work the SERS effect of polyelectrolyte layers on the Raman spectrum of acetic acid has been observed. Chitosan films doped with zinc complex have been analysed by Raman spectroscopy. The interpretation of the results obtained made it possible to establish that the interaction between the natural polymer and the zinc complex takes place at the level of the N-H and O-H groups. Bipyridine

ligands are often used in the formation of metallopolymer molecules with electrochromic properties. In this thesis, the SERS effect of a gold plate on the Raman spectra of bipyridine samples has been studied, showing an interesting improvement of bipyridine Raman signals. Graphite and graphene can improve the conductivity of electrochromic devices by improving their performance. In this thesis work, through the use of Raman spectroscopy, the structural characteristics of functionalized graphite and graphene nanoplates have been shown.

The SERS effect of Ag thin layer on the Raman spectra of deposited 6G rhodamine has been demonstrated. The Raman characterization of TiO_2 films has been shown.

In the second part of Chapter 4, electrochromic devices consisting of an electrochromic solution of viologen and ferrocene to which glycerolate bisphenol A has been added in certain proportions have been developed. The optical properties of the devices have been studied with UV-vis-NIR spectroscopy before and after polymerization induced by exposure to UV light. In particular, the analysis of the transmission properties of the devices in the coloured and transparent states (ON and OFF states, respectively) have been shown. In addition, the electrochemical properties of the devices have been studied by means of cyclic voltammetry measurements that show the differences between the ON and OFF states of the devices.

Concluding remarks have been made in the last chapter of the thesis, with research on electrochromic technology continuing with further structural analysis of materials.

Introduction

In 2017, buildings and appliances were responsible for around 30% of global final energy use. Building energy use increased 0.8% from 2016 and rose 20% between 2000 and 2017. This growth was primarily driven by structural factors such as increases in floor area, occupancy and access to services along with increases in activity, including changes in population, climate and the use of appliances. The two fastest-growing end-uses in buildings are space cooling and appliances. Energy consumption for space cooling has nearly doubled since 2000, driven largely by increased penetration of cooling equipment. Energy intensity per floor area in the residential sector increased by over 80% since 2000. Energy consumption by appliances has grown by 58% since 2000. Space heating, water heating, lighting and cooking have also experienced improvements of more than 20% in energy intensity per floor area since 2000 [1].

In addition, the recent events have product the actual global energy crisis which has driven up the cost of fuel and electricity with the oil prices that hit their highest level since 2008. The price of natural gas reached record highs, and as a result so did electricity in some markets [2].

In order to impose control prices on traditional energy sources, various instruments are being used in addition to the transition to sustainable and renewable energy sources, but once again the topic of energy efficiency is central.

The energy efficiency is defined as the least amount of energy required to perform the same tasks or produce the same results and can bring many significant economic and environmental benefits.

The development of the electrochromic technology can be part of this topic. In fact, an electrochromic device applied to the windows of the buildings could reduce energy consumption by up to 30% because of its intrinsic characteristic: the ability to absorb the IR radiation responsible for the heat carried by light.

The performances of electrochromic devices depends by the ionic and electronic conductivities of the materials used in the devices. Such properties are strictly related to the structural properties of the employed materials which have been deeper investigate by Raman Spectroscopy.

The Raman spectroscopy is a powerful technique, non-invasive and non-destructive which helps to study the evolution of the established interactions between the materials used in electrochromic device construction. Sometimes, in order to promote the Raman response some samples have been studied placed on gold or silver surfaces to use an effect called Surface Enhanced Raman Spectroscopy (SERS). Raman characterizations of thin films systems and single molecular systems have been successfully performed in the last years by SERS.

In the Chapter 1, it is shown a brief introduction on electrochromism effect and materials.

In the Chapter 2, it is shown a description of the electrolyte layer.

In the Chapter 3, the main techniques are descripted. The Raman effect is discussed from a classical and quantomechanical points of view. In the first part of the chapter, the mathematical tools involved in the description are adressed: some properties of matrices are briefly descripted, the description of the polarizability tensor α is also made. In the chapter, there are briefly descripted the UV-vis Spectroscopy and the cyclic voltammetry techniques.

The Chapter 4 is the result and discussion chapter. Here are shown the following works:

- Realization of electrolyte solutions made with the use of Polymethyl methacrylate (PMMA) polymers of different molecular weights and their structural analysis by Raman spectroscopy.
- Raman spectroscopic study of blends made with PMMA and polyethylene oxide (PEO) polymers in different proportions.
- Study of the interaction between folic acid and a polymer made of methacrylic acid (MMA) and ethylene glycol di-methacrylate (EGDMA).
- Analysis of the Raman response of an acetic solution (10% v/v) placed on the top of polyelectrolyte layers applied in combination with gold nanoparticles on glass substrate.
- Raman analysis of chitosan films complexed with inorganic complex.
- Analysis of the Raman response of bipyridine placed on gold plates.
- Raman characterization of functionalized graphite.
- Raman spectroscopic study of graphene nano-plates.

References

[1] International Energy Agency, *Energy Efficiency 2018 Analysis and outlooks to 2040*, https://www.iea.org/reports/energy-efficiency-2018

[2] International Energy Agency, *Global Energy Crisis*, https://www.iea.org/topics/global-energy-crisis

Chapter 1

Electrochromic Effect and Materials

1.1 Electrochromism

Some materials, by application of suitable electric potentials, undergo a change of their optical characteristic. This change is induced by reversible electrochemical oxidation and reduction so the process involved can be described basically as a redox reaction in which the species red_1 and ox_2 are initially in a transparent (bleached) state and, after the potential application, become ox_1 and red_2 switching in a coloured state [1,2]. Indeed, electrochromism is the reversible and visible change in transmittance that is associated with an electrochemically induced redox reaction. It is connected to the visible electronic absorption bands generated by the switching between redox states of the species involved [1-6].

There are several parameters that allow to characterize the electrochromism of an electrochromic device (ECD). One of the most peculiar features of those materials, crossed by incident light, is the transmittance (T) defined as the ability of letting the light crossing through its own body. In ECDs, the transmittance of the bleached state and that of the coloured state can be distinguished. The transmittance is mathematically defined as the ratio between the intensity of the light on each side of the material as shown in figure (1.1.1):

$$T_{b,c} = I_{b,c}/I_0 \tag{1.1.1}$$

Where the subscripts b and c refers to the intensity of the light incident on a bleached or coloured material, respectively.

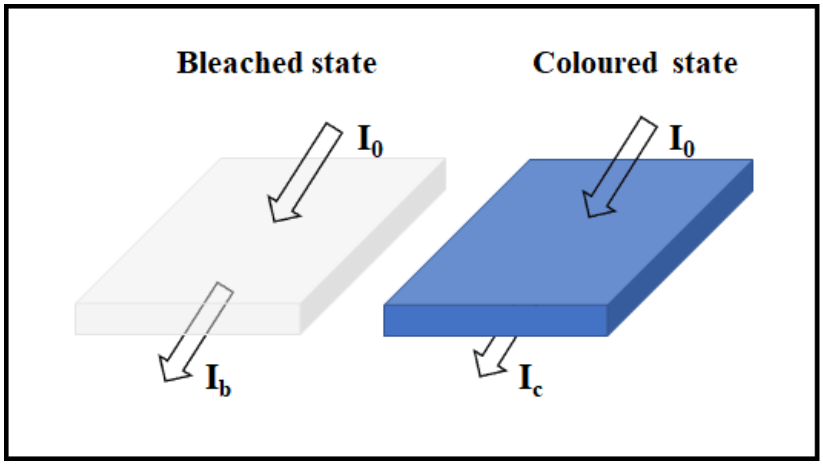

Figure 1.1.1. *Visualization of the light incident and passing through electrochromic devices in bleached and coloured states.*

Another characteristic of the materials is the absorbance related to the transmittance as:

$$A = -\log_{10} T \tag{1.1.2}$$

Similarly to the transmittance, the absorbance of the material in the bleached state and coloured state can be calculated by a suitable insertion of eq. (1.1.1) in eq. (1.1.2:

$$A_{b,c} = -\log_{10} I_{b,c}/I_0 = \log_{10} I_0/I_{b,c} \tag{1.1.3}$$

Absorbance is often called optical density (OD) [7] and related to the concentration of the so-called cromophore and to the length of the light path through the material:

$$A = \varepsilon c l \tag{1.1.4}$$

Where ε is the molar extinction coefficient of the material.

A very important operating parameter of an ECD is the spectral colouration efficiency, defined as CE(λ) that in the visible region is given by:

$$\mathrm{CE}(\lambda) = \frac{\Delta \mathrm{OD}(\lambda)}{Q} = (A_c - A_b)/Q = \Delta[\log(T_b/T_c)]/Q \tag{1.1.5}$$

Where Q is the injected charge per unit area and is proportional to the number of colour centres. The colouration efficiency, also called as electrochromic efficiency depends strongly on the sample preparation. The colouration efficiency is postulated to be positive from cathodically induced colouration and negative for anodically induced colouration. The colouration efficiency of a complete ECD CE_0, if CE_p and CE_s are respectively the primary and the secondary electro chromophore, will be given by:

$$\mathrm{CE}_0 = \mathrm{CE}_\mathrm{p} - \mathrm{CE}_\mathrm{s} \tag{1.1.6}$$

In addition to the parameters just discussed, there are other valuable features that describe the behaviour of the electrochromic devices: the switching time, the contrast ratio, the write-erase efficiency, the optical memory and the cycle life.

The switching time is the time taken by an ECD to reach the maximum colouration when the electrical field is switched on. It is possible to obtain an average value of the switching time by knowing the active surface of the ECD [8].

The contrast ratio is defined by:

$$CR = R_b/R_c \tag{1.1.7}$$

Where R_c is the intensity of the light diffusely reflected through the coloured state of the display and and R_b is the intensity of the light diffusely reflected from the bleached state with a white back plate.

The write erase efficiency is the percentage of the originally formed colouration that may be subsequently electro-bleached and is conveniently expressed as a ratio of absorbance changes [9].

The optical memory is defined as the time taken by an ECD to return in its bleached state from the coloured state after the removal of the electric field. In other words it is the time spent in its coloured form after the removal of the field [4,10]. Optical memory is very pronounced in the solid-state electrochromic devices.

The last characteristic, the life cycle of an ECD, is a measure of the stability of the devices. The life cycle is simply the number of time that an electrochromic device can be coloured and bleached, that is a cycle, before the appearance of deterioration.

1.2 Electrochromic devices

Electrochromic (EC) materials can be initially studied at a single working electrode, using potentiostatic or galvanostatic control and a three-electrode system with counter and working electrode in electrolyte liquid. For characterization, some electrochemical techniques are employed like coulometry, cyclic voltammetry, chronoamperometry sometimes, when required, together with in situ spectroscopic measurements [1,2]. In an electrochromic device the active species is a layer said electrochromic electrode or working electrode (as in a rechargeable battery) separated from a counter electrode (that is a charge balancing) with a convenient liquid or solid electrolyte. The colour change happens when applying the electric potential and charging and discharging the electrochemical cell [2]. A schematic diagram of an electrochromic device is shown in figure (1.2.1).

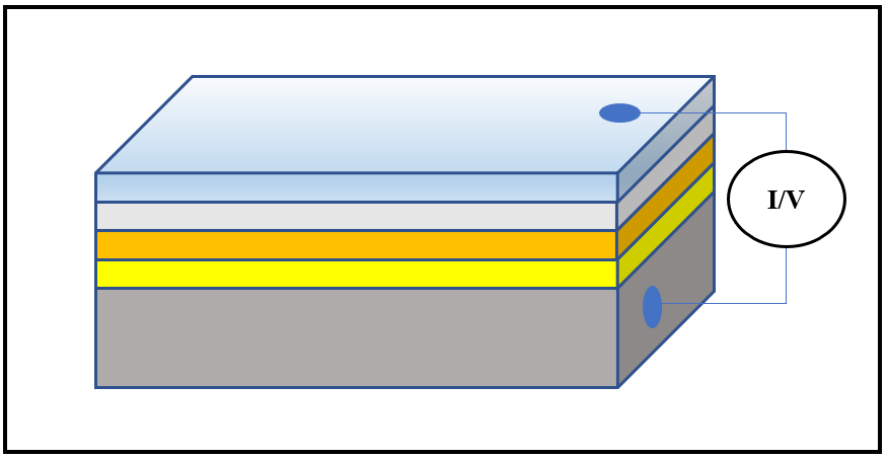

Figure 1.2.1. *Schematic configuration of an electrochromic device. The pale blue layer is the transparent glass, the pale grey is the ITO layer, the electrochromic material is the orange layer, the electrolyte is the yellow layer, the counter electrode is the grey layer.*

The electrochromic devices can work in transmissive or reflective mode (see Fig. 1.2.2) and the EC material must be coated with a transparent conductive glass.

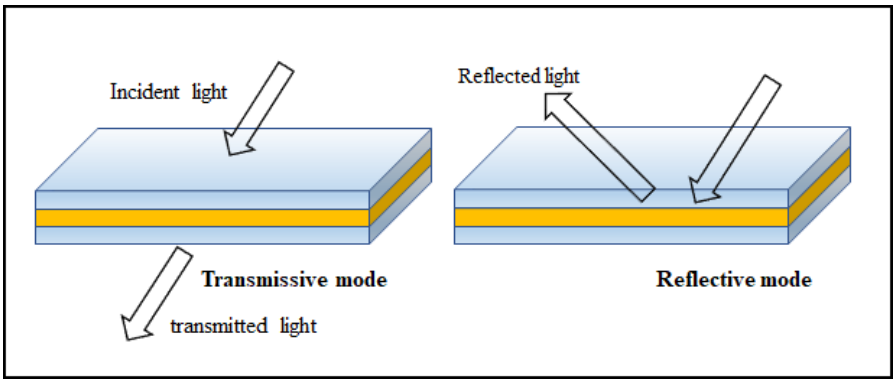

Figure 1.2.2. *Transmissive and reflective modes of operation of an ECD. The pale blue are ITO glass layers and the orange layers are the electrochromic material.*

In electrochromic devices that operate in reflective mode, the counter electrode can be of any material that provides a reversible electrochemical reaction. However, in variable light transmissive electrochromic devices (like the smart windows), the counter electrode is generally the transparent indium-tin-oxide (ITO) glass with the counter electrode chemical species that as to be either transparent in redox states or electrochromic but in a complementary way with the electrochromic material [2]. Electrochromic materials are said cathodic or anodic if the colour switching occur during reduction or oxidation respectively.

The species involved in process can be classified according to their nature for which three kinds of electrochromic devices can be identified [11]:

- Electrochromic materials of type 1: the species are always in solution during process.
- Electrochromic materials of type 2: the species are initially transparent and in solution and, after electric tension application, they form a solid layer on electrode surface.
- Electrochromic materials of type 3: The species are deposited on electrode as thin films.

Furthermore, electrochromic materials can be grouped in three general classes: the first one is represented by the transition metal-oxides, the second one is composed by organic compounds and the last one is made up of intercalated materials [3]. The subsequent paragraphs describe these materials.

1.3 Class 1 of Electrochromic materials: the transition metal oxides

The transition metal oxides (TMO) are commonly classified under inorganic materials. Since the first report in the 1960s of the electrochromic behaviour of the tungsten trioxide (WO_3) [4,12], several others TMOs in the form of thin films have shown electrochromic properties like molybdenum [1], nickel [1], iridium [13,14], rhodium [15], ruthenium [16], cobalt [17]. Thin films are generally prepared using deposing techniques on glass substrates as sol-gel method [18,19], chemical vapor deposition (CVD) [19,20], vacuum evaporation [21], sputtering [22], electrodeposition [23] or electrostatic spray-deposition (ESD) [24]. The principal characteristic of TMO's films is the capacity to be electrolytically commuted to a non-stoichiometric redox state which possess an intense electrochromic absorption band due to the charge transfer in the optical intervalence [2,4,9]. The most studied TMO is tungsten trioxide (WO_3) which has a roughly cubic structure which is best represented with an empty perovskite type formed by WO_6 octahedra sharing corners. The structure has empty spaces that allow to host guest ions (like Li^+) in the interstitial sites. The oxidative state of all tungsten atom in the structure is W^{VI} and the film is transparent, when electrochemical reduction to the W^V state occurs, the new oxidative state generates the electrochromic effect.

The explanation of the mechanism of coloration of the tungsten trioxide film is still subject to controversy but the process of injection and extraction of electrons and metal cations (Li^+, H^+, etc.) is nowadays widely accepted. However, it is pointed out that there are other models, as the non-localised electron model, that can explain the mechanism and whose description goes beyond the scope of this thesis [2,25,26]. Tungsten trioxide is a cathodically ion insertion material, consequently the blue coloration in the reduced form of the WO_3 thin film can be erased by electrochemical oxidation. If the inserted cation is Li^+ the electrochemical reaction can be written as follows:

$$WO_3 + x(Li^+ + e^-) \rightarrow Li_x W^{(VI)}_{(1-x)} W^{(V)}_x O_3 \qquad (1.3.1)$$

While the generalised reaction is:

$$WO_3 + xM^+ + xe^- \rightarrow M_x WO_3 \qquad (1.3.2)$$

The subscript in eq. (1.3.2) indicates the fractional number of sites of the WO_3 lattice filled by the metal cations. For low values of *x*, the films have an intense blue coloration

because of the photo-effected intervalence charge transfer process between adjacent tungsten atoms with different oxidation numbers. However, insertion of cations may become irreversible at higher values of *x*. The mechanism generates a metallic "bronze" which is red or golden in colour and it is promoted by cathodic polarization which induces insertion of ions and injection of electrons. In this manner, the inserted ions expand the lattice of the tungsten oxide while the electrons modify its optical properties. The injected electrons are trapped by a W^{VI} forming a W^{V} and in while M^{+} remains ionized in the interstitial spaces of the WO_3 lattice. The process gives rise to the tungsten bronze that possesses optical and electrical properties very different from those of the original WO_3. Indeed, the oxidized initial state of WO_3 has a pale-yellow colour and is a poor electrical conductor, while the reduced form (that is an intercalated $MxWO_3$ state) becomes highly conductive and it is blue in colour with absorption spectra of 0.5/0.6 μm. This model somehow implies delocalization of electrons because it could explain the enhancement of the conductivity observed during the insertion process. On figure (1.3.1) (reproduced from reference [2]) are shown the optical transmittance (a) and the cyclic voltammetry (b) of a WO_3 electrode. The measurements have been effectuated with a cell in which the Li^{+} ions act as the conducting electrolyte and the counter electrode is made of Li [2,25].

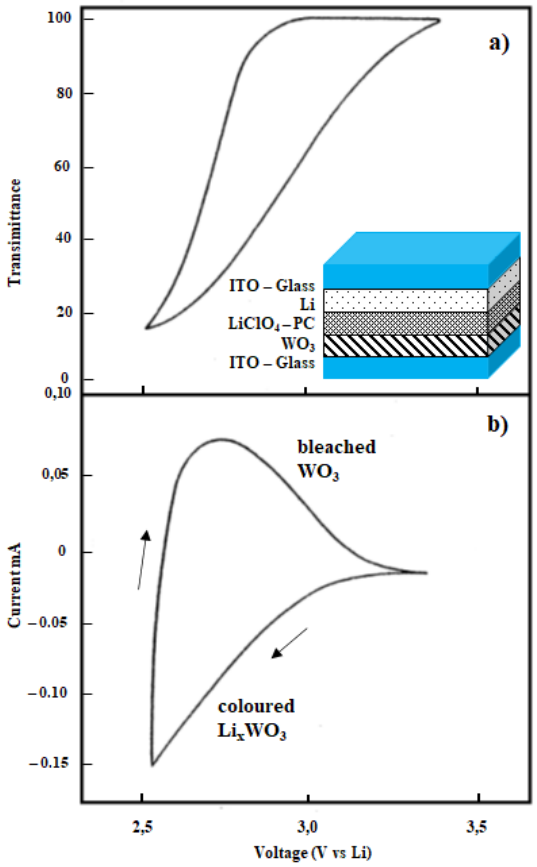

Figure 1.3.1. *Optical transmittance (a) and cyclic voltammetry (b) of a WO_3 electrode in a $LiClO_4$ – Propylene Carbonate (PC) solution. Light source: He – Ne laser (632.8 nm), scan rate: 20 mV/s, sample thickness 60 nm; reproduced from* reference [2].

Comparing the extrapolated optical and electrochemical response of the WO_3 electrode, it is possible to investigate the characteristics of the electrochromic process.

With the cathodic scan, the current can flow through the WO_3 electrode determining the generation of the bronze Li_xWO_3 species and the blue colour. The direct consequence of the blue colour is the decay of the transmittance to a minimum value that corresponds to the voltametric peak. The process is at this stage easily reversable: the Li^+ ions are removed with an inverted scan, so that the initial pale-yellow tungsten oxide is restored. Furthermore, the process can be repeated a large number of times but the observation of the voltammograms of the electrochemical process allows to notice slight differences between the initial cycle and the subsequent cycles. In figure (1.3.2) (reproduced from reference [2]) are shown the voltametric curves relative to the initial cycle (a) and to a stabilised cycle (b) of the insertion process [2,25].

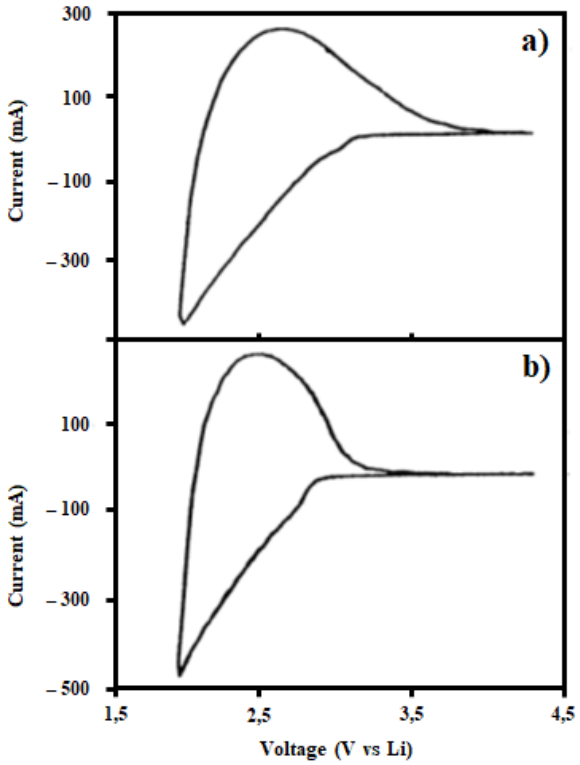

Figure 1.3.2. *Voltametric curves of the initial cycle (a) and a stabilised cycle (b) of a WO_3 electrode in a $LiClO_4$ – PC solution. Scan rate: 20 mV/s; sample thickness 250 nm; reproduced from reference* [2].

It can be deduced by observing the curves of Fig. (1.3.2) that the process evolves through an initial and permanent absorption of M^+ ions which is crucial for the subsequent process of reversable insertion – withdrawal reactions. The criticality of the initial step depends on the nature of the material that will undergo the electrochromic reaction because for some materials the cyclability depends strongly on it.

The high spectral coloration efficiency, together with the reversable clear to deep blue colouration, have made the amorphous tungsten oxide thin films the most important EC material and as well as the viologens that we will talk about later, is of great interest.

The many insertion/extraction films can be compared evaluating some of the operative parameters described in section 1.1. The CE(λ) is defined by eq.(1.1.5), where ΔOD represents a change in single pass, as cm^2/C, it depends strongly on the sample preparation and may vary from 40 to 100 cm^2/C. The switching time can contemporaneously vary from milliseconds up to few seconds. The life cycle, which is function also of the electrolytes that can be used to assemble the devices, can reach up to 10^6 cycles.

Many studies have been performed on electrochromic properties of WO_3 because of the possible commercial applications. In the optics of improving the operative parameters of ECD based on WO_3, several studies on the doping of pure films of WO_3 with other TMOs like TiO_2 and with metal ions like the use of europium (Eu^{3+}) have been published. The doping of WO_3 results in a best contrast ratio, a faster switching time and higher CE when compared with undoped WO_3 films [27-29]. In addition, the tungsten trioxide films have also been combined with other TMO films as Nb_2O_5, NiO, Mn/Ni oxides composite films, Ta_2O_5, V_2O_5 and other electrochromic materials conducting polymers (CPs), in order to make ECDs [29-34].

1.3.1 Polyoxometalates

The 3D structures made of three or more transition metal oxyanions linked together by shared oxygen atoms are known as polyoxometalates (POMs). The structures involved can have different variety of nuclearities, size and shapes due to the presence of up to hundreds of transition metals of group 5, and rarely group 6, in high oxidation states such as W, Mo, Nb, V, Ta etc. The electrochromic behaviour of the POMs is due to the mixed-valence coloured state species present in the lattice. The oxygen-to-metal (O → M) and ligand-to-metal charge transfer (LMCT) transitions do not cause any structural changes on the species. The d^1 electrons in the (O → M) enhance the absorption of visible light thanks to the intervalence CT among metal centers and d–d transitions. The POMs can be seen as electron reservoirs with high chemical and UV stabilities [29].

Among the possible several advantages of POMs over the organic and inorganic metal oxides, due to the possibility of tuning their EC properties through molecular design, a critical step is represented by their great solubility in water and in many organic solvents. The approach to make insoluble POM electrochromic films for liquid electrolyte-based ECDs, consist in the addition of a stabilizer in order to elude dissolution of the electrochromic POM into the liquid electrolyte. Moreover, the POMs EC films casted through solution evaporation are nonuniform and result in inhomogeneous aggregate formation that compromise the transparency of the film. In addition, POMs are very sensible to high temperatures because of the wreckage of their crystalline structures. The POM EC films are prepared using spin coating, layer by layer, and electrodeposition methods [29].

To this day, several polyoxometalates with EC behaviour have been reported. In particular, peroxo-polymolydotungstates in organic PC Li electrolyte-based ECD have shown reversable coloured and bleached states [35]. The problematic dissolution of PMOs in water and common organic solvents has been overtaken with the combination of the polyoxoanion $SiMo_{12}O_{40}^{4-}$ with the organic cation $[(CH_3)_2NC_6H_4(CH_3)_2]_4[(C_4H_9)_4N]^+$ [36]. Other POMs made with Mo have been reported in other publications [37,38].

1.3.2 Prussian blue

The coordination complex iron(III) hexacyanoferrate(II) known as Prussian blue (PB) is the prototype of class of polynuclear transition metal hexacyanometalates with general formula $M'_k[M''(CN)_6]_l$ (with k and l integers) where M' and M'' are transition metals with different oxidation numbers. Hexacyanometalates are generally insoluble mixed valence compounds. The charge/electron transfer take place between the atoms of given elements that have two different oxidation states. In the PB, that is a ferric ferrocyanide, a high-spin ferric ion is coupled to a low-spin ferrous ion by a cyanide bridge in which the ferric ion is coupled to the nitrogen atom and the ferrous ion to the carbon atom: Fe(III)–N≡C≡Fe(II). For a long time PB has been used in many domains as an inorganic pigment. However, the electrochromic properties of the PB have not been knew although its large use. The redox behaviour of the PB has been investigate at first time in 1978 with the preparation of thin films on platinum and gold electrodes [2,39,40]. The colourless reduced form of PB is known as Everitt's salt or "Prussian white" (PW) and is an iron (II) hexacyanoferrate (II), while there are two forms of oxidize PB. The completely oxidized form is known as "Prussian brown" (PX) (it is somewhere depicted as "Prussian Yellow (PY)) and is an iron (III) hexacyanoferrate (III), while the partially oxidized form is known as Berlin green or "Prussian green" (PG) and is a combination (1:2) of PB and PX [2,29,41]. The formation of PB films is generally made by electrochemical reduction of solutions containing Fe (III) and hexacyanoferrate(III) ions. Electrodeposition of PB is achieved principally by electron transfer process in the reduction of the soluble PX complex, in equilibrium with the above ions as in the subsequent equation [2,41]:

$$[Fe^{III}Fe^{III}(CN)_6] + e^- \rightarrow [Fe^{III}Fe^{II}(CN)_6]^- \qquad (1.3.3)$$

(PX) (PB)

Electroneutrality of the PB films is achieved with the presence of charge compensating cations that can be either Fe^{3+} or K^+ if the potential cycling is made with supporting electrodes that contain potassium. The equilibrium relative to the partial oxidation of PB in pure supporting electrodes lead to the formation of PG and could be represented by [2]:

$$\underset{\text{(PB)}}{3[Fe^{III}Fe^{II}(CN)_6]^-} \rightarrow \underset{\text{(PG)}}{[Fe^{III}\{Fe^{III}(CN)_6\}_2\{Fe^{II}(CN)_6\}]^-} + 2e^- \quad (1.3.4)$$

The above composition of the PG is the believed one for the bulk composition while in the thin films the continuous composition range between PB and PX lead to the golden yellow fully oxidized form.

Electrochemical oxidation of PB may forms the Prussian brown as in the following way:

$$\underset{\text{(PB)}}{[Fe^{III}Fe^{II}(CN)_6]^-} \rightarrow \underset{\text{(PX)}}{[Fe^{III}Fe^{III}(CN)_6]} + e^- \quad (1.3.5)$$

The reduction of PB yields PW which appears transparent as a thin film:

$$\underset{\text{(PB)}}{[Fe^{III}Fe^{II}(CN)_6]^-} + e^- \rightarrow \underset{\text{(PW)}}{[Fe^{II}Fe^{II}(CN)_6]^{2-}} \quad (1.3.6)$$

Electroneutrality of the above redox reactions (eqs. 1.3.3-1.3.6) is achieved with the concomitant ingress or egress of suitable ion in the film.

At this day, many ECDs based on the use of PB have been realized and characterized. As examples, the PB has been used as a sole EC material in a solid-state system based on a PB-containing Nafion composite film [2,42] and in a seven-segment display with the use of a PB-modified SnO_2 working and counter electrode [2,43]. A self-powered ECD PB/aluminium-based with intense colour but long switching times has been reported [29,44]. Thin films of PB analogues of Co, Cu and Ni have been reported and ECDs were made with their use [29,45].

1.4 Class 2 of Electrochromic materials: Organic EC.

Organic materials are known to exhibit some electrochromic behaviour. The viologens are a class of material that we will discuss later and that have been studied for their electrochromism in display devices and smart windows. The colouration of the organic species is achieved by a redox reaction, generally in a liquid solution, with a coupled material that undergoes the opposite redox reaction. The coupled material could be transparent at the oxidation state determined by the redox reaction or coloured in a complementary way to the primary organic EC. Other class of materials such as pyrazoline, biphenyl anthraquinoides and tetrathiafulvalene (TTF) systems and organometallics such as phthalocyanines of lanthanides and polytungsten anions show electrochromism and have been researched [3].

The mechanism of the organic electrochromic reactions can be listed in three types [3]:

- Type 1: a simple redox reaction which gives a coloured species.
- Type 2: a redox reaction coupled with an independent reaction leading to variable colour persistence.
- Type 3: the coupled action of a redox reaction with a chemical reaction induces the generation of an insoluble coloured species which affords a memory effect.

The drawbacks of the type 1 mechanisms, which are the simplest electrochromic processes, lies in the drift or diffusion of the coloured species, which could still be suppressed by the use of gel electrolytes. In the type 2 mechanisms, the colour drift is eliminated by conversion back to the bleached material, for example by oxidation. However, the continuous refreshing to maintain the coloured state represents a great drawback resulting in a reduced efficiency. The type 3 is the most attractive because of the energy saving due to no need to refresh continuously. The coloured species generated by the redox reaction are insoluble in the electrolyte, which make the ECDs stable. The only inconvenient is due to the reverse leakage current that can affect the long-term colouration [3].

1.4.1 Viologens

The viologen family consists of 1,1'-disubstitutes salt derivatives of the 4,4'-dipiridyum compounds ($C_{10}H_8N_2$) [2,3,46]. The general structures of the viologen molecules is

showed in figure (1.4.1) that illustrates the typical two-steps redox reactions involving one (1.4.1.b) or two electrons (1.4.1.c). The dication (Fig.1.4.1a) is the most stable redox state and is colourless if pure. In the radical form (Fig. 1.4.1.b) they are blue and generally reversable on oxidation, the stability of this redox state is related to the delocalization of the radical electron throughout the π-framework and to the delocalization of the positive charge that involves the 1,1' substituents which bear some of the charge [46]. The completely reduced form (Fig. 1.4.1.c) is electrochemically irreversible in the case of methyl viologen (MV) [2] or form an insoluble salt of bromide in the case of diheptylviologen – dibromide [3], two of the most studied viologens. In general, the insolubility of the radical cation and of the completely reduced form of the viologen is related to the length of the alkyl chain: the longer is the alkyl chain, the more insoluble they are [46].

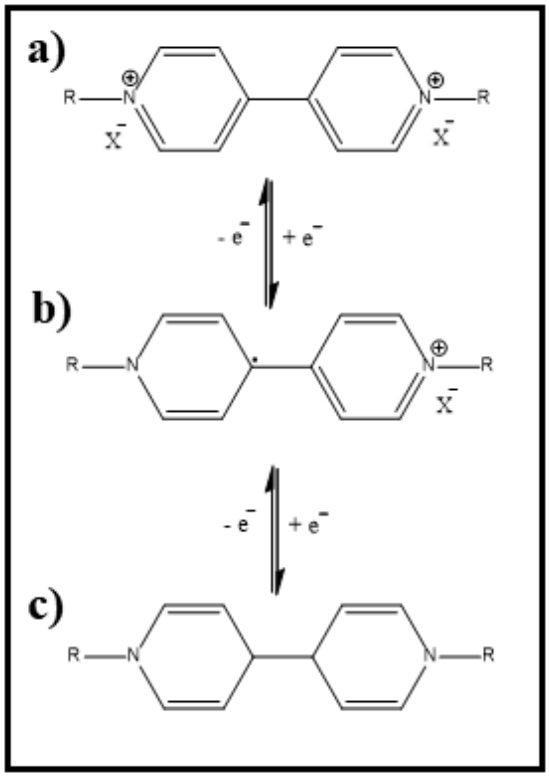

Figure 1.4.1. *Molecular structure of the viologen in the redox state: a) dicationic form; b) radical form; c) fully reduced form. R is a substitute (alkyl, cyclo-alkyl or other) and X is a halogen.*

The radical cation form of the viologens often show dimerization in aqueous solutions and at low temperatures in non-aqueous solutions. The diamagnetic dimers possess different spectral properties compared to the monomers (as example, the MV monomer is blue while the dimer is red) and can make electrochemical oxidation quite difficult [46].

1.4.2 Conducting Polymers

Aromatic organic molecules, mostly rings, are notoriously very stable due to the phenomenon of resonance that results in the delocalization of π–electrons. The chemical/electrochemical oxidation of numerous aromatic molecules produces electronically conducting polymers (CPs) [2,46]. The formation of CPs is achieved through generation of a radical cation species by an oxidative polymerization of monomers. At this stage, the mechanism involves either radical–cation / radical–cation coupling or direct attack of the radical–cation on a neutral monomer [46].

The oxidized states of CPs are doped with counter anions (p-doping) and possess a delocalised π–electron band structure. The energy gap between the highest occupied π–electron band (namely the valence band) and the lowest unoccupied band (the conduction band) determines the optical properties of the materials. The reduction of CPs with concurrent counter anions exit removes the electronic conjugation, to give the undoped and neutral electrically insulating form. CPs can also be cathodic–doped with cation insertion to balance the injected charge, in this case it is talked about n-doping [2,46].

CPs are potentially electrochromic materials in thin film forms, furthermore they offer the advantage of a hight degree of colour selection realized through the modification of various polymer systems via monomer functionalization and copolymerisation as well as the use of blends, laminates and composites [2]. The electrochromic changes are due to the redox switching that generate the new optical absorption bands in accompaniment with transfer of electrons/counter anions. The colour exhibited by the polymer is closely related to the band gap and the dopant ions. For this reason, there are three routes that allow the control of the colour. The first one is directly related to the polymer's band gap (defined as the onset of the π–π* transition) which is a function of the HOMO and LUMO relative energies. The suitable substitution of the polymer's repeat unit allow the determining by the substituents of the effective conjugation length and of the electron density of the polymer backbone. The second method is given by copolymerization of distinct monomer or homopolymerization of hybrid monomers containing several distinct units. The result is the observation of interesting combination of the single properties belonging to each homopolymer. Blends, laminates and composites offer a third method, similar to copolymers, for combining the electrochromic properties of several systems

[2]. Polypirrole, polyaniline and polythiophene are examples of CPs briefly descripted below.

Polypyrrole

The electrochemical polymerization of pyrrole can lead to the formation of Polypyrrole (Ppy) thin film, first species described here of the class of organic conducting polymers (CPs). The mechanism of polymerization involves oxidation and dimerization of pyrrole followed by aromatization and oxidation of the dimer, figure (1.4.2). The doped (oxidized) Ppy thin film is blue-violet while the electrochemical reduction produces a yellow-green undoped form. The removal of all dopant anions yields a pale-yellow film, however complete dedoping is achieved only for extremely Ppy thin films. So, in the construction of ECDs the required dimensions lead to low contrast ratio. Furthermore, the repetitive cycles of colour switching endured by ECDs cause the degradation of Ppy film [2].

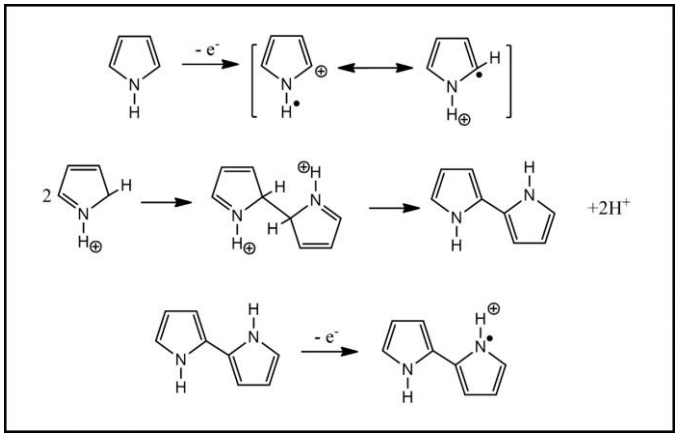

Figure 1.4.2. *Mechanism of the polymerization of pyrrole.*

Polyaniline

The polyaniline are an extensively studied species belonging to the class of CP. The electronic and electrochromic characteristics of the polyaniline depends obviously on its oxidation state but also on its protonation state. The interconversion pathways between the various forms of polyaniline related to its different redox states are showed in figure (1.4.3), the redox mechanisms shown involving the protonation–deprotonation of the polyaniline and/or anion ingress/egress [2,46]. Polyaniline films (PANI) are polyelectrochromic showing multi colour switching (transparent–yellow–green–dark blue–black), the yellow–green transition being very stable to repetitive colour switching [2,46]. The PANI possess two spectral bands at ≤330 nm (related to an aromatic π–π*

transition) and one at ≤440 nm (related to the formation of a radical cation in the polymer matrix). Application of increasing potential causes the absorbance decreasing of the lower band and the increasing of the last one. The ≤440 nm band decrease as a broad free carrier electron band ~800 nm is introduced. Great attention has been given to polyanilines with alkyl substituents because of the generally enhanced stability of the polyelectrochromic properties and in particular in the case of the poly(*o*-toluidine) and poly(*m*-toluidine) films. The lower conjugation length of poly(toluidines) causes the shift of redox potentials and of absorption maxima compared to the polyanilines [46].

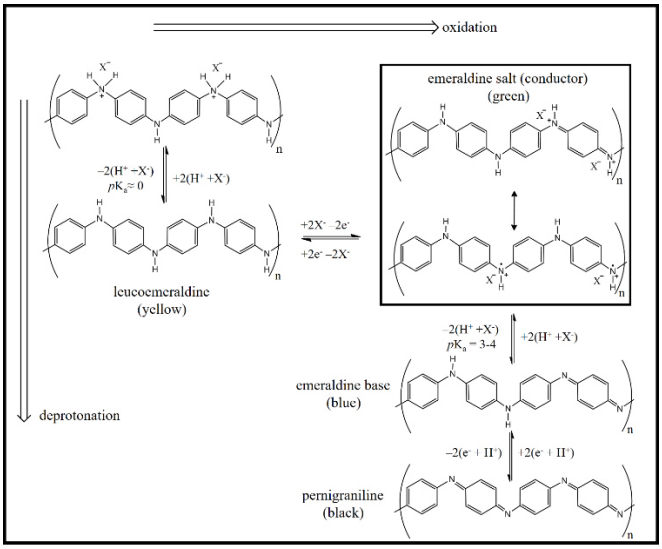

Figure 1.4.3. *Interconversion pathways of the forms relative to the various redox states of polyaniline*.

CP films of low surface area are relatively well prepared by electrochemical polymerization but the technique seems to be not suitable for larger areas. For the realization of large area, solution casting method or relatively easier techniques such as spin coating and dip coating represent better solutions and for this reason, synthesis of soluble polyanilines, such as poly(*o*-methoxyaniline), has been performed.

Polythiophene

The electrochromic properties of polythiophene are of special interest because of their chemical stability, ease of synthesis and processability. Like Ppy, polythiophene films can be prepared by electrochemical polymerization of thiophene. In thin film form, polythiophene possesses a blue colour (λ_{max} = 730 nm) in the oxidised state, and a red clolour (λ_{max} = 470 nm) in the reduced state. An important characteristic of polythiophenes is the possibility to tune the colour states in function of the thiophene monomers. Indeed, subtle modifications to the monomers can significantly modify spectral properties. An example is given by the 3-methylthiophene based oligomers for

which the relative position of methyl groups on the polymer backbone determines the colour availability. The available colours in oxidised states are blue, pale blue and violet while in the reduced states they are yellow, orange, red and purple [2,46].

Poly(3,4-(ethylenedioxy)thiophene) (PEDOT) is used in fabrication of materials that possess a band gap lower than those relative to simple polythiophene and alkyl-substituted polythiophene. Because of the lower band gap, PEDOT possesses an absorbance that is maximum in the near infrared region of the spectrum. In general, the substituted polythiophenes possess an exceptional stability in the doped state that is associated to an hight conductivity. Doped PEDOT is almost transparent in the visible region of the spectrum and coloured in the neutral state. Because PEDOT and its alkyl-substituted polythiophenes are cathodically electrochromic materials, they can be associated to anodically electrochromic materials to make ECDs [46].

1.4.3 Metallopolymers

A relatively new class of organic electrochromic materials is made of transition metal coordination complexes of organic ligands, because of the interesting chromophoric properties related to their intense colouration and redox reactivity. The mechanism involved in their chromophoric properties relate to the low-energy metal-to-ligand charge transfer (MLCT), the intervalence CT, the intraligand excitation and the relative visible-region electronic transitions. These transitions involve valence electrons and the reduction of the complex defines the alteration or elimination of the chromophoric characteristics. The spectroscopic and redox properties of the transition metal complexes would be sufficient for their direct use in solution phase ECDs, however polymeric systems have also been studied for potential use in all-solid-state systems. The reductive and oxidative electropolymerisation of polypyridyl complexes schemes have been described in the preparation of thin film metallopolymer. The reductive electropolymerisation technique is possible because of the ligand-centred nature of the three sequential reductions of complexes such as $[Ru^{II}(vbpy)_3]^{2+}$ (vbpy = 4-vinyl-4'-methyl-2,2'-bipyridine) in combination with the anionic polymerisability of suitable ligands like vinyl-substituted pyridyl ligands (Fig. 1.4.4) [46].

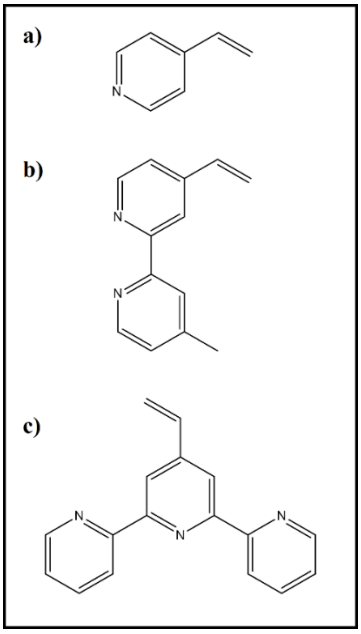

Figure 1.4.4. *Structures of various vinyl-substituted ligands. a) 4-vinyl-pyridine (vpy); b) 4-vinyl-4'-methyl-2,2'-bipyridine (vbpy); c) 4'-vinyl-2,2':6',2''-terpyridine (vtpy).*

Metallopolymers have been formed also with chloro-substituted pyridyl ligands, via electrochemically initiated carbon-halide bond cleavage. For either case, electrochemical reduction of the metal complexes determines the formation of radicals that are responsible of the generation of new carbon-carbon bond and oligomerisation. Because of their insolubility over a critical size, they are the oligomers that form the thin films of the electroactive metallopolymers on the electrode surface. Suitable choice of the metal could select the colour of the metallopolymer thin films. Electrochromicity results from loss of the MLCT absorption band on switching between the M(II) and the M(III) redox states [46].

Oxidative electropolymerisation has been employed with iron(II) and ruthenium (II) complexes with different 2,2'-bipiridyl ligands, amino and pendant aniline, and 2,2':6'2''-terpyridinyl ligands, amino and hydroxy-substituted [47-49]. A reaction mechanism similar to that of aniline has been suggested by the study of IR spectra for the electropolymerisation of the complex bis[3-(aminophenyl))-2,2':6,2''-terpyridinyl]iron(II). The colour switching on oxidation of modified electrode reversibly occur from purple, Fe(II), to pale rose, Fe(III). In the case of polymeric films of tpy substituted with an hydroxyphenil in position 2, the colour switch from brown to dark yellow, this colour probably due to an absorption band at 455 nm because of the quinone moieties that are formed during electropolymerisation. The IR spectra confirmed the

absence of hydroxyl groups in the brown films. Also oxidative polymeristion of complexes of the type $[M(phen)2(4,4'\text{-bipy})2]^{2+}$ (M = Fe, Ru, or Os; phen = 1,10-phenanthroline, 4,4'-bipy = 4,4'-bipyridine) give rise to matallopolymer films that result both oxidatively and reductively electrochromic [46].

1.5 Class 3 of Electrochromic materials: Intercalated materials.

Intercalated materials refer to the use of intercalated graphite for electrochromic materials [3]. As known, graphite is opaque and is not suitable for electrochromic applications such as smart windows, however the intercalated structures have been studied for the synthesis of electrochromic materials [3,50]. Intercalation of graphite has been performed historically by gas-phase reaction with alkaline metals. In this way, the intercalation of the metals between layers of graphite lattice does not change the crystallographic order of the graphite planes. Metals form different stoichiometric compounds such as C_6Li, $C_{12}Li$, C_8M, $C_{24}M$, $C_{36}M$, where M = K, Rb and Cs. Intercalation can be performed in phases in which, at higher stages, fewer interlayer spaces are occupied by metallic compounds. The stage number represents the number of carbon planes between intercalate planes, the lowest is 1 and is characteristic of C_6Li and C_8M. The stages possess different optical and colouration properties that are related to the electrochromic properties of the material. Intercalation compounds are formed by electrochemical means and in stages depending on the applied potential. The general reaction can be written as follows: $C_z + e^- + M^+ \rightleftharpoons C_z^- M^+$, where M^+ is an alkali metal ion and z represents the stage parameter [3,51]. The cell is made off a graphite back electrode while the front counter-electrode is a metal or graphite or a conductive transparent oxide. The layer between the electrode is a water-free aprotic electrolyte such as dimethyl sulfoxide. The control on the applied potential between 3 and 5 V allows the colouring of the cell ranging from the blue/black to the green and golden yellow, while reversing the polarity the colour switch again on black [3].

1.6 Hybrid Electrochromic Materials

Hybrid materials have received great attention from the scientific community due to their physical characteristics that combine the elasticity of organic polymers and the hight thermal and chemical stability of the inorganic materials. These kinds of materials can be placed in two categories [52]:

- hybrid materials of type 1: weak interactions such as Van der Walls forces and hydrogen bonds are characteristic of these materials.
- hybrid materials of type 2: in these materials strong interactions between inorganic and organic materials take place.

Hybrid materials have been studied for long time in combination with conductive polymers to form nano-structured hybrid electrochromic materials. The reason is to be found in the fact that in some hybrid EC materials fast switching speeds have been reported. In contrast, such materials have high contact resistance between the rigid nanostructures and very low colouration efficiency compared to conjugated polymer. In the other hand, electrochromic materials made off conjugated polymer as active layer still have low lifetime that poses serious problem for practical applications. So, the combination of the aforementioned positive characteristic of conjugated polymers and inorganic material could lead to a hybrid electrochromic material with good lifetime and colouration efficiency and rapid colouration switching times [52].

1.6.1 Nanocomposites as Type 1 Hybrid Materials

This category of hybrid materials includes nanocomposites with only some physical interactions between organic and inorganic materials. In the recent years, many studies have been reported on the blends of conjugated polymers with metal oxides. The incorporation of graphene or carbon nanotubes (CNT) as well as conductive metallic nanoparticles (Ag and Au) into conjugated polymer have been also reported. In general, such nanocomposite materials show improved electrochromic performances compared to normal conjugated polymers. Higher colouration efficiencies are due to the reduced charge transfer resistance mediated by the conductive nanoparticles such as CNT and graphene while the faster switching speed is due to the highly porous structure of the nanofillers such as metal oxides that ensure shorter diffusion length.

It is the main effort of the scientific community to improve the favourable properties and at the same time reduce the limiting properties of the components of the blends. One way to achieve these characteristics is to obtain a hybrid material with strong interfacial interactions by means of large interfacial areas.

In situ processes with use of organic acids have been employed in the fabrication of well-dispersed inorganic moieties into conjugated polymers and in the realization of large surface areas that enhance the interfacial reactions. Another process to obtain large surface areas is given by layer-by-layer (Lbl) assembly although the very restricted number of inorganic nanoparticles with suitable properties has limited the use of this technique [52].

1.6.2 Hybrids Materials of Type 2: strong interfacial interactions

This type of hybrid material are made following three issues:

- Firstly, enhancing of ion-transport properties by the control of the conjugated polymers structures.
- Secondly, enhancing of the electron-transfer between the chain of the conjugated systems.
- Last, enhancing of the donor-acceptor interactions between the organic and inorganic phases.

The ion-diffusion process, complicated by the rigid crystalline structure obtained by parallel packing of the conjugated chains, is responsible of the kinetics of colouration and bleaching processes of EC polymers. In order to facilitate the process, hybrid EC materials with star like geometry have been synthetized, with the use of polyhedral oligomeric silsesquioxane (POSS). Studies of POSS incorporated in a copolymer with PANI and doping of poly(styrenesulfonate) PSS with this copolymer have been reported which have improved EC characteristics [52].

The interaction between Ppy chains and octal(thiophenephenyl) silsesquioxane showed improved electrochromic properties of Ppy and nanocomposites of PEDOT embedded with fluoroalkyl phosphate based ionic liquid functionalized graphene (ILFG) and reduced graphene oxide (RGO) exhibit enhanced EC properties with respect to the PEDOT-RGO. The star like geometry has been combined with the Lbl assembly in the realization of a device made by multilayer thin films of copolymer POSS-PANI and

poly(2-acrylamidomethane-2-propanesulfonic acid) (PAMPS). Lbl assembly has been used in the realization of thin films made of water-soluble viologen-bridged polysilsesquioxane nanoparticles (PXV NPs) and PAMPS. The obtained solid state complementary electrochromic device was characterized by fast switching speed and high optical contrast. The substitution of PAMPS by sulfonated polyaniline (SPANI) in the multilayer thin films device leads to further enhancements because of the strong interactions between the POSS-PANI copolymer layer and the SPANI layer [52].

PANI has been used in the preparation of single-walled-carbon nanotube (SWCNT) covalently bonded to the conductive polymer. The resultant hybrid material has been uniformly dispersed in PSS-doped PANI matrix determining an improvement of the electron transport and of the interactions between SWCNT and PANI leading to an additional doping effect, improving colouration efficiency and switching kinetics as well as reducing the oxidation potential of PANI. The last characteristic is very attractive because of the lower potential needed to obtain the same contrast of the hybrid material with respect to the pure PANI and the consequent prolonged lifetime of the device.

The stability of the hybrid materials is a critical issue in many EC nanocomposites. The probable lack of strong interactions between conjugated polymers and inorganic materials has led to the realization of covalently bonded PANI-TiO_2 hybrids via sol gel process followed by oxidative polymerization by using a bifunctional compound to bridge the two phases. The amorphous structure of the PANI determined by the presence of covalently bonded TiO_2 improves the ion motions as well as colouration efficiency and optical contrast. Furthermore, the electron donor (PANI)-acceptor (TiO_2) interactions take place reducing the energy of the HOMO and determining a drastically enhancement of the electrochemical stability of PANI. It has been demonstrated that a dual-active-layer transmission EC device made of a PANI-TiO_2 hybrid containing 5.4 wt% TiO_2 and PEDOT: PSS showed no appreciable decay after 50 000 cycles of switching. The excellent lifetime of the device may be attributed to the prominent donor-acceptor interaction between PANI and TiO_2, which stabilizes charged radicals at the doped stat and hence prohibits over-oxidation [52].

Creation of interfacial ionic bonds is an alternative to creation of covalent bonded interfaces. A self-catalysed hydroamination method has been employed to treat TiO_2 nanoparticles which have ionically anchored methacrylic acid surface to create aniline-grafted TiO_2 (TiO_2-ANI) nanoparticles. These nanoparticles were then used to prepare TiO_2-PANI core-shell nanoparticles via oxidative polymerization of aniline. The hybrids

show simultaneously improved charge transport and electrochromic properties, including higher colouration efficiency, shorter response time and lower oxidation potentials, in comparison with either PANI alone or physical blend of PANI and TiO_2. This again demonstrated that chemical bonding approach can bring about stronger interactions between the conjugated polymer and metal oxide particles, improving the EC properties, especially lowering the oxidation potentials, more effectively than the conventional nanocomposite approach [52].

1.7 References

[1] A. Kraft, *Electrochromism: a fascinating branch of electrochemistry*, **ChemTexts 5, n. 1** (2019), 1.

[2] P.R. Somani, S. Radhakrishnan, *Electrochromic materials and devices: present and future*, **Materials Chemistry and Physics, 77** (2002), 117 – 133.

[3] C.M Lampert, *Electrochromic materials and devices for energy efficient windows*, **Solar Energy Materials, 11** (1984), 1 – 27.

[4] C.G. Granqvist, *Handbook of Inorganic Electrochromic Materials*, **Elsevier**, Amsterdam, (1995).

[5] P. Yao, M. Ye, W. Guo, X. Liu, *Aluminum Ion Electrolyte for Enhanced Electrochromism of Polyaniline*, **AIP Conference Proceedings 1864, 020063** (2017).

[6] C. Dulgerbaki, A.U. Oksuz, *Efficient Electrochromic Materials Based on PEDOT/WO3 Composites Synthesized in Ionic Liquid Media*, **Electroanalysis, 26** (2014), 2501 – 2512.

[7] D.C Harris, M.D. Bertolucci, *Symmetry and Spectroscopy*, **Dover publication, New York** (1978).

[8] K.H. Heckner, A. Kraft, *Similarities between electrochromic windows and thin film batteries*, **Solid state Ionics, 152 – 153** (2002), 899 – 905.

[9] P.M.S. Monk, R.J. Mortimer, D.R. Rosseinsky, *Electrochromism: Fundamentals and Applications*, **VCH, Weinheim** (1995).

[10] A.A. Argun, P.H. Aubert, B.C. Thompson, I. Schwendeman, C.L. Gaupp, J. Hwang, N.J. Pinto, D.B. Tanner, A.G. MacDiarmid, J.J. Reynolds, *Multicolored Electrochromism in Polymers: Structures and Devices*, **Chem. Mater., 16** (2004), 4401 – 4412.

[11] M. Castriota, E. Cazzanelli, G. De Santo, M. La Deda, R. Termine, *Electrochromic device*, WO 2013/054367 A1 (2013).

[12] C.G. Granqvist, *Electrochromic tungsten oxide films: review of progress 1993 – 1998*, **Sol Energy Mater Sol Cells, 60** (2000), 201 – 262.

[13] D.N. Buckley, L.D. Burke, *The Oxygen Electrode part 5*, **J. Chem Soc. Faraday, 72 (1)** (1975), 1447.

[14] D.N. Buckley, L.D. Burke, J.K. Mukahy, *The Oxygen Electrode part 7*, **J. Chem Soc. Faraday, 72 (1)** (1976), 1896.

[15] L.D. Burke, E.J.M. O'Sullivan, *Enhanced oxide growth at a rhodium surface in base under potential cycling conditions*, **J. Electroanal. Chem., 93** (1978), 11 – 18.

[16] L.D. Burke, D.P. Whelan, *The behaviour of ruthenium anodes in base*, **J. Electroanal. Chem., 103** (1979), 179 – 187.

[17] L.D Burke, M.E.G. Lyons, *Electrochemistry of hydrous oxide films, Modern aspects of electrochemistry*, **Plenum Press, New York** (1986), 169 – 248.

[18] G.R. Lee, J.A. Clayton, *Sol-Gel processing of transition-metal alkoxides for electronics*, **Adv. Mater**. **5, n. 6** (1993).

[19] J. Livage, *The gel route to transition metal oxides*, **J. of solid-state chem., 64** (1986), 322 – 330.

[20] R. Gordon, *Chemical vapor deposition of coatings on glass*, **J. of Non-Cryst. Sol., 218 (**1997), 81 – 91.

[21] R.J. Colton, A.M. Guzman, J.W. Rabalais, *Electrochromism in some thin-film transition-metal oxides characterized by x-ray electron spectroscopy*, **J. Appl. Phys., 49** (1978).

[22] J.M. Ngaruiya, O. Kappertz, S.H. Mohamed, M. Wuttig, *Structure formation upon reactive direct current magnetron sputtering of transition metal oxide films*, **Appl. Phys. Lett. 85, n. 5** (2004).

[23] S.G. Sayyed, M.A. Mahadik, A.V. Shaikh, J.S. Jang, H.M. Pathan, Nano-metal oxides-based supercapacitor via electrochemical deposition, **ES Energy Environ., 3** (2019), 25 – 44.

[24] Y. Jiang, M. Hu, D. Zhang, T. Yuan, W. Sun, B. Xu, M. Yan, *Transition metal oxides for high performance sodium ion battery anodes*, **Nano Energy, 5** (2014), 60 – 66.

[25] B. Scrosati, in *Laminated electrochromic displays*, **Springer Science+Business Media Dordrecht**, (1993).

[26] S.F. Cogan, T.D. Plante, M.A. Parker, R.D. Rauh, *Electrochromic solar attenuation in crystalline and amorphous Li_xWO_3*, **Solar Energy Materials, 14** (1986), 185 – 193.

[27] Y. Gui, D.J. Blackwood, *Honey-Comb Structured WO3/TiO2 Thin Films with Improved Electrochromic Properties*, **J. of The Electrochem. Soc., 162** (2015), 205 – 212.

[28] G. Luo, L. Shen, J. Zheng, C. Xu, *A europium ion doped WO3 film with the bi-functionality of enhanced electrochromic switching and tunable red emission*, **J. Mater. Chem. C, 5** (2017), 3488 – 3494.

[29] V. Rai, R.S. Singh, D.J. Blacwood, D. Zhili, *A Review on Recent Advances in Electrochromic Devices: A Material Approach*, **Adv. Eng. Mater., 22** (2020).

[30] C.J. Tang, J.L. He, C.C. Jaing, C.J. Liang, C.H. Chou, C.Y. Han, C.L. Tien, *An all-solid-state Electrochromic Device based on WO_3–Nb_2O_5 composite films prepared by fast-alternating bipolar-pulsed reactive magnetron sputtering*, **Coatings, 9, 9** (2019).

[31] D. Zhou, D. Xie, X. Xia, X. Wang, C. Gu, J. Tu, *All-solid-state electrochromic devices based on WO3/NiO films: material developments and future applications*, **Sci. China Chem., 60 n.1** (2017).

[32] C. Marcel, J.M. Tarascon, *An all-plastic WO_3 / H_2O polyaniline electrochromic device*, **Solid State Ionics ,143** (2001) 89 – 101.

[33] M.A. De Paoli, A. Zanelli, M. Mastragostino, A.M. Rocco, *An electrochromic device combining polypyrrole and WO3 II: solid-state device with polymeric electrolyte*, **J. of Electroanaly. Chem., 435** (1997), 217 – 224.

[34] M.C. Bernard, A.J. Hugo – Le Goff, W. Zeng, *Elaboration and study of a PANI/PAMPS/WO_3 all solid-state electrochromic device*, **Electrochimica Acta, 44** (1998), 781 – 796.

[35] K. Hinokuma, K. Ogasawara, A. Kishimoto, S. Takano, T. Kudo, *Electrochromism of spin-coated $MoO_3 \cdot nH_20$ thin films from peroxo-polymolybdate*, **Solid State Ionics, 53-56** (1992), 507 – 512.

[36] X.M. Zhang, B.Z. Shan, Z.P. Bai, X.Z. You, C.Y. Duan, *Electrochromism and X-ray Crystal Structure of a Mixed-Valence Charge-Transfer Complex* $[(CH_3)_2NC_6H_4NH(CH_3)_2]_4[(C_4H_9)_4N]SiMo_{12}O_{40}$, **Chem. Mater., 9** (1997), 2687 – 2689.

[37] X.Z. You, B.Z. Shan, X.M. Zhang, S.J. Zheng, Z.P. Bai, *Absorption spectra of an electrochromic window based on molybdovanadophosphoric acid, Prussian Blue and a solid polymer electrolyte*, **J. of Applied Electrochem., 27** (1997), 1297 – 1299.

[38] T. He, Y. Ma, Y. Cao, W. Yang, J. Yao, *Preparation and electrochromism of alkylammonium molybdate thin films*, **J. of Non-Cryst. Sol., 315** (2003), 7 – 12.

[39] V.D. Neff, *Electrochemical Oxidation and Reduction of Thin Films of Prussian Blue*, **J. Electrochem. Soc., 125** (1978), 886 – 887.

[40] D. Ellis, M. Eckhoff, V.D. Neff, *Electrochromism in the Mixed-Valence Hexacyanides. 1. Voltammetric and Spectral Studies of the Oxidation and Reduction of Thin Films of Prussian Blue*, **J. Phys. Chem., 85** (1981), 1225 – 1231.

[41] V. Plichon, S. Besbes, *Electrochemical investigations of* K^+*-free Prussian blue films*, **Electrochimica Acta, 37** (1992), 501 – 506.

[42] K. Honda, J. Ochiai, H. Hayashi, *Polymerization of Transition Metal Complexes in Solid Polymer Electrolytes*, **J. Chem. Soc., Chem. Commun., 1** (1986), 168.

[43] K. Itaya, K. Shibayama, H. Akahoshi, S. Toshima, *Prussian blue modified electrodes: An application for a stable electrochromic display device***, J. Appl. Phys., 53** (1982), 804.

[44] J. Wang, L. Zhang, L. Yu, Z. Jiao, H. Xie, X.W. Lou, X.W. Sun, *A bi-functional device for self-powered electrochromic window and self-rechargeable transparent battery applications*, **Nat. Commun., 5** (2014), 4921.

[45] T.C. Liao, W.H. Chen, H.Y. Liao, L.C. Chen, *Multicolor electrochromic thin films and devices based on the Prussian blue family nanoparticles*, **Sol. Energy Mater. Sol. Cells, 145** (2016), 26 – 34.

[46] R.J. Mortimer, *Organic electrochromic materials*, **Electrochimica Acta, 44** (1999), 2971 – 2981.

[47] C.D. Ellis, L.D. Margerum, R.W. Murray, T.J. Meyer, *Oxidative Electropolymerization of Polypyridyl Complexes of Ruthenium*, **Inorg. Chem., 22** (1983), 1283 – 1291.

[48] C.P. Horwitz, Q. Zuo, *Oxidative Electropolymerization of Iron and Ruthenium Complexes Containing Aniline-Substituted 2,2'-Bipyridine Ligands*, **Inorg. Chem., 31** (1992), 1607 – 1613.

[49] K. Hanabusa, A. Nakamura, T. Koyama, H. Shirai, *Electropolymerization and Characterization of Terpyridinyl Iron(II) and Ruthenium(l1) Complexes*, **Polymer Int., 35** (1994), 231 – 238.

[50] P. Pfluger, H.U. Künzi, H.-J. Güntherodt, *Discovery of a new reversible electrochromic effect*, **Appl. Phys. Lett., 35** (1979), 771 – 772.

[51] J.O. Besenhard, The Electrochemical Preparation and Properties of Ionic Alkali-Metal and NR_4-Graphite Intercalation Compounds in Organic Electrolytes, **Carbon., 14** (1976), 111 – 115.

[52] V.K. Thakur, G. Ding, J. Ma, P.S. Lee, X. Lu, *Hybrid Materials and Polymer Electrolytes for Electrochromic Device Applications*, **Adv. Mater., 24** (2012), 4071 – 4096.

Chapter 2

Electrolyte Layer and Materials

2.1 Fundamental on Electrolytes

To date, all electrochemical device despite their much-diversified chemistries and applications, such as electrolytic cells, capacitors, batteries, electrochromic devices or fuel cells, require the use of electrolytes to perform their unique role as medium for the transfer of charges in the form of ions [1,2]. In general, electrolytes are electrolytic solution-types generally in a liquid state in the service-temperature range, consisting of salts (electrolytes solutes) dissolved in solvents that can be protic like water or aprotic like organic molecules. The distinction between the solvents is conventionally done with the terms aqueous (protic) and nonaqueous (aprotic), despite the fact that some nonaqueous solvents (by definition) like ethanol and anhydrous ammonia have active protons (and so they are effectively protic) [1].

The physical localization of the electrolyte layer causes its interaction with the two electrode layers of the ECD and therefore makes it necessary to be compatible with the materials used for the electrochromic effect. The immediately consequence of this requirement is the research of the best electrolyte layer when new materials are employed in the construction of the electrode layers (responsible for the electrochromic effect) of an ECD [1].

In a general way, the electrolyte layer defines how fast the energy could be released by controlling the mass flow within the ECD. This task should ideally be performed without the electrolyte undergoing chemical change during ECD operation. Therefore an electrolyte needs to be electrochemically stable against the cathode and the anode of the dispositive. In addition to the electrochemical stability, an electrolyte layer should have the following characteristics [1]:

- good ionic conduction together with electronic insulation.
- wide electrochemical window.
- inert to all the components of the dispositive.
- robust against electrical, mechanical and thermal abuses.
- environmentally friendly.

Lithium has been initially considered as an anode material in the construction of batteries, because of its two unique properties related to the great electronegativity and to the low mass that could ideally makes hight voltage cells. However, serious problems related to the cycle life and safety of the dispositive caused the abandon of the lithium as negative

electrode. Then the research was driven toward the use of the lithium ion rather than the lithium metallic. The use of the lithium ion has begun with the consideration of the "host" – "guest" chemistry, also known as the intercalation (or insertion) electrodes. The concept has been initially adapted to cathode materials, with the host materials being mostly transition metal oxides or chalcogenides with stable crystal lattices [1,3-6]. The process consists in the injection and extraction of electrons that produces redox reactions on the host lattice and consequently regional electroneutrality loss that can be compensated by intercalation/deintercalation of mobile ions. The application of the concept to an anodic material did not take place until carbonaceous materials were used in the manufacture of intercalation anodes allowing the construction of "lithium-ion batteries" (LIBs) in the early 90. The electrolyte solvent has several effects on the process [1]:

- The reductive decomposition of the solvents produces a protective thin film on the surface of the carbonaceous anode named as Solid Electrolyte interface (SEI), figure (2.1.1). SEI is an ionic conductor and an electronic insulator.
- The reductive decomposition occurs only in the first charge of the device, so that the carbonaceous anode can be cycled many times.
- The chemical structure of the electrolyte solvents critically influences the nature of the protective film.

SEI formed on the carbonaceous anode is responsible in enabling an electronic dispositive to work reversibly.

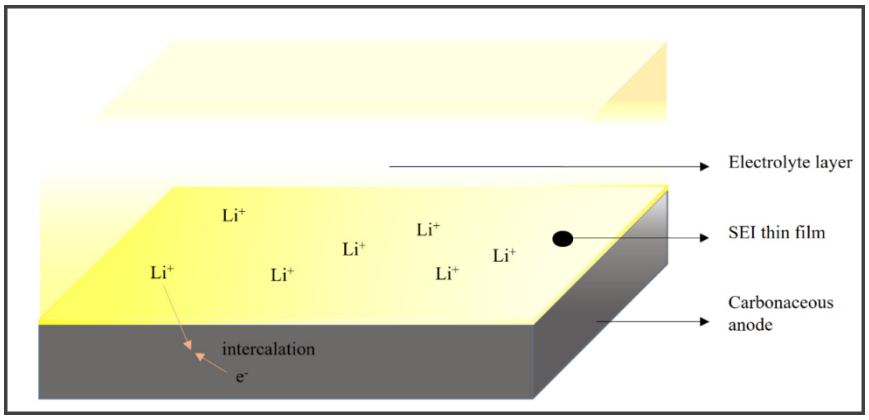

Figure 2.1.1. *Intercalation of Li^+ ion and SEI thin film formation over a carbonaceous anode.*

If the LIBs, over the last two decades, have dominated advanced consumer electronics and electric vehicles due to high energy density, power density, and long cycling stability, however the limited resources and uneven distribution of lithium cause its rising price to applicable in large scale storage. The necessity for developing a low-cost and high-

performance battery system have pushed the researcher toward the use of sodium and potassium that possess similar electrochemical properties [7-9]. A large number of published works refer to the improvement in the use of Sodium ion batteries (NIBs) and Potassium ion batteries (KIBs) [10-12].

2.2 Overview of the Electrolyte Components

Electrolyte layer can be either in liquid, gel or solid form. Normally, electrolyte layer is composed of one or more liquid solvents and one or more salts which dissociate and provide the ions [1]. The mixed solvent formulation is done because the diverse and often contradicting requirements of electronic device applications can hardly be met by a single compound. For this reason solvents of very different physical and chemical properties are used together to perform various functions simultaneously. On the other hand, use of mixture of salts is not usual because of the limitation in the choice of the anions [1].

2.2.1 Solvents

Accordingly with the basic requirements for electrolytes, ideal electrolyte solvents should meet several minimal criteria, as follows [1]:

- High dielectric constant (ε), in order to be able to dissolve salts to sufficient concentrations.
- Low viscosity (η), greater fluidity eases the ion transport.
- Inert with respect to all cell components especially the charged electrodes during cell operations.
- Low melting point (T_m) and high boiling point (T_b), in order to be liquid in a wide range of temperatures.
- High flash point (T_f) in order to be safe, nontoxic and economic.

Despite the fact that they have an excellent power of solvation of the salts, the solvents with active protons are avoided in the construction of ECDs because of the reduction of the proton and the oxidation of the corresponding anions normally occurring in their operating range (within 4,5 V).

The nonaqueous compounds that generally have a lower solvation power, must still dissolve a sufficient amount of lithium salts and for this reason only the solvents that bring polar group such as nitrile (C≡N), carbonyl (C=O), ether linkage (C–O–C) and sulfonyl (S=O) are considered in the preparation of electrolyte layer. The most commonly nonaqueous solvents used in the ECDs belong to the families of organic esters and ethers, they are listed along with their physical properties in table (2.2.1 – 2.2.2) [1].

It can be noted that the dielectric constants, polarities and viscosities of cyclic and acyclic ethers are similar. On the other hand, the same parameters are very different for cyclic or acyclic esters, with these physical parameters growing from acyclic to cyclic molecules. So viscosity, polarity and dielectric constants of esters depend directly on the molecular cyclicity [1].

Solvent[a]	**Structure**	**(M)**	**(ε)**	**(T_m)/°C**	**(T_b)/°C**	**(η)/cP 25 °C**	**(T_f)/°C**	**Dipole Moment / debye**	**(d)/g cm^{-3} (25 °C)**
EC	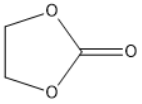	88	89.78	36.4	248	1.90 (40 °C)	160	4.61	1.321
PC	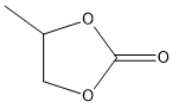	102	64.92	-48.8	242	2.53	132	4.9	1.200
BC	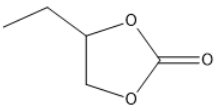	116	53	-53	240	3.2			
γBL	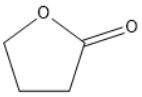	86	39	-43.5	204	1.73	97	4.23	1.199
γVL	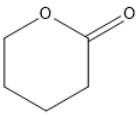	100	34	-31	208	2.0	81	4.29	1.057
NMO	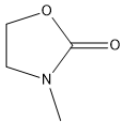	101	78	15	270	2.5	110	4.52	1.170
DMC	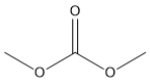	90	3.107	4.6	91	0.59 (20 °C)	18	0.76	1.063
DEC	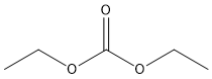	118	2.805	-74.3	126	0.75	31	0.96	0.969
EMC	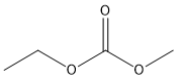	104	2.958	-53	110	0.65		0.89	1.006
EA	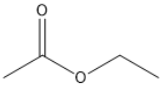	88	6.02	-84	77	0.45	-3		0.902
MB	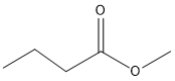	102		-84	102	0.6	11		0.898
EB	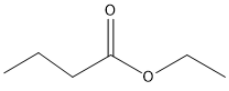	116		-93	120	0.71	19		0.878

Table 2.2.1. *Organic Carbonates and Esters as electrolyte solvents. [a] EC: ethylene carbonate; PC: propylene carbonate; BC: butylene carbonate; γBL: butyrolactone; γVL: valerolactone; NMO: methyloxazolidin-2-one; DMC: dimethyl carbonate; DEC: diethyl carbonate; EMC: ethyl methyl carbonate; EA: ethyl acetate; MB: methyl butyrate; EB: ethyl butyrate (reproduced from reference [1]).*

Solvent[a]	Structure	(M)	(ε)	(T_m)/ °C	(T_b)/° C	(η)/cP 25 °C	(T_f)/° C	Dipole Moment / debye	(d)/g cm^{-3} (25 °C)
DMM		76	2.7	-105	41	0.33	-17	2.41	0.86
DME	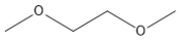	90	7.2	-58	84	0.46	0	1.15	0.86
DEE	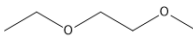	118		-74	121		20		0.84
THF		72	7.4	-109	66	0.46	-17	1.7	0.88
2-Me-THF	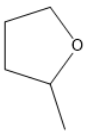	86	6.2	-137	80	0.47	-11	1.6	0.85
1,3-DL	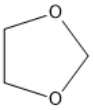	74	7.1	-95	78	0.59	1	1.25	1.06
4-Me-1,3-DL	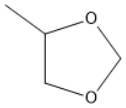	88	6.8	-125	85	0.60	-2	1.43	0.983
2-Me-1,3-DL	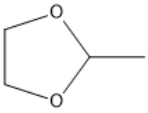	88	4.4			0.54			

Table 2.2.2. *Organic Ethers as electrolyte solvents. [a] DMM: dimethoxymethane; DME: dimethoxyethane; diethoxyethane; THF: tetrahydrofuran; 2-Me-THF: 2-methyl tetrahydrofuran; 1,3-DL: 1,3-dioxolane; 4-Me-1,3-DL: 4-methyl-1,3-dioxolane; 2-Me-1,3-DL: 2-methyl-1,3-dioxolane (reproduced from reference [1]).*

Cyclic diesters of carbonic acid have initially attracted attention because of their high dielectric constant (so the ability to dissolve a wide variety of lithium salts) and therefore, once recognized, their ability to form an SEI on carbonaceous anodes. In this contest, Propylene carbonate (PC) and ethylene carbonate (EC) have been employed widely [1]. However some problematic aspects due to the fade of capacity of lithium cells employing PC or the presence of side reaction and Li dendrite formation and the high melting point of ethylene carbonate have advised against their use as single solvent [1,13].

It is because of the poor cycling efficiency associated to potential hazard in PC use that has pushed research into adopting ethers as electrolyte solvents. Despite the better cycling efficiency reported for THF, 2-Me-THF and polymethoxy ethers, the poor capacity

retention have made some trouble in the use of electrolytes ether-based [1,14-16]. In addition, oxidative decomposition on the cathode surfaces of the ethers have been reported at relatively low potential.

The high melting point of EC has not favoured its use in the early LIBs, but the consideration of EC as an electrolyte cosolvent has begun in the early 70. As example, mixing of EC with a small percentage of PC can suppress the inconvenient of melting point and allow the formation of a room-temperature melt. Further investigations have demonstrated better bulk ion conductivity and better interfacial properties on EC-based electrolytes as compared with PC [1].

However, despite the melting-point suppression by the solute and other cosolvents, the higher liquidus temperatures of the electrolyte due to EC remained a factor limiting the low-temperature applications of the lithium cells [1].

2.2.2 Lithium Salts

As for solvents, whose criteria have been previously listed, an ideal electrolyte solute should have the following characteristics for use in electronic devices [1]:

- High dissociation rate in nonaqueous media associated to high mobility of the solvated ions.
- Stability of the anions against oxidative decomposition at the cathode.
- The anion should be inert to electrolyte solvents and together with the cations should be inert toward all the other components of the cells.
- The anion should be nontoxic and remain stable against thermally induced reactions.

The choice of possible lithium salt suitable for electrolytic applications is rather limited when compared to that of aprotic organic compounds usable as electrolytic solvents. The small ionic radius of lithium represents an obstacle in the solubility of the lithium salts in low dielectric media. Halides as LiCl and LiF and the oxides Li_2O generally fail to meet the first ideal characteristic of an electrolyte solute (the solubility requirement). However, if the anion is replaced by soft Lewis base such as Br^-, I^-, S^{2-} or carboxylates ($R–CO_2^-$), an improvement is normally achieved but at the same time a decrease in the anodic stability of the salt is observed [1].

Lithium salts used in ECDs are generally formed by the Li^+ ion accompanied by a complex anion because of their good solubility in dielectric solvents. An example is given

by the lithium hexafluorophosphate ($Li^+PF_6^-$), in which the anion could be viewed as a simpler anion (F^-) complexed by the Lewis acid (PF_5). The stability of the anion is given by the delocalization of the formal negative charge given by the Lewis acid that is an electron withdrawing ligand.

Other complex lithium salts such as $LiAlX_4$ have been used in lithium batteries but because of their extreme chemical reactivity in the dielectric media, they have been abandoned.

Conversely, lithium salts with anions based on milder Lewis acids such as the lithium perchlorate ($Li^+ClO_4^-$), have been investigated because of their improved stability in organics media under normal operating conditions. Some lithium salts are listed in table (2.2.3) together with some physical properties [1].

Salt	**Structure**	**Molecular weight**	**T_M/°C**	**$T_{decomp.}$/°C in solution**	**σ/mScm^{-1} (1.0 M, 25 °C) in PC**	**σ/mScm^{-1} (1.0 M, 25 °C) in EC/DMC**
$LiBF_4$	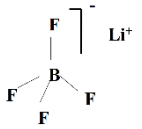	93.9	293	> 100	3.4	4.9
$LiPF_6$	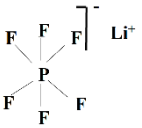	151.9	200	~80 (EC/DMC)	5.8	10.7
$LiAsF_6$	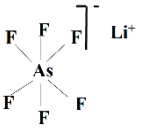	195.9	340	> 100	5.7	11.1
$LiClO_4$	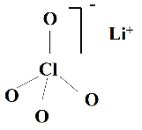	106.4	236	> 100	5.6	8.4
Li Triflate	$Li^+CF_3SO_3^-$	155.9	> 300	> 100	1.7	
Li Imide	$Li^+[N(SO_2CF_3)_2]^-$	286.9	234	> 100	5.1	9.0
Li Beti	$Li^+[N(SO_2CF_2CF_3)_2]^-$					

Table 2.2.3. *Lithium salts as electrolytes solutes (reproduced from reference [1]).*

The most popular lithium salt used especially in research laboratories is still the $LiClO_4$ because of its low cost and ease of handling. However this electrolyte solute is not practicable on an industrial scale because of the high oxidizing degree of chlorine (VII) that make the anion perchlorate to be very reactive toward the organic solvents in some operating conditions such as high temperatures. Other salts studied based on stabilized anions are the lithium trifluoromethanesulfonate (Li Triflate) and the derivatives of Li Bis(trifluoromethanesulfonyl)imide (LiIm), however, severe Al corrosion suffered by devices made with their use in electrolyte layers has severely limited its use. The limitations of these salts together with the ones of the $LiBf_4$ (thermally unstable) and $LiAsF_6$ (toxic) have determined the use of $LiPF_6$ as the universal solute for electrolytes although it suffers of thermal instability such as the $LiBf_4$ [1].

2.2.3 State-of-the-art

To date, the commercialised lithium-ion devices have all the same skeletal components of the electrolyte although within the different compositions that belong to the different companies. The indispensable components on which are based the electrolytes are EC as the solvent and $LiPF_6$ as the solute. Linear carbonates, as DMC, DEC or EMC are used as cosolvents in many cases in order to improve some characteristics of the electrolyte composition. This state-of-the-art electrolyte composition ($LiPF_6$/EC/Linear carbonate) has certain limitations on the performances of the electronic devices (such as the batteries) that use it. There is a low temperature limit, determined by the EC solvent because of its high melting point, below which the characteristics of the devices decay rapidly although reversibly. Conversely, the deterioration of the performances over the hight temperature limit, determined by the reactivity of the salt with the solvents, is permanent because of the irreversible reactions between the electrolyte solute and solvent. In addition, the products of these reactions are often gaseous determining in some cases hazardous pressure build-up in the batteries [1].

2.3 Polymeric Electrolytes

Solid polymer and gel polymer electrolytes can be viewed as a special variation of the solution-type electrolyte. In solid polymer the solvents are polar macromolecules that dissolve the salts while in gel polymer electrolyte a small portion of high polymer is soaked with or swollen by the same liquid electrolyte and it is employed as the mechanical matrix [1]. An exception is represented by molten salts or ionic liquids (ILs) electrolytes for which no solvents are employed and the dissociation of salts is achieved by thermal disintegration of the salt lattice [1].

In ECDs different classes of electrolytes can be employed: liquid electrolyte, ceramic electrolyte, solid (inorganic) electrolyte and polymeric electrolyte [17]. The latter class of electrolyte have been adapted to be employed in advanced electrochemical devices, especially for lithium-ion batteries and electrochromic applications [17-19]. There are several practical issues that put constrains on the design of ECDs and the main task is to choose an electrolyte with desired properties. In general, the factors that lead to the use of polymer electrolytes in the construction of ECDs are as follows [17]:

- Easy processing, polymer electrolytes can easily form flexible films. The thickness of the flexible film is a controllable factor, and polymer electrolytes can be easily processed on large areas, that is, an advantage for industrial applications. Furthermore, different components of ECDs can be assembled or laminated via well-developed technologies.
- Novel Separator, polymer electrolyte can be by itself a separator or alternatively, a porous separator can be used.
- Mechanical Strength, the better mechanical strength of polymeric electrolyte makes the ECDs robust. Attention should be paid in the choice of polymeric electrolyte because the performance of the devices depend on its characteristic thermal and potential stability windows.
- Wide range of working temperature, polymer electrolytes intrinsically possess the ability to operate over a wide range of temperature as compared to the other counterparts.
- Reduced reactivity, liquid electrolytes suffer the thermodynamic instability of the solvents toward lithium. Conversely, polymer electrolytes offer a better stability because of the much lower liquid content.

- Enhanced protection and stability, ECDs fabricated with polymeric electrolytes offer better safety, good optical contrast and memory effect, they are tolerant to shock, vibration and mechanical deformation. The poor or no liquid content of polymer electrolytes employed in ECDs construction allow their easy sealing in vacuum plastic sheets as compared to metal containers which are subject to corrosion.
- Act as Binder, polymer electrolytes can act as binder, facilitating the good electrical contact with the electrodes and the good adherence to the electrochromic layers, resulting in highly desirable electrochromic properties.
- Enhanced endurance, polymeric electrolytes ensure enhanced endurance to possible changes in electrode volume during cycling.

The exact formulation of electrolyte is very important regarding the cycle life of the ECDs. Furthermore, electrochemical stability plays a fundamental role in the long life of the devices. In addition, the interface between the electrolyte layer and both the electrode layers is responsible for the performance of the ECD [17]. Concerning the use of polymeric electrolyte in electrochromic applications, the following requirements should be met:

- High ionic conductivity, this requirement facilitates the motion of the ions within the EC film determining the colour variation. To do this, the polymer electrolytes should be a good ionic conductor as well as an electronic insulator. Since it is the amorphous structure of the polymer matrix chain that allows the ions to be transported frequently, it is important that given polymer electrolytes have quite amorphous structures.
- Electron donating ability, allows coordinate interactions with metal cations.
- The local segmental motions of polymer that depends on the rotation of the bonds are directly related to the ionic conduction mechanism, consequently the energy of the rotational motions of polymers should be low.
- Wide potential window, the electrochemical window defines the operating range of electrolyte layer without its degradation. The limit points of potential correspond to the redox process concerning the electrolyte (oxidation and reduction) and they should be set in the electrochemical window of the electrolyte which should be wide, to ensure stability upon cycling.
- Polymer electrolytes should have good thermal stability during cycling.

- Along with the latter requirement, polymer electrolytes should have good electrochemical stability, ideally in the range from 0 V to as high as 4,5 V vs Li/Li^+. Furthermore, chemical stability is required so that no side reactions can occur even when the electrodes or cell packaging materials come into contact.
- The polymer electrolyte layer should have a high transmittance to ensure the maximum transparency of an ECD in the bleached state.
- In an ECD the electrolyte layer needs to be confined to specific areas in order to avoid malfunctions due to leakage currents or unexpected electrochemical reactions.
- Polymer electrolytes need to be robust under stressful operating modes, such as electrical or mechanical abuses. In addition, it must have good adhesion to the adjacent layers as well as long term stability against UV radiation.
- Polymer electrolytes should be inexpensive and environmentally friendly. To ensure recycling the electrolyte layer should be easily removable from the electrodes.

In ECDs applications, polymer electrolytes can be classified in four categories: solid polymer electrolytes, gel polymer electrolytes, polyelectrolytes and composite polymer electrolytes. The former category is defined as solvent free systems in which the ionic conducting phase is formed by dissolved salts in a polar polymer matrix [20,21]. The polymer gels, or gel polymer electrolytes are formed by adding a larger quantity of solvents or even so liquid plasticizer to a polymer matrix obtaining a stable gel with the polymer host structure [22,23]. The polyelectrolytes refer to polymers that bear ionized units, they are a particular category because of their charged functional groups that are covalently bonded to the polymer backbone [24-27]. The last category regard the composite polymer electrolytes consisting in the addition of inorganic material or ionic liquids to the polymer gel electrolyte [28-30].

2.3.1 Solid Polymer Electrolytes

As already mentioned, solid polymer electrolytes are systems without solvents that bring an ionic conducting phase that is the result of the dissolution of salts in some polymer matrix. The salts that are commonly used in such systems are the lithium perchlorate ($liClO_4$), lithium tetrafluorophosphate ($LiPF_4$) and hexafluorophosphate ($LiPF_6$), methanesulfonate ($LiCF_3SO_3$), lithium bis (trifluoromethylsulfonyl) imide

($LiN(SO_2CF_3)_2$) and lithium bis (oxalate) borate ($LiB(C_2O_4)_2$. In table (2.3.1) are listed the polymer host commonly used to dissolve these salts [17].

Polymer electrolyte	acronym	Repeating unit
Poly(vinyl fluoride)	PVDF	$-(CH_2CF_2)_n-$
Poly(methyl methacrylate)	PMMA	$-(CH_2C(CH_3)(COOCH_3))_n-$
Poly(vinyl chloride)	PVC	$-(CH_2CHCl)_n-$
Poly(ethylene oxide)	PEO	$-(CH_2CH_2O)_n-$
Polyacrylonitrile	PAN	$-(CH_2(CH_3)CH_2O_n-$
Poly(dimethyl siloxane)	PDMS	$-[SIO(-CH_3)_2]_n-$
Poly(propylene oxide)	PPO	$-(CH(-CH_3)CH_2O)_n-$
Poly[bis(methoxy ethoxy ethoxide)-phospazene]	PMEP	$-[N=P(-O(CH_2CH_2O)_2CH_3)_2)_n-$
Poly(vinylidene fluoride hexafluoropropylene)	PVDF-HFP	$-(CH_2CF_2)_n-(CF(CF_3)CF_2)_m-$

Table 2.3.1. *Solid polymer electrolyte usually employed (reproduced from reference [17]).*

These materials can form thin films by using solvent evaporating coating technique. The ionic conducting mechanism of the polymers take place in their amorphous phase and it depends directly on their local segmental motions. The mechanism is related to the polymer chains dynamics and on the consequently creation of free volume in the amorphous phase. Without adding of any organic solvents, in solid polymer electrolytes the polymer is used as host matrix in which the lithium salt is incorporated. The conductivity of these systems is typically low, generally lower than 10^{-6} -10^{-8} S/cm at room temperature [17].

2.3.2 Gel Polymer Electrolytes

Liquid plasticizer and / or solvents which are able to form a stable gel with a polymer host structure, can be incorporated in larger quantity into the polymer matrix, obtaining as a result a gel polymer electrolyte. A gel polymer electrolyte can also be classified as a two-phase-system made with a ionically conducting medium that is entrapped in the polymer host structure. The gels combine the properties of the solid to be cohesive and the properties related to a liquid regarding the diffusive transport. If compared to the solid polymer electrolytes, the gel polymer electrolytes have lower mechanical properties but

higher ambient ionic conductivities, up to 10^{-3} S/cm at room temperature for some of them. There are some characteristics of these systems that make them unsuitable for some manufacturing processes related to safety concern because of the possible internal short circuits due to their morphologies, poor mechanical properties and considerable viscosities. Furthermore, gel polymer electrolytes are sensible to the UV light and thermal stress that can cause degradation in the long run.

To overcome some of these problems, plasticizer materials are also often added to adjust the physical characteristics of the overall blend. The mechanical properties of the gels can be improved also by adding components that can be cross-linked. However, when plasticization occurs it is necessary to establish a compromise between the increase of the ionic conductivity and the decrease of the mechanical properties. The conduction indeed depends dramatically on the presence of immobilized solvent in the polymer matrix that could be viewed as a stiffener for the solvent which as always solvates the salt determining the formation of the conduction medium. Two conduction paths have been postulated for this behaviour :

- For low concentration of polymer (< 30 wt%), the gel is considered to be made of liquid electrolyte entrapped in a polymer matrix (in this systems, electroactive species can migrate through the solvent phase surrounding the polymer matrix).
- For high concentrations of polymer (> 30 wt%), the electrolyte and the polymer chains may establish some strong interactions determining a restricted ion motion that is reflected in a decreasing in conductivity. In such case, the conductivity is probably a result of cumulative contribution of ionic motion as well as heterogeneous nature of gel polymer electrolyte.

Gel polymer electrolytes have been the subject of much research pertaining to electrochromic devices in recent years [31-34]. A large number of polymer matrix materials have been studied with the most popular ones that have been poly ethylene oxide (PEO), poly acrylonitrile (PAN), poly methyl methacrylate (PMMA), poly vinyl fluoride (PVDF) and poly vinylidene fluoride hexafluorophosphate PVDF-HFP (Table 2.3.1) [17].

2.3.3 Polyelectrolytes

Polyelectrolytes are a different class of polymer electrolytes from the precedent two categories because in these compounds the charged functional group of electrolytes is covalently bounded to the polymer backbone. Furthermore, charged polymers can combine the characteristics of both polymers and electrolytes and their self ion-generating group is responsible for the ionic conductivity, that generally occurs via cation mobility while the anions remain motionless. The most common ionomer electrolyte is that of perfluoro sulfonic ionomer, including Nafion and its derivatives. Polyelectrolytes are naturally present also in the human cells: proteins, polysaccharides, ribonucleic acid (RNA) and desoxyribonucleic acid (DNA) are all polyelectrolytes. The repeating units of polyelectrolytes bring either a positive or negative charged and ionizable group, so polyelectrolytes can be classified in two groups: cationic or anionic. A third classification occurs when a polyelectrolyte has both the positively and negatively charged groups, in this case reference is made to polyampholyte electrolytes. Polyelectrolytes are very interesting in new applications and variety of fields as well as for the exploration of novel phenomena because of the control by several parameters that can be had on their conformation and their interactions. However, polyelectrolytes are poorly flexible and exhibit ambient-temperature conductivities around or below 10^{-6} S/cm.

Polymer electrolytes and polyelectrolytes differ in the mobility of the anions. In the former ones the anions and cations of the dissolved salts are mobile in the polymer matrix while in the polyelectrolytes, the anions of the salt are covalently bounded to the polymer matrix thus only the cations are mobile. Therefore, the polyelectrolyte is also called a single ion conductor and its cation transference number is close to 1.0, which is one of most important requirements for electrochemical applications. However, flexible polyelectrolytic films suitable for use in devices still need to be prepared [17].

2.3.4 Composite Polymer Electrolytes

This class of polymer electrolytes is made up of polymer gel electrolytes to which inorganic materials are added. In this way, both mechanical, such as the mechanical strength and the interfacial stability, and electrochemical, the conductivity, properties are expected to be improved as well as electrolyte/electrode compatibility and safety. It has

been found that adding a quantity of inorganic filler material can improve the properties of polymer gel electrolytes in electrochromic applications. These fillers can be ionic conductive as zeolites or neutral as Al_2O_3, SiO_2, MgO. The particle size and characteristics affect dramatically the effect of the fillers. Assuming that the conductivity of composite electrolytes is somewhat improved compared to electrolytes that do not possess nanoparticles, it is also true that the conductivity at room temperature is still quite low for practical applications. A complete understanding about the materials or the dominant conduction mechanism has yet to emerge. A major challenge in further developing new electrolytes is the lack of structure–properties models [17].

2.4 Polymer Electrolytes in Electrochromic Devices

As it has been mentioned earlier in this chapter, ECDs need an electrolyte layer that serves as medium for the transfer of charges in the form of ions between the electrochromic layer and the electrode layers. The suitable ionic conductivity of an ECD should be, depending on the application, in the range from 10^{-4} to 10^{-7} S/cm to achieve acceptable dynamic. At the same time, electrical conductivity need to be very low, preferably below 10^{-12} S/cm. As it has been depicted earlier in chapter, active research on highly ion-conducting electrolytes is currently underway, particularly in the context of the development of batteries and fuel cells. The huge quantity of information available in literature facilitates strongly practical ECD construction although it is necessary to kept in mind that in addition to the usual requirements of electrochemical and thermal stabilities of the electrolytes, for ECDs the electrolytes should be stable under different light exposure. Pioneering studies on ECDs with polymer as a component of the electrolyte layer have been focused on the use of poly sulfonic acids demonstrating that the use of poly-AMPS was better than poly-SSA, poly-ESA and Nafion. To this date, a large number of polymer electrolytes have been developed and successively used in ECD applications. The most commonly used polymer electrolytes are polyethylene oxide (PEO), polyethylene glycol (PEG), boronate esters, sodium polystyrene sulfonate, waterborne polyurethane, polyester and PEO, polyvinyl alcohol (PVA), poly acrylonitrile (PAN), poly methyl methacrylate (PMMA), poly ethyl methacrylate (PEMA), poly (2-ethoxyethyl methacrylate) (PEO-EMA), poly vinyl chloride (PVC), poly (vinyl sulfones) (PVS) and poly vinyl fluoride (PVDF). The basic properties of some of these polymer systems are given in next sections.

2.4.1 PEO/PEG based Polymer Electrolytes

PEO or PEG is an oligomer or polymer of ethylene oxide. PEO and PEG are chemically identical, their difference is related to the molecular mass of the oligomer (or polymer) that is below 20000 g/mol for PEG and above this limit for PEO. For this reason their chemical properties are almost equal and they are used with various molecular weights in different applications. The different physical properties are related to the interactions that can occur as the chain length increases due to the resulting effects. PEO-based electrolytes

have been the earliest and extensively studied host structures for polymer electrolytes formation, especially in the field of lithium batteries. As it can be viewed in figure (2.4.1), PEO has a polar ether group and a significant segmental mobility. Therefore, PEO is compatible for a wide range of salts and has an effectively high lithium ion stability.

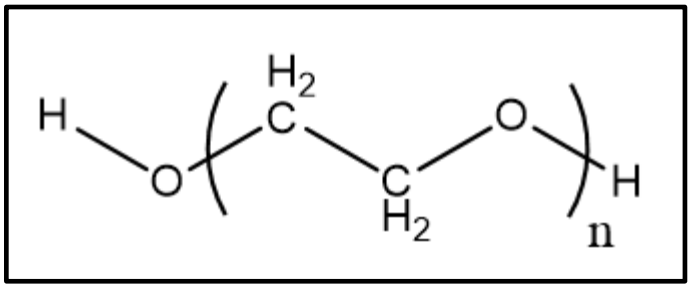

Figure 2.4.1. *Structure of Polyethylene glycol (PEG) or polyethylene oxide (PEO).*

Through the use of metallic coordination polymerization of ethylene oxide, high molecular weights of PEO can be easily reached. The oxygen atom of the ether moiety has an excellent electron-donor power and can make coordinate bonds with cations compensating at the same time the reticular energy of the salt. The synthesis and modification of PEO is very simple and it can be made in form of film in a variety of size and shapes.

Along with the positive characteristics, the oligomer has however several disadvantages related to its high crystallinity, low melting point, a limited operating temperature range, a low hydroxide ion transference number and poor interfacial characteristics. The oligomer shows a range of conductivities between 10^{-8} and 10^{-4} S/cm in the temperature range from 40 °C to 100 °C which exclude practical applications at ambient temperature. In order to improve the ionic dissociation capacity of the PEO have been studied and developed some methodologies such as the use of salts with low lattice energy, the addition of polar plasticizer and the addition of microscopic fillers. In the last case, the addition is made to avoid crystallization of the polymer and to establish some interactions between the microparticles and the polymer to consequently enhance the ion transport. Among the lithium-ion conductor, most of the work has been reported on $(PEO)_8$–$LiClO_4$. The electrolyte has eight hetero atoms per lithium ion and is characterized by high ionic conductivity and high value of activation energy (E_a). However, this system has a low Li^+ conductivity at room temperature limiting its application in ECDs. To overcome this limitation, other systems have been studied such as PEO-$LiSO_3CF_3$ and PEO-$LiN(SO_2CF_3)_2$ [35,36].

The Lbl assembly of linear poly (ethylene imide) (LPEI) poly acrylic acid (PAA) and PEO has been used to form a multilayer polymer electrolyte film made of four polyionic layers per each deposition cycle. The resulting structure of the PANI:DBSA electrochromic device combines the electrostatic and hydrogen bonding. The Lbl assembly technique, that is based on sequential deposition of oppositely charged species on a charge substrate, is a captivating procedure which offers several advantages in its use in many applications. The most valuables features are represented by the possibility of making a thin film by the use of components consisting of species with multiple ionic charges that can be deposited from aqueous solutions [37].

The study has indicated the growth behaviour of the dried tetralayer films, showing that films made with high molecular weight PEO (300000) grew linearly while not the ones made with low molecular weight PEO (20000). The films showed similar thickness (±4 nm difference) with ticker lighter film and thinner heavier film. The maximum ionic conductivity of the resulting solid polymer electrolyte tetralayer films was 9.1 x 10^{-4} S/cm, with tetralayers with PEO (20000) films slightly more conductive than those with PEO (300000). The measurements of the conductivity made in plane or through plane on each sample were showed to be similar indicating isotropic conducting characteristics and good intermixing of the polymers. The conductivity was showed to increment in conditions of high humidity leading to the determination of a critical effect of the water plasticization toward the ionic conduction.

It has been shown that the oxidation of the PANI-DSBA, obtained through the application of a negative bias to the film, produces a transparent layer that facilitates the passage of the incoming light and works in transmission mode. With the application of a reverse bias, the reduction of the PANI-DSBA was achieved and the layer was shown to operate in absorption mode, not letting the incoming light pass through anymore. The electrochromic behaviour was driven by the transport of mobile ions between the PANI-DBSA and the solid LBL electrolyte. The highest modulation for the transmissive devices has been found to be ~38% at a wavelength of 670 nm [37].

The properties of transmissive device based on indium-tin-oxide (ITO)/tungsten compound film (TCF)/PEO electrolyte/Prussian blue film (PBF)/ITO have been studied obtaining transmittance around 55.7% in optimal conditions with the response speed that was a function of the electrolyte conductivity [17].

Many other hybrid electrolytes based upon PEO were successfully used for electrochromic applications. PEO is also defined as amphiphilic because it is soluble in

water and organic solvents. Being soluble in water has made it very popular with its non-toxic intrinsic properties and used as one of the most important polymers in ECD production. Below is a brief description of the results achieved with the use of PEO as a polymer electrolyte in different electrochromic devices [17].

An electrochromic window has been reported, fabricated with Prussian blue and electrodeposited WO_3 film, with PEO used as electrolyte in the gel form. It has been reported a prototype solid-state ECD based on a four-layer sandwich structure, with the configuration of glass/IZO/WO/polymer electrolyte/IZO/glass with the polymer electrolyte obtained by sol gel derivation of a crosslinked PEO/siloxane xerogels prepared using lithium trifluoromethanesulfonyl imide salt (LiTFSI).

In addition to using PEO as electrolyte, PEO/V_2O_5 xerogel films have been reported as nanocomposite films that showed interesting multi-electrochromic behaviour with improved Li^+ ions insertion and extraction charge capacity and reversibility. ECDS made with the combination of poly (3-methylthiophene) (PMT), poly(3,4-ethylenedioxythiophene) (PEDOT) and niobium pentoxide (Nb_2O_5) and a polymer electrolyte prepared using poly poly(epichlorohydrin-co-ethylene oxide) (P (EP I-EO)) + $LiClO_4$.

A PEO based gel polymer electrolyte plasticized with ethylene carbonate/propylene carbonate or (N-butyl-3-methylpyridinium) trifluoromethanesulphonylimide (PTFSI) has been prepared with use of lithium perchlorate and lithium trifluoromethanesulphonylimide as the salts for an ECD of polypirrole (PPy). The polycarbonate plasticization of a gel polymer of PEO/$LiClO_4$ has been reported in the realization of an ECD made with poly(2,5-dimethoxyaniline) (PDMA) and tungsten oxide (WO_3) as the electrodes. The electrochromic behaviour of an ECD fabricated with PB and PEDOT as complementary electrochromic materials on poly(ethylene terephthalate) (PET) coated with ITO as flexible electrode was studied. In this system, the electrolyte was a solid polymer film made with the solvent casting method using doping of $LiclO_4$ in the network of poly(trimethylene carbonate)/Poly (ethylene oxide) (pTMC/PEO).

A composite electrolyte based on polyethylene glycol (PEG) and titanium oxide prepared by sol gel method using different molar ratio between PEG and titanium isopropoxide with Lithium iodide as salt, was used in an ECD having configuration ITO/WO_3/polymer electrolyte/ITO. Significatively change in the speed of colouration/decolouration cycles have been observed with the bleaching time reduced from 22 to 2.5 s under + 1.0 V

polarization and the colouring time reduced from 16 to 2.2 s under – 1.5 V. An ECD with the same configuration but with the use of polymer electrolyte with $LiCLO_4$ instead of lithium iodide has been also studied. Indeed in this case the electrolyte was polymeric nanocomposites of PEG and titanium oxide (PEG-Ti) with lithium salt (LiI and $LiClO_4$) obtained by sol gel method in acidic medium. The choice of lithium salt was decisive in the optical properties of ECD based on tungsten oxide thin film and PEG-Ti-Lix electrolyte which showed excellent optical contrast in the wavelength range from 300 to 2500 nm. In fact, the device made with LiI salt was very fast in the colour change but showed a yellow colour in the bleached state. On the contrary, with the $LiClO_4$ alt the device was transparent in visible region but the optical contrast was small [17].

2.4.2 PMMA based Polymer Electrolytes

Poly(methyl methacrylate) (PMMA) is a plastic material made from polymers of methyl methacrylate, the methyl ester of methacrylic acid (Fig. 2.4.2). It is a hard thermoplastic that is transparent to the light (in some cases more than glass) and unbreakable depending on the blend.

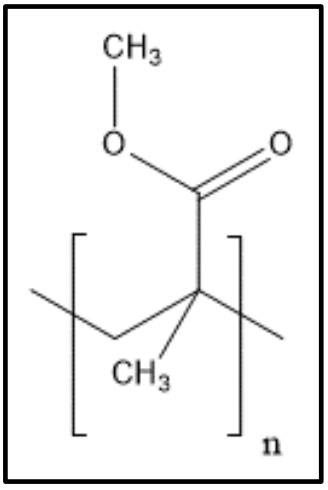

Figure 2.4.2. *Structure of poly(methyl methacrylate) (PMMA).*

As discussed in the previous paragraph (2.4.1), at least in the earliest studies PEO showed low ionic conductivity with various lithium salt due to high degree of crystallization. To overcome the disadvantages of PEO, the researchers' focus was turned on the use of PMMA and PVDF for electrochromic applications. The flexible backbone of PMMA as well as its amorphous phase characterize its high ionic conductivity, that associated to its high transparency, environmental stability, good gelatinizing properties, high solvent

retention ability and high compatibility with the liquid electrolytes have made it of particular interest in the field of ECDs. Among the positive characteristics of PMMA we found the ease of handling and the good processability, furthermore PMMA has good outdoor weatherability and good resistance to acid and a high grade of dissolution in solvents. In addition, PMMA is compatible with most of the polymers, it has higher surface resistance and good interfacial stability regarding the lithium electrodes. As it can be seen in figure (2.4.2), the presence of a polar functional group which has high affinity for Li^+ in its polymer chain allows the formation of complexation between PMMA and inorganic salts that can therefore be easily solvated. The glass transition temperature T_g of 120 °C of PMMA gives it an amorphous morphology. The PMMA is mostly used in gel form in the electrochromic applications because in this form it has the higher ionic conductivity. The oxygen atoms of the PMMA with lone pairs are expected to form coordinate bonds with the lithium ions [17].

Below are reported some of the use of PMMA for polymeric electrolytes in ECDS together with some of the observed properties [17].

An excellent lamination material made with a layer of PPG-PMMA-LiclO_4 (with PPG, poly(propylene glycol) has been used in an ECD prepared with films of tungsten and vanadium oxides. A gel electrolyte used in a ECD made with the configuration glass/ITO/WO_3/gel electrolyte/ITO/glass was prepared by the dissolution of PMMA in different solvents such as PC, EC and γBL and lithium imide (Li$N(CF_3SO_2)_2$ as the salt. The gel electrolytes obtained with the γBL solvent have shown maximum ionic conductivity in the range of 1.26 x 10^{-2} S/cm attributable to the solvent separated ion pair. Thus the ECDs made with incorporation of such electrolytes have shown interesting properties for window applications [17].

An electrochromic double polymer device obtained using PMMA as a polymer gel electrolyte has been studied. The gel has been obtained by the addition through the help of a syringe of acetonitrile (ACN) and PC to PMMA and Li[N(SO2CF3)2] contained in an argon-purged flask. The composition of the gel in terms of weight was 70: 20: 7: 3 (ACN: PC: PMMA: Li[N(SO2CF3)2]). The electrochromic layers of the ECDs were made up different conducting polymer films of 3,4-ethylenedioxythiophene. The devices thus constituted showed high contrast and extremely high colouration efficiencies up to 1400 cm^2/C narrow (ca. 100nm) wavelength ranges. Furthermore, the devices have retained up to 60% of their optical response after 10000 deep, double potential steps, a useful characteristic for electrochromic applications [17].

A polymer gel electrolyte made with above mentioned same composition in terms of weight and the substitution of Li[N(SO2CF3)2] by $TBAPF_6$ (Tetrabutylammonium hexafluorophosphate) has been used for an all-polymeric ECD. In order to enhance the durability of the device, the gel polymer electrolyte has been evaporated at the edges during the sealing process. The cathode and anode electrochromic layers were made with poly(3,4-proplenedioxythiophene) ($PProDOTMe_2$) and poly [3,6-bis(2-(3,4-ethylenedioxy)thienyl)-N-methylcarbazole] (PBEDOT-N-MeCz) respectively. The ECD had excellent properties in terms of transmittance change (51% at the wavelength of 540 nm), stability and contrast loss of 5% after 32000 switches. Colouration efficiency at the highest contrast (80%) was of 395 cm^2/C reached in a switching time of 8 s [17].

Flexible electrochromic devices that include a plasticized system of $LiCLO_4$-PMMA (MW: 120 000) have been studied. The plasticization has been carried out with PC to form a transparent and conductive gel. The electrochromic materials of the devices were fabricated using the Suzuki-Miyaura cross-coupling reaction obtaining different derivatives of poly(4-butyltriphenylamine). The obtained ECDs have shown several colour transitions such as yellow, green, khaki and reddish-brown. This particular plasticization of PMMA-$LiCLO_4$ with PC from which a polymer gel is obtained has been employed several times in different electrochromic devices. For example, the electrochromic properties fluorene-azulene based conjugated polymer associated with this electrolyte have been observed. In addition, a gel polymer composition was obtained by casting solution and made of ACN: PC: PMMA (350000): $LiClO_4$ with ratio by weight of 70:20:7:3. ACN as high vapor pressure solvent has been added to the gel polymer in order to improve the mixing of its components. The polymer gel electrolyte has been used to investigate the electrochromic properties of electrodeposited films of poly(1, 4-bis (2-[3',4'-ethylenedioxy] thienyl) -2- methoxy -5-2"- ethyl hexyl oxybenzene) (P(BEDOT-MEHB)). The P(BEDOT-MEHB) films exhibited very high colouration efficiency values: as high as 680 cm^2/C at 535 nm and –360 cm^2/C at 760 nm. A similar electrolyte of following composition, $LiClO_4$: ACN: PMMA: PC in the ratio by weigh of 3:70:7:20 has been used in the study of the electrochromic properties of polystyrene functionalized carbazole/polyethylenedioxythiophene (PS-Carb/PEDOT) ECD. The configuration of the assembled device was ITO-coated glass/anodically colouring polymer (PS-Carb)//gel electrolyte//cathodically colouring polymer (PEDOT)/ITO coated glass. The device has shown a switching colouration from bleached to blue and dark blue colours on applied potential and switching time and optical contrast were found to be 1.1 s and 38%,

respectively. The electrochromic properties of a device made of PEDOT, PB and PMMA as gel polymer electrolyte were also observed, reporting high colouration efficiency and long-term cycling stability [17].

Studies have been performed on the use of PMMA polymer electrolyte with ammonium salts. Thus, a gel polymer electrolyte made from ACN containing PMMA and tetrabutylammonium tetrafluoroborate (TBATFB) in the composition TBATFB: PMMA: polycarbonate: ACN in the ratio by weight of 3: 7: 20: 70 has been prepared and used with electrochromic poly(indole-6-carboxylic acid) (PIn). Another work has reported the preparation of a polymer electrolyte obtained from dissolution of seven weight equivalents (wt. eq.) of PMMA in 70 wt. eq. of acetonitrile (ACN). 3 wt. eq. of TBAFB as supporting electrolyte were added to the mixture before plasticization which has been performed with 20 wt. eq. of PC and heating. The gel polymer electrolyte has been used in dual ECDs made with electrochemically deposited conducting copolymers of thiophene-functionalised monomers, 2-[(3-thienylcarbonyl)oxy] ethyl 3-thiophene carboxylate (TOET), 2,3-bis-[(3-thienylcarbonyl)oxy] propyl 3-thiophene carboxylate (TOPT), and 3-[(3-thienylcarbonyl)oxy]-2,2-bis-[(3-thienylcarbonyl)oxy]propyl 3-thiophene carboxylate (TOTPT), and PEDOT as counterpart. The configuration of the devices was as follows, ITO-coated glass/conducting copolymer/gel electrolyte/ PEDOT/ITO. The ECDs have shown red and blue colours, good optical memory in the red coloured state and switching times between two colours of 1 s, furthermore they reached 95% of the total transmission change. An all-solid-state electrochromic display made with PB and WO_3 and PMMA as gel electrolyte obtained using PC and EC as solvents, has shown good conductivity of 10^{-3} S/cm at room temperature as well as excellent electrochromism and memory effects.

2.4.3 PVDF based Polymer Electrolytes

Poly(vinyl fluoride) (PVDF) is a polymer that has recently been used in ECDs. PVDF has many advantageable properties such as durability, ease of fabrication high permittivity and hydrophobicity; it has good thermomechanical properties and it is thermally and chemically stable and also chemically resistant. The semicrystalline structure of PVDF is showed in figure (2.4.3) and gives it an amorphous phase and a crystalline one that guarantee respectively flexibility and thermal stability.

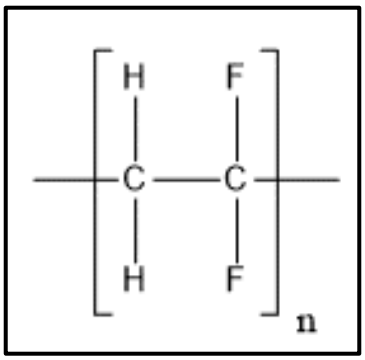

Figure 2.4.3. *Structure of poly(vinyl fluoride) (PVDF).*

The high dielectric constant simplifies the ionization of dissolved salts, resulting in higher charge carrier density, and its responsible for a high electrochemical stability window due to its anodic stability because of the presence of electron-withdrawing functional groups. Furthermore, PVDF is soluble in high-boiling point solvents such as N-methyl-2-pyrrolidone (NMP), N-dimethylformamide (DMF) and dimethylacetamide (DMAc).

Unfortunately, PVDF does not solvate very well the lithium salts due to its low donor number and consequently cannot be used in polymer-salt complexes. The copolymers generally possess two phases: the amorphous one is responsible for entrapment of liquid electrolytes and the crystalline part maintains their mechanical properties. In fact, at date copolymers of PVDF have been successfully used for polymeric electrolytes and as binders for electrodes in the battery applications. The uses of PVDF and derivatives such as poly (vinylidene fluoride-co-hexafluoro propene) P(VDF-HFP) and poly (vinylidene fluoride-trifluoro ethylene) (PVDF-TrFE) for electrochromic applications are relatively new and the studies are still in progress [17].

There are some examples of using PVDF-based electrolytic layers for ECDs in the literature [38-40]. Electrochromic devices made with P(VDF-TrFE) in the form of solid and gel polymer electrolytes and polyaniline as electrochromic devices have shown especially with the solid form of polymer prominent effect of the transverse internal interfacial impedance resulting in the reduced ionic conductivity of the electrolytes. Average values of the conductivities were found to be 3.46×10^{-7} S/cm for the solid electrolyte and 6.26×10^{-6} for the gel electrolyte. The polymer electrolyte solidification process has been studied. Polymer electrolytes prepared with polar polymer host of P(VDF-TrFE) and non-polar polymer host have shown different light modulations. Solid and gel polar polymer electrolytes based ECDs have shown stable and reversible light

modulation up to 30% for the former and 65% for the latter while non-polar polymer electrolytes have shown less than 10% light modulation. The gel-state device performances were affected by the number of dissociate ions, while the light modulation of the solid-state devices in the bulk electrolyte and at the electrolyte/electrochromic material layer was depending on the ionic movement.

The plasticization process of PVDF polymeric electrolytes, as example using low molecular weight PEO, can lead to substantial improvements of its ionic conductivity and segmental mobility and also on the ion dissociation. The plasticization is achieved normally using low molecular weight polyethers and polar organic solvents. In fact, crystallization of PEO occurs only with the use of high molecular weight PEO. With the use of PEO, no liquid plasticizer was necessary and high ionic conductivities have been reached [17].

Electrospun P (VDF-HFP) nanofibrous membranes could theoretically also host ILs but only in small quantities, because the presence of larger amounts causes the reduced dimensional retention by the polymer, and the formation of a gelled mass. However, treated P (VDF-HFP) nanofibrous membranes with supercritical carbon dioxides ($SCCO_2$) have showed remarkable improvements in mechanical properties due to the creation of interfiber junctions during treatment. Furthermore, treated membranes possess ionic conductivities very close to that of the neat ILs and anyway higher that of the corresponding IL/PVDF gel [17].

2.4.4 Gelatine-based Polymer Electrolytes

The attention of researcher is nowadays turned on the development of light and safe ECDs easily producible and storable with distribution of energy at low cost. For this reason, the development of new electrolytes replacing existing synthetic polymers has become necessary. Natural polymers could therefore represent a new route to synthetize polymeric electrolytes from renewable sources because of their intrinsic biodegradability, eco-friendliness, low production costs and good physical and chemical properties. Among natural polymers, polysaccharides and proteins are best candidate due to their abundance in environment. Gelatine (Fig. 2.4.4) is a nontoxic natural biomacromolecule comprised of bioactive polypeptides derived by the partial hydrolysis of collagen.

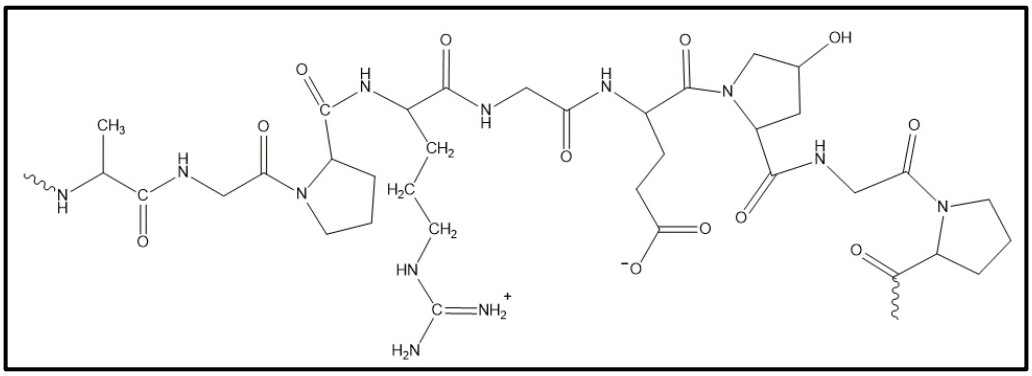

Figure 2.4.4. *Structure of gelatine.*

Used as solid polymer electrolytes, with the addition of $LiclO_4$ as lithium salt and glycerol as plasticizer, in film form it has shown an ionic conductivity of 1.53 x 10^{-5} S/cm at room temperature and of 4.95 x 10^{-4} S/cm at 80 °C. In general the use of gelatine seems to be suitable for electrochromic applications [17].

2.4.5 Ionic Liquids based Polymer Electrolytes

As mentioned above, ionic liquids (ILs) are molten salts liquid at room temperature (<100 °C). The use of ILs has concerned especially electrochemical applications because of their intrinsically ionic conductivities [41-44]. Although they no needs to additional salts for conduction, special requirements could necessitate the addition of some specific ions in ILs and the most added salts are represented by lithium ones. Several properties of ILs are advantageous such as ionic conductivity, transference number, electrochemical window or chemical and physical characteristics such as melting point, non-volatility, density viscosity and observed temperature of solidification.

ILs are also recyclable after the use and so, quite interesting in term of eco friendliness. In this contest, a new class of ionic liquids has been used recently for electrochromic applications: the room temperature ionic liquids (RTIL) which are salts having melting point at or below room temperature [45-48]. The chemical and physical properties of RTIL are identical to those of high temperature molten salts but unlike the latter, RTIL at room temperature are liquid and therefore more manageable. Although ILs show promising characteristics when used as electrolytes in EC applications, their high cost usually renders them unfit for use as the only electrolyte.

2.5 References

[1] K. Xu, *Nonaqueous Liquid Electrolytes for Lithium-Based Rechargeable Batteries*, **Chem. Rev., 104** (2004), 4303 – 4417.

[2] X. Fu, *Polymer electrolytes for electrochromic devices*, In C. Sequeira, D. Santos, *Polymer Electrolytes, Fundamentals and Applications*, **Woodhead Publishing Series in Electr. and Opt. Mater.,** (2010) 471 – 523.

[3] M.S. Whittingham, *Electrical Energy Storage and Intercalation Chemistry*, **Science, 192** (1976), 1126 – 1127.

[4] M.S. Whittingham, *Chemistry of intercalation compounds: metal guests in chalcogenide hosts*, **Prog. Solid St. Chem.,12** (1978), 41 – 99.

[5] (a) K. Mizushima, P.C. Jones, P.J. Wiseman, J.B. Goodenough, *A new cathode material for batteries of high energy density*, **Mater. Res. Bull., 15** (1980), 783 – 789.

(b) K. Mizushima, P.C. Jones, P.J. Wiseman, J.B. Goodenough, *A new cathode material for batteries of high energy density*, **Solid State Ionics, 3/4** (1981), 171 – 174.

[6] D.W. Murphy, P.A. Christian, *Solid State Electrodes for High Energy Batteries*, **Science, 205** (1979), 651 – 656.

[7] K. Song, C. Liu, L. Mi, S. Chou, W. Chen, C. Shen, *Recent Progress on the Alloy-Based Anode for Sodium-Ion Batteries and Potassium-Ion Batteries*, **Small, 17** (2021), 1903194.

[8] J. Chen, X.L. Fan, X. Ji, T. Gao, S. Hou, X.Q. Zhou, L. N. Wang, F. Wang, C.Y. Yang, L. Chen, C.S. Wang, *Intercalation of Bi nanoparticles into graphite results in an ultra-fast and ultra-stable anode material for sodium-ion batteries*, **Energy Environ. Sci., 11** (2011), 1218 – 1225.

[9] J.Y Hwang, S.T. Myung, Y.K. Sun, *Sodium-ion batteries: present and future*, **Chem. Soc. Rev., 4**, (2017), 3529 – 3614.

[10] B. Jache, J.O. Binder, T. Abe, P. Adelhelm, *A comparative study on the impact of different glymes and their derivatives as electrolyte solvents for graphite co-intercalation*

electrodes in lithium-ion and sodium-ion batteries, Phys. **Chem. Chem. Phys., 18** (2016), 14299 – 14316.

[11] B. Li, J. Zhao, Z. Zhang, C. Zhao, P. Sun, P. Bai, J. Yang, Z. Zhou, Y. Xu, *Electrolyte-Regulated Solid-Electrolyte Interphase Enables Long Cycle Life Performance in Organic Cathodes for Potassium-Ion Batteries*, **Adv. Funct. Mater., 29** (2019), 1807137.

[12] Z. Li, Y. Zhang, J. Zhang, Y. Cao, J. Chen, H. Liu, Y. Wang, *Sodium-Ion Battery with a Wide Operation-Temperature Range from -70 to 100°C*, **Angew. Chem., 134** (2022), e202116930.

[13] P. Arora, R.E. White, M. Doyle, *Capacity Fade Mechanisms and Side Reactions in Lithium – Ion Batteries*, **Jour. Electrochem. Soc., 145** (1998), 3647 – 3667.

[14] K.M. Abraham, J.L. Goldman, D.I. Natwig, *Characterization of Ether Electrolytes for Rechargeable Lithium Cells*, **Jour. Electrochem. Soc., 129** (1982), 2404 – 2409.

[15] K.M. Abraham, D.M. Pasquariello, F.J. Martin, *Mixed Ether Electrolytes for Secondary Lithium Batteries with Improved Low Temperature Performance*, **Jour. Electrochem. Soc., 133** (1986), 661 – 666.

[16] F.W. Dampier, *Insoluble Sulfide Positive Electrodes for Organic Electrolyte Lithium Secondary Batteries*, **Jour. Electrochem. Soc., 128** (1981), 2501 – 2506.

[17] V.K. Thakur, G. Ding, J. Ma, P.S. Lee, X. Lu, *Hybrid Materials and Polymer Electrolytes for Electrochromic Device Applications*, **Adv. Mater., 24** (2012), 4071 – 4096.

[18] X.Z. Yuan, S. Zhang, J.C. Sun, H. Wang, *A review of accelerated conditioning for a polymer electrolyte membrane fuel cell*, **Jour. of Pow. Sources, 196** (2011), 9097 – 9106.

[19] J.M.C. Puguan, W.J. Chung, H. Kim, *Ion-conductive and transparent PVdF-HFP/silane-functionalized ZrO2 nanocomposite electrolyte for electrochromic applications*, **electrochimica Acta, 196** (2016), 236 – 244.

[20] V. Neburchilov, J. Martin, H. Wang, J. Zhang, *A review of polymer electrolyte membranes for direct methanol fuel cells*, **Journal of Power Sources, 169** (2007), 221 – 238.

[21] F.B. Dias, L. Plomp, J.B.J. Veldhuis, *Trends in polymer electrolytes for secondary lithium batteries,* **Journal of Power Sources, 88** (2000), 169 – 191.

[22] X. Cheng, J. Pan, Y. Zhao, M. Liao, H. PengGel, *Polymer Electrolytes for Electrochemical Energy Storage*, **Adv. Energy Mater., 8** (2018), 1702184.

[23] K.S. Ngai, S. Ramesh, K. Ramesh, J.C. Juan, *A review of polymer electrolytes: fundamental, approaches and applications*, **Ionics, 22** (2016), 1259 – 1279.

[24] K. Kurihara, *Polyelectrolyte brushes studied by surface forces measurement*, Advances in **Colloid and Interface Science, 158** (2010) 130 – 138.

[25] Q. Zhao, Q.F. An, Y. Ji, J. Qian, C. Gao, *Polyelectrolyte complex membranes for pervaporation, nanofiltration and fuel cell applications*, **Journal of Membrane Science, 379** (2011), 19 – 45.

[26] B. Wyatt, C.M. Gunther, M.W. Liberatore, *Increasing viscosity in entangled polyelectrolyte solutions by the addition of salt*, **Polymer, 52** (2011), 2437 – 2444.

[27] J. Kötz, S. Kosmella, T. Beitz, *Self-assembled polyelectrolyte systems*, **Progress in Polymer Science, 26** (2001), 1199 – 1232.

[28] F. Capuano, F. Croce, B. Scrosati, Composite Polymer Electrolytes, **J. Electrochem. Soc., 138** (1991), 1918 – 1922.

[29] A.M. Stephan, K.S. Nahm, *Review on composite polymer electrolytes for lithium batteries*, **Polymer, 47** (2006) 5952 – 5964.

[30] S. Tang, W. Guo, Y. Fu, *Advances in Composite Polymer Electrolytes for Lithium Batteries and Beyond*, **Adv. Energy Mater., 11** (2021), 2000802.

[31] W. Chen, S. Liu, L. Guo, G. Zhang, H. Zhang, M. Cao, L. Wu, T. Xiang, Y. Peng, *A Self-Healing Ionic Liquid-Based Ionically Cross-Linked Gel Polymer Electrolyte for Electrochromic Devices*, **Polymers, 13** (2021), 742.

[32] W. Chen, C. Zhu, L. Guo, M.Y. Yan, L. Wu, B. Zhu, C. Qi, S. Liu, H. Zhang, Y. Peng, A novel ionically crosslinked gel polymer electrolyte as an ion transport layer for high-performance electrochromic devices, **J. Mater. Chem. C, 7** (2019), 3744 – 3750.

[33] S.-Y. Lin, Y.-C. Chen, C.-M. Wang, C.-Y. Wen, T.-Y. Shih, *Study of MoO3–NiO complementary electrochromic devices using a gel polymer electrolyte*, **Solid State Ionics, 212** (2012), 81 – 87.

[34] F. Zhang, G. Dong, J. Liu, S. Ye, X. Diao, *Polyvinyl butyral-based gel polymer electrolyte films for solid-state laminated electrochromic devices*, **Ionics, 23** (2017), 1879 – 1888.

[35] S.J. Visco, M. Liu, M.M. Doeff, Y.P. Ma, C. lampert, L.C. De Jonghe, *Polyorganodisulfide electrodes for solid-state batteries and electrochromic devices*, Solid State Ionics, 60 (1993), 175 – 187.

[36] P. Baudry, M.A. Aegerter, D. Deroo, B. Valla, *Electrochromic Window with Lithium Conductive Polymer Electrolyte*, **J. Electrochem. Soc., 138** (1991), 460 – 465.

[37] C.A. Nguyen, A.A. Argun, P.T. Hammond, X.H. Lu, P.S. Lee, *Layer-by-Layer Assembled Solid Polymer Electrolyte for Electrochromic Device*, **Chem. Mat., 23** (2011), 2142 – 2149.

[38] S. Xiong, J. Wei, P. Jia, L. Yang, J. Ma, X. Lu, *Water-Processable Polyaniline with Covalently Bonded Single-Walled Carbon Nanotubes: Enhanced Electrochromic Properties and Impedance Analysis*, **ACS Appl. Mater. Interfaces, 3** (2011), 782 – 788.

[39] M. Fabretto, T. Vaithianathan, C. Hall, J. Mazurkiewicz , P.C. Innis, G.G. Wallace, P. Murphy, *Faradaic charge corrected colouration efficiency measurements for electrochromic devices*, **Electrochimica Acta, 53** (2008), 2250 – 2257.

[40] C.Y. Hsu, K.M. Lee, J.H. Huang, K.R.J. Thomas, J.T. Lin, K.C. Ho, *A novel photoelectrochromic device with dual application based on poly(3,4-alkylenedioxythiophene) thin film and an organic dye*, Journal of Power Sources, 185 (2008), 1505 – 1508.

[41] M. Yoshizawa, A. Narita, H. Ohno, *Design of Ionic Liquids for Electrochemical Applications*, **Aust. J. Chem., 57** (2004), 139 – 144.

[42] G.B. Appetecchi, S. Scaccia, C. Tizzani, F. Alessandrini, S. Passerini, *Synthesis of Hydrophobic Ionic Liquids for Electrochemical Applications*, **J. Electrochem. Soc., 153 A** (2006), 1685 – 1691.

[43] D. Wei, A. Ivaska, *Applications of ionic liquids in electrochemical sensors*, **analytica chimica acta, 607** (2008), 126 – 135.

[44] M.J.A. Shiddiky, A.A.J. Torriero, *Application of ionic liquids in electrochemical sensing systems*, **Biosensors and Bioelectronics, 26** (2011), 1775 – 1787.

[45] A. Kavanagh, R. Copperwhite, M. Oubaha, J. Owens, C. McDonagh, D. Diamond, R. Byrne, *Photo-patternable hybrid ionogels for electrochromic applications*, **J. Mater. Chem., 21** (2011), 8687 – 8693.

[46] N. Jordão, H. Cruz, A. Branco, F. Pina, L.C. Branco, *Electrochromic Devices Based on Disubstituted Oxo-Bipyridinium Ionic Liquids*, **ChemPlusChem, 80** (2015), 202 – 208.

[47] A. Branco, L.C. Branco, F. Pina, *Electrochromic and magnetic ionic liquids*, **Chem. Commun., 47** (2011), 2300 – 2302.

[48] T.Y. Yun, H.C. Moon, *Highly stable ion gel-based electrochromic devices: Effects of molecular structure and concentration of electrochromic chromophores*, **Organic Electronics, 56** (2018), 178 – 185.

Chapter 3

Experimental Techniques

3.1 Matrices: certain properties and special cases

3.1.1 Terminology

Matrix calculation is a complex argument that goes beyond the scope of the following discussion that is focused on the description of some fundamental properties of the matrices referred to in the classical and quantomechanical arguments of Raman spectroscopy addressed later.

Matrices are represented in the text with bold type. For a general treatment, bold, italic, upper case Latin letters should be used, for example, $\boldsymbol{A}$. In the description where specific quantities are considered, another bold type will still be appropriate. An example is done by the matrix of polarizability tensor components which is represented by $\boldsymbol{\alpha}$ [1].

The element of a general matrix is therefore indicated by italic upper case Latin letters with two subscripts that denote the row and the column whose intersection defines the location of the matrix element. A_{ij} represents the element of the general matrix $\boldsymbol{A}$ which is located at the intersection of the ith row and jth column. In the same way, α_{ij} describes the ij element of the specific matrix $\boldsymbol{\alpha}$. The matrix component that derives from the rearrangement of another matrix is designated by the use of brackets. For example, for the matrix $\tilde{\boldsymbol{A}}$ formed by interchanging the rows and the columns of the matrix $\boldsymbol{A}$, the components are written $\left(\tilde{A}\right)_{ij} = A_{ji}$, that is the ij component of $\tilde{\boldsymbol{A}}$ is the ji component of $\boldsymbol{A}$ [1].

The determinant of the square matrix $\boldsymbol{A}$ is written det $\boldsymbol{A}$, the trace of the same matrix, defined as $\sum_i A_{ii}$, is written tr$\{\boldsymbol{A}\}$. The unit matrix which has $A_{ij} = 1$ if $i = j$ and $A_{ij} = 0$ if $i \neq j$ is written $\boldsymbol{I}$. An alternative way of defining $\boldsymbol{I}$ is given by a matrix whose elements are given by the Kronecker delta δ_{ij}.

The most valuable property of the matrices is that relatively complicated mathematical relationships may be represented by simple equations in which only the symbols for matrices are used, for example, $\boldsymbol{C} = \boldsymbol{AB}$. This written form of matrix equations is called compact matrix notation [1].

When the elements of a matrix are set out as an array they will be enclosed in square brackets and the dimension of an array will be given in round brackets with the number of rows first and the number of columns after. To illustrate these conventions, let's see

the following example: let be given a column matrix with *n* elements in a (*n* x 1) array and a row matrix with *m* elements in a (*m* x 1) array.

A square matrix which is a (2 x 2) array of elements would be written:

$$\begin{bmatrix} A_{11} & A_{12} \\ A_{21} & A_{22} \end{bmatrix}$$

a column matrix $\boldsymbol{B}$ which is a (2 x 1) array as:

$$\begin{bmatrix} B_{11} \\ B_{21} \end{bmatrix}$$

And a row matrix $\boldsymbol{C}$ which is a (1 x 2) array as:

$$\begin{bmatrix} C_{11} & C_{12} \end{bmatrix}$$

3.1.2 Special matrices

A *transposed matrix* is represented by $\widetilde{\boldsymbol{A}}$ and is determined by interchanging the rows and the columns of the matrix $\boldsymbol{A}$. Using the bracket notation, the components of such matrix are given by $\left(\tilde{A}\right)_{ij} = A_{ji}$. Taking into account that for the transposed product of two matrices the sequence of the matrices forming the product must be reversed we have that:

$$\left(\widetilde{\boldsymbol{AB}}\right) = \widetilde{\boldsymbol{B}}\widetilde{\boldsymbol{A}} \tag{3.1.1}$$

The rule applies for every matrix involved in the product. There are two special cases of transposed matrices, when $\widetilde{\boldsymbol{A}} = \boldsymbol{A}$ the matrix $\boldsymbol{A}$ is said to be symmetric, when $\widetilde{\boldsymbol{A}} = -\boldsymbol{A}$ the matrix $\boldsymbol{A}$ is said to be skew symmetric. The former matrix has $A_{ij} = A_{ji}$ for all *i*, *j* and is necessarily square, the latter matrix has $A_{ij} = -A_{ji}$ for all *i*, *j* and is necessarily square with all components on the leading diagonal zero [1].

A *matrix of the cofactors* is represented by $\boldsymbol{A}'$ and is the matrix of the cofactors of $\boldsymbol{A}$'s elements.

More precisely, the cofactor element $(\boldsymbol{A}')_{ij}$ is $(-1)^{i+j}$ times the value of the complementary minor of $\boldsymbol{A}$, that is the determinant formed from the elements of $\boldsymbol{A}$ that results after the removal of the row *i* and column *j* in which the element A_{ij} appears.

An *adjoint matrix* is represented by $\widetilde{\boldsymbol{A}}'$ and is formed by taking the transpose of $\boldsymbol{A}'$, the matrix of the cofactors of the elements of $\boldsymbol{A}$. In this way $\left(\tilde{A}'\right)_{ij} = A'_{ji}$ [1].

The square matrix $\boldsymbol{A}$ for which:

$$detA = 0 \tag{3.1.2}$$

is said to be a *singular matrix*. Quite the opposite, if the determinant of a matrix $\boldsymbol{A}$ is non-zero, then the matrix is said to be non-singular.

An *inverse matrix* is given by $\boldsymbol{A^{-1}}$ and defined as follows:

$$\boldsymbol{AA^{-1} = A^{-1}A = I} \tag{3.1.3}$$

The inverse of $\boldsymbol{A}$ is formed by dividing $\widetilde{\boldsymbol{A}}'$, the adjoint of $\boldsymbol{A}$, by the determinant of $\boldsymbol{A}$, so that:

$$\boldsymbol{A^{-1}} = \widetilde{\boldsymbol{A}}'/detA \tag{3.1.4}$$

It is important to note that only square matrices possess inverses. The inverse of a product of matrices applies for every matrix in the product and is given by:

$$\boldsymbol{(AB)^{-1} = B^{-1}A^{-1}} \tag{3.1.5}$$

A square matrix $\boldsymbol{A}$ with real elements is said to be an *orthogonal matrix* if its inverse is equal to its transpose such that:

$$\boldsymbol{A^{-1}} = \widetilde{\boldsymbol{A}} \text{ or } \boldsymbol{A\widetilde{A} = I} \tag{3.1.6}$$

and for the elements:

$$(\boldsymbol{A^{-1}})_{ij} = \left(\widetilde{\boldsymbol{A}}\right)_{ij} = \boldsymbol{A}_{ji} \tag{3.1.7}$$

Eqs. (3.1.1.4) and (3.1.1.6) lead to affirms that for an orthogonal matrix $\boldsymbol{A}$:

$$detA = \pm\mathbf{1} \tag{3.1.8}$$

So, the columns and the rows of an orthogonal matrix form an orthonormal set of vectors:

$$\sum_s A_{si}A_{sj} = \sum_k A_{ik}A_{jk} = \delta_{ij} \tag{3.1.9}$$

A *complex conjugate matrix* is represented by $\boldsymbol{A^*}$and is the result of the set of the complex conjugates, each of which is related to a complex element of $\boldsymbol{A}$. More simply, $(A^*)_{ij} = A*_{ij}$. The complex conjugate resulting from a product of matrices does not change the sequence of the matrices:

$$\boldsymbol{(AB)^* = A^*B^*} \tag{3.1.10}$$

A *conjugate transpose matrix* is represented by $\boldsymbol{A^\dagger}$ and is formed by transposing the complex conjugate matrix, so that:

$$\boldsymbol{A^\dagger} = \left(\widetilde{\boldsymbol{A}}^*\right) \tag{3.1.11}$$

and for the elements:

$$\left(A^{\dagger}\right)_{ij} = \left(\tilde{A}^{*}\right)_{ij} = \left(A^{*}\right)_{ji} \tag{3.1.12}$$

A *unitary matrix* is given by a square matrix whose conjugate transpose matrix $\boldsymbol{A}^{\dagger}$ is also its inverse:

$$\boldsymbol{A}^{\dagger} = \boldsymbol{A}^{-1} \tag{3.1.13}$$

An *hermitian matrix* is a square matrix that possesses the following properties:

$$\boldsymbol{A}^{\dagger} = \boldsymbol{A} \tag{3.1.14}$$

Hermitian matrices have $A_{ij} = A*_{ji}$ for all *i*, *j* and consequently the diagonal elements are real.

A *skew hermitian matrix* is a square matrix that possesses the following properties:

$$-\boldsymbol{A}^{\dagger} = \boldsymbol{A} \tag{3.1.15}$$

Skew hermitian matrices have $A_{ij} = -A*_{ji}$ for all *i*, *j* and consequently the diagonal elements are zero ore pure imaginary.

A real symmetric matrix is effectively a special case of an hermitian matrix. Indeed, considering that $\boldsymbol{H} = \boldsymbol{A} + i\boldsymbol{B}$ is hermitian with both $\boldsymbol{A}$ and $\boldsymbol{B}$ real, then $-\boldsymbol{H}^{\dagger} = \widetilde{\boldsymbol{A}} - i\widetilde{\boldsymbol{B}}$. Remembering that by definition for an hermitian matrix is worth the eq. (3.1.14), so the real and imaginary part of the matrix are symmetric and skew symmetric respectively. Thus, a real hermitian matrix is also symmetric.

In the same way, a real orthogonal matrix will be unitary since if $\boldsymbol{U} = \boldsymbol{A} + i\boldsymbol{B}$ is unitary, by definition $\boldsymbol{U} = (\boldsymbol{U}^{\dagger})^{-1}$ and $\boldsymbol{U}^{\dagger}\boldsymbol{U} = \boldsymbol{I}$, hence $\left(\widetilde{\boldsymbol{A}} + i\widetilde{\boldsymbol{B}}\right)(\boldsymbol{A} - i\boldsymbol{B}) = \boldsymbol{I}$. Then since $\boldsymbol{B} = \widetilde{\boldsymbol{B}} = 0$ for a real matrix, $\boldsymbol{A}\widetilde{\boldsymbol{A}} = \boldsymbol{I}$.

Anyway, a complex symmetric matrix cannot be hermitian not either a complex orthogonal matrix unitary [1].

With the sum of a symmetric matrix and a skew-symmetric matrix can be written any square matrix that possesses real elements, that is:

$$\boldsymbol{A} = 1/2\left(\boldsymbol{A} + \widetilde{\boldsymbol{A}}\right) + 1/2\left(\boldsymbol{A} - \widetilde{\boldsymbol{A}}\right) \tag{3.1.16}$$

If instead a square matrix possesses complex elements, then it can be written as the sum of a skew-symmetric matrix and an hermitian matrix because:

$$\boldsymbol{A} = 1/2\left(\boldsymbol{A} + \boldsymbol{A}^{\dagger}\right) + \mathbf{1}/2(\boldsymbol{A} - \boldsymbol{A}^{\dagger}) \tag{3.1.17}$$

3.1.3 Matrix representation of simultaneous linear equations

Consider now a set of simultaneous linear equations as follow [1]:

$$\begin{array}{ccccccccc} a_{11}x_1 + & a_{12}x_2 + & \dots a_{1j}x_j + & \dots + & a_{1n}x_n & = & b_1 \\ a_{21}x_1 + & a_{22}x_2 + & \dots a_{2j}x_j + & \dots + & a_{2n}x_n & = & b_2 \\ \vdots & \vdots & \vdots & & \vdots & \vdots & \\ a_{n1}x_1 + & a_{n2}x_2 + & \dots a_{nj}x_j + & \dots + & a_{nn}x_n & = & b_n \end{array} \tag{3.1.18}$$

where a_{ij} and b_i are coefficients. There is a compact matrix form that can be used to write these equations:

$$\boldsymbol{Ax} = \boldsymbol{b} \tag{3.1.19}$$

Where $\boldsymbol{A}$ is a square matrix of (n x n) a_{ij} coefficients, $\boldsymbol{x}$ is in this case a column matrix of (n x 1) x_j coefficients and $\boldsymbol{b}$ is a column matrix of (n x 1) b_j coefficients. The premultiplication of both size of eq. (3.1.19) by $\boldsymbol{A}^{-1}$ gives:

$$\boldsymbol{x} = \boldsymbol{A}^{-1}\boldsymbol{b} \tag{3.1.20}$$

So, the equations are solved knowing $\boldsymbol{A}^{-1}$, but $\boldsymbol{A}^{-1}$ exists only if $det\ \boldsymbol{A} \neq \boldsymbol{0}$, differently the solution of these equations is trivial, that is $\boldsymbol{x} = 0$.

Considering now the parity $\boldsymbol{b} = \lambda\boldsymbol{x}$, eq. (3.1.19) becomes:

$$\boldsymbol{Ax} = \lambda\boldsymbol{x} \tag{3.1.21}$$

where λ represents a scalar quantity and is called an eigenvalue of $\boldsymbol{A}$, with $\boldsymbol{x}$ that is an eigenvector. For a general (n x n) square matrix $\boldsymbol{A}$ there are n eigenvalues and n eigenvectors. Eq. (3.1.21) can be rewrite in the following way:

$$(\boldsymbol{A} - \lambda\boldsymbol{I})\boldsymbol{x} = \boldsymbol{0} \tag{3.1.22}$$

This result determines that there are n equations in the form:

$$\begin{array}{cccccc} (a_{11}-\lambda)x_1 + & a_{12}x_2 \cdots + & a_{1j}x_j + & \ldots a_{1n}x_n & = & 0 \\ a_{21}x_1 + & (a_{22}-\lambda)x_2 \cdots + & a_{2j}x_j + & \ldots a_{2n}x_n & = & 0 \\ \vdots & \vdots & \vdots & \vdots & \vdots & \\ a_{n1}x_1 + & a_{n2}x_2 \cdots + & \ldots a_{nj}x_j + & \ldots (a_{nn}-\lambda)x_n & = & 0 \end{array} \tag{3.1.23}$$

and that:

$$det(\boldsymbol{A}-\lambda\boldsymbol{I}) = 0 \tag{3.1.24}$$

to have a non-trivial solution. The values of the n roots $\lambda_1, \lambda_2, \ldots, \lambda_n$ are the solution of eq (3.1.24) and the eigenvectors can be determined within a normalization factor from eq. (3.1.21). Defining a matrix notation for the set of n eigenvectors and eigenvalues, it can be stated that $\boldsymbol{x}_j$ is a column matrix of (n x 1) components of the associated eigenvector having eigenvalue of λ_j, with $N_j x_{ij} (i = 1,2,\ldots,n)$ components where N_j is a normalization constant. The n column matrices $\boldsymbol{x}_j (j = 1,2,\ldots,n)$ can form a square matrix $\boldsymbol{X}$ of order (n x n) and the n eigenvalues can form a diagonal matrix $\boldsymbol{\Lambda}$ with entries λ_j on the diagonal, that is:

$$\boldsymbol{AX} = \boldsymbol{X\Lambda} \tag{3.1.25}$$

Multiplying both size of eq. (3.1.25) on the left by $\boldsymbol{X}^{-1}$ it follows that:

$$\boldsymbol{X}^{-1}\boldsymbol{AX} = \boldsymbol{\Lambda} \tag{3.1.26}$$

The similarity transformation enables the matrix $\boldsymbol{A}$ to be cast in diagonal form by the matrix $\boldsymbol{X}$. If $\boldsymbol{X}$ is complex and unitary, the transformation is said to be congruent and because $\boldsymbol{X}^{-1} = \boldsymbol{X}^{\dagger}$ (see eq. (3.1.11) for the definition of $\boldsymbol{X}^{\dagger}$) then eq. (3.1.26) becomes:

$$\boldsymbol{X}^{\dagger}\boldsymbol{AX} = \boldsymbol{\Lambda} \tag{3.1.27}$$

For a real orthogonal matrix $\boldsymbol{X}$, $\boldsymbol{X}^{-1} = \widetilde{\boldsymbol{X}}$, where $\widetilde{\boldsymbol{X}}$ is the transpose, the transformation is said to be real orthogonal and eq. (3.1.26) becomes:

$$\widetilde{\boldsymbol{X}}\boldsymbol{AX} = \boldsymbol{\Lambda} \tag{3.1.28}$$

The eigenvectors can be normalized to unit length using:

$$\boldsymbol{X}^{\dagger}\boldsymbol{X} = \boldsymbol{I} \tag{3.1.29}$$

or

$$\widetilde{\boldsymbol{X}}\boldsymbol{X} = \boldsymbol{I} \tag{3.1.30}$$

3.1.4 Diagonalization of a matrix

Considering the following definition of a matrix $\boldsymbol{R}$, that is real orthogonal so that $\boldsymbol{R}^{-1} = \boldsymbol{R}$ and det $\boldsymbol{R} = 1$, we have:

$$\boldsymbol{R} = \begin{bmatrix} \cos\alpha & -\sin\alpha \\ \sin\alpha & \cos\alpha \end{bmatrix} \tag{3.1.31}$$

The diagonalisation of the matrix can be performed by founding the eigenvalues λ_1 λ_2 of $\boldsymbol{R}$ from the determinantal equation:

$$\begin{bmatrix} \cos\alpha - \lambda & -\sin\alpha \\ \sin\alpha & \cos\alpha - \lambda \end{bmatrix} = 0 \tag{3.1.32}$$

whose characteristic roots λ_j are given by:

$$\lambda_1 = \mathrm{e}^{-i\alpha} = \cos\alpha - \mathrm{i}\sin\alpha \tag{3.1.33}$$

$$\lambda_2 = \mathrm{e}^{i\alpha} = \cos\alpha + \mathrm{i}\sin\alpha \tag{3.1.34}$$

The eigenvectors of $\boldsymbol{R}$ can be found using:

$$\begin{bmatrix} \cos\alpha & -\sin\alpha \\ \sin\alpha & \cos\alpha \end{bmatrix} \begin{bmatrix} N_j a_j \\ N_j b_j \end{bmatrix} = \lambda_j \begin{bmatrix} N_j a_j \\ N_j b_j \end{bmatrix} \tag{3.1.34}$$

where j = 1 or 2. For each λ_j it can be found that:

$$b_1 = \mathrm{i}a_1 \tag{3.1.35}$$

$$b_2 = -\mathrm{i}a_2 \tag{3.1.36}$$

The normalised eigenvectors can be determined using eq. (3.1.29) where the unitary matrix is given by:

$$\boldsymbol{X} = \begin{bmatrix} N_1 a_1 & N_2 a_2 \\ N_1 b_1 & N_2 b_2 \end{bmatrix} \tag{3.1.37}$$

Using eqs. (3.1.35) and (3.1.36) it is found that $(N_1 a_1)^2 = (N_2 a_2)^2 = 1/2$ and taking $N_1 a_1 = -1/\sqrt{2}$ and $N_2 a_2 = 1/\sqrt{2}$, so:

$$\boldsymbol{X} = \begin{bmatrix} -1/\sqrt{2} & 1/\sqrt{2} \\ -\mathrm{i}/\sqrt{2} & -\mathrm{i}/\sqrt{2} \end{bmatrix} \tag{3.1.38}$$

Now performing a similarity transformation on $\boldsymbol{R}$ with the use of $\boldsymbol{X}$ and its conjugate transpose $\boldsymbol{X}^{\dagger}$ we have that:

$$\boldsymbol{X}^{\dagger}\boldsymbol{R}\boldsymbol{X} = \begin{bmatrix} \mathrm{e}^{-\mathrm{i}\alpha} & 0 \\ 0 & \mathrm{e}^{\mathrm{i}\alpha} \end{bmatrix} = \begin{bmatrix} \lambda_1 & 0 \\ 0 & \lambda_2 \end{bmatrix} \tag{3.1.39}$$

That is, the transformed matrix is diagonal. Furthermore, the trace of a matrix is invariant under similarity transformation.

3.2 The Polarizability Tensor

3.2.1 General definition of a tensor

The representation of a tensor involves the choice of a basis system and the specification of a set of components for the tensor in that system. In this specific discussion, the chosen basis system is the cartesian system (x; y; z).

A second rank tensor is the result of a direct product of two vectors, which for a general tensor is given by [1]:

$$\boldsymbol{T}^{\{2\}} = \boldsymbol{AB} \tag{3.2.1}$$

where the superscript {2} denotes the rank. Each of the following nine terms in the expansion of $\boldsymbol{AB}$ involves dyads which are the product of two vector components:

$$\begin{aligned}\boldsymbol{AB} &= \left(\boldsymbol{e}_x A_x + \boldsymbol{e_y} A_y + \boldsymbol{e_z} A_z\right)\left(\boldsymbol{e}_x B_x + \boldsymbol{e_y} B_y + \boldsymbol{e_z} B_z\right) \\ &= A_x B_x \boldsymbol{e}_x \boldsymbol{e}_x + A_x B_y \boldsymbol{e}_x \boldsymbol{e}_y + A_x B_z \boldsymbol{e}_x \boldsymbol{e}_z + A_y B_x \boldsymbol{e}_y \boldsymbol{e}_x + A_y B_y \boldsymbol{e}_y \boldsymbol{e}_y \\ &\quad + A_y B_z \boldsymbol{e}_y \boldsymbol{e}_z + A_z B_x \boldsymbol{e}_z \boldsymbol{e}_x + A_z B_y \boldsymbol{e}_z \boldsymbol{e}_y + A_z B_z \boldsymbol{e}_z \boldsymbol{e}_z\end{aligned} \tag{3.2.2}$$

where $\boldsymbol{e}_x$, $\boldsymbol{e}_y$ and $\boldsymbol{e}_z$ are the unit vectors. The tensor $\boldsymbol{T}^{\{2\}}$ is a linear operator which sends a vector $\boldsymbol{V}$ into another vector according to the following rule:

$$\boldsymbol{T}^{\{2\}}(\boldsymbol{V}) = \boldsymbol{AB}(\boldsymbol{V}) = \boldsymbol{A}(\boldsymbol{B} \cdot \boldsymbol{V}) \tag{3.2.3}$$

When the tensor $\boldsymbol{T}^{\{2\}}$ acts on a vector dyad, the result is a scalar according to the rule:

$$\boldsymbol{T}^{\{2\}}(\boldsymbol{VW}) = \boldsymbol{AB}(\boldsymbol{VW}) = (\boldsymbol{B} \cdot \boldsymbol{V})(\boldsymbol{A} \cdot \boldsymbol{W}) \tag{3.2.4}$$

3.2.2 Reduction of the polarizability tensor

The polarizability tensor $\boldsymbol{\alpha}$ present in the equation of the induced electric dipole, which we will see later in the next section, is a second-rank tensor represented by the following 3×3 matrix:

$$\boldsymbol{\alpha}^{\{2\}} \cong \begin{bmatrix} \alpha_{xx} & \alpha_{xy} & \alpha_{xz} \\ \alpha_{yx} & \alpha_{yy} & \alpha_{yz} \\ \alpha_{zx} & \alpha_{zy} & \alpha_{zz} \end{bmatrix} \tag{3.2.5}$$

the trace of the polarizability tensor is:

$$\mathrm{Tr}\boldsymbol{\alpha} = \alpha_{xx} + \alpha_{yy} + \alpha_{zz} \tag{3.2.6}$$

The reduction of the polarizability tensor in the cartesian system is given by:

$$\boldsymbol{\alpha} = \boldsymbol{\alpha}^{(0)} + \boldsymbol{\alpha}^{(1)} + \boldsymbol{\alpha}^{(2)} \tag{3.2.7}$$

where the irreducible tensors $\boldsymbol{\alpha}^{(0)}$, $\boldsymbol{\alpha}^{(1)}$ and $\boldsymbol{\alpha}^{(2)}$ are a diagonal tensor, an anti-symmetric traceless tensor and a symmetric traceless tensor, respectively.

Defining the mean polarizability, a as:

$$a = \frac{1}{3}\left(\alpha_{xx} + \alpha_{yy} + \alpha_{zz}\right) = \frac{1}{3}\mathrm{Tr}\boldsymbol{\alpha} \tag{3.2.8}$$

The trace of a matrix is invariant under rotation of the axis system, so that the mean polarizability is an invariant of the tensor. A second-rank tensor like the polarizability tensor generally possesses three invariants.

We have that:

$$\boldsymbol{\alpha}^{(0)} = \begin{matrix} a & 0 & 0 \\ 0 & a & 0 \\ 0 & 0 & a \end{matrix} \tag{3.2.9}$$

and the trace of the diagonal tensor is:

$$\mathrm{Tr}\boldsymbol{\alpha}^{(0)} = 3a \tag{3.2.10}$$

The anti-symmetric traceless tensor $\boldsymbol{\alpha}^{(1)}$ becomes:

$$\boldsymbol{\alpha}^{(1)} = \begin{matrix} 0 & \left(\frac{\alpha_{xy}-\alpha_{yx}}{2}\right) & \left(\frac{\alpha_{xz}-\alpha_{zx}}{2}\right) \\ -\left(\frac{\alpha_{xy}-\alpha_{yx}}{2}\right) & 0 & \left(\frac{\alpha_{yz}-\alpha_{zy}}{2}\right) \\ -\left(\frac{\alpha_{xz}-\alpha_{zx}}{2}\right) & -\left(\frac{\alpha_{yz}-\alpha_{zy}}{2}\right) & 0 \end{matrix} \tag{3.2.11}$$

and the trace is:

$$\mathrm{Tr}\boldsymbol{\alpha}^{(1)} = 0 \tag{3.2.12}$$

For the symmetric traceless tensor:

$$\boldsymbol{\alpha}^{(2)} = \begin{matrix} \alpha_{xx} - a & \left(\frac{\alpha_{xy}+\alpha_{yx}}{2}\right) & \left(\frac{\alpha_{xz}+\alpha_{zx}}{2}\right) \\ \left(\frac{\alpha_{yx}+\alpha_{xy}}{2}\right) & \alpha_{yy} - a & \left(\frac{\alpha_{yz}+\alpha_{zy}}{2}\right) \\ \left(\frac{\alpha_{zx}+\alpha_{xz}}{2}\right) & \left(\frac{\alpha_{yz}+\alpha_{zy}}{2}\right) & \alpha_{zz} - a \end{matrix} \tag{3.2.13}$$

and the trace is:

$$\mathrm{Tr}\boldsymbol{\alpha}^{(2)} = 0 \tag{3.2.14}$$

3.3 The Raman effect

3.3.1 Classical theory of Raman scattering

The discovery of the Raman scattering in 1928 has determined the increasing publication of a relevant number of reports on the argument, regarding the theories, instrumentations, applications and interpretations of the spectra [1-7].

When a monochromatic radiation of frequency ω_1 is incident on a sample, it can be transmitted, reflected or, in addition, scattered. The scattered radiation generally possesses the same frequency as the incident radiation and it is called Rayleigh $(\omega_s) = \omega_1$, it is also said as elastic scattering. But in some case the scattered radiation can be an inelastic scattering and can possesses either a frequency that is lower than the one of the incident radiation $(\omega_s) = \omega_1 - \omega_M$ or greater than the one of the incident radiation $(\omega_s) = \omega_1 + \omega_M$. The former inelastic scattering is also said as Raman Stokes while the latter is also said as Raman anti-Stokes.

In both the classical and quantum mechanical treatments of the Raman spectroscopy addressed later, the scattered radiation is due to the oscillating electric dipole moments induced in a molecule by the electromagnetic fields. The contributions of the oscillating magnetic dipole and of the electric quadrupole are several orders of magnitude smaller than that of the oscillating electric dipole and they are not considered in this work.

The intensity (I) of the scattered radiation radiated by an oscillating electric dipole induced by the electric field of the incident radiation ω_1 is given by:

$$I = \frac{\omega_s^4 p_0^2 \sin^2\theta}{32\pi^2 \varepsilon_0 c_0^3} \tag{3.3.1}$$

Where p_0 is the amplitude of the induced electric dipole, θ is the angle between the electrical field and the axis of the dipole and $\omega_s$is the frequency of the electrical dipole. Introducing the relation $\omega_s = 2\pi c_0 \tilde{\nu}_s$ eq. (3.3.1) becomes:

$$I = \frac{\pi^2 c_0 \tilde{\nu}_s^4 p_0^2 \sin^2\theta}{2\varepsilon_0} \tag{3.3.2}$$

Considering a single molecule which is free to vibrate but not to rotate, the objective is to calculate the frequency-dependent linear induced electric dipole vectors named $\boldsymbol{p}^{(1)}$ using the relationship:

$$\boldsymbol{p}^{(1)} = \boldsymbol{\alpha} \cdot \boldsymbol{E} \tag{3.3.3}$$

where $\boldsymbol{E}$ is the electric field vector of the incident, plane wave, monochromatic radiation of frequency ω_1 and $\boldsymbol{\alpha}$ is the polarizability tensor of the molecule described in section 3.2. The molecule is then space-fixed in an equilibrium configuration and the nuclei may vibrate about their equilibrium

positions. Now, the variation of the polarizability with vibrations can be expressed by expanding each component α_{xy} of the polarizability tensor $\boldsymbol{\alpha}$ in a Taylor series with respect to the normal coordinates of vibration:

$$\alpha_{xy} = \left(\alpha_{xy}\right)_0 + \sum_k \left(\frac{\partial \alpha_{xy}}{\partial Q_k}\right)_0 Q_k + \frac{1}{2}\sum_{k,l}\left(\frac{\partial^2 xy}{\partial Q_k Q_l}\right)_0 Q_k\, Q_l \ldots \qquad (3.3.4)$$

where $(\alpha_{\rho\sigma})_0$ is the value of $\alpha_{\rho\sigma}$ at the equilibrium configuration, Q_k, Q_l ... are the normal coordinates of vibration related to the molecular vibrational frequencies ω_k, ω_l ..., and the summations are over all normal coordinates. The derivatives are to be taken at the equilibrium configuration and this is why they bear the subscript "0". If the Taylor series is truncated at the first power of Q, then reference is made to the so-called electrical harmonic approximation, and one can concentrate at least initially on a single normal mode of vibration Q_k. So, equation (3.3.4) may be written in the form:

$$\left(\alpha_{xy}\right)_k = \left(\alpha_{xy}\right)_0 + \left(\alpha'_{xy}\right)_k Q_k \qquad (3.3.5)$$

Where:

$$\left(\alpha'_{xy}\right)_k = \left(\frac{\partial \alpha_{xy}}{\partial Q_k}\right)_0 \qquad (3.3.6)$$

The $\left(\alpha'_{xy}\right)_k$ are components of $\boldsymbol{\alpha'}_k$, a new tensor that can be called as derived polarizability tensor because of its components that are polarizability derivatives with respect to the normal coordinates Q_k. In vectors form eq. (3.3.5) becomes:

$$\boldsymbol{\alpha}_k = \boldsymbol{\alpha}_0 + \boldsymbol{\alpha'}_k Q_k \qquad (3.3.7)$$

where $\boldsymbol{\alpha}_k$ is a tensor with components $\left(\alpha_{xy}\right)_k$, and the scalar quantity Q_k multiplies the components of the derived polarizability tensor. In the harmonic approximation Q_k is defined as:

$$Q_k = Q_{k_0}\cos(\omega_k t + \delta_k) \qquad (3.3.8)$$

where Q_{k_0} represents the normal coordinate amplitude and δ_k is a phase factor. Substituting eq. (3.3.8) into eq. (3.3.7) we have:

$$\boldsymbol{\alpha}_k = \boldsymbol{\alpha}_0 + \boldsymbol{\alpha'}_k Q_{k_0}\cos(\omega_k t + \delta_k) \qquad (3.3.9)$$

The electric field is frequency-dependent and this is given by:

$$\boldsymbol{E} = \boldsymbol{E}_0 \cos \omega_1 t \tag{3.3.10}$$

Introducing eq. (3.3.9) into eq. (3.3.3) and taking into account eq. (3.3.10) we obtain:

$$\boldsymbol{p}^{(1)} = \boldsymbol{\alpha}_0 \boldsymbol{E}_0 \cos \omega_1 t + \frac{1}{2} \boldsymbol{\alpha'}_k \boldsymbol{E}_0 Q_{k_0} [\cos(\omega_1 t + \omega_k t + \delta_k) + \cos(\omega_1 t - \omega_k t - \delta_k)] \tag{3.3.11}$$

Because of the trigonometric identity:

$$\cos A \cos B = \frac{1}{2} [\cos(A + B) + \cos(A - B)] \tag{3.3.12}$$

The first term of eq. (3.3.11), $\boldsymbol{\alpha}_0 \boldsymbol{E}_0 \cos \omega_1 t$, represents the classical Rayleigh scattering whereas the second terms, $\frac{1}{2} \boldsymbol{\alpha'}_k \boldsymbol{E}_0 Q_{k_0} \cos[\omega_1 t \pm (\omega_k t + \delta_k)]$, define the classical Raman scattering, where the Raman Stokes is given by $\frac{1}{2} \boldsymbol{\alpha'}_k \boldsymbol{E}_0 Q_{k_0} \cos(\omega_1 t + \omega_k t + \delta_k)$, and the Raman anti-Stokes by $\frac{1}{2} \boldsymbol{\alpha'}_k \boldsymbol{E}_0 Q_{k_0} \cos(\omega_1 t - \omega_k t - \delta_k)$. The Rayleigh scattering possesses the same phase as that of the incident field while in the Raman scattering the quantity δ_k defines the phase of the normal vibration Q_k respect to the electric field. The Raman Stokes and anti-Stokes scatterings depend on the electric dipoles oscillating at $(\omega_1 \pm \omega_k)$ generated by the modulation of electric dipole oscillating at ω_1 by the oscillating molecule. The necessary condition for Raman scattering requires that at least one component of the derived polarizability tensor $\boldsymbol{\alpha'}_k$ is non-zero. From eq. (3.3.6) the components of $\boldsymbol{\alpha'}_k$, that is the $\left(\alpha'_{xy}\right)_k$, are the derivative with respect to the normal coordinate of vibration Q_k taken at the equilibrium position. Hence, the gradient with respect to the normal coordinate, in its equilibrium position, of at least one component of the polarizability tensor must be non-zero to reach the condition to have the Raman scattering.

In the present discussion, the condition to have eq. (3.3.11) is given by harmonic approximation. When mechanical anharmonicity is taken into account, the time dependence of the normal coordinate Q_k includes terms involving $\cos(2\omega_k t + \delta_{2k})$, $\cos(3\omega_k t + \delta_{3k})$, etc related to the so-called overtones, and also terms involving $\cos(\omega_k t + \delta_{kl})$, $\cos\left(\omega_l t + \delta'_{kl}\right)$ which relate to combination bands. The consequence of the electrical anharmonicity reflect on the eq. (3.3.4) and higher terms than the first in Taylor expansion must be considered resulting into additional induced electric dipoles with frequencies $\omega_1 \pm 2\omega_k$ etc, and $\omega_1 \pm (\omega_k \pm \omega_l)$ etc.

The classical theory of Raman spectroscopy has many limitations, as example, it cannot be applied to molecular rotations because the relative discrete rotational energy levels

belong to quantum states. In addition, it cannot explain the intensity difference between Stokes and anti-Stokes scattering. These aspects of the Raman scattering theory can be described with a quantum approach as described in the next section.

3.3.2 Quantum mechanical theory of Raman scattering

A general model of the quantum theory is based on the photon population of electromagnetic radiation incident on a molecule. In such system, n_1 photons are characterized by an energy $\hbar\omega_1$, where ω_1 is the frequency of the incident radiation, and the molecules possess an initial energetic level equal to E_i. The interaction of the radiation with the molecule leads to $(n_1 - 1)$ photons that have the same frequency of the incident radiation and to the creation of a new photon that has an energy $\hbar\omega_s$, where ω_s is the frequency of the scattered photon. The final energetic level of the system will be equal to E_f. In the overall process, energy must be conserved so that $\omega_s = \omega_1 - \omega_M$ where $\omega_M = 2\pi(E_f - E_i)/h$. It is important to remember that the energy $\hbar\omega_1$ does not correspond to any electronic transition energy but it mostly determines some perturbation on the molecule. If $\hbar\omega_1$ approaches electronic transition energy, then an enhancement of the scattered intensity can be observed.

The global scattering model involves a two photons process, one incident and one scattered. It describes Rayleigh scattering when the energy levels of the initial and the final levels are equal, that is $E_f = E_i$, so that $\omega_s = \omega_1$ and $\omega_M = 0$. If the energy levels of Raman scattering are such that $E_f > E_i$, then $\omega_s = \omega_1 - \omega_M$ and this is the case of the Stokes Raman scattering; In the case of that $E_f < E_i$, we have $\omega_s = \omega_1 + \omega_M$ and this is the anti-Stokes Raman scattering. Absorption without energy conservation is called *virtual* absorption and the resulting state is described as *virtual state*.

The time-dependent perturbation theory is usefully applied to the description of the Raman effect. The induced electric dipole described in the classical theory is replaced by the transition electric dipole generated by a transition in the molecule from an initial state, *i*, to a final state, *f*, that is determined by the incident electric field of the radiation that has a frequency equal to ω_1.

The total induced transition electric dipole is then given by:

$$(\boldsymbol{p})_{fi} = \left(\boldsymbol{p}^{(1)}\right)_{fi} + \left(\boldsymbol{p}^{(2)}\right)_{fi} + \left(\boldsymbol{p}^{(3)}\right)_{fi} + \cdots \qquad (3.3.13)$$

where $\left(\boldsymbol{p}^{(1)}\right)_{fi}$ is the unique term that is linear in $\boldsymbol{E}$, and so it will be the only one considered in a simplified approach to Raman scattering. There is a further transition moment correlated to the permanent electric dipole transition given by the term $\left(\boldsymbol{p}^{(0)}\right)_{fi}$ but it is independent from the electrical field of the incident radiation and so need not be considered here because it is not involved in Raman effect. The total transition electric dipole is given by:

$$(\boldsymbol{p})_{fi} = \left\langle \psi_f^{'} \middle| \hat{\boldsymbol{p}} \middle| \psi_i^{'} \right\rangle \tag{3.3.14}$$

where ψ_i' and ψ_f' are the time-dependent perturbed wave functions of the initial and final states of the molecule and $\hat{\boldsymbol{p}}$ is the electric dipole moment operator.

The ψ_i' and ψ_f' wave functions can be represented by the series expansions:

$$\psi_i' = \psi_i^{(0)} + \psi_i^{(1)} + \psi_i^{(2)} + \cdots + \psi_i^{(n)} \tag{3.3.15}$$

and

$$\psi_f' = \psi_f^{(0)} + \psi_f^{(1)} + \psi_f^{(2)} + \cdots + \psi_f^{(n)} \tag{3.3.16}$$

where the superscripts (0), (1), (2), … (n) indicate the order of modification to the unperturbed state (given by $\psi_i^{(0)}$), that is $\psi_i^{(1)}$ indicates the first-order modification to $\psi_i^{(0)}$ and so on. It is important to state that because the field acts once on $\psi_i^{(0)}$ to give $\psi_i^{(1)}$ and twice to give $\psi_i^{(2)}$, then in the present discussion of Raman effect it is allowed to neglect the higher orders. Introducing the eqs. (3.3.15) and (3.3.16) and considering the terms linearly dependent to the electric field, we have that eq. (3.3.14) becomes:

$$\left(\boldsymbol{p}^{(1)}\right)_{fi} = \left\langle \psi_f^{(1)} \middle| \hat{\boldsymbol{p}} \middle| \psi_i^{(0)} \right\rangle + \left\langle \psi_f^{(0)} \middle| \hat{\boldsymbol{p}} \middle| \psi_i^{(1)} \right\rangle \tag{3.3.17}$$

However, to maintain generality in the treatment, the electric field amplitude should be considered to be complex and eq. (3.3.17) could be rewritten as:

$$\left(\tilde{\boldsymbol{p}}^{(1)}\right)_{fi} = \left\langle \psi_f^{(1)} \middle| \hat{\boldsymbol{p}} \middle| \psi_i^{(0)} \right\rangle + \left\langle \psi_f^{(0)} \middle| \hat{\boldsymbol{p}} \middle| \psi_i^{(1)} \right\rangle \tag{3.3.18}$$

In this case, the real part of the induced transition electric dipole moment $\left(\boldsymbol{p}^{(1)}\right)_{fi}$ is defined as:

$$\left(\boldsymbol{p}^{(1)}\right)_{fi} = \left(\tilde{\boldsymbol{p}}^{(1)}\right)_{fi} + \left(\tilde{\boldsymbol{p}}^{(1)}\right)_{fi}^{*} \tag{3.3.19}$$

Where $\left(\tilde{\boldsymbol{p}}^{(1)}\right)_{fi}^{*}$ represents the conjugate complex of $\left(\tilde{\boldsymbol{p}}^{(1)}\right)_{fi}$.

The component $\left(p_x^{(1)}\right)_{fi}$ for real wave functions can be expressed using the time-independent unperturbed wave functions ψ_i, ψ_r and ψ_f of the states *i*, *r* and *f*, respectively. The relation between ψ_r and the corresponding time-dependent wave function is given by:

$$\Psi_r = \psi_r e^{-i(\omega_r - i\Gamma_r)t} \tag{3.3.20}$$

where

$$\omega_r = \frac{E_r}{\hbar} \tag{3.3.21}$$

With E_r is the energy of the state *r* and the coefficient $(2\Gamma_r)$ is related to the full width of the level *r*. The lifetime of the state *r* is related to the coefficient $(2\Gamma_r)$ by the uncertainty principle:

$$\tau_r = \frac{\hbar}{2\Gamma_r} \tag{3.3.22}$$

Thus, the component $\left(p_x^{(1)}\right)_{fi}$ is given by:

$$\begin{aligned}\left(p_x^{(1)}\right)_{fi} = \frac{1}{2\hbar}\sum_{r\neq i}\Bigg\{&\frac{\langle\psi_f|\hat{p}_x|\psi_r\rangle\langle\psi_r|\hat{p}_y|\psi_i\rangle}{\omega_{ri}-\omega_1-i\Gamma_r}\tilde{E}_{y_0}e^{-i(\omega_1-\omega_{fi})t}+\\&+\frac{\langle\psi_f|\hat{p}_x|\psi_r\rangle\langle\psi_r|\hat{p}_y|\psi_i\rangle}{\omega_{ri}+\omega_1+i\Gamma_r}\tilde{E}_{y_0}^{*}e^{i(\omega_1+\omega_{fi})t}\Bigg\}+\\&+\frac{1}{2\hbar}\sum_{r\neq f}\Bigg\{\frac{\langle\psi_f|\hat{p}_y|\psi_r\rangle\langle\psi_r|\hat{p}_x|\psi_i\rangle}{\omega_{rf}-\omega_1-i\Gamma_r}\tilde{E}_{y_0}^{*}e^{i(\omega_1+\omega_{fi})t}+\\&+\frac{\langle\psi_f|\hat{p}_y|\psi_r\rangle\langle\psi_r|\hat{p}_x|\psi_i\rangle}{\omega_{rf}+\omega_1+i\Gamma_r}\tilde{E}_{y_0}e^{-i(\omega_1-\omega_{fi})t}\Bigg\}+\\&+complex\ conjugate\end{aligned} \tag{3.3.23}$$

where $\tilde{E}_{y_0}$ is the y component of the complex amplitude of the plane harmonic electromagnetic wave of frequency ω_1 of the incident radiation. The double subscript on ω indicates a correspondence of the frequency with the energy difference between the levels.

Another assumption is that to consider the lifetime of initial and final states *i* and *f* infinite so that $\Gamma_i = \Gamma_f = 0$. As a result, the total wave functions expressed in eq. (3.3.20) for those states will be:

$$\Psi_i = \psi_i e^{-i\omega_i t} \tag{3.3.24}$$

$$\Psi_f = \psi_f e^{-i\omega_f t} \tag{3.3.25}$$

The exponential terms of eq. (3.3.23) contains two types of terms as regards their frequency dependence, in particular $(\omega_1 - \omega_{fi})$ and $(\omega_1 + \omega_{fi})$. The terms that in eq. (3.3.23) involve $(\omega_1 - \omega_{fi})$ describe the generation of the scattering provided that $(\omega_1 - \omega_{fi}) > 0$. The nature of the scattering depends on ω_{fi}, that is:

$\omega_{fi} > 0$ Stokes Raman scattering

$\omega_{fi} = 0$ Rayleigh scattering

$\omega_{fi} < 0$ anti-Stokes Raman scattering

In the rotational and vibrational transitions which do not involve a change of the electronic state, the condition that $\hbar(\omega_1 - \omega_{fi}) > 0$ is always satisfied for excitation frequencies in the visible and ultraviolet regions of the spectrum.

The terms that in eq. (3.3.23) involve $(\omega_1 + \omega_{fi})$ describe induced emission of two quanta, $\omega_1 + \omega_{fi}$ and ω_1, from an initial state, that is an excited level ω_i, to a lower level ω_f, if $\omega_1 + \omega_{fi} > 0$.

It follows that the Stokes and anti-Stokes Raman part of the *x* component of the real induced transition electric dipole moment is:

$$\left(p_x^{(1)}\right)_{fi} = \frac{1}{2\hbar} \sum_{r \neq i,f} \left\{ \frac{\langle \psi_f | \hat{p}_x | \psi_r \rangle \langle \psi_r | \hat{p}_y | \psi_i \rangle}{\omega_{ri} - \omega_1 - i\Gamma_r} + \frac{\langle \psi_f | \hat{p}_y | \psi_r \rangle \langle \psi_r | \hat{p}_x | \psi_i \rangle}{\omega_{rf} + \omega_1 + i\Gamma_r} \right\} \tilde{E}_{y_0} e^{-i\omega_s t} + + complex\ conjugate \tag{3.3.26}$$

where ω_s is the absolute frequency of the scattered radiation defined as:

$$\omega_s = \omega_1 - \omega_{fi} \tag{3.3.27}$$

The components $(\alpha_{xy})_{fi}$ of the general transition polarizability $(\boldsymbol{\alpha})_{fi}$ are then given by:

$$(\alpha_{xy})_{fi} = \frac{1}{\hbar}\sum_{r\neq i,f}\left\{\frac{\langle\psi_f|\hat{p}_x|\psi_r\rangle\langle\psi_r|\hat{p}_y|\psi_i\rangle}{\omega_{ri}-\omega_1-i\Gamma_r}+\frac{\langle\psi_f|\hat{p}_y|\psi_r\rangle\langle\psi_r|\hat{p}_x|\psi_i\rangle}{\omega_{rf}+\omega_1+i\Gamma_r}\right\} \quad (3.3.28)$$

In eq. (3.3.28) the summation is over the states r that carry the restriction $r \neq i, f$. Normally, the summation should consist of all the states including the initial and final states. But in a lot of cases, their contributions to the polarizability are either zero or very small and thus negligible. Eq. (3.3.28) is in fact complex because of the presence of $i\Gamma_r$ in the denominators, but whatever the sign of this term, certain frequency conditions lead to ignoring the contribution of $i\Gamma_r$. Therefore, the transition polarizability becomes unambiguously real and is given by:

$$(\alpha_{xy})_{fi} = \frac{1}{\hbar}\sum_{r\neq i,f}\left\{\frac{\langle\psi_f|\hat{p}_x|\psi_r\rangle\langle\psi_r|\hat{p}_y|\psi_i\rangle}{\omega_{ri}-\omega_1}+\frac{\langle\psi_f|\hat{p}_y|\psi_r\rangle\langle\psi_r|\hat{p}_x|\psi_i\rangle}{\omega_{rf}+\omega_1}\right\} \quad (3.3.29)$$

Using this real transition polarizability, eq. (3.3.26) should be expressed as:

$$\left(p_x^{(1)}\right)_{fi} = \frac{1}{2}(\alpha_{xy})_{fi}\left(\tilde{E}_{y_0}e^{-i\omega_s t}+\tilde{E}_{y_0}^{*}e^{i\omega_s t}\right) \quad (3.3.30)$$

That can be, with the use of the x component of the time-independent complex transition moment amplitude and its conjugate complex, conveniently expressed as:

$$\left(p_x^{(1)}\right)_{fi} = \frac{1}{2}\left\{\left(\tilde{p}_{x_0}^{(1)}\right)_{fi}e^{-i\omega_s t}+\left(\tilde{p}_{x_0}^{(1)}\right)_{fi}^{*}e^{i\omega_s t}\right\} \quad (3.3.31)$$

where

$$\left(\tilde{p}_{x_0}^{(1)}\right)_{fi} = (\alpha_{xy})_{fi}\tilde{E}_{y_0} \quad (3.3.32)$$

$$\left(\tilde{p}_{x_0}^{(1)}\right)_{fi}^{*} = (\alpha_{xy})_{fi}\tilde{E}_{y_0}^{*} \quad (3.3.33)$$

The electric field amplitude could be real so that $\tilde{E}_{y_0} = \tilde{E}_{y_0}^{*} = E_{y_0}$ and $\left(\tilde{p}_{x_0}^{(1)}\right)_{fi} = \left(\tilde{p}_{x_0}^{(1)}\right)_{fi}^{*}$ which may be substituted by $\left(p_{x_0}^{(1)}\right)_{fi}$. Thus eq. (3.3.31) becomes:

$$\left(p_x^{(1)}\right)_{fi} = \frac{1}{2}\left(p_{x_0}^{(1)}\right)_{fi}\left(e^{-i\omega_s t}+e^{i\omega_s t}\right) \quad (3.3.34)$$

with

$$\left(p_{x_0}^{(1)}\right)_{fi} = (\alpha_{xy})_{fi}E_{y_0} \quad (3.3.35)$$

Transforming eq. (3.3.34) to trigonometric representation led to:

$$\left(p_x^{(1)}\right)_{fi} = \left(p_{x_0}^{(1)}\right)_{fi} \cos \omega_s t \tag{3.3.36}$$

Introducing eq. (3.3.35) in eq. (3.3.36) we obtain:

$$\left(p_x^{(1)}\right)_{fi} = \left(\alpha_{xy}\right)_{fi} E_{y_0} \cos \omega_s t \tag{3.3.37}$$

The results of the quantum approach are generally similar to those of the classical treatment, the electric field has the same classical form. The difference is in the transition polarizability that, in the quantum mechanical treatment, is defined in terms of wave functions and energy levels of the system. In this way, the characteristics of the scattered radiation are related to th properties of the scattering molecules.

Considering the eq. (3.3.28), its derivation does not carry any restriction regarding the relationship between the frequency of an incident photon ($\hbar\omega_1$) and any absorption energy ($\hbar\omega_{ri}$) in the scattering material. In the same way, no restriction was made about the energies of the state ψ_r which in principle could lie above the final state ψ_f, below the initial state ψ_i, or between them (figure 3.3.1). In the frequency denominators ($\omega_{ri} - \omega_1 - i\Gamma_r$) which appear in the first term of eq. (3.3.28), the magnitude of ω_1 and ω_r are relatively important because of their involved difference.

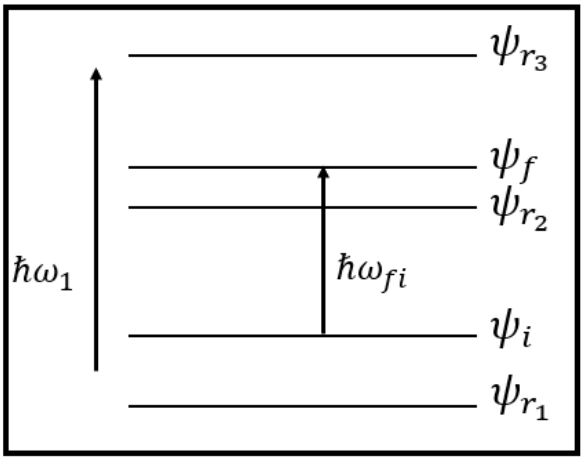

Figure 3.3.1. *Energy levels of the ψ_r states, reproduced from reference [7].*

There are two limiting cases to be considered:

1) in the first one the frequency of the incident radiation is very much smaller than any absorption energy, $\omega_1 \ll \omega_{ri}$. Then, $\omega_{ri} - \omega_1 \approx \omega_{ri}$ for all the states ψ_r and the Γ_r can be neglected because they are very small relative to the ω_{ri}.

2) In the second case the frequency of the incident radiation is close to one or more particular absorption energy, $\omega_1 \approx \omega_{ri}$. Then, $\omega_{ri} - \omega_1 - i\Gamma_r$ tends to $-i\Gamma_r$ for a particular state ψ_r and the terms that possess such denominators will dominate in the sum over *r*.

The first case is illustrated in figure (3.3.2.a) [7], here the incident radiation of frequency ω_1 induces a transition from an initial stationary state ψ_i to a so-called virtual state from which it makes a transition to a final stationary state ψ_f. It is important to remember that the involved virtual states are not stationary states and do not correspond to a well-defined value of the energy because they are not a solution of a time-independent Schrödinger equation.

As ω_1 approaches, or is almost equal to, a molecular transition frequency ω_{ri}, or at last is large enough to reach the dissociative continuum energy levels, figure (3.3.2.a/b/c)) respectively, the second case takes shape. The intensity of resonance Raman scattering can be expected to be orders of magnitude greater than normal Raman scattering. The second frequency denominator $(\omega_{rf} + \omega_1 + i\Gamma_r)$ which appears in the second term of eq. (3.3.28), involves the sum of ω_{rf} and ω_1 and therefore cannot become either small or zero. Thus, the contribution of this term to $(\alpha_{xy})_{fi}$ can be neglected if one or more terms of the first term of eq. (3.3.28) is dominant, except in the case of stimulated emission.

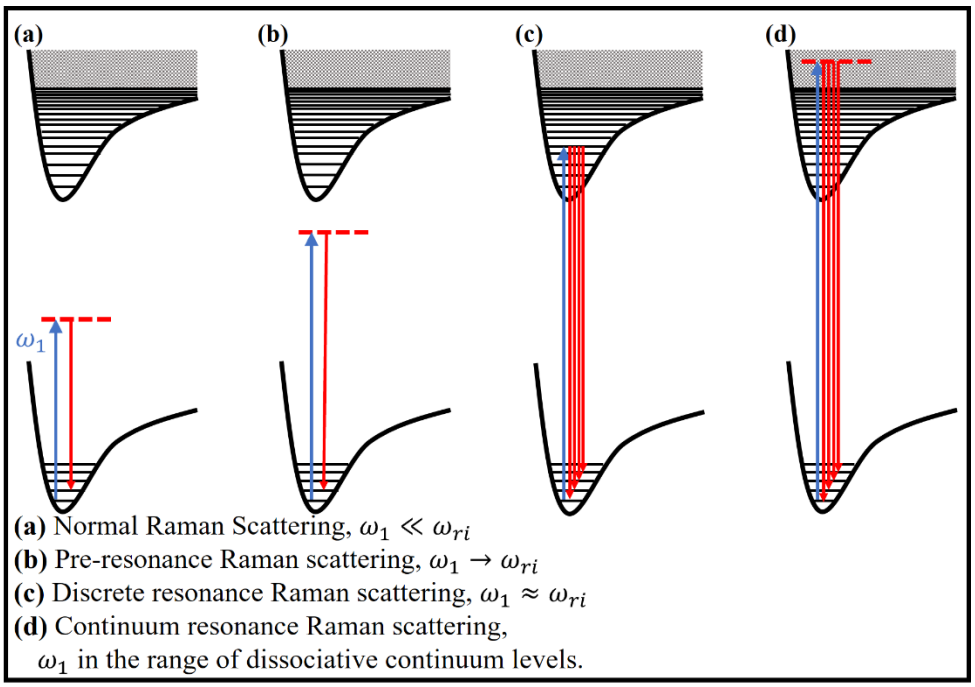

Figure 3.3.2. *Raman scattering processes, reproduced from reference [7].*

Looking at the numerator of the first term of eq. (3.3.28), it involves the product of two transition electric dipole terms: $\langle\psi_r|\hat{p}_y|\psi_i\rangle$ and $\langle\psi_f|\hat{p}_x|\psi_r\rangle$. The first term represents a transition from an initial state ψ_i to a virtual state ψ_r, the second term is a transition from the virtual state ψ_r to a final state ψ_f. For normal Raman scattering, where $\omega_1 \ll \omega_{ri}$, the $(\alpha_{xy})_{fi}$ is determined by a weighted sum over the states ψ_r, of the product, the weighting for each state ψ_r being inversely proportional to $(\omega_{ri} - \omega_1 - i\Gamma_r)$. In other words, normal Raman scattering involves all possible virtual states from which the transition from the initial state to the final state has to pass through, provided that the electric dipole transition moment between the virtual states and both the initial and final states, is non-zero. In contrast, for resonance Raman scattering, the virtual states ψ_r for which $\omega_1 \approx \omega_{ri}$ will predominate in the sum over the states ψ_r and $(\alpha_{xy})_{fi}$ will determined by the properties of a limited number of states ψ_r.

Normal Raman scattering is essentially a ground electronic state property, while in the resonance Raman scattering, the properties of excited vibronic and rovibronic states can be investigated.

3.3.3 The Born-Oppenheimer approximation

The general formula for $(\alpha_{xy})_{fi}$ is more manageable when some simplifications are taken. The first fundamental step is to introduce the Born-Oppenheimer approximation. When the *j*-th electronic nuclear state ψ^j is expressed as a function of the quantum numbers (e^j), (v^j) and (R^j) of its electronic, vibrational and rotational parts respectively, as follows:

$$\psi^j = \psi(e^j, v^j, R^j) \tag{3.3.38}$$

And the same expanded notation is taken for the energy:

$$\omega_j = \omega_{e^j v^j R^j} \tag{3.3.39}$$

The Born-Oppenheimer approximation, also called adiabatic approximation, allows to express eq. (3.3.38) as a product of the electronic, vibrational and rotational functions, and eq. (3.3.39) as a sum of three contributions:

$$\psi^j = \psi_e^j \psi_v^j \psi_R^j \tag{3.3.40}$$

$$\omega_{e^j v^j R^j} = \omega_{e^j} + \omega_{v^j} + \omega_{R^j} \tag{3.3.41}$$

Applying the eqs. (3.3.40) and (3.3.41) and knowing that the xy component of a polarizability tensor operator $\hat{\alpha}_{xy}(e^r, v^r, R^r)$ is given by:

$$\hat{\alpha}_{xy}(e^r, v^r, R^r) = \frac{1}{\hbar} \sum_{\substack{e^r v^r R^r \neq \\ e^i v^i R^i, \\ e^f v^f R^f}} \left\{ \frac{\hat{p}_x |\psi_e^r \psi_v^r \psi_R^r\rangle\langle\psi_R^r \psi_v^r \psi_e^r| \hat{p}_y}{\omega_{e^r e^i} + \omega_{v^r v^i} + \omega_{R^r R^i} - \omega_1 - i\Gamma_{e^r v^r R^r}} + \right. \\ \left. + \frac{\hat{p}_y |\psi_e^r \psi_v^r \psi_R^r\rangle\langle\psi_R^r \psi_v^r \psi_e^r| \hat{p}_x}{\omega_{e^r e^f} + \omega_{v^r v^f} + \omega_{R^r R^f} + \omega_1 + i\Gamma_{e^r v^r R^r}} \right\} \tag{3.3.42}$$

The eq. (3.3.28) becomes:

$$\left(\alpha_{xy}\right)_{e^f v^f R^f : e^i v^i R^i} = \left\langle \psi_R^f \psi_v^f \psi_e^f \middle| \hat{\alpha}_{xy}(e^r, v^r, R^r) \middle| \psi_e^i \psi_v^i \psi_R^i \right\rangle \tag{3.3.43}$$

Let now consider, as before, the denominator of first term in eq. (3.3.42). If a hypothetic electronic state (e^r) is not the ground electronic state, that is $e^r \neq e^g$ then the magnitudes of the rotational contribution to the energy, $\hbar\omega_{R^r R^i}$, can be neglected because very small compared to the vibronic energies. We shall have:

$$\omega_{e^r e^g} + \omega_{v^r v^i} - \omega_1 \gg 0 \tag{3.3.44}$$

Eq. (3.3.44) is satisfied only for ω_1 that is much smaller than any vibronic absorption frequency, $\omega_{e^r e^g} + \omega_{v^r v^i}$, or electronic absorption frequency, $\omega_{e^r e^g}$ if $\omega_{v^r v^i} = 0$. If the electronic state (e^r) is the ground electronic state, that is $e^r = e^g$, then $\omega_{e^r e^g} = 0$ and the term $\omega_{R^r R^i}$ can be neglected provided:

$$\omega_1 \gg \omega_{v^r v^i} + \omega_{R^r R^i} \tag{3.3.45}$$

In the frequency denominator of the second term in eq. (3.3.42), the term $\omega_{R^r R^f}$ can be neglected in all cases if the condition that ω_1 is sufficiently well removed from the microwave region is respected, so we have that:

$$\omega_{e^r e^f} + \omega_{v^r v^f} + \omega_1 \gg 0 \tag{3.3.46}$$

The condition is necessary when $\omega_{e^r e^f} = 0$, as in the case of both final and intermediate electronic states when they are the ground states. The last terms on the frequency denominators of eq. (3.3.42), that is $\Gamma_{e^r v^r R^r}$, depends on the rotational quantum numbers, but the contribution is so small that the term can be replaced by $\Gamma_{e^r v^r}$.

Assuming the above frequency conditions and with $e^i = e^g$, it will be obtained:

$$\hat{\alpha}_{xy}(e^r,v^r)=\frac{1}{\hbar}\sum_{\substack{e^rv^r\neq\\ e^gv^i,\\ e^fv^f}}\left\{\frac{\hat{p}_x|\psi_e^r\psi_v^r\rangle\langle\psi_v^r\psi_e^r|\hat{p}_y}{\omega_{e^re^g}+\omega_{v^rv^i}-\omega_1-i\Gamma_{e^rv^r}}+\right.$$
$$\left.+\frac{\hat{p}_y|\psi_e^r\psi_v^r\rangle\langle\psi_v^r\psi_e^r|\hat{p}_x}{\omega_{e^re^f}+\omega_{v^rv^f}+\omega_1+i\Gamma_{e^rv^r}}\right\} \tag{3.3.47}$$

In the same manner, eq. (3.3.43) becomes:

$$\left(\alpha_{xy}\right)_{e^fv^fR^f:e^gv^iR^i}=\left\langle\psi_R^f\psi_v^f\psi_e^f\middle|\hat{\alpha}_{xy}(e^r,v^r)\middle|\psi_e^g\psi_v^i\psi_R^i\right\rangle \tag{3.3.48}$$

After the transformation of the polarizability tensor operator $\hat{\alpha}_{xy}(e^r,v^r)$ from the space-fixed axes x, y, z to $\hat{\alpha}_{x'y'}(e^r,v^r)$ in the molecule-fixed axes x',y',z', by using direction cosines $l_{xx'}$, $l_{yy'}$, eq. (3.3.48) becomes:

$$\left(\alpha_{xy}\right)_{e^fv^fR^f:e^gv^iR^i}=\left\langle\psi_R^f\middle|l_{xx'}l_{yy'}\middle|\psi_R^i\right\rangle\left\langle\psi_v^f\psi_e^f\middle|\hat{\alpha}_{x'y'}(e^r,v^r)\middle|\psi_e^g\psi_v^i\right\rangle \tag{3.3.49}$$

The eq. (3.3.49) involves the product of two terms on its right-hand side. This is because the rotational transitions depend on direction cosine operators whereas the internal molecular coordinates act on the other terms. In the vast majority of the cases, Raman scattering is observed in experimental conditions in which the rotational structure is not resolved. For this reason, the scattering may should

be called as a pure vibrational Raman scattering associated with the transitions as from the state $\psi_e^g\psi_v^i$ to the state $\psi_e^g\psi_v^f$. In treating this type of scattering the isotropic averages of intensity expressions are finally formed. Hence, for vibrational transitions with no resolved rotational structure and for $e^i=e^g$, eq. (3.3.49) becomes:

$$\left(\alpha_{xy}\right)_{e^fv^f:e^gv^i}=\left\langle\psi_v^f\psi_e^f\middle|\hat{\alpha}_{x'y'}(e_1^r,v^r)\middle|\psi_e^g\psi_v^i\right\rangle \tag{3.3.50}$$

Now, introducing eq. (3.3.47) into eq. (3.3.50) we have:

$$\left(\alpha_{xy}\right)_{e^fv^f:e^gv^i}=\frac{1}{\hbar}\sum_{\substack{e^rv^r\neq\\ e^gv^i,\\ e^fv^f}}\left\{\frac{\left\langle\psi_v^f\psi_e^f\middle|\hat{p}_x|\psi_e^r\psi_v^r\rangle\langle\psi_v^r\psi_e^r|\hat{p}_y\middle|\psi_e^g\psi_v^i\right\rangle}{\omega_{e^re^g}+\omega_{v^rv^i}-\omega_1-i\Gamma_{e^rv^r}}+\right.$$
$$\left.+\frac{\left\langle\psi_v^f\psi_e^f\middle|\hat{p}_y|\psi_e^r\psi_v^r\rangle\langle\psi_v^r\psi_e^r|\hat{p}_x\middle|\psi_e^g\psi_v^i\right\rangle}{\omega_{e^re^f}+\omega_{v^rv^f}+\omega_1+i\Gamma_{e^rv^r}}\right\} \tag{3.3.51}$$

The eq. (3.3.51) defines the xy component of the transition polarizability that will be considered in the next simplifications considered in following section.

3.3.4 The Placzek transition polarizability

Let consider the cases for which both the initial and final vibrational states are non-degenerate and belong the ground electronic state for which $e^f = e^i = e^g$. For these conditions eq. (3.3.51) becomes:

$$\left(\alpha_{xy}\right)_{e^g v^f : e^g v^i} = \frac{1}{\hbar} \sum_{\substack{e^r v^r \neq \\ e^g v^i, \\ e^g v^f}} \left\{ \frac{\langle \psi_v^f \psi_e^g | \hat{p}_x | \psi_e^r \psi_v^r \rangle \langle \psi_v^r \psi_e^r | \hat{p}_y | \psi_e^g \psi_v^i \rangle}{\omega_{e^r e^g} + \omega_{v^r v^i} - \omega_1 - i\Gamma_{e^r v^r}} + \right. \tag{3.3.52}$$

$$\left. + \frac{\langle \psi_v^f \psi_e^g | \hat{p}_y | \psi_e^r \psi_v^r \rangle \langle \psi_v^r \psi_e^r | \hat{p}_x | \psi_e^g \psi_v^i \rangle}{\omega_{e^r e^g} + \omega_{v^r v^f} + \omega_1 + i\Gamma_{e^r v^r}} \right\}$$

The summation over all r states can now be split in two parts, one where $e^r = e^g$ and so $\omega_{e^r e^g} = 0$, and the other where $e^r \neq e^g$, obtaining for eq. (3.3.52):

$$\left(\alpha_{xy}\right)_{e^g v^f : e^g v^i} = \left(\alpha_{xy}\right)_{e^g v^f : e^g v^i}^{(e^r = e^g)} + \left(\alpha_{xy}\right)_{e^g v^f : e^g v^i}^{(e^r \neq e^g)} \tag{3.3.53}$$

In order that:

$$\left(\alpha_{xy}\right)_{e^g v^f : e^g v^i}^{(e^r = e^g)} = \frac{1}{\hbar} \sum_{v^r \neq v^i, v^f} \left\{ \frac{\langle \psi_v^f \psi_e^g | \hat{p}_x | \psi_e^g \psi_v^r \rangle \langle \psi_v^r \psi_e^g | \hat{p}_y | \psi_e^g \psi_v^i \rangle}{(\omega_{v^r v^i} - \omega_1)} + \right.$$

$$\left. + \frac{\langle \psi_v^f \psi_e^g | \hat{p}_y | \psi_e^g \psi_v^r \rangle \langle \psi_v^r \psi_e^g | \hat{p}_x | \psi_e^g \psi_v^i \rangle}{(\omega_{v^r v^f} + \omega_1)} \right\} \tag{3.3.54}$$

where the $\omega_{v^r v^i}$ and $\omega_{v^r v^f}$ are relative to vibrational levels in the ground electronic state and the term $\Gamma_{e^r v^r}$ is equal to zero. In the case of $e^r \neq e^g$, the ψ_e^r represent excited electronic states and if the following condition is respected:

$$\omega_{e^r e^g} \gg \omega_1 \gg \omega_{v^r v^i} \text{ or } \omega_{v^r v^f} \tag{3.3.55}$$

then the terms $\omega_{v^r v^i}$ and $\omega_{v^r v^f}$ relative to the $\omega_{e^r e^g}$ can be neglected. This good approximation can be assumed for the term $\Gamma_{e^r v^r}$ too. Therefore, the second part of eq. (3.3.53) is given by:

$$\left(\alpha_{xy}\right)_{e^g v^f : e^g v^i}^{(e^r \neq e^g)} = \frac{1}{\hbar} \sum_{\substack{e^r \neq e^g \\ v^r \neq v^i, v^f}} \left\{ \frac{\langle \psi_v^f \psi_e^g | \hat{p}_x | \psi_e^r \psi_v^r \rangle \langle \psi_v^r \psi_e^r | \hat{p}_y | \psi_e^g \psi_v^i \rangle}{(\omega_{e^r e^g} - \omega_1)} + \right. \tag{3.3.56}$$

$$+\frac{\left\langle \psi_v^f \psi_e^g \middle| \hat{p}_y \middle| \psi_e^r \psi_v^r \right\rangle \left\langle \psi_v^r \psi_e^r | \hat{p}_x | \psi_e^g \psi_v^i \right\rangle}{(\omega_{e^r e^g} + \omega_1)}\Bigg\}$$

In both eq. (3.3.54) and eq. (3.3.56) the electric dipole moment operator is a function of a set of electronic coordinates ξ and of a set of nuclear coordinates Q:

$$\hat{p}_x = \hat{p}_x(\xi, Q) \tag{3.3.57}$$

The set of nuclear coordinates Q is a set of internal nuclear coordinates that involves a displacement from the equilibrium nuclear configuration Q_0. It is known as normal coordinates. Further simplifications are introduced with the use of adiabatic permanent electric dipole moment and of adiabatic dynamic polarizability of the system in the lowest electronic level. With these conditions, the nuclei are fixed in a configuration Q and only the electrons are free to move. The adiabatic factors are functions of the nuclear coordinates Q and so they are denoted as: $\hat{p}_x(Q)$ and $\hat{\alpha}_{xy}(Q)$. The adiabatic permanent electric dipole is then given by:

$$\hat{p}_x(Q) = \langle \psi_0(\xi, Q) | \hat{p}(\xi, Q) | \psi_0(\xi, Q) \rangle \tag{3.3.58}$$

and the adiabatic dynamic polarizability by:

$$\hat{\alpha}_{xy}(Q)$$
$$= \frac{1}{\hbar} \sum_{e^r \neq e^g} \Bigg\{ \frac{\langle \psi_0(\xi, Q) | \hat{p}_x(\xi, Q) | \psi_e^r(\xi, Q) \rangle \langle \psi_e^r(\xi, Q) | \hat{p}_y(\xi, Q) | \psi_0(\xi, Q) \rangle}{(\omega_{e^r e^g} - \omega_1)} +$$
$$+ \frac{\langle \psi_0(\xi, Q) | \hat{p}_y(\xi, Q) | \psi_e^r(\xi, Q) \rangle \langle \psi_e^r(\xi, Q) | \hat{p}_x(\xi, Q) | \psi_0(\xi, Q) \rangle}{(\omega_{e^r e^g} + \omega_1)} \Bigg\} \tag{3.3.59}$$

Where $\psi_0(\xi, Q)$ corresponds to ψ_e^g and the sum is over the electronic coordinates ξ. With the use of eq. (3.3.58) the eq. (3.3.54) becomes:

$$\left(\alpha_{xy}\right)_{e^g v^f : e^g v^i}^{(e^r = e^g)} = \frac{1}{\hbar} \sum_{v^r \neq v^i, v^f} \Bigg\{ \frac{\langle \psi_v^f | \hat{p}_x(Q) | \psi_v^r \rangle \langle \psi_v^r | \hat{p}_y(Q) | \psi_v^i \rangle}{(\omega_{v^r v^i} - \omega_1)} +$$
$$+ \frac{\left\langle \psi_v^f \middle| \hat{p}_y(Q) \middle| \psi_v^r \right\rangle \left\langle \psi_v^r | \hat{p}_x(Q) | \psi_v^i \right\rangle}{(\omega_{v^r v^f} + \omega_1)} \Bigg\} \tag{3.3.60}$$

With the use of eq. (3.3.60), that is the ionic part of the vibrational transition polarizability, Raman scattering that involves only the virtual excited vibrational states is described, the molecule is fixed on the ground electronic state.

Simplification of eq. (3.3.56) is achieved by invoking the closure theorem with respect to the complete set of vibrational states in each electronic state:

$$\left(\alpha_{xy}\right)_{e^g v^f : e^g v^i}^{(e^r \neq e^g)} = \frac{1}{\hbar} \sum_{e^r \neq e^g} \left\{ \frac{\left\langle \psi_v^f \psi_e^g \middle| \hat{p}_x \middle| \psi_e^r \right\rangle \left\langle \psi_e^r \middle| \hat{p}_y \middle| \psi_e^g \psi_v^i \right\rangle}{(\omega_{e^r e^g} - \omega_1)} + \right. \\ \left. + \frac{\left\langle \psi_v^f \psi_e^g \middle| \hat{p}_y \middle| \psi_e^r \right\rangle \left\langle \psi_e^r \middle| \hat{p}_x \middle| \psi_e^g \psi_v^i \right\rangle}{(\omega_{e^r e^g} + \omega_1)} \right\} \tag{3.3.61}$$

We know that because of the eq. (3.3.59):

$$\frac{1}{\hbar} \sum_{e^r \neq e^g} \left\{ \frac{\left\langle \psi_e^g \middle| \hat{p}_x \middle| \psi_e^r \right\rangle \left\langle \psi_e^r \middle| \hat{p}_y \middle| \psi_e^g \right\rangle}{(\omega_{e^r e^g} - \omega_1)} + \frac{\left\langle \psi_e^g \middle| \hat{p}_y \middle| \psi_e^r \right\rangle \left\langle \psi_e^r \middle| \hat{p}_x \middle| \psi_e^g \right\rangle}{(\omega_{e^r e^g} + \omega_1)} \right\} =$$

$$\frac{1}{\hbar} \sum_{e^r \neq e^g} \left\{ \frac{\left\langle \psi_0(\xi, Q) \middle| \hat{p}_x(\xi, Q) \middle| \psi_e^r(\xi, Q) \right\rangle \left\langle \psi_e^r(\xi, Q) \middle| \hat{p}_y(\xi, Q) \middle| \psi_0(\xi, Q) \right\rangle}{(\omega_{e^r e^g} - \omega_1)} + \right. \\ \left. + \frac{\left\langle \psi_0(\xi, Q) \middle| \hat{p}_y(\xi, Q) \middle| \psi_e^r(\xi, Q) \right\rangle \left\langle \psi_e^r(\xi, Q) \middle| \hat{p}_x(\xi, Q) \middle| \psi_0(\xi, Q) \right\rangle}{(\omega_{e^r e^g} + \omega_1)} \right\} \tag{3.3.62}$$

Then, eq. (3.3.61) becomes:

$$\left(\alpha_{xy}\right)_{e^g v^f : e^g v^i}^{electronic} = \left\langle \psi_v^f \middle| \hat{\alpha}_{xy}(Q) \middle| \psi_v^i \right\rangle \tag{3.3.63}$$

Where the label $e^r \neq e^g$ has been replaced by the label *electronic* because the eq. (3.3.63) defines the electronic part of the vibrational transition polarizability. For normal conditions, $\omega_1 \gg \omega_{v^r v^i}$, the contribution of the ionic part of the vibrational transition polarizability is irrelevant and so only the electronic part remains, then eq. (3.3.63) can be written as:

$$\left(\alpha_{xy}\right)_{v^f : v^i} = \left\langle \psi_v^f \middle| \hat{\alpha}_{xy}(Q) \middle| \psi_v^i \right\rangle \tag{3.3.64}$$

For which $e^f = e^i = e^g$.

Eq. (3.3.64) shows that the components of the Placzek pure vibrational transition polarizability are matrix elements of the adiabatic polarizability, defined by eq. (3.3.60), which is a function of the nuclear coordinates Q only. The valuable property of the Placzek pure vibrational transition polarizability defined by eq. (3.3.64) is given by the fact that being the wave functions real, however unlike the general transition polarizability given by eq. (3.3.43), it is symmetric with respect to interchange of the indices x,y and does not have an antisymmetric part. The frequency conditions defined in eq. (3.3.55) determine the possible application of the Placzek transition polarizability only

in the normal pure Raman scattering with the employing of an optical excitation source and the absence of absorption in the visible region. The general transition polarizability can be written using the Placzek pure vibrational transition polarizability, so in analogy to the eq. (3.3.48), for transitions that are confined in the ground state, it will have:

$$\left(\alpha_{xy}\right)_{v^f R^f : v^i R^i} = \left\langle \psi_R^f \middle| \left(\hat{\alpha}_{xy}\right)_{v^f v^i} \middle| \psi_R^i \right\rangle \tag{3.3.65}$$

Eq. (3.3.65) is the basis of the treatment of the normal rotational Raman scattering.

3.3.5 Herzberg-Teller vibronic coupling

Defining the x component of the pure electronic transition electric dipole moment related to the electronic transition from the state ψ_e^r to the state ψ_e^f as follow:

$$\left(p_x\right)_{e^f e^r} = \left\langle \psi_e^f \middle| \hat{p}_x \middle| \psi_e^r \right\rangle \tag{3.3.66}$$

The eq. (3.3.51) for the xy cartesian component of the transition polarizability can be rewritten as:

$$\left(\alpha_{xy}\right)_{e^f v^f : e^g v^i} = \frac{1}{\hbar} \sum_{\substack{e^r v^r \neq \\ e^g v^i, \\ e^f v^f}} \left\{ \frac{\left\langle \psi_v^f \middle| \left(p_x\right)_{e^f e^r} \middle| \psi_v^r \right\rangle \left\langle \psi_v^r \middle| \left(p_y\right)_{e^r e^g} \middle| \psi_v^i \right\rangle}{\omega_{e^r e^g} + \omega_{v^r v^i} - \omega_1 - i\Gamma_{e^r v^r}} + \right.$$
$$\left. + \frac{\left\langle \psi_v^f \middle| \left(p_y\right)_{e^f e^r} \middle| \psi_v^r \right\rangle \left\langle \psi_v^r \middle| \left(p_x\right)_{e^r e^g} \middle| \psi_v^i \right\rangle}{\omega_{e^r e^g} + \omega_{v^r v^i} + \omega_1 + i\Gamma_{e^r v^r}} \right\} \tag{3.3.67}$$

The eqs. (3.3.51) and (3.3.66) have been obtained by the use of the adiabatic approximation, so the coupling between electronic and nuclear motions have been neglected. It is the case of the expressed form in the eqs. (3.3.40) and (3.3.41). However, the electronic transition moment has a dependence on the normal coordinates of vibration Q which arises from the functional dependence of the Hamiltonian that may be expressed by an expansion in the nuclear displacements around the equilibrium configuration Q_0:

$$\hat{H}_e(Q) = \left(\hat{H}_e\right)_0 + \sum_k \left(\frac{\partial \hat{H}_e}{\partial Q_k}\right)_0 Q_k + \frac{1}{2} \sum_{k,l} \left(\frac{\partial \hat{H}_e}{\partial Q_k Q_l}\right) Q_k \, Q_l + \cdots \tag{3.3.68}$$

where Q_k, Q_l are the normal coordinates. The second and higher terms of expansion are the perturbation that can mix electronic states. The set of electronic functions at the equilibrium nuclear configuration can be represented by $\psi_e(\xi, Q_0)$. It can be considered

that the normal coordinate dependence of the electronic functions is the result of the vibrational perturbation mixing the $\psi_e(\xi, Q_0)$. For small displacements Q_k as in transitions of the type $v_f = v_i + 1$, the perturbation is just described by the second term of eq. (3.3.67). Therefore, setting $\psi_e^r(Q)$ equal to $\psi_e^{r'}(Q_0)$ that arises from the electronic Hamiltonian mixing of the unperturbed state $\psi_e^r(Q_0)$ with other unperturbed states $\psi_e^s(Q_0)$ and using the coupling integral $h_{e^s e^r}^k$ defined as follows:

$$h_{e^s e^r}^k = \left\langle \psi_e^s(Q_0) \middle| \left(\frac{\partial \hat{H}_e}{\partial Q_k}\right)_0 \middle| \psi_e^r(Q_0) \right\rangle \tag{3.3.69}$$

the perturbed sates are as follows:

$$\psi_e^{r'}(Q_0) = \psi_e^r(Q_0) + \frac{1}{\hbar} \sum_{e^s \neq e^r} \sum_k \frac{h_{e^s e^r}^k}{\omega_{e^r} - \omega_{e^s}} Q_k \psi_e^s(Q_0) \tag{3.3.70}$$

and

$$\psi_e^{r'^*}(Q_0) = \psi_e^{r*}(Q_0) + \frac{1}{\hbar} \sum_{e^s \neq e^r} \sum_k \psi_e^{s*}(Q_0) \frac{h_{e^r e^s}^k}{\omega_{e^r} - \omega_{e^s}} Q_k \tag{3.3.71}$$

Where $\hbar\omega_{e^r}$ and $\hbar\omega_{e^s}$ are the energies of the unperturbed states and $\left(h_{e^s e^r}^k\right)^* = h_{e^r e^s}^k$. The introduction of the electronic perturbation acts in a certain manner on the products of components of electronic transition dipoles present in the numerators of the two terms in the expression for $\left(\alpha_{xy}\right)_{e^f v^f : e^g v^i}$ given by eq. (3.3.67). Effectively, the first product becomes $\left\langle \psi_e^{f'} \middle| \hat{p}_x \middle| \psi_e^{r'} \right\rangle \left\langle \psi_e^{r'} \middle| \hat{p}_y \middle| \psi_e^{g'} \right\rangle$, now using eqs. (3.3.70) and (3.3.71) it will be obtained:

$$\left\langle \psi_e^{r'} \middle| \hat{p}_y \middle| \psi_e^{g'} \right\rangle = \left\{ \langle \psi_e^r(Q_0)| + \frac{1}{\hbar} \sum_{e^s \neq e^r} \sum_k \langle \psi_e^s(Q_0)| \frac{h_{e^r e^s}^k}{\omega_{e^r} - \omega_{e^s}} Q_k \right\} |\hat{p}_y| \left\{ \langle \psi_e^g(Q_0)| + \frac{1}{\hbar} \sum_{e^s \neq e^r} \sum_k \frac{h_{e^t e^g}^k}{\omega_{e^g} - \omega_{e^t}} Q_k |\psi_e^t(Q_0)\rangle \right\} \tag{3.3.72}$$

Adapting the compact form of eq. (3.3.66) with the rights indexes we have:

$$\left(p_y\right)_{e^{r'}e^{g'}} = \left(p_y\right)_{e^re^g} + \frac{1}{\hbar}\sum_{e^s\neq e^r}\sum_k \frac{h^k_{e^re^s}}{\omega_{e^r}-\omega_{e^s}} Q_k \left(p_y\right)_{e^se^g} + \\ + \frac{1}{\hbar}\sum_{e^t\neq e^g}\sum_k \left(p_y\right)_{e^re^t} \frac{h^k_{e^te^g}}{\omega_{e^g}-\omega_{e^t}} Q_k \tag{3.3.73}$$

It is showed in eq. (3.3.73) that the transition electric dipole $\left(p_y\right)_{e^{r'}e^{g'}}$ depends not only on the term $\left(p_y\right)_{e^re^g}$ but also on additional contributions due to the transition electric dipoles of the types $\left(p_y\right)_{e^se^g}$ and $\left(p_y\right)_{e^re^t}$ that are determined by the application of the perturbation by the electric Hamiltonian. Similar considerations can be applied to the x component of the electronic transition dipole in the numerator of the first term in eq. (3.3.67), obtaining:

$$\left(p_x\right)_{e^{f'}e^{r'}} = \left(p_x\right)_{e^fe^r} + \frac{1}{\hbar}\sum_{e^s\neq e^r}\sum_k \left(p_x\right)_{e^fe^s} \frac{h^k_{e^se^r}}{\omega_{e^r}-\omega_{e^s}} Q_k + \\ + \frac{1}{\hbar}\sum_{e^t\neq e^f}\sum_k \frac{h^k_{e^fe^t}}{\omega_{e^f}-\omega_{e^t}} Q_k \left(p_y\right)_{e^te^r} \tag{3.3.74}$$

The amount of contribution terms that arise from the electric Hamiltonian perturbation to the k*th* vibrational mode is proportional to the appropriate coupling integral and the displacement Q_k and is inversely proportional to the energy difference between the two states involved. In particular, this latter condition requires that the involved states have to be relatively close in energy.

The replacement in eq. (3.3.67) of the terms $\left(p_x\right)_{e^fe^r}$ and $\left(p_y\right)_{e^re^g}$ with the ones of eqs. (3.3.73) and (3.3.74), that is $\left(p_x\right)_{e^{f'}e^{r'}}$ and $\left(p_y\right)_{e^{r'}e^{g'}}$ respectively, lead to a rather complicated result:

$$\left(\alpha_{xy}\right)_{e^fv^f:e^gv^i} = A^{\mathrm{I}} + B^{\mathrm{I}} + C^{\mathrm{I}} + D^{\mathrm{I}} \tag{3.3.75}$$

where:

$$A^{\mathrm{I}} = \frac{1}{\hbar} \sum_{\substack{e^{r}v^{r} \neq \\ e^{g}v^{i}, \\ e^{f}v^{f}}} \left\{ \frac{\left\langle \psi_v^f \middle| (p_x)_{e^f e^r} \middle| \psi_v^r \right\rangle \left\langle \psi_v^r \middle| (p_y)_{e^r e^g} \middle| \psi_v^i \right\rangle}{\omega_{e^r v^r : e^g v^i} - \omega_1 - i\Gamma_{e^r v^r}} + \right.$$

$$\left. + \frac{\left\langle \psi_v^f \middle| (p_y)_{e^f e^r} \middle| \psi_v^r \right\rangle \left\langle \psi_v^r \middle| (p_x)_{e^r e^g} \middle| \psi_v^i \right\rangle}{\omega_{e^r v^r : e^f v^f} + \omega_1 + i\Gamma_{e^r v^r}} \right\} \tag{3.3.76}$$

$$B^{\mathrm{I}} = \frac{1}{\hbar^2} \sum_{\substack{e^{r}v^{r} \neq \\ e^{g}v^{i}, \\ e^{f}v^{f}}} \left\{ \frac{\left\langle \psi_v^f \middle| \sum_{e^s \neq e^r} \sum_k (p_x)_{e^f e^s} \frac{h^k_{e^s e^r}}{\omega_{e^r} - \omega_{e^s}} Q_k \middle| \psi_v^r \right\rangle \left\langle \psi_v^r \middle| (p_y)_{e^r e^g} \middle| \psi_v^i \right\rangle}{\omega_{e^r v^r : e^g v^i} - \omega_1 - i\Gamma_{e^r v^r}} + \right.$$

$$\left. + \frac{\left\langle \psi_v^f \middle| \sum_{e^s \neq e^r} \sum_k (p_y)_{e^f e^s} \frac{h^k_{e^s e^r}}{\omega_{e^r} - \omega_{e^s}} Q_k \middle| \psi_v^r \right\rangle \left\langle \psi_v^r \middle| (p_x)_{e^r e^g} \middle| \psi_v^i \right\rangle}{\omega_{e^r v^r : e^f v^f} + \omega_1 + i\Gamma_{e^r v^r}} \right\} +$$

$$+ \frac{1}{\hbar^2} \sum_{\substack{e^{r}v^{r} \neq \\ e^{g}v^{i}, \\ e^{f}v^{f}}} \left\{ \frac{\left\langle \psi_v^f \middle| (p_x)_{e^f e^r} \middle| \psi_v^i \right\rangle \left\langle \psi_v^r \middle| \sum_{e^s \neq e^r} \sum_k \frac{h^k_{e^r e^s}}{\omega_{e^r} - \omega_{e^s}} Q_k (p_y)_{e^s e^g} \middle| \psi_v^i \right\rangle}{\omega_{e^r v^r : e^g v^i} - \omega_1 - i\Gamma_{e^r v^r}} + \right. \tag{3.3.77}$$

$$\left. + \frac{\left\langle \psi_v^f \middle| (p_y)_{e^f e^r} \middle| \psi_v^r \right\rangle \left\langle \psi_v^r \middle| \sum_{e^s \neq e^r} \sum_k \frac{h^k_{e^r e^s}}{\omega_{e^r} - \omega_{e^s}} Q_k (p_x)_{e^s e^g} \middle| \psi_v^i \right\rangle}{\omega_{e^r v^r : e^f v^f} + \omega_1 + i\Gamma_{e^r v^r}} \right\}$$

$$C^{\mathrm{I}} = \frac{1}{\hbar^2} \sum_{\substack{e^{r}v^{r} \neq \\ e^{g}v^{i}, \\ e^{f}v^{f}}} \left\{ \frac{\left\langle \psi_v^f \middle| \sum_{e^t \neq e^f} \sum_k \frac{h^k_{e^f e^t}}{\omega_{e^f} - \omega_{e^t}} Q_k (p_x)_{e^t e^r} \middle| \psi_v^r \right\rangle \left\langle \psi_v^r \middle| (p_y)_{e^r e^g} \middle| \psi_v^i \right\rangle}{\omega_{e^r v^r : e^g v^i} - \omega_1 - i\Gamma_{e^r v^r}} + \right.$$

$$+\frac{\left\langle \psi_v^f \middle| \sum_{e^t \neq e^f} \sum_k \frac{h^k_{e^f e^t}}{\omega_{e^f} - \omega_{e^t}} Q_k \left(p_y\right)_{e^t e^r} \middle| \psi_v^r \right\rangle \langle \psi_v^r | (p_x)_{e^r e^g} | \psi_v^i \rangle}{\omega_{e^r v^r : e^f v^f} + \omega_1 + i\Gamma_{e^r v^r}} \Bigg\} +$$

$$+\frac{1}{\hbar^2} \sum_{\substack{e^r v^r \neq \\ e^g v^i, \\ e^f v^f}} \Bigg\{ \frac{\langle \psi_v^f | (p_x)_{e^f e^r} | \psi_v^r \rangle \left\langle \psi_v^r \middle| \sum_{e^t \neq e^g} \sum_k (p_y)_{e^r e^t} \frac{h^k_{e^t e^g}}{\omega_{e^g} - \omega_{e^t}} Q_k \middle| \psi_v^i \right\rangle}{\omega_{e^r v^r : e^g v^i} - \omega_1 - i\Gamma_{e^r v^r}} + \tag{3.3.78}$$

$$+\frac{\left\langle \psi_v^f \middle| (p_y)_{e^f e^r} \middle| \psi_v^r \right\rangle \left\langle \psi_v^r \middle| \sum_{e^t \neq e^g} \sum_k (p_x)_{e^r e^t} \frac{h^k_{e^t e^g}}{\omega_{e^g} - \omega_{e^t}} Q_k \middle| \psi_v^i \right\rangle}{\omega_{e^r v^r : e^f v^f} + \omega_1 + i\Gamma_{e^r v^r}} \Bigg\}$$

$$D^{\mathrm{I}} = \frac{1}{\hbar^3} \times$$

$$\times \sum_{\substack{e^r v^r \neq \\ e^g v^i, \\ e^f v^f}} \Bigg\{ \frac{\left\langle \psi_v^f \middle| \sum_{e^s \neq e^r} \sum_k (p_x)_{e^f e^s} \frac{h^k_{e^s e^r}}{\omega_{e^r} - \omega_{e^s}} Q_k \middle| \psi_v^r \right\rangle \left\langle \psi_v^r \middle| \sum_{e^{s'} \neq e^r} \sum_{k'} \frac{h^{k'}_{e^r e^{s'}}}{\omega_{e^r} - \omega_{e^{s'}}} Q_{k'} \left(p_y\right)_{e^{s'} e^g} \middle| \psi_v^i \right\rangle}{\omega_{e^r v^r : e^g v^i} - \omega_1 - i\Gamma_{e^r v^r}} + \tag{3.3.79}$$

$$+\frac{\left\langle \psi_v^f \middle| \sum_{e^s \neq e^r} \sum_{k'} (p_x)_{e^f e^{s'}} \frac{h^{k'}_{e^{s'} e^r}}{\omega_{e^r} - \omega_{e^{s'}}} Q_{k'} \middle| \psi_v^r \right\rangle \left\langle \psi_v^r \middle| \sum_{e^s \neq e^r} \sum_k \frac{h^k_{e^r e^s}}{\omega_{e^r} - \omega_{e^s}} Q_k \left(p_y\right)_{e^s e^g} \middle| \psi_v^i \right\rangle}{\omega_{e^r v^r : e^g v^i} - \omega_1 - i\Gamma_{e^r v^r}} \Bigg\}$$

In the term A^{I} there are two products of two unperturbed electronic transition dipoles. The term B^{I} involves four terms in which there are products of one unperturbed electronic transition dipole with electronic transitions dipoles that arise from Herzberg-Teller coupling of two excited electronic states. The term C^{I} involves products of one unperturbed electronic transition dipole with electronic transitions dipoles that arise from Herzberg-Teller coupling of one excited electronic state and either the initial or final electronic state. The last term D^{I} involves two products of two electronic transition dipoles both of which arise from Herzberg-Teller coupling.

The eqs. (3.3.76-3.3.79) can be simplify by the use of the Born-Oppenheimer approximation for which the electronic transition moments and the coupling integral do not operate on vibrational wavefunctions. Therefore eq. (3.3.74) becomes:

$$\left(\alpha_{xy}\right)_{e^f v^f : e^g v^i} = A^{\mathrm{II}} + B^{\mathrm{II}} + C^{\mathrm{II}} + D^{\mathrm{II}} \tag{3.3.80}$$

where:

$$A^{\mathrm{II}} = \frac{1}{\hbar} \sum_{\substack{e^r v^r \neq \\ e^g v^i, \\ e^f v^f}} \left\{ \frac{(p_x)_{e^f e^r} (p_y)_{e^r e^g}}{\omega_{e^r v^r : e^g v^i} - \omega_1 - i\Gamma_{e^r v^r}} + \frac{(p_y)_{e^f e^r} (p_x)_{e^r e^g}}{\omega_{e^r v^r : e^f v^f} + \omega_1 + i\Gamma_{e^r v^r}} \right\} \langle \psi_v^f | \psi_v^r \rangle \langle \psi_v^r | \psi_v^i \rangle \tag{3.3.81}$$

$$\begin{aligned} B^{\mathrm{II}} = \frac{1}{\hbar^2} \sum_{\substack{e^r v^r \neq \\ e^g v^i, \\ e^f v^f}} \sum_{e^s \neq e^r} \sum_k \Bigg\{ & \frac{(p_x)_{e^f e^s} h^k_{e^s e^r} (p_y)_{e^r e^g}}{(\omega_{e^r} - \omega_{e^s})(\omega_{e^r v^r : e^g v^i} - \omega_1 - i\Gamma_{e^r v^r})} + \\ & + \frac{(p_y)_{e^f e^s} h^k_{e^s e^r} (p_x)_{e^r e^g}}{(\omega_{e^r} - \omega_{e^s})(\omega_{e^r v^r : e^f v^f} + \omega_1 + i\Gamma_{e^r v^r})} \Bigg\} \langle \psi_v^f | Q_k | \psi_v^r \rangle \langle \psi_v^r | \psi_v^i \rangle + \\ & + \frac{1}{\hbar^2} \sum_{\substack{e^r v^r \neq \\ e^g v^i, \\ e^f v^f}} \sum_{e^s \neq e^r} \sum_k \Bigg\{ \frac{(p_x)_{e^f e^r} h^k_{e^r e^s} (p_y)_{e^s e^g}}{(\omega_{e^r} - \omega_{e^s})(\omega_{e^r v^r : e^g v^i} - \omega_1 - i\Gamma_{e^r v^r})} + \\ & + \frac{(p_y)_{e^f e^r} h^k_{e^s e^r} (p_x)_{e^s e^g}}{(\omega_{e^r} - \omega_{e^s})(\omega_{e^r v^r : e^f v^f} + \omega_1 + i\Gamma_{e^r v^r})} \Bigg\} \langle \psi_v^f | \psi_v^r \rangle \langle \psi_v^r | Q_k | \psi_v^i \rangle \end{aligned} \tag{3.3.82}$$

$$\begin{aligned} C^{\mathrm{II}} = \frac{1}{\hbar^2} \sum_{\substack{e^r v^r \neq \\ e^g v^i, \\ e^f v^f}} \sum_{e^t \neq e^f} \sum_k \Bigg\{ & \frac{h^k_{e^f e^t} (p_x)_{e^t e^r} (p_y)_{e^r e^g}}{(\omega_{e^f} - \omega_{e^t})(\omega_{e^r v^r : e^g v^i} - \omega_1 - i\Gamma_{e^r v^r})} + \\ & + \frac{h^k_{e^f e^t} (p_y)_{e^t e^r} (p_x)_{e^r e^g}}{(\omega_{e^f} - \omega_{e^t})(\omega_{e^r v^r : e^f v^f} + \omega_1 + i\Gamma_{e^r v^r})} \Bigg\} \langle \psi_v^f | Q_k | \psi_v^r \rangle \langle \psi_v^r | \psi_v^i \rangle + \\ & + \frac{1}{\hbar^2} \sum_{\substack{e^r v^r \neq \\ e^g v^i, \\ e^f v^f}} \sum_{e^t \neq e^f} \sum_k \Bigg\{ \frac{(p_x)_{e^f e^r} (p_y)_{e^r e^t} h^k_{e^t e^g}}{(\omega_{e^g} - \omega_{e^t})(\omega_{e^r v^r : e^g v^i} - \omega_1 - i\Gamma_{e^r v^r})} + \\ & + \frac{(p_y)_{e^f e^r} (p_x)_{e^r e^t} h^k_{e^t e^g}}{(\omega_{e^g} - \omega_{e^t})(\omega_{e^r v^r : e^f v^f} + \omega_1 + i\Gamma_{e^r v^r})} \Bigg\} \langle \psi_v^f | \psi_v^r \rangle \langle \psi_v^r | Q_k | \psi_v^i \rangle \end{aligned} \tag{3.3.83}$$

$$D^{\mathrm{II}} = \frac{1}{\hbar^3} \times$$

$$\times \sum_{\substack{e^r v^r \neq \\ e^g v^i, \\ e^f v^f}} \sum_{e^s, e^{s'} \neq e^r} \sum_{k,k'} \left\{ \frac{(p_x)_{e^f e^s} h^k_{e^s e^r} h^{k'}_{e^r e^{s'}} (p_y)_{e^{s'} e^g} \langle \psi^f_v | Q_k | \psi^r_v \rangle \langle \psi^r_v | Q_{k'} | \psi^i_v \rangle}{(\omega_{e^r} - \omega_{e^s})(\omega_{e^r} - \omega_{e^{s'}})(\omega_{e^r v^r : e^g v^i} - \omega_1 - i\Gamma_{e^r v^r})} + \right.$$

$$\left. + \frac{(p_y)_{e^f e^{s'}} h^{k'}_{e^{s'} e^r} h^k_{e^r e^s} (p_y)_{e^s e^g} \langle \psi^f_v | Q_{k'} | \psi^r_v \rangle \langle \psi^r_v | Q_k | \psi^i_v \rangle}{(\omega_{e^r} - \omega_{e^{s'}})(\omega_{e^r} - \omega_{e^s})(\omega_{e^r v^r : e^g v^i} + \omega_1 + i\Gamma_{e^r v^r})} \right\} \tag{3.3.84}$$

The simplification of eqs. (3.3.81-3.3.84) depends on the understanding of the relationship between the vibronic absorption frequencies $\omega_{e^r v^r : e^g v^i}$, or equivalently $\omega_{e^r e^g} + \omega_{v^r v^i}$ and the frequency of exciting radiation, that is ω_1. The relative Raman scattering process are showed in Fig. (3.3.2). When the frequency ω_1 is far from any vibrational absorption frequencies, that is $\omega_{e^r e^g} + \omega_{v^r v^i} \gg \omega_1$, the effect of the term $\omega_{v^r v^i}$ in the expression $\omega_{e^r e^g} + \omega_{v^r v^i} - \omega_1$, can be neglected. Moreover, if $\omega_1 \gg \omega_{v^r v^i}$, then the term $\omega_{e^r e^g} + \omega_{v^r v^i} + \omega_1$ can be substituted by $\omega_{e^r e^g} + \omega_1$. The term $i\Gamma_{e^r v^r}$ is very small with respect to both the terms $\omega_{e^r e^g} + \omega_1$ and $\omega_{e^r e^g} - \omega_1$ and so it can be neglected. These conditions are the typical ones for the non-resonant normal and vibronic Raman scattering for which $e^f \neq e^g$. An important consequence of these simplifications in the frequency denominators is that the summation over the set of vibrational states in each electronic state e^r becomes allowed because the denominators do not depend on the vibrational states. In order to take into account the relative magnitudes of these contributions, it is useful in the non-resonance case to use Taylor series expansions of $(p_x)_{e^f e^r}$:

$$(p_x)_{e^f e^{r'}} = (p_x)_{e^f e^r} + \sum_k (p_x)^k_{e^f e^{r'}} Q_k \tag{3.3.85}$$

where:

$$(p_x)^k_{e^f e^{r'}} = \left(\frac{\partial (p_x)_{e^f e^r}}{\partial Q_k} \right)_0 \tag{3.3.86}$$

The derivatives with respect to the normal coordinates implicitly contains the vibronic coupling of states ψ^r_e to other electronic states. The comparison of eqs. (3.3.85-3.3.86) with eq. (3.3.73) leads to the following result:

$$(p_x)^k_{e^f e^{r'}} = \frac{1}{\hbar} \left\{ \sum_{e^s \neq e^r} (p_x)_{e^f e^s} \frac{h^k_{e^s e^r}}{\omega_{e^r} - \omega_{e^s}} + \sum_{e^t \neq e^f} \frac{h^k_{e^f e^t}}{\omega_{e^f} - \omega_{e^t}} (p_x)_{e^t e^r} \right\} \tag{3.3.87}$$

Corresponding relationships for $(p_y)^k_{e^{f'}e^{r'}}$, $(p_x)^k_{e^{r'}e^{g'}}$ and $(p_y)^k_{e^{r'}e^{g'}}$ are readily obtained. Taking into account the conditions relative to the non-resonant normal electronic and vibronic Raman scattering, we have:

$$(\alpha_{xy})_{e^f v^f : e^g v^i} = A^{\mathrm{III}} + B^{\mathrm{III}} + C^{\mathrm{III}} + D^{\mathrm{III}} \tag{3.3.88}$$

where:

$$A^{\mathrm{III}} = \frac{1}{\hbar} \sum_{e^r \neq e^g, e^f} \left\{ \frac{(p_x)_{e^f e^r} (p_y)_{e^r e^g}}{\omega_{e^r e^g} - \omega_1} + \frac{(p_y)_{e^f e^r} (p_x)_{e^r e^g}}{\omega_{e^r e^f} + \omega_1} \right\} \langle \psi_v^f | \psi_v^i \rangle \tag{3.3.89}$$

$$B^{\mathrm{III}} + C^{\mathrm{III}} = \frac{1}{\hbar} \sum_{e^r \neq e^g, e^f} \sum_k \left\{ \frac{(p_x)^k_{e^f e^r} (p_y)_{e^r e^g} + (p_x)_{e^f e^r} (p_y)^k_{e^r e^g}}{(\omega_{e^r e^g} - \omega_1)} + \right. \tag{3.3.90}$$

$$\left. + \frac{(p_y)_{e^f e^r} (p_x)^k_{e^r e^g} + (p_y)^k_{e^f e^r} (p_x)_{e^r e^g}}{(\omega_{e^r e^g} + \omega_1)} \right\} \langle \psi_v^f | Q_k | \psi_v^i \rangle$$

$$D^{\mathrm{III}} = \frac{1}{\hbar} \sum_{e^r \neq e^g, e^f} \sum_{k,k'} \left\{ \frac{(p_x)^k_{e^f e^r} (p_y)^{k'}_{e^r e^g}}{(\omega_{e^r e^g} - \omega_1)} \right. \tag{3.3.91}$$

$$\left. + \frac{(p_y)^{k'}_{e^f e^r} (p_x)^k_{e^r e^g}}{(\omega_{e^r e^g} + \omega_1)} \right\} \langle \psi_v^f | Q_k Q_{k'} | \psi_v^i \rangle$$

In the case of the normal pure vibrational scattering, the condition $e^f = e^g$ introduces further simplification with respect to the eqs. (3.3.88-3.3.90). In this case:

$$(\alpha_{xy})_{e^f v^f : e^g v^i} = (\alpha_{xy})_{v^f : v^i} = A^{\mathrm{IV}} + B^{\mathrm{IV}} + C^{\mathrm{IV}} + D^{\mathrm{IV}} \tag{3.3.92}$$

where:

$$A^{\mathrm{IV}} = \frac{1}{\hbar} \sum_{e^r \neq e^g} \left\{ \frac{(p_x)_{e^g e^r} (p_y)_{e^r e^g}}{\omega_{e^r e^g} - \omega_1} + \frac{(p_y)_{e^g e^r} (p_x)_{e^r e^g}}{\omega_{e^r e^f} + \omega_1} \right\} \langle \psi_v^f | \psi_v^i \rangle \tag{3.3.93}$$

$$B^{\mathrm{IV}}+C^{\mathrm{IV}}=\frac{1}{\hbar}\sum_{e^r\neq e^g}\sum_{k}\left\{\frac{(p_x)^k_{e^ge^r}\left(p_y\right)_{e^re^g}+(p_x)_{e^ge^r}\left(p_y\right)^k_{e^re^g}}{(\omega_{e^re^g}-\omega_1)}+\right.$$
$$\left.+\frac{\left(p_y\right)_{e^ge^r}(p_x)^k_{e^re^g}+\left(p_y\right)^k_{e^ge^r}(p_x)_{e^re^g}}{(\omega_{e^re^g}+\omega_1)}\right\}\langle\psi_v^f|Q_k|\psi_v^i\rangle \tag{3.3.94}$$

$$D^{\mathrm{IV}}=\frac{1}{\hbar}\sum_{e^r\neq e^g}\sum_{k,k'}\left\{\frac{(p_x)^k_{e^ge^r}\left(p_y\right)^{k'}_{e^re^g}}{(\omega_{e^re^g}-\omega_1)}\right.$$
$$\left.+\frac{\left(p_y\right)^{k'}_{e^ge^r}(p_x)^k_{e^re^g}}{(\omega_{e^re^g}+\omega_1)}\right\}\langle\psi_v^f|Q_kQ_{k'}|\psi_v^i\rangle \tag{3.3.95}$$

The functions of eqs. (3.3.93-3.3.95) are real, and electric dipole interaction Hamiltonian operator is hermitian. Consequently, the numerators of eq. (3.3.93) are equal and similarly the numerators of eqs. (3.3.94-3.3.95). Thus, because of the form of the denominators that is $(a+b)$ and $(a-b)$, using the algebraic identity $\frac{1}{(a+b)}+\frac{1}{(a-b)}=\frac{2a}{(a^2-b^2)}$, we have:

$$A^{\mathrm{IV}}_{Real}=\frac{1}{\hbar}\sum_{e^r\neq e^g}\frac{2\omega_{e^re^g}}{\omega^2_{e^re^g}-\omega_1^2}\left\{(p_x)_{e^ge^r}\left(p_y\right)_{e^re^g}\right\}\langle\psi_v^f|\psi_v^i\rangle \tag{3.3.96}$$

$$B^{\mathrm{IV}}_{Real}+C^{\mathrm{IV}}_{Real}=\frac{1}{\hbar}\sum_{e^r\neq e^g}\sum_{k}\frac{2\omega_{e^re^g}}{\omega^2_{e^re^g}-\omega_1^2}\left\{(p_x)^k_{e^ge^r}\left(p_y\right)_{e^re^g}\right.$$
$$\left.+(p_x)_{e^ge^r}\left(p_y\right)^k_{e^re^g}\right\}\langle\psi_v^f|Q_k|\psi_v^i\rangle \tag{3.3.97}$$

$$D^{\mathrm{IV}}_{Real}=\frac{1}{\hbar}\sum_{e^r\neq e^g}\sum_{k,k'}\frac{2\omega_{e^re^g}}{\omega^2_{e^re^g}-\omega_1^2}(p_x)^k_{e^ge^r}\left(p_y\right)^{k'}_{e^re^g}\langle\psi_v^f|Q_kQ_{k'}|\psi_v^i\rangle \tag{3.3.98}$$

The next step consists of an expansion as Taylor series in Q of the adiabatic polarizability and to introduce the expansion in eq. (3.3.64) in order to obtain the following result:

$$\left(\alpha_{xy}\right)_{v^fv^i}=\left(\alpha_{xy}(Q)\right)_0\langle\psi_v^f|\psi_v^i\rangle+\sum_k\left(\frac{\alpha_{xy}(Q)}{\partial Q_k}\right)_0\langle\psi_v^f|Q_k|\psi_v^i\rangle$$

$$+\frac{1}{2}\sum_{k}\sum_{l}\left(\frac{\partial^2\alpha_{xy}(Q)}{\partial Q_k\partial Q_l}\right)_0\langle\psi_v^f|Q_kQ_l|\psi_v^i\rangle+\cdots \tag{3.3.99}$$

Now, comparing eq. (3.3.99) with eqs. (3.3.96-3.3.98) it is obtained

$$\left(\alpha_{xy}(Q)\right)_0=\frac{1}{\hbar}\sum_{e^r\neq e^g}\frac{2\omega_{e^re^g}}{\omega_{e^re^g}^2-\omega_1^2}(p_x)_{e^ge^r}\left(p_y\right)_{e^re^g} \tag{3.3.100}$$

$$\left(\frac{\alpha_{xy}(Q)}{\partial Q_k}\right)_0=\frac{1}{\hbar}\sum_{e^r\neq e^g}\sum_{k}\frac{2\omega_{e^re^g}}{\omega_{e^re^g}^2-\omega_1^2}\Big\{(p_x)_{e^ge^r}^{k}\left(p_y\right)_{e^re^g} \tag{3.3.101}$$

$$+(p_x)_{e^ge^r}\left(p_y\right)_{e^re^g}^{k}\Big\}$$

$$\left(\frac{\partial^2\alpha_{xy}(Q)}{\partial Q_k\partial Q_l}\right)_0=\frac{1}{\hbar}\sum_{e^r\neq e^g}\sum_{k,k'}\frac{2\omega_{e^re^g}}{\omega_{e^re^g}^2-\omega_1^2}(p_x)_{e^ge^r}^{k}\left(p_y\right)_{e^re^g}^{k'} \tag{3.3.102}$$

The eqs. (3.3.100-3.3.102) are given for only one normal coordinate Q_k and they relate to transition polarizability components for a specific transition that involves a change in only one vibrational quantum number (v_k). It is important to note that the eq. (3.3.102) is valid only to the first order in $(p_x)_{e^ge^r}^{k}$ because if the Taylor series is taken to the second derivative terms containing vibronic coupling between ψ_e^r and other electronic states will appear in the eq. (3.3.102). The non-resonant pure vibrational transition polarizability determines the properties of the Rayleigh and of the normal Raman scattering such as selection rules, intensities and polarization.

Different kind of approximations are evoked in the case of electronic and/or vibronic resonance Raman scattering. In the case of the electronic and vibronic resonance Raman scattering the eq. (3.3.80) becomes:

$$\left(\alpha_{xy}\right)_{e^fv^f:e^gv^i}=A^{\mathrm{V}}+B^{\mathrm{V}}+C^{\mathrm{V}}+D^{\mathrm{V}} \tag{3.3.103}$$

where:

$$A^{\mathrm{V}}=\frac{1}{\hbar}(p_x)_{e^fe^r}\left(p_y\right)_{e^re^g}\sum_{v^r}\frac{\left\langle\psi_v^{f(f)}\middle|\psi_v^{r(r)}\right\rangle\left\langle\psi_v^{r(r)}\middle|\psi_v^{i(g)}\right\rangle}{\omega_{e^rv^r:e^gv^i}-\omega_1-i\Gamma_{e^rv^r}} \tag{3.3.104}$$

$$B^{\mathrm{V}} = \frac{1}{\hbar^2}(p_x)_{e^f e^s} \frac{h^k_{e^s e^r}}{(\omega_{e^r} - \omega_{e^s})} (p_y)_{e^r e^g} \sum_{v^r} \frac{\left\langle \psi_v^{f(f)} \middle| Q_k \middle| \psi_v^{r(r)} \right\rangle \left\langle \psi_v^{r(r)} \middle| \psi_v^{i(g)} \right\rangle}{(\omega_{e^r v^r : e^g v^i} - \omega_1 - i\Gamma_{e^r v^r})}$$

$$+ \tag{3.3.105}$$

$$+ \frac{1}{\hbar^2}(p_x)_{e^f e^r} \frac{h^k_{e^r e^s}}{(\omega_{e^r} - \omega_{e^s})} (p_y)_{e^s e^g} \sum_{v^r} \frac{\left\langle \psi_v^{f(f)} \middle| \psi_v^{r(r)} \right\rangle \left\langle \psi_v^{r(r)} \middle| Q_k \middle| \psi_v^{i(g)} \right\rangle}{(\omega_{e^r v^r : e^g v^i} - \omega_1 - i\Gamma_{e^r v^r})}$$

$$C^{\mathrm{V}} =$$

$$= \frac{1}{\hbar^2} \frac{h^k_{e^f e^t}}{(\omega_{e^f} - \omega_{e^t})} (p_x)_{e^t e^r} (p_y)_{e^r e^g} \sum_{v^r} \frac{\left\langle \psi_v^{f(f)} \middle| Q_k \middle| \psi_v^{r(r)} \right\rangle \left\langle \psi_v^{r(r)} \middle| \psi_v^{i(g)} \right\rangle}{(\omega_{e^r v^r : e^g v^i} - \omega_1 - i\Gamma_{e^r v^r})} +$$

$$+ \frac{1}{\hbar^2}(p_x)_{e^f e^r} (p_y)_{e^r e^t} \frac{h^k_{e^t e^g}}{(\omega_{e^g} - \omega_{e^t})} \sum_{v^r} \frac{\left\langle \psi_v^{f(f)} \middle| \psi_v^{r(r)} \right\rangle \left\langle \psi_v^{r(r)} \middle| Q_k \middle| \psi_v^{i(g)} \right\rangle}{(\omega_{e^r v^r : e^g v^i} - \omega_1 - i\Gamma_{e^r v^r})} \tag{3.3.106}$$

$$D^{\mathrm{V}} = \frac{1}{\hbar^3}(p_x)_{e^f e^s} \frac{h^k_{e^s e^r} h^{k'}_{e^r e^{s'}}}{(\omega_{e^r} - \omega_{e^s})(\omega_{e^r} - \omega_{e^{s'}})} (p_y)_{e^{s'} e^g} \times$$

$$\times \sum_{v^r} \frac{\left\langle \psi_v^{f(f)} \middle| Q_k \middle| \psi_v^{r(r)} \right\rangle \left\langle \psi_v^{r(r)} \middle| Q_{k'} \middle| \psi_v^{i(g)} \right\rangle}{(\omega_{e^r v^r : e^g v^i} - \omega_1 - i\Gamma_{e^r v^r})} \tag{3.3.107}$$

Where the additional superscripts indicate the electronic state to which they refer and the restrictions $e^r \neq e^g, e^f$; $e^s, e^{s'} \neq e^r$ and $e^f, e^g \neq e^t$ are still applied. The eqs. (3.3.104-3.3.107) have been obtained considering the term $\omega_{e^r e^g} + \omega_{v^r v^i}$ of the excited electronic state as be the dominant one in the sum over the states in the expression of the transition polarizability. Furthermore, only the first terms of eqs. (3.3.81-3.3.84) are significant because the second terms contribute only a slowly varying background and may be neglected. An additional simplification considered is the restriction of the sum over vibrational states to the vibrational states of one electronic state. Where Herzberg-Teller coupling is involved, only a single excited state in terms B^{V} and C^{V}, respectively *s* and *t*, have been considered, and only two excited states in term D^{V}. In addition, the summation on the normal coordinates has been restrict just to a single normal coordinate in in terms

B^{V} and C^{V}, and to a couple of normal coordinates in D^{V}. For normal vibrational resonant Raman scattering the further condition is that the initial and final electronic states are equal: $e^f = e^g$. The eqs. (3.3.103-3.3.107) become:

$$\left(\alpha_{xy}\right)_{e^f v^f : e^g v^i} = A^{\mathrm{VI}} + B^{\mathrm{VI}} + C^{\mathrm{VI}} + D^{\mathrm{VI}} \tag{3.3.108}$$

where:

$$A^{\mathrm{VI}} = \frac{1}{\hbar}(p_x)_{e^g e^r}\left(p_y\right)_{e^r e^g} \sum_{v_k^r} \frac{\left\langle \psi_{v_k}^{f(g)} \middle| \psi_{v_k}^{r(r)} \right\rangle \left\langle \psi_{v_k}^{r(r)} \middle| \psi_{v_k}^{i(g)} \right\rangle}{\omega_{e^r v_k^r : e^g v_k^i} - \omega_1 - i\Gamma_{e^r v_k^r}} \tag{3.3.109}$$

$$B^{\mathrm{VI}} =$$

$$= \frac{1}{\hbar^2}(p_x)_{e^g e^r} \frac{h^k_{e^s e^r}}{(\omega_{e^r} - \omega_{e^s})}\left(p_y\right)_{e^r e^g} \sum_{v_k^r} \frac{\left\langle \psi_{v_k}^{f(g)} \middle| Q_k \middle| \psi_{v_k}^{r(r)} \right\rangle \left\langle \psi_{v_k}^{r(r)} \middle| \psi_{v_k}^{i(g)} \right\rangle}{\left(\omega_{e^r v_k^r : e^g v_k^i} - \omega_1 - i\Gamma_{e^r v_k^r}\right)} +$$

$$+ \frac{1}{\hbar^2}(p_x)_{e^g e^r} \frac{h^k_{e^r e^s}}{(\omega_{e^r} - \omega_{e^s})}\left(p_y\right)_{e^s e^g} \sum_{v_k^r} \frac{\left\langle \psi_{v_k}^{f(g)} \middle| \psi_{v_k}^{r(r)} \right\rangle \left\langle \psi_{v_k}^{r(r)} \middle| Q_k \middle| \psi_{v_k}^{i(g)} \right\rangle}{\left(\omega_{e^r v_k^r : e^g v_k^i} - \omega_1 - i\Gamma_{e^r v_k^r}\right)} \tag{3.3.110}$$

$$C^{\mathrm{VI}} =$$

$$= \frac{1}{\hbar^2} \frac{h^k_{e^g e^t}}{(\omega_{e^g} - \omega_{e^t})}(p_x)_{e^t e^r}\left(p_y\right)_{e^r e^g} \sum_{v_k^r} \frac{\left\langle \psi_{v_k}^{f(g)} \middle| Q_k \middle| \psi_{v_k}^{r(r)} \right\rangle \left\langle \psi_{v_k}^{r(r)} \middle| \psi_{v_k}^{i(g)} \right\rangle}{\left(\omega_{e^r v_k^r : e^g v_k^i} - \omega_1 - i\Gamma_{e^r v_k^r}\right)} +$$

$$+ \frac{1}{\hbar^2}(p_x)_{e^g e^r}\left(p_y\right)_{e^r e^t} \frac{h^k_{e^t e^g}}{(\omega_{e^g} - \omega_{e^t})} \sum_{v_k^r} \frac{\left\langle \psi_{v_k}^{f(g)} \middle| \psi_{v_k}^{r(r)} \right\rangle \left\langle \psi_{v_k}^{r(r)} \middle| Q_k \middle| \psi_{v_k}^{i(g)} \right\rangle}{\left(\omega_{e^r v_k^r : e^g v_k^i} - \omega_1 - i\Gamma_{e^r v_k^r}\right)} \tag{3.3.111}$$

$$D^{\mathrm{VI}} = \frac{1}{\hbar^3}(p_x)_{e^g e^s} \frac{h^k_{e^s e^r} h^{k'}_{e^r e^{s'}}}{(\omega_{e^r} - \omega_{e^s})\left(\omega_{e^r} - \omega_{e^{s'}}\right)}\left(p_y\right)_{e^{s'} e^g}$$

$$\times \sum_{v_k^r, v_{k'}^r} \frac{\left\langle \psi_{v_k}^{f(g)} \middle| Q_k \middle| \psi_{v_k}^{r(r)} \right\rangle \left\langle \psi_{v_{k'}}^{r(r)} \middle| Q_{k'} \middle| \psi_{v_{k'}}^{i(g)} \right\rangle}{\left(\omega_{e^r v_k^r : e^g v_k^i} - \omega_1 - i\Gamma_{e^r v_k^r}\right)} \tag{3.3.112}$$

For a detailed treatment not discussed here, the eqs. (3.3.103-3.3.107) and (3.3.108-3.3.112) are the starting point of the electronic and vibronic resonance Raman scattering, respectively.

3.3.6 Intensity of Raman scattering radiation

The amount of radiation energy which passes through a surface of unit area perpendicular to the propagation direction in one second is defined as irradiance of the incident radiation and has units of W m^{-2}; it is given by:

$$\mathcal{R} = \frac{1}{2} c_0 \varepsilon_0 E_0^2 \tag{3.3.113}$$

The irradiance $\mathcal{R}$ must not be confused with the radiant intensity of a point source, which is defined as the ratio of the time-averaged power $d\Phi$, in a given direction contained in a conical beam of solid angle $d\Omega$ about this direction, to the solid angle $d\Omega$, and has units of W sr^{-1}:

$$I = \frac{d\Phi}{d\Omega} \tag{3.3.114}$$

The relationship between the intensity of the Rayleigh and Raman scattered radiation from a single molecule and the irradiance $\mathcal{R}$ of the incident radiation is given in a general form by:

$$I = \sigma' \mathcal{R} \tag{3.3.115}$$

Where $\sigma'$is the first differential scattering cross-section per molecule and it has the unit of m^2 sr^{-1} $molecule^{-1}$. The total scattering cross-section per molecule, σ, has the unit m^2 $molecule^{-1}$ and is defined by:

$$\sigma = \int_0^{4\pi} \sigma' d\Omega \tag{3.3.116}$$

The scattered intensity can be function also of the wavenumber and this dependence is considered in the definition of the second differential cross-section, σ'' that has the units m sr^{-1} $molecule^{-1}$:

$$\sigma'' = \frac{\partial \sigma'}{\partial \tilde{\upsilon}} = \frac{\partial^2 \sigma}{\partial \tilde{\upsilon} \partial \Omega} \tag{3.3.117}$$

Unlike the intensity *I*, the several cross sections do not depend on the incident irradiance but are characteristic of the materials.

If we consider the scattering radiation from a small volume element containing N free rotating identical molecules of an ideal gas coming from the transition v^i to v^f, the population of the initial state will contribute to the scattering Raman as follows:

$$N_{v^i} = N g_{v^i} \frac{e^{-\frac{E_{v^i}}{kT}}}{Q_v} \tag{3.3.118}$$

where g_{v^i} is the vibrational degeneracy of the initial state, E_{v^i} is the energy of a molecule in the initial state and Q_v is the sum over the vibrational states or vibrational partition function defined by:

$$Q_v = \sum_j g_{v^j} e^{-\frac{E_{v^j}}{kT}} \tag{3.3.119}$$

where the summation is over all the vibrational states *j*.

Let write in explicit form the relation between the amplitude of the components of the induced electric moment vector and the components of the electric field before to go ahead with the considerations regarding the scattering geometry shown in figure (3.3.2):

$$\begin{aligned} \left(p_{x_0}\right) &= (\alpha_{xx})E_{x_0} + \left(\alpha_{xy}\right)E_{y_0} + (\alpha_{xz})E_{z_0} \\ \left(p_{y_0}\right) &= \left(\alpha_{yx}\right)E_{x_0} + \left(\alpha_{yy}\right)E_{y_0} + \left(\alpha_{yz}\right)E_{z_0} \\ \left(p_{z_0}\right) &= (\alpha_{zx})E_{x_0} + \left(\alpha_{zy}\right)E_{y_0} + (\alpha_{zz})E_{z_0} \end{aligned} \tag{3.3.120}$$

In the eq. (3.3.120) the components of the Placzek pure vibrational transition polarizability, which have been defined in eq. (3.3.64), are involved. In order to obtain eq. (3.3.64) the rotational transitions of the molecules were ignored. This situation influences the intensity of the scattered radiation, because for free rotating molecules it will involve isotropic average of the squares of the transition polarizability tensor components, such as $\langle(\alpha_{xx})^2\rangle$, $\langle\left(\alpha_{xy}\right)^2\rangle$.

Let now consider the geometry shown in figure (3.3.3) where $\boldsymbol{e}_x$, $\boldsymbol{e}_y$ and $\boldsymbol{e}_z$ are the unit vectors associated to the Cartesian axis system x, y, z. The terms $\boldsymbol{n}_0^i$, $\boldsymbol{n}_0^s$ are the unit vector that define the direction of propagation of the incident and scattered observed radiations, respectively.

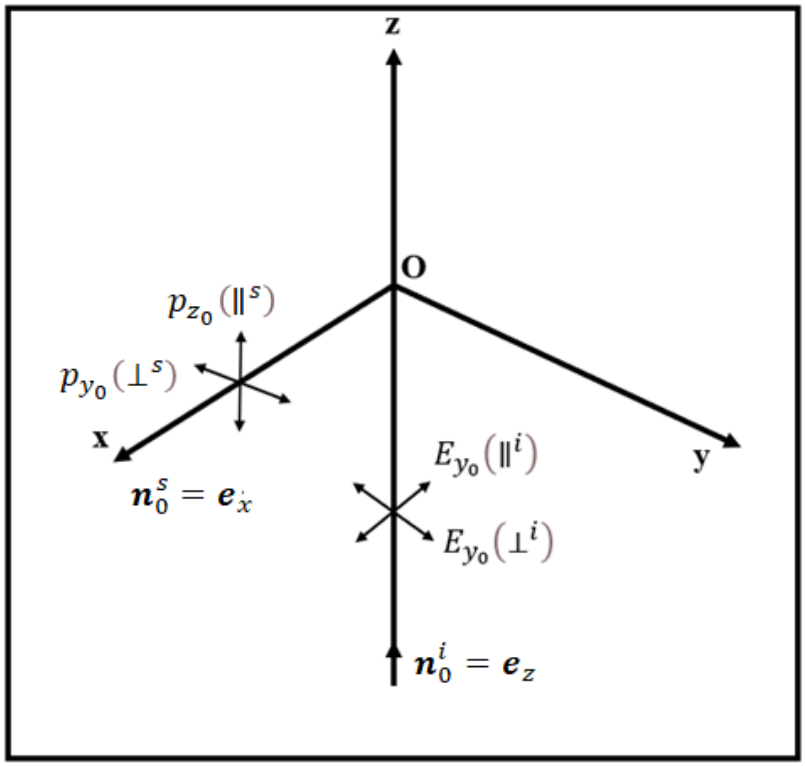

Figure 3.3.3. *Components of* $\boldsymbol{E}_0$ *and* $\boldsymbol{p}_0$ *when* $\boldsymbol{n}_0^i = \boldsymbol{e}_z$ *and* $\boldsymbol{n}_0^s = \boldsymbol{e}_x$*, respectively, reproduced from reference [7].*

In the case of the linear polarized incident radiation that it is propagating along z ($\hat{n}_0^i = \hat{e}_z$), the components of its electric field are restricted to $E_{x_0}(\|^i)$, $E_{y_0}(\perp^i)$ whereas for the scattered radiation, that it is propagating with a scattering angle θ equal to 90° along x ($\hat{n}_0^s = \hat{e}_x$), the components of polarization are restricted to $P_{y_0}(\perp^s)$, $P_{z_0}(\|^s)$. The symbols in the brackets $(\|^{i\ or\ s})$, $(\perp^{i\ or\ s})$, indicate whether the components of the scattered (s) or incident (i) radiations are parallel or perpendicular with respect to the scattering plane defined by the unit vectors $\hat{e}_x$ and $\hat{e}_z$. If it is the intensity of the radiation polarized perpendicular to the scattering $I(\pi/2\,, \perp^s, \perp^i)$ plane that is observed, the only active components of the transition polarizability tensor along the diagonal will be (α_{yy}), therefore $I(\pi/2\,, \perp^s, \perp^i)$ will involves its isotropic average $\langle(\alpha_{yy})^2\rangle$, whereas for other configurations, the

isotropic averages relative to active off-diagonal terms of the transition polarizability tensor will be involved.

The other possible geometric configurations shown in Fig. (3.3.3) are:

- $I(\pi/2\,,\parallel^s,\perp^i)$, for which (α_{zy}) will be the active components and its isotropic average $\langle(\alpha_{zy})^2\rangle$ will be the term involved in the intensity of the scattered radiation.
- $I(\pi/2\,,\parallel^s,\parallel^i)$, for which (α_{zx}) will be the active components and $\langle(\alpha_{zx})^2\rangle$ will contributes to the intensity.
- $I(\pi/2\,,\perp^s,\parallel^i)$, for which (α_{yx}) will be the active components and $\langle(\alpha_{yx})^2\rangle$ will contributes to the intensity.

Surprisingly, all the isotropic averages of the off-diagonal components of the transition polarizability are equal to each other while they are not equal to the isotropic averages of the diagonal components. Moreover, only in the first case, when $I(\pi/2\,,\perp^s,\perp^i)$ the components of the electrical field and the polarization are parallel each other while in all the other cases they are perpendicular. So two appropriate measures of intensity of the scattered radiation are sufficient in order to characterize a symmetric transition polarizability tensor in the Cartesian basis: one should be $I(\pi/2\,,\perp^s,\perp^i)$ and the other one can be any of the other three, but generally $I(\pi/2\,,\parallel^s,\perp^i)$ is chosen.

If the components of the electric field of the incident radiation are $E_{x_0}(\parallel^i)=0$ and $E_{y_0}(\perp^i)\neq 0$, the components of the amplitude of the transition electric dipole moment $\boldsymbol{p}_0$ for a single molecule will be:

$$p_{y_0}(\perp^s)=(\alpha_{yy})E_{y_0}(\perp^i) \tag{3.3.121}$$

$$p_{z_0}(\parallel^s)=(\alpha_{zy})E_{y_0}(\perp^i) \tag{3.3.122}$$

The intensity of the scattered radiation by N_{ν^i} molecules of an ideal gas in the initial state ν^i and in a geometric configuration equivalent to that just described is obtained by multiplying for N_{ν^i} the eqs. (3.3.1-3.3.2) where $\theta=90°$ and taking into account the eqs. (3.3.121-3.3.122) but by using isotropic average of the corresponding square of the component of the transition polarizability tensor. Thus:

$$I(\pi/2\,,\perp^s,\perp^i)=\frac{N_{\nu^i}\omega_s^4\langle(\alpha_{yy})^2\rangle E_{y_0}^2(\perp^i)}{32\pi^2\varepsilon_0 c_0^3}=\frac{\pi^2 c_0 N_{\nu^i}\tilde{\nu}_s^4\langle(\alpha_{yy})^2\rangle E_{y_0}^2(\perp^i)}{2\varepsilon_0} \tag{3.3.123}$$

$$I(\pi/2\,,\parallel^s,\perp^i)=\frac{N_{\nu^i}\omega_s^4\langle(\alpha_{zy})^2\rangle E_{y_0}^2(\perp^i)}{32\pi^2\varepsilon_0 c_0^3}=\frac{\pi^2 c_0 N_{\nu^i}\tilde{\nu}_s^4\langle(\alpha_{zy})^2\rangle E_{y_0}^2(\perp^i)}{2\varepsilon_0} \tag{3.3.124}$$

Remembering that the transition polarizability tensor is symmetric, so the isotropic average can be expressed as:

$$\langle\left(\alpha_{yy}\right)^2\rangle = \frac{45a^2 + 4\gamma}{45} \tag{3.3.125}$$

$$\langle\left(\alpha_{zy}\right)^2\rangle = \frac{\gamma^2}{15} \tag{3.3.126}$$

where in a general way:

$$a = \frac{1}{3}\left(\alpha_{xx} + \alpha_{yy} + \alpha_{zz}\right) \tag{3.3.127}$$

and

$$\gamma^2 = \frac{1}{2}\left\{\left|\alpha_{xx} - \alpha_{yy}\right|^2 + \left|\alpha_{yy} - \alpha_{zz}\right|^2 + \left|\alpha_{zz} - \alpha_{xx}\right|^2\right\} + \\ + \frac{3}{4}\left\{\left|\alpha_{xy} + \alpha_{yx}\right|^2 + \left|\alpha_{xz} + \alpha_{zx}\right|^2 + \left|\alpha_{yz} + \alpha_{zy}\right|^2\right\} \tag{3.3.128}$$

The introduction of the irradiance $\mathcal{R}$ defined in eq. (3.3.113) in the eqs. (3.3.123-3.3.124), taking into account the eqs. (3.3.125-3.3.126), determines that:

$$I\left(\pi/2\,,\perp^s,\perp^i\right) = \frac{N_{\nu^i}\omega_s^4}{16\pi^2\varepsilon_0^2 c_0^4}\left\{\frac{45a^2+4\gamma}{45}\right\}\mathcal{R} = \frac{\pi^2 c_0 N_{\nu^i}\tilde{\nu}_s^4}{\varepsilon_0^2}\left\{\frac{45a^2+4\gamma}{45}\right\}\mathcal{R} \tag{3.3.129}$$

$$I\left(\pi/2\,,\parallel^s,\perp^i\right) = \frac{N_{\nu^i}\omega_s^4}{16\pi^2\varepsilon_0^2 c_0^4}\left\{\frac{\gamma^2}{15}\right\}\mathcal{R} = \frac{\pi^2 c_0 N_{\nu^i}\tilde{\nu}_s^4}{2\varepsilon_0^2}\left\{\frac{\gamma^2}{15}\right\}\mathcal{R} \tag{3.3.130}$$

The total intensity of the scattered radiation for $\boldsymbol{n}_0^{\boldsymbol{i}} = \boldsymbol{e}_z$ is given by the sum of eqs. (3.3.129-3.3.130), note that no care is devoted to the polarization of the scattered radiation:

$$I\left(\pi/2\,,\perp^s+\parallel^s,\perp^i\right) = \frac{N_{\nu^i}\omega_s^4}{16\pi^2\varepsilon_0^2 c_0^4}\left\{\frac{45a^2+7\gamma^2}{45}\right\}\mathcal{R} = \frac{\pi^2 c_0 N_{\nu^i}\tilde{\nu}_s^4}{\varepsilon_0^2}\left\{\frac{45a^2+7\gamma^2}{45}\right\}\mathcal{R} \tag{3.3.131}$$

The ratio between the eq. (3.3.130) and the eq. (3.3.129) defines the depolarization ratio also known as the degree of depolarization $\rho\left(\pi/2\,,\perp^i\right)$:

$$\rho\left(\pi/2\,,\perp^i\right) = \frac{I\left(\pi/2\,,\parallel^s,\perp^i\right)}{I(\pi/2\,,\perp^s,\perp^i)} = \left\{\frac{3\gamma^2}{45a^2 + 4\gamma^2}\right\} \tag{3.3.132}$$

In the case of inversion of the components of the electric field of the incident radiation, namely $E_{x_0}\left(\parallel^i\right) \neq 0$ and $E_{y_0}\left(\perp^i\right) = 0$, the active components of the transition polarizability tensor given by eq. (3.3.120) will be off-diagonal, $I\left(\pi/2\,,\perp^s,\parallel^i\right)$ will be equals to $I\left(\pi/2\,,\parallel^s,\parallel^i\right)$ and is given in eq. (3.3.130). When $\gamma \neq 0$ the depolarization ratio

$\rho(\pi/2, \|^i)$ is equal to 1. Consider now the case for $\boldsymbol{n_0^s} = \boldsymbol{e}_z$ $(\theta = 0)$, and $\boldsymbol{n_0^s} = -\boldsymbol{e}_z$ $(\theta = \pi)$. The involved components of the transition electric dipole moment $(\boldsymbol{p}_0)$ are $p_{y_0}(\perp^s)$ and $p_{x_0}(\|^s)$. From the eq. (3.3.120), the active components of the transition polarizability tensor, when $E_{x_0}(\|^i) = 0$ and $E_{y_0}(\perp^i) \neq 0$, are (α_{yy}) and (α_{xy}). The corresponding intensity of the scattered radiations are given by eq. (3.3.129) in the case of $I(0\ or\ -\pi, \perp^s, \perp^i)$ and by eq. (3.3.130) in the case of $I(0\ or\ -\pi, \|^s, \perp^i)$. Otherwise, if $E_{y_0}(\perp^i) = 0$ and $E_{x_0}(\|^i) \neq 0$, the active components of the transition polarizability tensor are (α_{xx}) and (α_{yx}). In this case, the corresponding intensity of the scattered radiations $(0\ or\ -\pi, \perp^s, \|^i)$ and $(0\ or\ -\pi, \|^s, \|^i)$ are given by eqs. (3.3.130) and (3.3.129) respectively. All the relationships for the intensity conduce to two geometries: in a first case the electrical vectors of the incident and the scattered radiations are parallel to each other, this is the case of the expression that involves *a* and *γ*; in the second case, the electric vectors are perpendicular and the expression involves only *γ*.

3.3.7 Raman Scattering in Solid

The Raman effect has been descripted in a theorical way in the previous paragraphs. It has been seen that the vibration is quantized and this is the case also in solid system where the reticular vibration, or elastic wave, is quantized [8,9]. In particular, while for the electromagnetic wave the energy quantum is the photon, in the case of the reticular vibration it is called phonon. It is important to note that almost all the concepts developed for the photon are also valid for the phonon. Considering again a monochromatic light beam of frequency ω_1, the light will propagate with the propagation vector $\boldsymbol{k}_1$, $|\boldsymbol{k}_1| = \omega_1 \cdot \eta(\omega_1)/c_0$ where $\eta(\omega_1)$ is the refractive index. In the same manner, the propagation vector of the scattered light is $\boldsymbol{k}_s$, $|\boldsymbol{k}_s| = \omega_s \cdot \eta(\omega_s)/c_0$. The scattering frequency and the scattered vector are respectively defined as follows:

$$\omega = \omega_1 - \omega_s \tag{3.3.133}$$

and

$$\boldsymbol{k} = \boldsymbol{k_1} - \boldsymbol{k_s} \tag{3.3.134}$$

The conservation of the energy and of the moment laws, eqs. (3.3.133-3.3.134), must be satisfied to have Raman scattering.

In a perfect crystal, the elementary excitations, that is phonons, are represented by the wave vector $\boldsymbol{q}$ and the frequency ω_q, whose correlation is given by a dispersion relation that specifies a frequency ω_q for each value of $\boldsymbol{q}$. The first order process is characterised by a single elementary excitation, then the scattered wave vector and the scattering frequency are equal to $\boldsymbol{q}$ and ω_q respectively.

In the typical visible – near infrared set up, the order of magnitude of the maximum phonon wave vector ($\cong 10^4$ cm^{-1}) that is excited by the light is about three orders of magnitude smaller than the wavevectors corresponding to the Brillouin zone boundary of characteristic crystals ($\cong 10^7$ cm^{-1}). Consequently, for first order process that conserve the wave vector only the elementary excitations close to the centre of the Brillouin zone must be considered. In this case, $\boldsymbol{q} \cong 0$ and the many unit cells of a perfect crystal vibrate in phase. This implies the possibility to use the point group symmetry in order to evaluate the symmetry of the vibration, treating the unit cells as molecules. This is an enormous advantage because unlike the space group symmetry, which has 230 groups, the point group symmetry has only 32. The theoretical treatment of the Raman effect on solid crystalline systems can be deal with the above exposed theories.

In imperfect crystals, with a small concentration of defects, as well as in solid solutions or in amorphous solids, the condition of the conservation of the wave vector is no longer respected. Therefore, the Raman spectra show such features depending on the density of the states of the particular excitation, determining the fundamental role of the Raman Spectroscopy in the characterization of such systems.

However, the condition of the conservation of the wave vector has to be studied with some attention when the systems are constituted by quantum structures such as artificial multilayer systems which display size quantization, or confinement, along one or more directions. The size quantization occurs when there is a small characteristic length so that along this direction the motion is quantized into distinct energy levels, as in a quantum well. For electrons typical lengths are in the nanometres range and the structures are said to be nanostructures.

Let consider a binary alloy system as example. It can be viewed as a perfect host crystal that contains some impurities that have the same valence but a smaller mass than the atoms of the host crystal. The own local vibrational modes related to the impurities are often seen by Raman spectroscopy. From an atomic point of view, the heavier host atoms cannot follow the motion of the faster impurities and this results as a narrow band in the

Raman spectra. The reason is because the local frequency modes associated to the light impurities will be well above the local frequency mode related to the host crystal, and the direct coupling is not possible. Otherwise, if the impurities are heavier than the atoms of the host crystal, the direct coupling occurs and the associated mode will not be anymore local. The Raman band related to that mode will be much broader than before. The Raman spectra collected on amorphous materials will generally consist in broad bands with maxima approximatively close to the frequency of the same mode of the material in the crystalline phase that shows a narrow band. For this reason, Raman spectroscopy is a useful tool in the study of the structural phase transitions. Most studies show effects on the materials due to thermal or pressure modifications that usually are opposite: an increasing temperature tends to increase the inter atomic distance while an increasing pressure tends to reduce the inter atomic distance.

3.3.8 Raman Scattering in Polymer

Raman spectroscopy in polymer science is very commonly used, due to the fact that it can provide information on the characterization of the molecular compositions, segmental orientational, chain conformation and, quite important, as regards intermolecular interactions. Furthermore, Raman spectroscopy is conveniently often used in the study of biological systems because of the low Raman scattering of the water molecules. Raman spectroscopy is currently used in an area of interest: the study of systems that show disordered chains which can affect macroscopic properties such as ionic conductivity, mechanical properties, solvation efficiency, corrosion inhibition etc. This is because the relative intensity and the frequency of the Raman bands depend on the relative concentrations of the specific localized structures.

Although the technique works very well for above systems and for those that involve well defined structures and precise assignments to the Raman band, it is not easy to get results. This is because for disordered systems, the Raman bands appear generally as broad and weak bands that can often be overlapped. Therefore, in order to have information of the macroscopic properties of the systems, it is often necessary to make some efforts in the resolution of these features.

The Raman spectra often show the changes of polarizability associated with different carbon-carbon backbone conformations. As it is known, the Raman scattering is associated with the transition of the polarizability tensor, so the Raman spectra that are

collected in polarization way provide several information on the structures of disordered samples and even on those in solution or melt.

3.4 Surfaces Enhanced Raman Spectroscopy

It has been on the late 1970s that a first recognition of an observed phenomenon in 1974 gave impetus to what would later be called SERS [10-12]. Initially, the use of SERS was limited to a narrow circle of the scientifical community, as it required mastery of the optics and lasers used in Raman spectroscopy, as well as the electrochemistry involved in the process. However, the 1997 discovery of the single-molecule SERS led to the use of SERS also as an analytical technique of investigation [13,14]. Thus, today there are thousands of scientific research, articles and books dealing with the topic in the most diverse fields: chemistry, physics, materials and surface sciences, nanoscience and life sciences in general (medicine, biology, etc.) [15-22].

3.4.1 Fundamental on SERS

The SERS effect is explained through two different mechanisms, the electromagnetic enhancement (EM) and the chemical enhancement (CM). The former mechanism is responsible for an enhancement factor (EF) in a wide range (10^3-10^{10}) while the latter is significantly much smaller with EF in the range of one to three orders of magnitude.

EM is related to the interaction between the plasmon of a metal (that is, the quantum of energy associated with the oscillations of a plasma, formed in metals by conduction electrons) and the photons of the incident radiation.

CM is related to the electronic properties of the adsorbed molecules on the surface of the metal and consequently on the increasing in their electronic polarizability $\alpha_{\mathrm{molecule@metal}}$ on the induced dipole μ_{ind} [23].

3.4.1.a Electromagnetic enhancement (EM)

When the incident light come onto the metal surface, the conduction electrons of the metal can be resonantly excited by the electromagnetic wave. Taking in mind the classical harmonic oscillator model, the resonance frequency of the plasma oscillation (plasmon) of metal, ω_{max} depends on the dielectric functions of the metal $\varepsilon_{\mathrm{metal}}(\omega)$and the surrounding medium $\varepsilon_{\mathrm{m}}(\omega)$. The typical plasmon peaks of colloidal silver and gold are

observed in the visible region of the electromagnetic spectrum, so the optical frequencies are sufficient to excite these metals.

In figure (3.4.1.a) is shown a gold nanoparticle that undergoes a charge separation due to the oscillation of conduction electrons generated by incoming laser radiation [23].

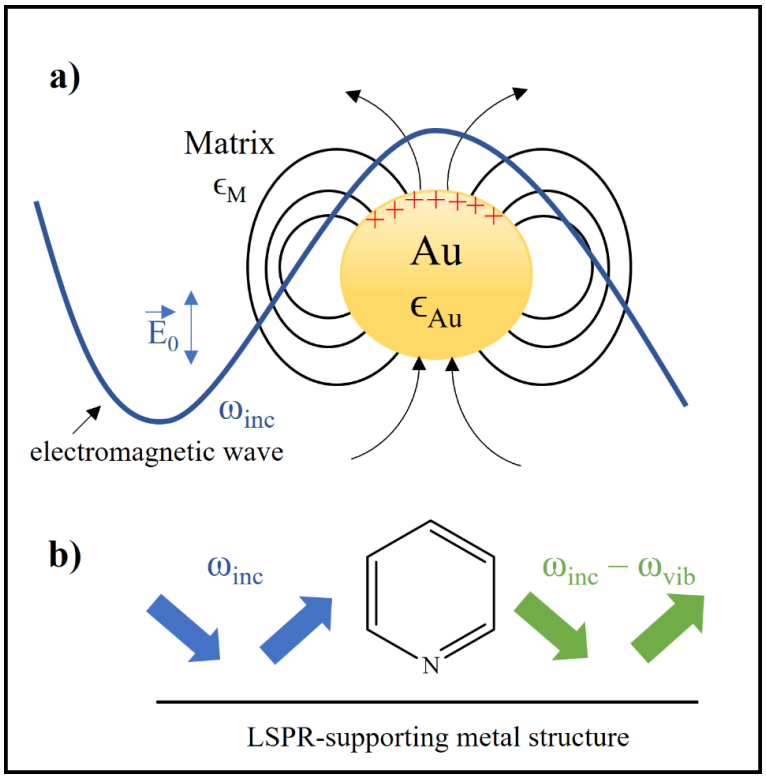

Figure 3.4.1. *EM in SERS: a) the excitation of a dipolar localized surface plasmon resonance (LSPR) generates a Hertzian dipole on a gold nanoparticle; b) The scattered LSPR-supporting metal structure by the elastic light enhances both the incoming electric field (ω_{inc} blue) and the outgoing electric field ($\omega_{inc} - \omega_{vib}$ green)* reproduced from reference [23].

The radiation has angular frequency equal to ω_{inc} and amplitude E_0. It is the oscillating electric field of the radiation that determines the charge separation. This type of resonance is a particular case of plasmonic resonance, named dipolar Localized Surface Plasmon Resonance (LSPR). The polarizability of the nanoparticle metal α_{metal} together with the incident electric field strength $E(\omega_{\mathrm{inc}})$ define the magnitude of the induced dipole $\mu_{\mathrm{ind(metal)}}$, that is $\mu_{\mathrm{ind(metal)}} = \alpha_{\mathrm{metal}}\, E_0(\omega_{\mathrm{inc}})$. The resulting localized induced dipole μ_{ind} changes his sign in function of the angular frequency ω_{inc} of the electromagnetic wave that is the external driving force. The resulting Hertzian dipole on the nanoscale can emit radiation at the same frequency ω_{inc} (Fig. 3.4.1).

In summary, in figure (3.4.1.a) the resonant elastic light has been dispersed by gold nanoparticle resulting in an increased local electric field $E_{\mathrm{loc}}(\omega_{\mathrm{inc}})$ close to the metal sphere relative to the incident electric field $E_0(\omega_{\mathrm{inc}})$ [23].

In figure (3.4.1.b) it is shown the interaction between the local electric field $E_{\mathrm{loc}}(\omega_{\mathrm{inc}})$ and a molecule near the surface of the gold nanoparticle. Also in the molecule induced dipoles can be generated $\mu_{\mathrm{ind}} = \alpha_{\mathrm{molecule}}\, E_{\mathrm{loc}}(\omega_{\mathrm{inc}})$. Both the induced dipole moment μ_{ind} and the incident local electric field $E_{\mathrm{loc}}(\omega_{\mathrm{inc}})$ are vectorial properties while the electronic polarizability of the molecule $\alpha_{\mathrm{molecule}}$ as described above, is a tensor of rank two with nine components. Remembering the classical theory of the Raman scattering, the phenomenon of inelastic light scattering can be explained by considering a molecule vibrating with angular eigenfrequency ω_{vib}, modulating the incident electric field $E_0(\omega_{\mathrm{inc}})$. As usual, the three dipole components that occur are the Rayleigh scattering, $\mu_{\mathrm{ind}}(\omega_{\mathrm{inc}})$, the Stokes Raman scattering, $\mu_{\mathrm{ind}}(\omega_{\mathrm{inc}} - \omega_{\mathrm{vib}})$, and the anti-Stokes Raman scattering, $\mu_{\mathrm{ind}}(\omega_{\mathrm{inc}} + \omega_{\mathrm{vib}})$. In figure (3.4.1.b) it is shown the Stokes Raman scattering with angular frequency $\omega_{\mathrm{inc}} - \omega_{\mathrm{vib}}$ for one particular vibrational mode. The frequency-shifted radiation (the left green arrow in Fig.3.4.1.b) is sufficient to excite a LSPR of the metal sphere of figure (3.4.1.a). So, elastic light can be dispersed by the metal sphere (the right green arrow in Fig.3.4.1.b) and the emitted radiation is detected in the far field [23].

The SERS intensity is a function of both the incident electric field (ω_{inc}) and the outcoming electric field $(\omega_{\mathrm{inc}} - \omega_{\mathrm{vib}})$, so that $I_{\mathrm{SERS}} = I_{\mathrm{inc}}(\omega_{\mathrm{inc}})I(\omega_{\mathrm{inc}} - \omega_{\mathrm{vib}}) = |E_{\mathrm{inc}}(\omega_{\mathrm{inc}})|^2 |E(\omega_{\mathrm{inc}} - \omega_{\mathrm{vib}})|^2$. To obtain a SERS enhancement is therefore necessary that the incident radiation ω_{inc} and the Stokes Raman scattered radiation $\omega_{\mathrm{inc}} - \omega_{\mathrm{vib}}$ are in resonance with the plasmon peak of the metal sphere. The typical $|E|^4$ approximation of the SERS intensity is obtained for an incident laser radiation ω_{inc} close to a Stokes Raman scattering for one particular vibration $\omega_{\mathrm{inc}} - \omega_{\mathrm{vib}}$, that is $\omega_{\mathrm{inc}} \approx \omega_{\mathrm{inc}} - \omega_{\mathrm{vib}}$ or $\omega_{\mathrm{inc}} \gg \omega_{\mathrm{vib}}$.

The electric field strength of the dipolar radiation scales by a factor of three with respect to the distance resulting in a predicted and observed dependence of the SERS intensity from the distance by a factor of twelve [23].

3.4.1.b Chemical enhancement (CM)

The EM is not enough to fully explain the SERS effect on its own. This is because being a non-selective amplifier of the Raman scattering by any molecules adsorbed, or at least very close to a particular metal surface, there should not be a difference by a factor of 200 between the SERS intensities of CO and N_2 under the same experimental conditions. Charge transfer (CT) mechanism should happen between the electronic ground state of the adsorbed molecule and the metal, changing the polarizability of the molecule and resulting in a change of the Raman cross-section. The energy levels of the adsorbate molecules and those of the free molecules are different resulting in the possibility for the excitation radiation to be coincident with an electronic absorption band of the adsorbate molecule but not with one of free molecule. In these conditions, the electronic states of adsorbate molecules are broadened by their interaction with the metal surface resulting in a resonance Raman mechanism (the resonant excitation of electronic transitions, see Fig.3.2.2) and at the same time, the photoinduction can lead to new electronic excitation channels.

In figure (3.4.2) are shown the typical energy levels (Highest Occupied Molecular Orbital, HOMO, and Lowest Unoccupied Molecular Orbital, LUMO) for an adsorbed molecule symmetrically disposed with respect to the Fermi level of the metal.

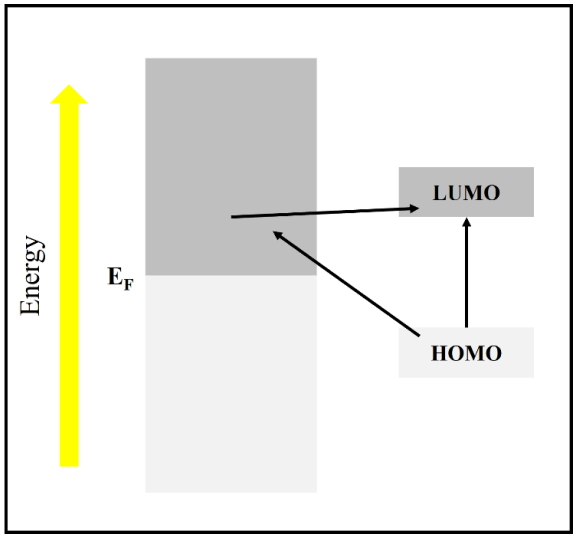

Figure 3.4.2. *Energy levels for an adsorbed molecule. The HOMO and LUMO are broadened into resonances by their interaction with the metal states. The Fermi energy determines the orbital occupancy. CT mechanism can occur, with some excitations that are shown.*

3.5 Raman Microprobe equipment

For the Raman analysis conducted in this work, the instrument used is microRaman-LABRAM by Horiba Jobin-Yvon Srl. The instrument operates in a back scattering geometry, that is ($\theta = \pi$), allowing the combination of a Raman spectrometer with an optical microscope. In this way, the Raman spectra are collected in the micrometre region (order ≅ 2 – 5 μm) of the samples [1,24]. In the following table (3.5.1) [7] are summarized all the main parts of the instrument.

Element	Characteristics
Laser	HeNe 17 MW power, polarised 500:1, emission wavelength 632.817 nm
Holographic Notch Filter	Super Notch Plus with the use of a dichroic mirror. Drop off Stokes edge < 120 cm^{-1}; now 200 cm^{-1}
Confocal Hole	Adjustable between 0 and 1500 μm (scaled on the sample with a factor: 1,4xObjective magnification)
Mcroscope	Hight stability BX40, focus graduation 1 μm. Objectives 10x NA 0.25; 50x NA 0.7; 100x NA 0.9. Other objectives available (Long work distance 20x, 50x). Illumination by transmission and reflection for opaque samples. Macro adapter for mounting of macro 40 mm objective under microscope. Colour camera for the observation of the sample.
External Lasers available and Laser entrance	(Notch or edge filter exchange is required) Ar^+, 457.8, 514.532 nm; Kr^+ 647.1, 725.5 nm; YAG doubled, diode pumped 532 nm, Laser diode 785 nm. Removable mirrors for external Laser. HeNe beam can be directed externally through the external laser entrance for easier external laser alignment.
Spectrograph	Stigmatic 300 mm focal length spectrograph. Two gratings mounted on the same shaft 1800 g/mm (holographic) and 600 g/mm (ruled or holographic). Sinus arm drive. Laser diode for alignment.
CCD Detector	Peltier cooled 1024x256, 16-bit dynamic range (pixel size 27 μm)
Separated electronic box	Alimentation of the Laser, drive of hole, slit, gratings, shutters, scanners, alimentation of the Laser diode for alignment.
Computer	Labspec software and VITEC video card for TV image digitalization
Options	Motorised XY microscope stage for point by point or laser scanning imaging. Resolution 0.1 μm, reproducibility 1 μm. Raman 90x60 mm. Y piezo table for imaging with laser scanning (X direction), range 100 μm. "PIFOC" Z-actuator for automatic focusing of microscope objective or z-scanning (range 0-100 μm). Autofocus device for microscope objective (correction of focus between + / –5 μm). Temperature controlled cells. Set of filters (notch + interferential) for external laser.

Table 3.5.1. *Main features of the Raman instrument, reproduced from reference [7].*

Raman spectroscopy is nowadays commonly used in the study either of small samples or small impurities (or heterogeneities) in larger samples. The recording of single Raman spectrum from several points of a sample is allowed at one location at a time because of

the small spot size. Moreover, the collection of Raman spectra from different points is called as point to point mapping (Fig. 3.5.1) [7].

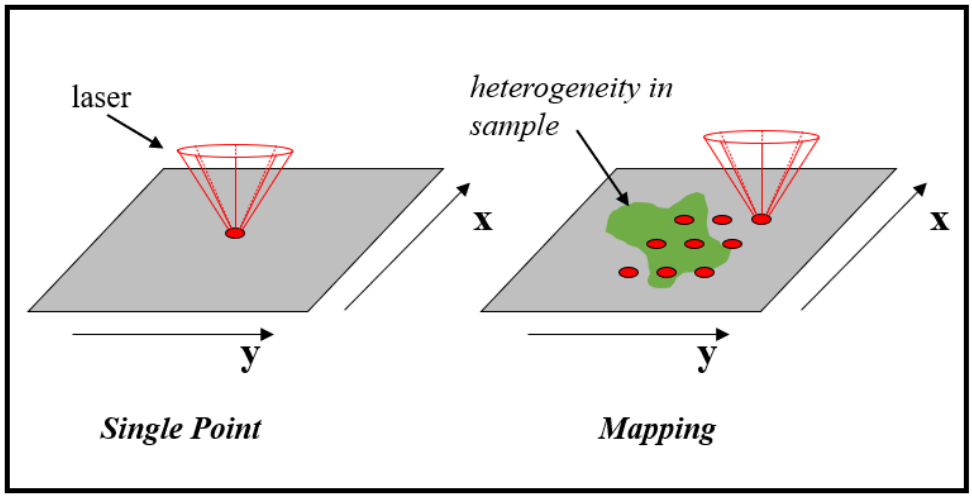

Figure 3.5.1. *Two imaging modes for microRaman spectroscopy, reproduced from reference [7].*

The Raman imaging is a method that allows to obtain Raman spectra resulting from different points of the sample in one time. The method is now possible because of the developing of the two-dimensional detectors that have improved the microspectroscopy technique. Examples of such method include the possibility to have image resulting from light with a particular Raman shift of a component so that the spatial distribution can be followed, or it is possible to display the Raman spectra relative to selected points of a stored spectroscopic image. It is also possible to make a profile of the intensity variation of a particular Raman feature observed along a line on the sample. The set up allows to acquire and/or display the spectroscopic results from a data set of intensity as a function of the three independent spatial coordinates x, y and z (depth) and of a fourth independent coordinate, the Raman shift. The mapping is a technique in which the laser is focused on the sample plane so that the Raman spectra, acquired from a selected region of the sample, are showed using an imaging spectrograph onto a charge coupled device (CCD), thus generating a two-dimensional data set of intensity vs Raman shift.

The laser spot size and the optic used to collect the Raman spectra define the spatial resolution and the diameter of the laser beam at the focal spot is given by:

$$Spot\ diameter = 2w_0 = f\theta_d \tag{3.5.1}$$

where w_0 is the beam waist, f is the objective lens focal length and θ_d represents the full angle divergence of the laser expressed in radiant. Alternatively, the spot diameter could be given by:

$$Spot\ diameter = 2w_0 = 1.27\lambda f/w_e \quad (3.5.2)$$

where it is related to the pupil aperture of the objective lens w_e.

The use of a laser combined with microscope as in the microRaman configuration requires some precautions such the use of dichroic mirrors (or beamsplitter), which selectively reflect the laser wavelengths (Fig. 3.5.2) [7].

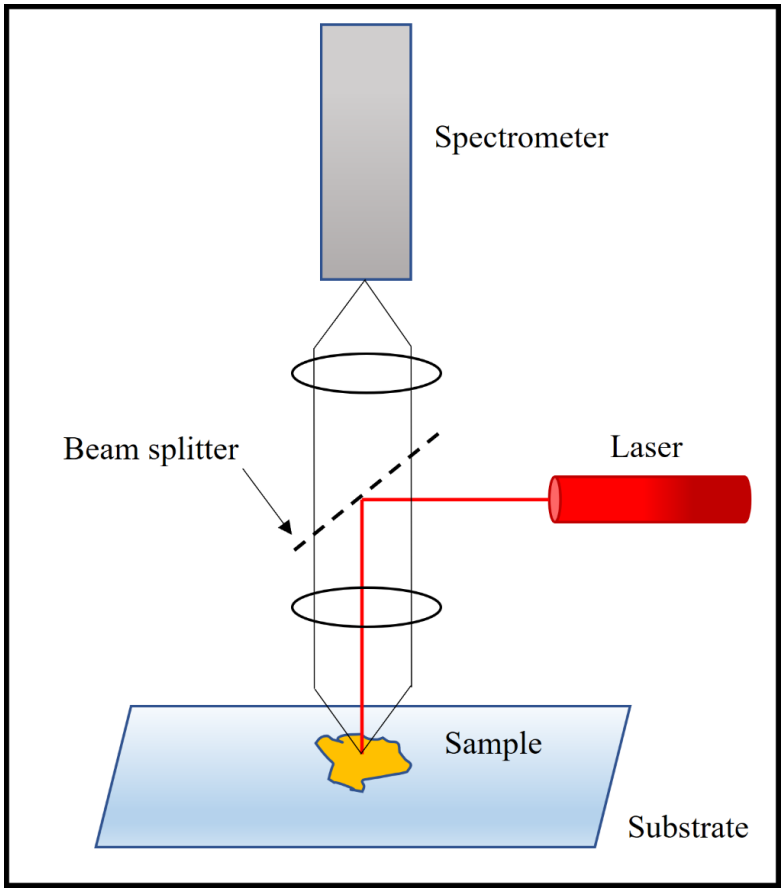

Figure 3.5.2. *The beam splitter combines the laser and collection axes, reproduced from reference [7].*

The dichroic mirror in modern microRaman apparatus is based on holographic optical elements. Its reflectivity is strongly dependent on the wavelength of the source and for this reason each laser sources require a specific beam splitter. Furthermore, the dichroic mirror must be very reflective to the laser radiation and at the same time, highly transmissive for the Raman shifted radiations.

The Labram instrument is equipped with an holographic notch filter that is characteristic of the He-Ne source and acts as a beam splitter but in a better way. In fact, the filter is quite perpendicular to the collection axis allowing to transmit high fraction of the Raman shifted radiation to the spectrometer. At the same time, the filter rejects the elastic scattering (Rayleigh scattering), making it more efficient than a beam splitter. The figure

(3.5.3) [24] depicts the back scattering geometry of the Labram: the Raman source (Laser, in red) is transmitted to the sample by mirrors, the back scattered radiation (in blue) pass through the holographic notch filter that cuts the Rayleigh scattering and only allows Raman scattering to reach the spectrograph. The yellow arrow indicates the optical path of the microscope.

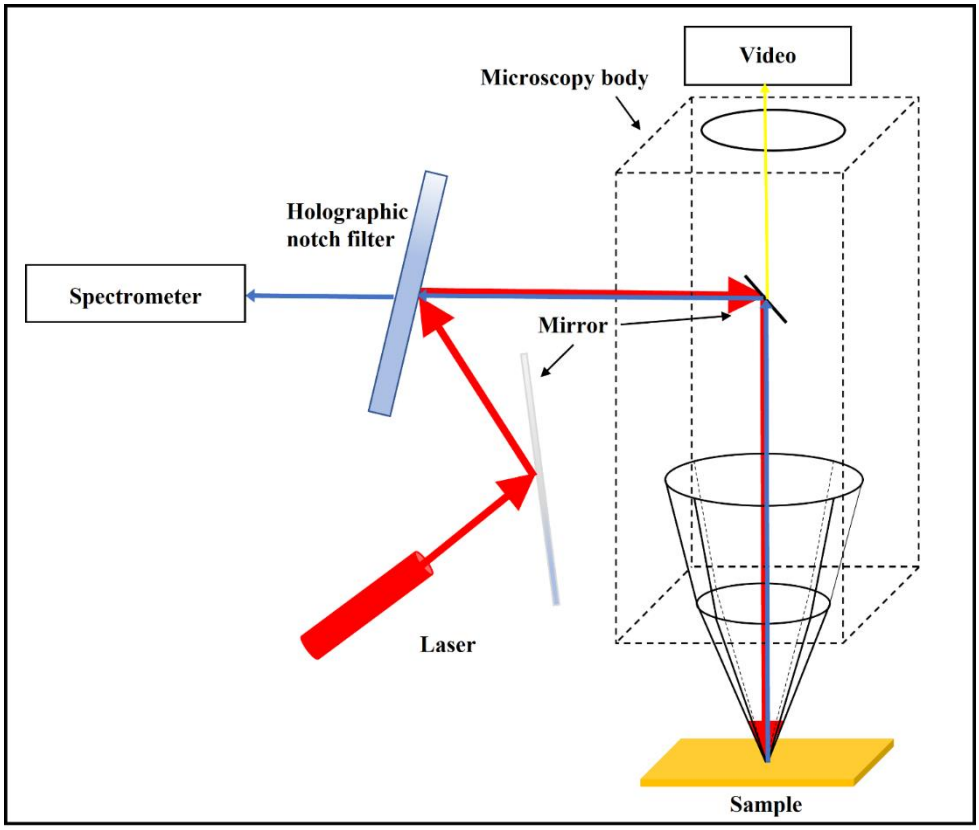

Figure 3.5.3. *The back scattering geometry in Labram equipped with holographic notch filter, reproduced from reference [7].*

The Labram is equipped with a confocal hole that allows to decrease the depth of the focus. MicroRaman is therefore a confocal one and is quite useful in the analysis of thin films and/or samples made by more layers made of different materials. Often, the substrates can overlap the Raman signals emitted by thin films, this is because the studied layers could be thinner than the depth of the focus, leading to Raman spectra that represent average of the layers. In figure (3.5.4) [7] are shown the principles of confocal and conventional microscopes. There are shown the pathways of the scattered radiation from two points situated at different depth named Z_1 and Z_2. In a conventional microscope, (on the right of Fig. 3.5.4), the spectrometer aperture (also named as slit) allows the passage of the two scattered radiation toward the spectrometer. As mentioned above, the Raman spectrum reflects the average sample composition of the two different points. In the case

of the confocal microscope instead, the confocal hole allows to select a smaller region of the depth sample by blocking the scattered radiation of point Z_2.

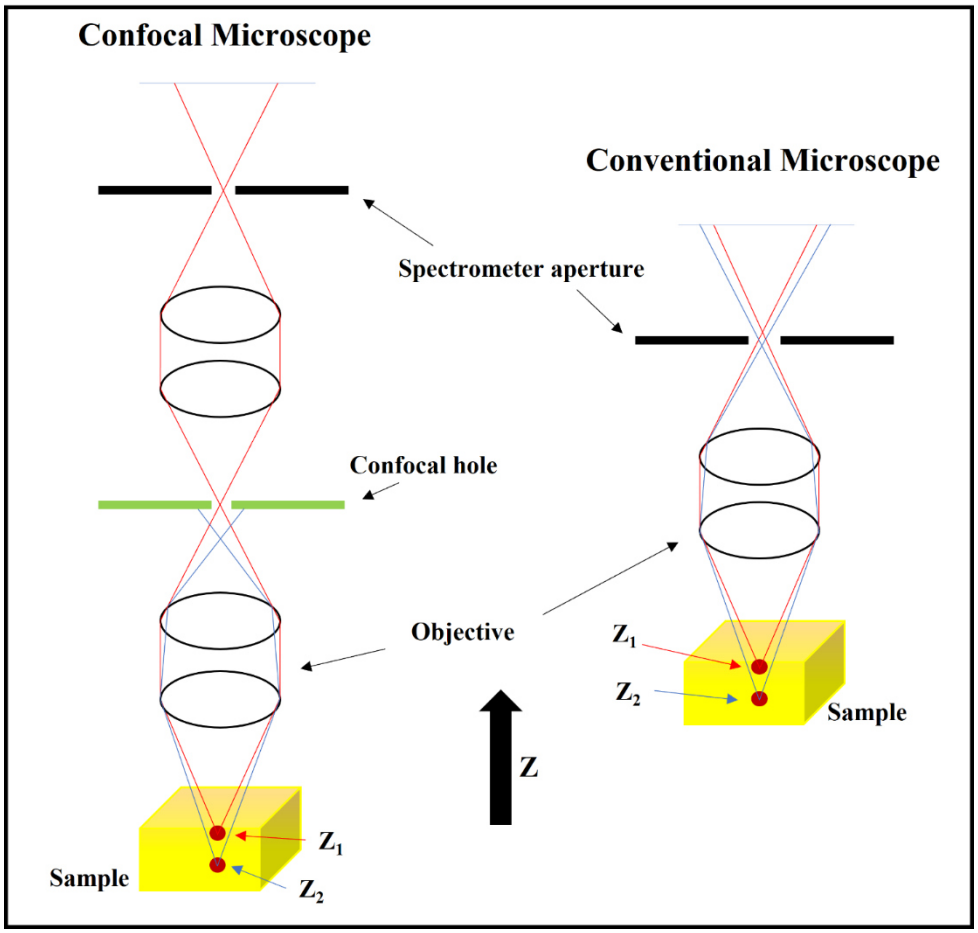

Figure 3.5.4. *The description of a confocal microscope and of a conventional one, reproduced from reference [7].*

Because it is responsible of a lower effective path length, the confocal hole causes also a decrease in the signals intensities. The Labram is able to perform a z-scan by remote control on a computer thanks to confocal optics.

3.6 Cyclic Voltammetry

Nowadays Cyclic Voltammetry (CV) represents an essential tool in the first electrochemical characterization of electrochemical species, because it is useful for the comprehension of the mechanisms involved in redox reactions [25,26].

The cyclic voltammogram is the result of current-potential curves in a triangular waveform obtained by the cyclization of the potential during an experiment [25]. The electrochemical properties of redox reactions related to given materials can be theoretically uniquely identified by CV with the identification of the peak current and peak potential and the shape analysis of the curve.

A normal voltammetric experiment consists in the use of three electrode configuration immersed in solution of salt that acts as supporting electrolyte [25]. In figure (3.6.1) are shown the three electrodes in typical electrochemical cell used in CV. The working electrode is the one on which the measurements are made [25].

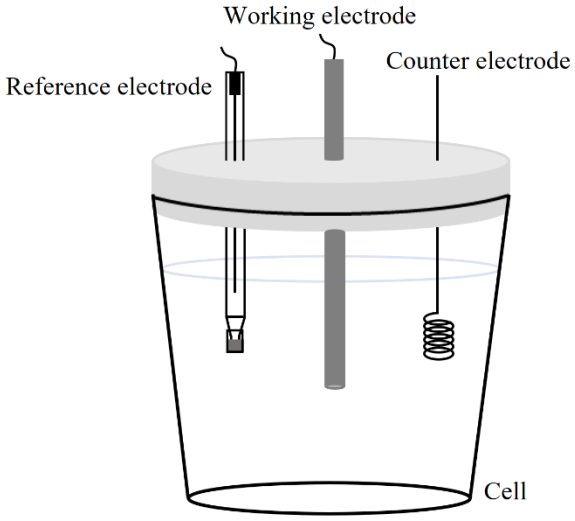

Figure 3.6.1. *Electrochemical cell for CV measurements, reproduced from reference [25].*

Working electrodes are made with different materials such as mercury, platinum, gold, graphite, glassy carbon and others and the use of a given working electrode for a specific depends on its potential window and on their effects on the electrode transfer process [25]. Furthermore, working electrodes can be made in different shapes such as spherical, rod and others. A popular electrode for voltammetric studies is represented by hanging mercury drop electrode (HMDE) [25].

Reference electrodes are used to establish well-defined potential against which working electrode potentials can be measured and they are of three types: aqueous and non-aqueous reference electrodes and quasi-reference electrodes. The most common aqueous reference electrode is the silver/silver chloride electrode (Ag/AgCl) because of the toxicity of the saturated calomel electrode (SCE) which contains mercury and the difficulty of using the standard hydrogen electrode (SHE) in routine activities [25]. For non-aqueous reference electrode the silver/silver ion (Ag/Ag^+) electrode is normally used while for quasi-reference electrodes, platinum, gold and Ag/AgCl wire are simply used.
The counter electrode said also auxiliary electrode is a necessary part of the circuit through which the voltammetric current flows. It has to be stable and non-reactive and must facilitate the passage of current with the aid of high surface area. Counter electrodes can also be spiral wire or glaze made of platinum or carbonaceous materials [25].
In figure (3.6.2) it is shown an electric circuit, named as potentiostat, that is the usual electrochemical setup for a voltammetric experiment [25]. In CV, the potential of working electrode is controlled by the use of a reference electrode through which almost no current has to flow during experiment.

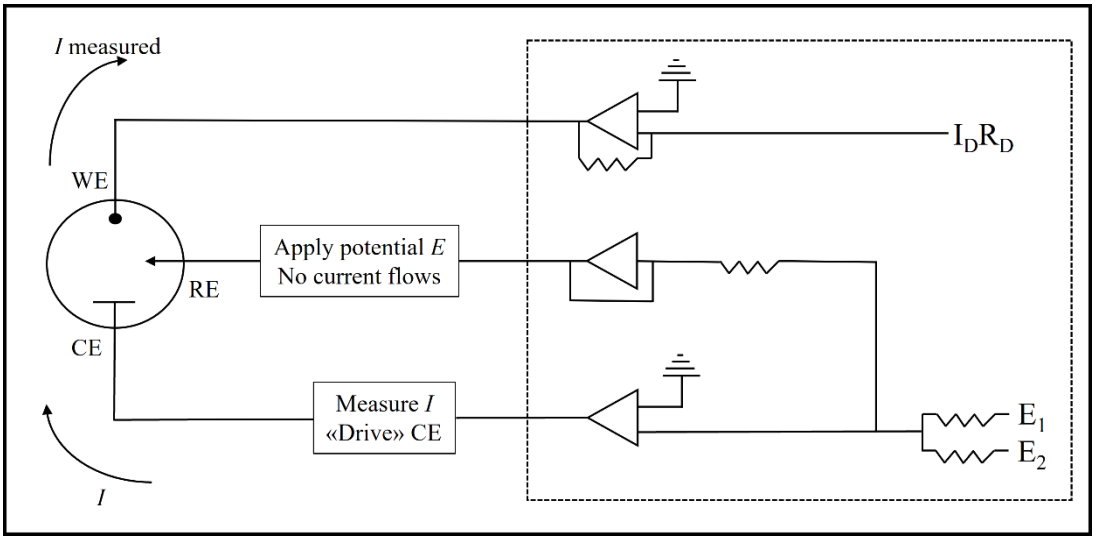

Figure 3.6.2. *Electronic representation of a simple Potentiostat connected to an electrochemical cell of three electrode configuration; WE, RE and CE stand for working electrode, reference electrode and counter electrode, respectively. Reproduced from reference [25].*

The experiment is conducted in an unstirred solution and the working electrode is stationary. The potential is then controlled linearly from a starting potential E_1 to a switching potential E_2 and from this point in the opposite direction to E_3 resulting in a triangular potential cycle as it is shown in figure (3.6.3) [25].

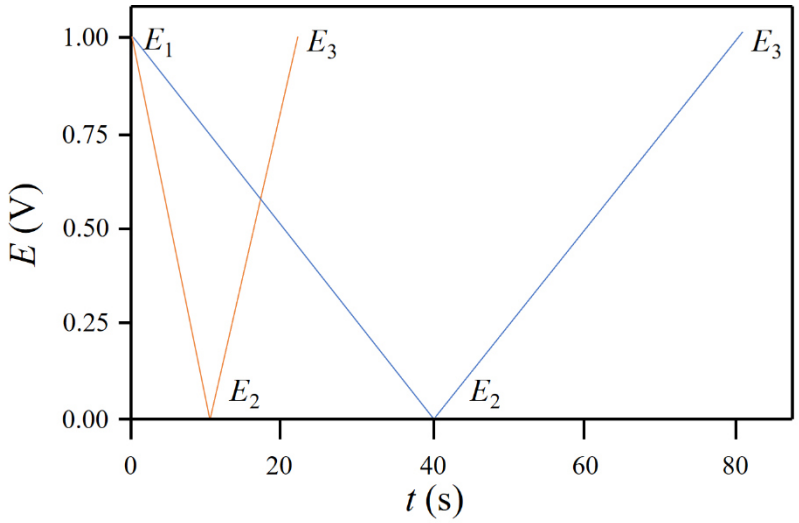

Figure 3.6.3. *Triangular potential cycle obtained at 100 mV s^{-1} for (a) and 25 mV s^{-1} for (b). Reproduced from reference [25].*

Conventionally in CV E_1 and E_3 have the same values. In a CV experiment, the resulting graph is the result of the summation of two potential ramps known as half-cycles (figure 3.6.4). One can perform multiple half-cycles or only one half-cycle depending on information needed. The potential scan rate of a CV experiment ($v = \delta E/\delta t$) is variable and affects its timescale, and for conventional experiments it ranges from few millivolts per second to several volts per second [25].

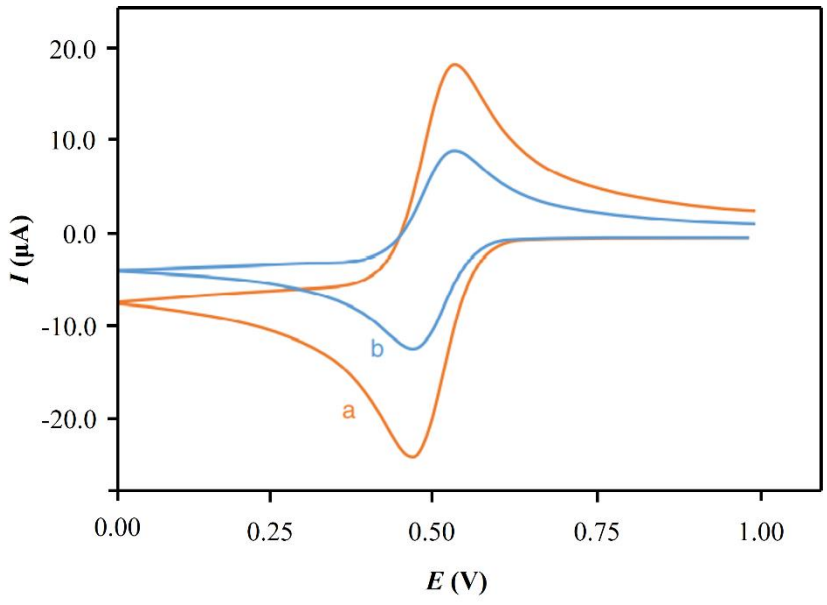

Figure 3.6.4. *Cyclic Voltammograms obtained at 100 mV s^{-1} for (a) and 25 mV s^{-1} for (b). The redox reaction is a one-electron reduction process. Reproduced from reference [25].*

In the cyclic voltammogram of a reversible electron transfer process, when only the oxidized (ox) form is present, the initial potential E_I is more positive than the formal

potential of the species $E^{0'}$ which is in turn more positive than the switching potential E_2. Then it results that the forward half-cycle is a negative going scan [25]. At this stage, it is possible to see of a cathodic peak due to the reduction of (ox) to a reduced form (red). Similarly, when a positive going scan is effectuated it is possible to see an anodic peak due to the re-oxidation of the previously obtained (red) form [25].

The ratio of the (ox) and (red) forms is proportional to the difference between the applied potential and $E^{0'}$ as it follows in the Nernst equation:

$$E - E^{0'} = \frac{RT}{nF} \ln \frac{[ox]}{[red]} \tag{3.6.1}$$

Where R is the gas constant (J K^{-1} mol^{-1}), T the absolute temperature (K), n the number of transferred electrons, and F Faraday's constant [25]. Furthermore, the difference in the concentration of the (ox) and (red) forms between the solution and on the surface of the electrode is responsible of a gradient of diffusion of the electroactive species governed by the Fick's laws as it can be seen in reference [25]. Together with some initially and boundary conditions these equations are the base for complicated mathematical representations of relationship between current and time or between current and potential that can be founded in literature [25].

However, the Randles and Sevcik equation relates the peak current (I_p, Amperes) to the concentration of the species as it follows:

$$I_p = -269An^{3/2}C_{ox}D_{ox}^{1/2}v^{1/2} \tag{3.6.2}$$

Where A is the surface area of the electrode (cm^2), n the number of transferred electrons, C_{ox} and D_{ox} are the concentration of species (mol cm^{-3}) and the diffusion constant of species (cm^2 s^{-1}) respectively, assumed that in the initial time there is only the (ox) form in solution, and v is the scan rate (V s^{-1}) [25]. A cyclic voltammogram for a reversible electrochemical reaction is shown in figure (3.6.5). It is usual in CV experiments to use the half-wave potential $E_{1/2}$ instead of the formal potential $E^{0'}$ [25].

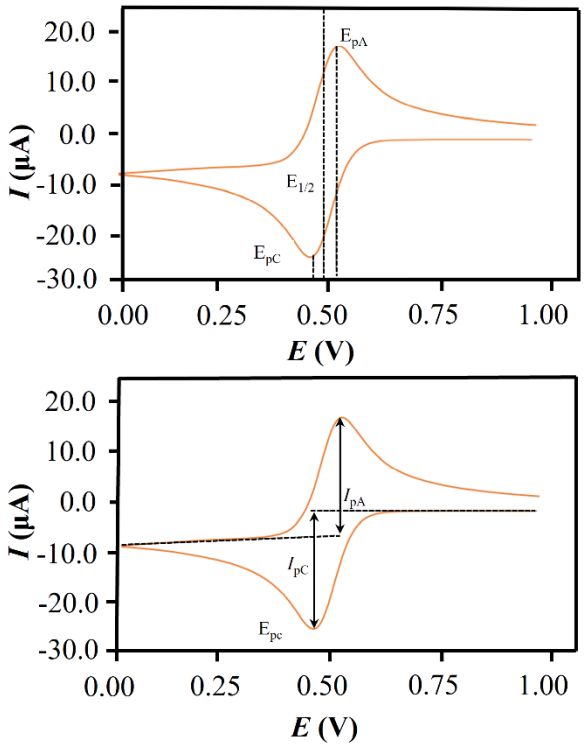

Figure 3.6.5. *Cyclic voltammogram for the reduction of 1 mM electroactive species with $E_{1/2}$ =0.5 V at scan rate of 100 mV s−1 for the characteristic potentials of a cyclic voltammograms (Top) and for the characteristic of peak currents (bottom), reproduced from reference [25].*

For a reversible redox process the averaged peaks potential of both oxidation and reduction processes is given by:

$$E_{1/2} = \frac{E_{pC}+E_{pA}}{2} \tag{3.6.3}$$

where E_{pC} and E_{pA} are the cathodic (reduction) peak potential and the anodic (oxidation) peak potential respectively [25]. For redox process where the (ox) and (red) forms have the same diffusion constant, the $E_{1/2}$ has the same value of $E^{0'}$.

3.7 UV-vis Spectroscopy

Ultraviolet(UV)-visible(vis) spectroscopy is part of the electronic spectroscopy that also includes photoelectron, electron energy loss and X-ray absorption spectroscopy. In electron spectroscopy, when the incident radiation interacts with a material, an energy quantum, the photon, may be absorbed resulting in an electronic transition without modification of the incoming radiation. The system can return in the ground state with emission of a photon or may be subjected to reflectance that is a combination of both emission and absorption [27]. If the incident radiation is coupled with an internal process, then the emitted photon has a different frequency and the quantized energy change is given by:

$$\Delta E = h\upsilon = hc/\lambda = hc\tilde{\nu} \quad (3.7.1)$$

where ν is the frequency of the radiation, h is the Planck constant, c is the speed of light in the vacuum and λ is the vacuum wavelength [27]. It is important to say that ν has the unity of nm while its reciprocal wavenumber $\tilde{\nu}$ has the unity of cm^{-1} and it is commonly used because of its very useful proportionality to the energy [27-28].

The UV and VIS ranges are normally between 200 – 400 nm (or 50 000 – 25 000 cm^{-1}) and between 400 – 800 nm (or 25 000 – 12 500 cm^{-1}) respectively [27].

When the incident radiation comes onto a single atom (a purely theorical hypothesis) a totally electronic transition can be obtained, while in the more realistic case of molecules, rotational and vibrational motions are also excited although the electronic transitions are more energetic than the other because two energetic levels are involved [27]. For this reason, it is the difference in electronic energy that mostly determines the position of a transition that involves all the electronic, rotational and vibrational states. However, in polyatomic molecules, again the most common case, the fine rotational structure is difficult to resolve and also the vibrational structure has to be taken in account, therefore the UV-vis spectra show bands instead of lines. The intensities of the bands are related to the absorbance or optical density that is defined mathematically by the Lambert-Beer law and describes the interaction between the radiation and matter:

$$A = \varepsilon c l \quad (3.7.2)$$

where c is concentration in mol L^{-1}, l is the pathway length in cm and ε is the extinction coefficient of the material (that has the units L mol^{-1} cm^{-1}).

Absorbance is also defined as follows:

$$A = \log_{10}(I_0/I) = \log_{10}(1/T) \tag{3.7.3}$$

that is:

$$T = I/I_0 \tag{3.7.4}$$

where T is the transmittance of the material and I represents the intensity of the radiation that has passed beyond the sample and I_0 represents the initial intensity of the radiation. Transmittance is often used as percent transmittance (= 100 T). Absorbance and percent transmittance are normally plotted versus wavelength (in nm) or versus wavenumber (in cm^{-1}) [27].

The transitions between different states are subjected to some selection rules related to the transition moment integral ($\int \psi_n^* \mu \psi_m d\tau$). In short, if the transition moment is zero then the transition is forbidden while any non-zero result means that the transition is allowed. A forbidden transition does not mean that the transition does not actually take place but rather defines its relative intensity that is much lower than an allowed transition [27]. The multiplicity of the states define the first selection rule for which $\Delta S = 0$. The second selection rule is related to the symmetry of the states and the direct product of the wave functions representing the two states must contain the totally symmetric representation. The third selection rule is valid for molecules with a centre of symmetry and is named as Laporte rule or parity rule: only transitions with a change of parity are allowed [27]. In figure (3.7.1) are shown the transitions according to the transition moment integral. The electrons can be promoted from the ground state S_0 (a singlet state) into higher electronic states (S_1, S_2) then some radiative, fluorescence and phosphorescence (forbidden process for the symmetry selection rule), and non-radiative, internal conversion and intersystem crossing, processes can take place [27].

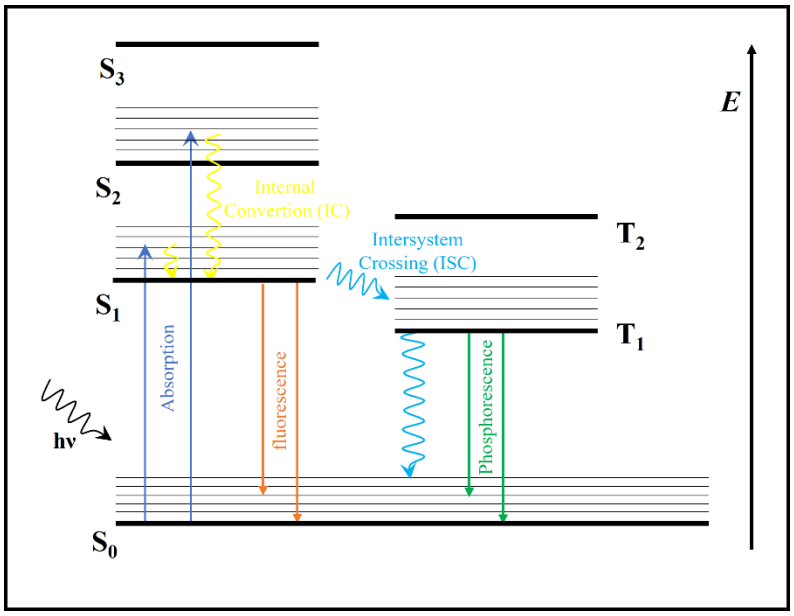

Figure 3.7.1. *Diagram of the electronic transition for a molecule. The radiative (fluorescence and phosphorescence) and non-radiative (IC, ISC) transitions are shown. S: singlet; T: triplet; S_0 is the ground state.*

According to molecular orbital theory (MO), electrons in polyatomic molecules are essentially s and p electrons that can occupy bonding orbitals, antibonding orbitals and non-bonding orbitals [27]. In the first case, the s-type electrons are named as σ electrons and the p-type electrons are named as π electrons. If the electrons occupy an antibonding orbital, then they are named as σ* and π*. The non-bonding electrons are named as n and the corresponding orbitals are generally between the bonding and antibonding orbitals[27]. There is no universal notation for electronic transitions, usually notation according to the MO representation, Mulliken notation and group theory notation are used (see table 3.7.1).

Notation	Symbols Ground states	Symbols Excited states	Examples
MO representation	σ, π, n	σ*, π*	$\sigma \rightarrow \sigma^*$ $\pi \rightarrow \pi^*$ $n \rightarrow \sigma^*$ $n \rightarrow \pi^*$
Mulliken	N	Q, V, R	$V \leftarrow N$ $Q \leftarrow N$ $R \leftarrow N$
Group Theory	Irred. repr. incl. multiplicity	Irred. repr. incl. multiplicity	$^1A_1 \leftarrow {}^1A_1$ $^1B_2 \leftarrow {}^1A_1$ $^1E_{1u} \leftarrow {}^1A_{1g}$

Table 3.7.1. *Different notations for electronic transitions. Reproduced from reference [27].*

3.6 References

[1] D.A. Long, *Raman Spectroscopy*, **McGraw-Hill, Inc., New York** (1977).

[2] R.L. McCreery, *Raman Spectroscopy for Chemical Analysis*, **John Wiley & Sons, New York** (2000).

[3] D.A. Long, *The Raman Effect*, **John Wiley & Sons, Chichester** (2002).

[4] R.S. Krishnan, R.K. Shankar, *Raman Effect: History of the Discovery*, **J. Raman Spectrosc., 10** (1981).

[5] M. Diem, *Introduction to Modern Vibrational Spectroscopy*, **John Wiley & Sons, New York** (1993).

[6] R. Loudon, *The quantum theory of light,* **Oxford University Press, Oxford** (1973).

[7] M. Castriota, *Development and Spectroscopic Charcaterization of Materials for Applications in Electrochromic Devices and Novel Liquid Crystalline Cells*, **PhD thesis in Sciences and Technologies of the Mesophases and of the Molecular Materials, XVI° Cycle**, Academic year 2003 – 2004.

[8] C. Kittel, *Introduction to Solid State Physics*, **John Wiley & Sons, New York** (1995).

[9] R. Merlin, A. Pinczuk, W.H. Weber, *in Raman Scattering in Material Science*, **edited by W.H. Weber and R. Merlin, Springer, Berlin,** (2000).

[10] M. Fleischmann, P.J. Hendra, A.J. McQuillan, *Raman Spectra of Pyridine Adsorbed at a Silver Electrode*, **Chem. Phys. Lett., 26** (1974), 163 – 166.

[11] M.G. Albrecht, J.L. Creighton, *Anomalously Intense Raman Spectra of Pyridine at a Silver Electrode*, **J. Am. Chem. Soc., 99** (1977), 5215 – 5217.

[12] D.L. Jeanmaire, R.P. Van Duyne, *Heterocyclic, Aromatic, and Aliphatic Amines Adsorbed on the Anodized Silver Electrode*, **J. Electroanal. Chem., 84** (1997), 1 – 20.

[13] S. Nie, S.R. Emory, *Probing Single Molecules and Single Nanoparticles by Surface-Enhanced Raman Scattering*, **Science, 275** (1997), 1102 – 1106.

[14] K. Kneipp, Y. Wang, H. Kneipp, L.T. Perelman, I. Itzkan, R.R. Dasari, M.S. Feld *Single Molecule Detection Using Surface-Enhanced Raman Scattering (SERS)*, **Phys. Rev. Lett., 78** (1997), 1667 – 1670.

[15] D. Grasseschi, H.E. Toma, *The SERS effect in coordination chemistry*, **Coord. Chem. Rev., 333** (2017), 108 – 131.

[16] P.G. Etchegoin, C. Galloway, E.C. Le Ru, *Polarization-dependent effects in surface-enhanced Raman scattering (SERS)*, **Phys. Chem. Chem. Phys., 8** (2006), 2624 – 2628.

[17] D.S. Kim, A. Honglawan, S. Yang, D.K. Yoon, *Arrangement and SERS Applications of Nanoparticle Clusters Using Liquid Crystalline Template*, **ACS Appl. Mater. Interfaces, 9** (2017), 7787 – 7792.

[18] H. Ko, S. Singamaneni, V.V. Tsukruk, *Nanostructured Surfaces and Assemblies as SERS Media*, **Small, 4** (2008), 1576 – 1599.

[19] W. Xie, P. Qiu, C. Mao, *Bio-imaging, detection and analysis by using nanostructures as SERS substrates*, **J. Mater. Chem., 21** (2011), 5190 – 5202.

[20] E. Lopez-Tobar, B. Hernández, A. Chenal, Y.M. Coïc, J.G. Santos, E. Mejia-Ospino, J.V. Garcia-Ramos, M. Ghomi, S. Sanchez-Cortes, *Large size citrate-reduced gold colloids appear as optimal SERS substrates for cationic peptides*, **J. Raman Spectrosc., 48** (2017), 30 – 37.

[21] L.A. Lane, X. Qian, S. Nie, *SERS Nanoparticles in Medicine: From Label-Free Detection to Spectroscopic Tagging*, **Chem. Rev., 115** (2015), 10489 – 10529.

[22] P.L. Stiles, J.A. Dieringer, N.C. Shah, R.P. Van Duyne, *Surface-Enhanced Raman Spectroscopy*, **Annu. Rev. Anal. Chem., 1** (2008), 601 – 626.

[23] S. Schlükler, *Surface-Enhanced Raman Spectroscopy: Concepts and Chemical Applications*, **Angew. Chem. Int., 53** (2014), 4756 – 4795.

[24] G. Turrell, J. Corset, *Raman Microscopy: Developments and Applications*, **Academic Press, San Diego,** (1996).

[25] L. Khalafi, M. Rafiee, *Cyclic Voltammetry*, in Z. Wang, *Encyclopedia of Physical Organic Chemistry*, **John Wiley & Sons** (2017), .

[26] N. Elgrishi, K.J. Rountree, B.D. McCarthy, E.S. Rountree, T.T. Eisenhart, J.L. Dempsey, **J. Chem. Educ., 95** (2018), 197 – 206.

[27] H. Förster, *UV/VIS Spectroscopy*, In: H.G. Karge, J. Weitkamp, *Characterization I. Molecular Sieves* – **Science and Technology, vol 4. Springer, Berlin, Heidelberg,** (2004), 337 – 426.

[28] D.C. Harris, M.D. Bertolucci, *Symmetry and Spectroscopy*, **Oxford University Press**., (1978).

Chapter 4

Results and discussion

The first part of the chapter deals with spectroscopic studies of different materials that can have a positive impact on the performance of ECDs both from a working performances point of view and on the manufacture of devices. In fact, the use of electrolytic polymers can increase the performance of ECDs as well as the use of natural polymers can result in a better green and environmentally sustainable impact. For these reasons, following works on different materials have been conducted:

- Poly methyl methacrylate (PMMA)-based polymer electrolytes have been realised and characterized by Raman spectroscopy.
- It is shown the Raman analysis of blends of PMMA and polyethylene glycol (PEO) in different proportions.
- The Raman characterization of a blend made with folic acid and a polymer consisting in methacrylic acid (MAA) and ethylene glycol di-methacrylate (EGDMA) has been conducted.
- The effect of multiple layers of Poly(allylamine hydrochloride) (PAH) and Poly(styrenesulfonate) (PSS) polyelectrolyte in combination with gold nanoparticles applied on glass on the Raman response of a 10% acetic acid solution (v/v) is reported.
- It is shown the Raman spectroscopic study of the interaction in Chitosan polymer films and inorganic complex.
- The effect of Ag layer on the Raman response of Rhodamine 6G has been studied.
- It is shown the SERS effect of gold nanoparticles on the Raman spectrum of bipyridine sample.
- The Raman characterization of functionalised Graphite is reported.
- It is shown the Raman spectroscopic investigation of Graphene nano-plates on Silica support.
- The Raman characterization of TiO_2 films has been made.

In the second part of the chapter, the realization of an electrochromic device made with the use of a viologen, ferrocene and bisphenol A glycerolate is reported. The devices have been characterized by Raman spectroscopy and their optical properties have been studied by UV-vis Spectroscopy. Furthermore, the electronic properties of the devices have been investigated by cyclic Voltammetry.

4.1 Raman spectroscopic study of polymer electrolyte layer based on PMMA

Polymeric electrolytes are of great importance in the fabrication of electrochromic devices because of their possibility to be used as ion conductor between electrodes of the device [1-4]. In this study, a series of polymethylmethacrylates (PMMA) with different averaged molecular weights were used to obtain several electrolyte solutions (ES) for prospective Electrochromic Devices (ED) application. The first part of the study is focused on the research of the best Lithium-based electrolyte solution. The polymethylmethacrylates were dissolved in chloroform and then mixed with an ES made of $LiClO_4$ in propylene carbonate and bisphenol A glycerolate diacrylate (BPA).

The Raman spectra of the single components were acquired and discussed and successively the Raman spectra of the PMMA-based ES before and after polymerization. The polymerization was performed with the aid of the photo initiator *Irgacure 651* in small quantities with respect to the BPA's weight.

In the second part of the study six PMMA-based ES were made with use of $LiClO_4$ and CF_3SO_3Li (triflate) without the use of generally unsuitable organic solvents (like $CHCl_3$) due to known environmental problems. The PMMA-based ES were then analysed by Raman spectroscopy.

In figure (4.1.1) are shown the molecular structures of all the above-mentioned components of the mixtures obtained.

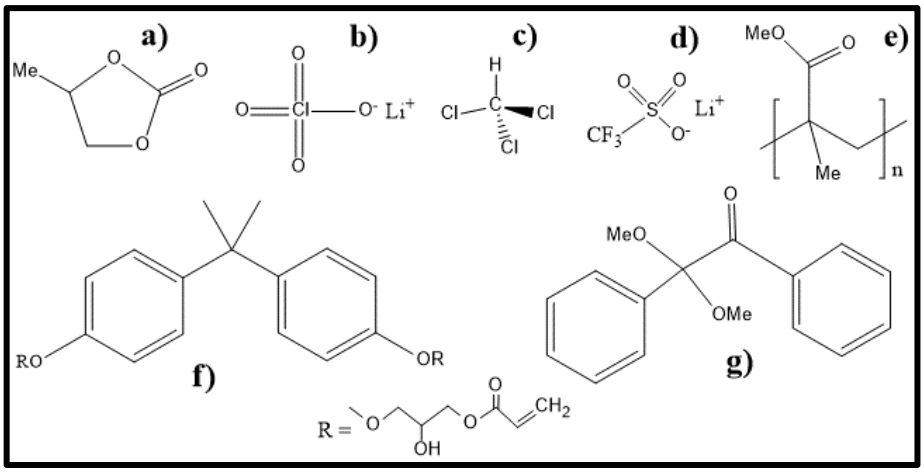

Figure 4.1.1. *Molecular structure of. a) propylene carbonate (PC); b) lithium perchlorate ($LiClO_4$); c) Chloroform ($CHCl_3$); d) lithium trifluoromethanesulfonate (triflate, CF_3SO_3Li); e) polymethylmethacrylate (PMMA); f) bisphenol A glycerolate diacrylate (BPA); g) 2,2-dimethoxy-2-phenylacetophenone (Irgacure 651).*

4.1.1 Experimental

All chemicals were purchased from Sigma-Aldrich®. The Lithium electrolyte solution (ES) were prepared from an $LiClO_4$ 1M solution in propylene carbonate (PC) and Bisphenol A glycerolate (1 glycerol/phenol) diacrylate (BPA) with 2% in weight of Irgacure 651. Four preliminary ES were prepared, with the weight percentages summarized in table (4.1.1) (left). They were evaluated on the basis of repeatability and ease of handling. Identified the best solution among them (through the evaluation of ease of handling), other 4 solutions were progressively prepared with percentages in table (4.1.1) (right).

	$LiClO_4$ 1M in PC	**BPA (2% Irgacure)**		**LiClO4 1M in PC**	**BPA (2% Irgacure)**
ES 1	20%	80%	**ES 5**	55%	45%
ES 2	40%	60%	**ES 6**	45%	55%
ES 3	60%	40%	**ES 7**	70%	30%
ES 4	80%	20%	**ES 8**	50%	50%

Table 4.1.1: ***Weight percentages of electrolyte solutions (ES).***

The dispositive displayed in figure (4.1.2) were prepared with the ES 3, 4 and 5. As already mentioned, dissolving a polymer in an electrolyte solution may reach its conductivity, however in this case, solid PMMA were first dissolved in chloroform (20%, 30% and 40% by weight solutions for PMMA

996000 Gel Permeation Chromatography (GPC), 120000 GPC and 15000 GPC respectively, called 996, 120 and 15 below) in order to obtain a transparent gel, Fig. (4.1.3), the only solution of PMMA 15 seems to assume a slightly opaque transparency). The solutions thus reached were mixed with the best electrolyte solution (ES 5: 55% of $LiClO_4$/45% of BPA) in proportion 1:1, Fig. (4.1.4). With these solutions three cells were prepared, Fig. (4.1.5).

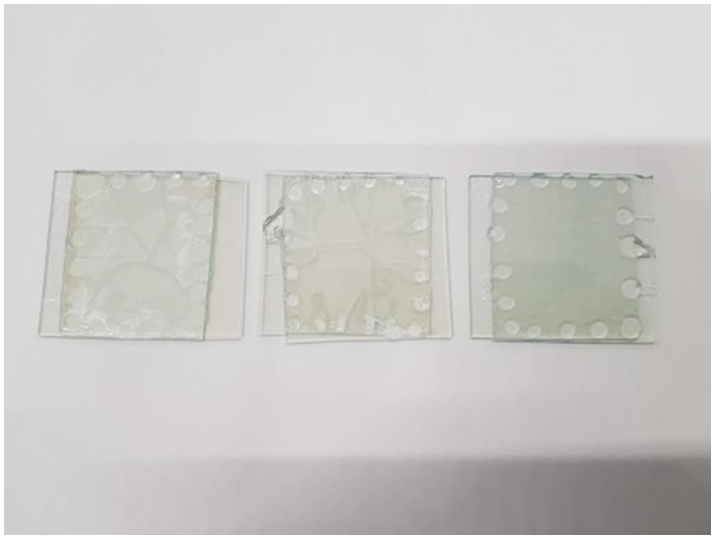

Figure 4.1.2. *Dispositive realized with electrolyte solutions; from left to right 60%, 80% and 55% in weight of $LiClO_4$.*

Figure 4.1.3. *PMMA's solutions in $CHCl_3$.*

Figure 4.1.4. *Electrolyte solutions 1:1 with PMMA's solutions: PMMA 996 on the left, PMMA 120 in the middle and PMMA 15 on the right*.

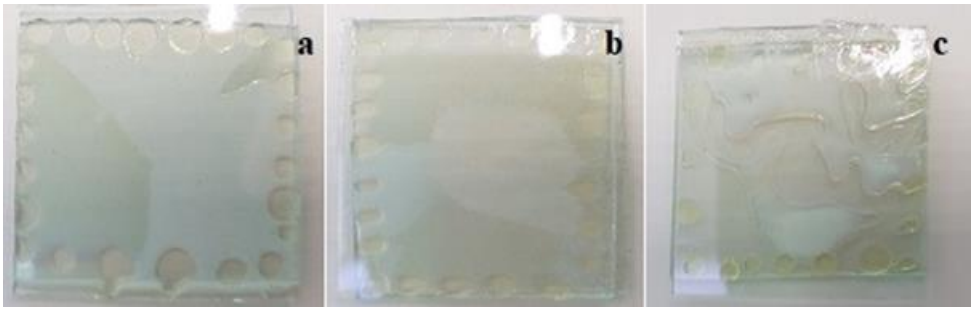

Figure 4.1.5. *Devices made with PMMA ES, a) PMMA 15, b) PMMA 120, c) PMMA 996*.

The solution with PMMA 996 was difficult to process due to its high viscosity, then the cell obtained with it wasn't homogeneous and was really hard to obtain. All the cells were exposed to UV radiation under a UV lamp (from Jelosil, HG 200 L model, optical power per unit area 0,043 W/cm^2) and then cured for about 1 minute and a half. As showed in figure (4.1.6), after polymerization ES inserted into the cell takes the form of a solid film on ITO surface.

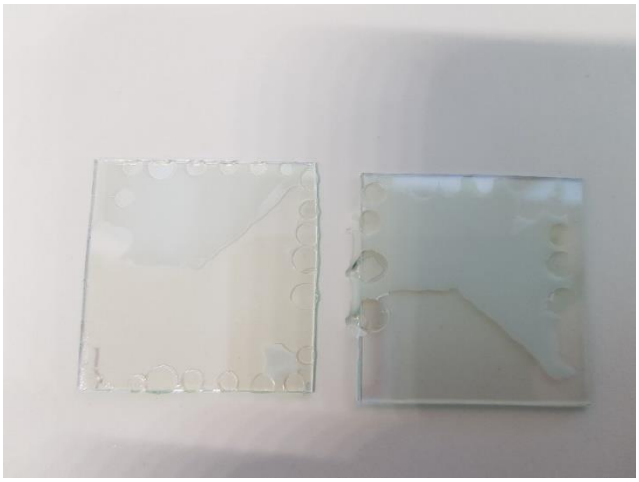

Figure 4.1.6. *ES take a solid film form on ITO surface after polymerization.*

Raman spectroscopy measurements were performed by using a microRaman-LABRAM (from Jobin Yvon Srl-Horiba), equipped with an optical microscope, in order to collect Raman spectra from small regions of the sample, such as 2-5µm. Raman measurements were all performed with a 532 nm green laser source (with a power in output of 50 mW), using generally optical filter D03. Every spectrum recorded is a result of several acquisitions (up to 25).

In the second part of the experiment, six PMMA-based ES were prepared. As before, all chemicals were purchased from Sigma-Aldrich®. The solutions were all prepared with 10% by weight of PMMA dissolved directly in a solution 1M of Lithium perchlorate in propylene carbonate or in a solution 1M of Lithium trifluoromethanesulfonate. In particular, we have used the same PMMA used previously: PMMA 15000 GPC, PMMA 120000 GPC and PMMA 996000 GPC. The table (4.1.2) summarize the details of each realized solution.

PMMA 10% by weight	**$LiClO_4$ 1M solution**	**$LiCF_3SO_3CH_3$ 1M solution**
15000 GPC	ES (1)	ES (4)
120000 GPC	ES (2)	ES (5)
996000 GPC	ES (3)	ES (6)

Table 4.1.2. *Details of the components of the prepared solutions.*

The solution, as already mentioned, were prepared by dissolving the pre-calculated quantities of PMMA in the saline solutions of propylene carbonate made previously. In this step, the PC solutions were increased to 100°C to improve the dissolution of the

PMMA. At room temperature the solutions obtained were inhomogeneous and the dissolution was difficult. The prepared solutions were used to made six dispositive and analysed by Raman spectroscopy. Raman spectroscopy measurements were performed by using the aforenoted microRaman-LABRAM. Raman measurements were allperformed with a 532 nm green laser source (with a power in output of 50 mW), using generally optical filter D03. Every spectrum recorded is a result of several acquisition (up to 30).

4.1.2 Results and discussion

First, the Raman spectra of single components showed in figure (4.1.1) were acquired. The Raman spectrum of BPA and irgacure were acquired together because of the negligible concentration of the last one respect to all the other components of the ES. The first range Raman spectrum of PC is showed in figure (4.1.7.a) and the second range is showed in figure (4.1.7.b). All the characteristic Raman bands of Propylene Carbonate are visible. They are given in table (4.1.3) together with assignments and references

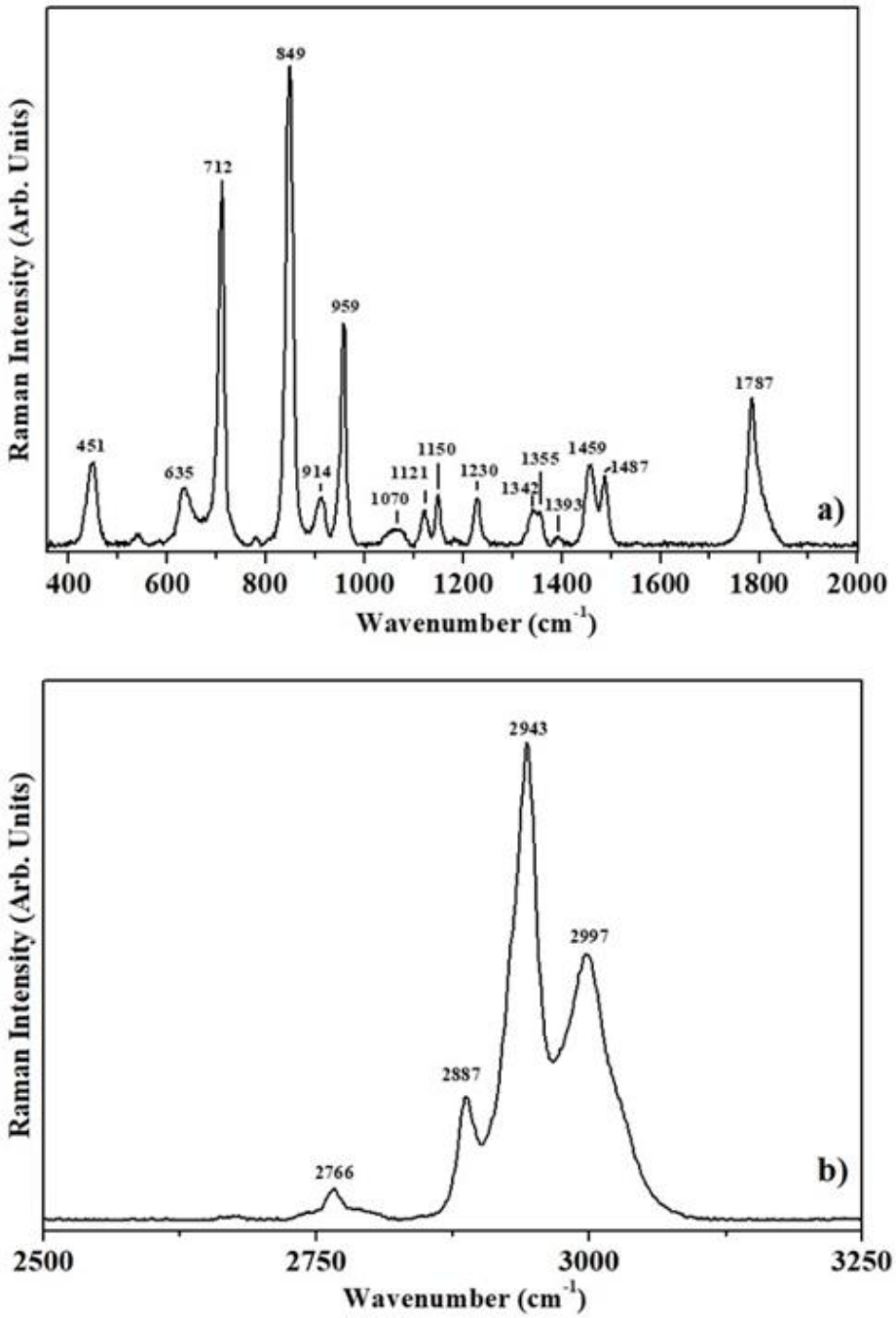

Figure 4.1.7. *Raman spectrum of Propylene Carbonate, a) first range (350 – 2000 cm^{-1}); b) second range (2500 – 3250 cm^{-1}).*

Frequency (cm^{-1})	Assignments	References	Frequency (cm^{-1})	Assignments	References
	Bending 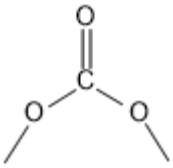				
451		[5]	1342	Bending (CH_3)	[6]
	Ring deformation	[6]			
635			1355	Bending (CH_3)	[5] [6]
712	Symmetric ring deformation	[5] [6] [7]	1393	Wagging ($–OCH_2$) Bending (CH_3)	[5] [6] [6]
849	Symmetric ring vibration + (CH_3) and (O–C–C) bending	[5] [6]	1459	Asymmetric bending (CH_3)	[5]
914			1487	Bending ($–OCH_2$) (CH_3) umbrella	[5] [6]
	Symmetric stretching 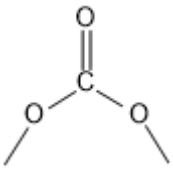				
959		[5]	1787	(C=O) stretching	[5] [6]
1070			2766	(C–H) stretching	[5] [6]
1121	(CH_3) wagging + (C–H) bending	[6]	2887	($C–H_2$) stretching	[5] [6]
1150	(C–C) + (C–O) stretching	[6]	2943	($C–H_3$) stretching	[5] [6]
	Asymmetric stretching 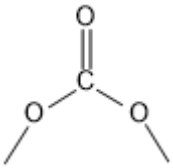				
1230		[5]	2997	($C–H_3$) stretching	[5] [6]

Table 4.1.3. *Raman vibrational modes and assignments of propylene carbonate*.

The Raman spectrum acquired on solid crystalline $LiClO_4$ is shown in figure (4.1.8). The observed Raman bands are given in table (4.1.4).

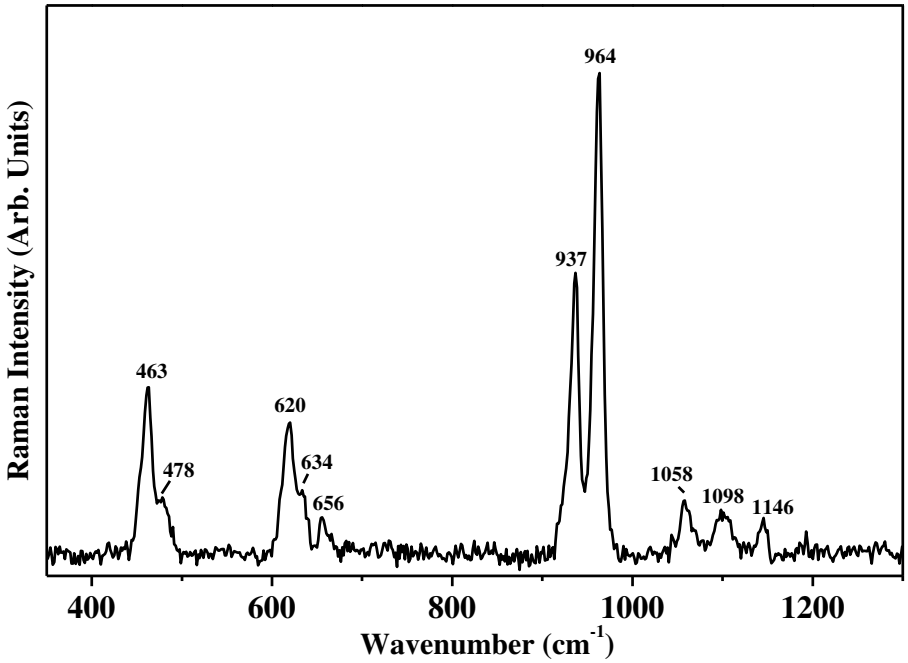

Figure 4.1.8. *Raman spectrum of crystalline $LiClO_4$ in the range 350 – 1300 cm^{-1}.*

Frequency (cm^{-1})	Assignments [a]	reference
463	v_2 (A')	[8]
478 (sh)	v_2	[8]
620	v_4 (A')	[8]
634 (sh)	v_4	[8]
656	v_4	[8]
937	v_1 (A_1)	[8]
964	v_1 (A')	[8]
1058	v_3 (A'')	[8]
1098	v_3 (A' ^{37}Cl)	[8]
1146	v_3 (A')	[8]

Table 4.1.4. *Observed Raman bands of crystalline $LiClO_4$.* sh: shoulder. [a] *v: stretching.*

The Raman spectrum of liquid chloroform is presented in figure (4.1.9). The characterist Raman bands are summarized in table (4.1.5), the assignments and relative references are also given.

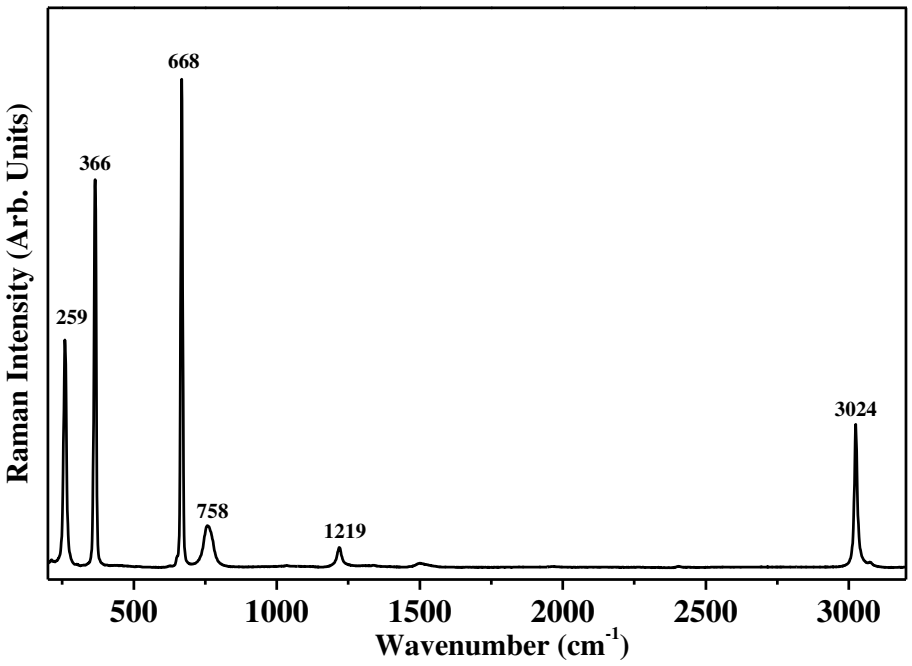

Figure 4.1.9. *Raman spectrum of liquid chloroform in the range 250 – 3200 cm^{-1}.*

Frequency (cm^{-1})	Assignments [a]	reference
259	deg v_6	[9]
366	sym v_3	[9]
668	sym v_2	[9]
758	deg v_5	[9]
1219	deg v_4	[9]
3024	sym v_1	[9]

Table 4.1.5. *Observed Ramab bands of $CHCl_3$ and their assignment. [a] deg: 2 fold degenerate; sym: symmetric.*

The Li–Triflate salt is very hygroscopic and tends to form a solution absorbing water from air in few hours. The Raman spectrum of the solution is quite different from the one of the crystalline salt. The Raman spectrum aquired on solid CF_3SO_3Li is shown in figure (4.1.10). In table (4.1.6) the observed Raman bands and their attribution are given together with the references. The band appearing at 1070 cm^{-1} is ascribable to the $CF_3SO_3^-$ anion of the lattice [10].

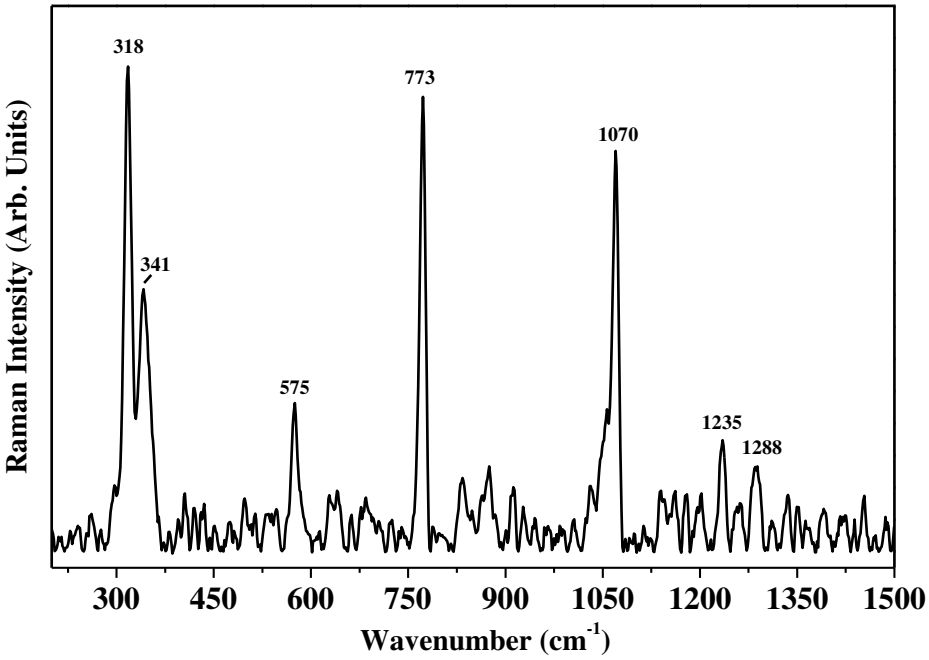

Figure 4.1.10. *Raman spectrum of solid CF_3SO_3Li in the range 200 – 1500 cm^{-1}. The spectrum has been digitally smoothed.*

Frequency (cm^{-1})	Assignments [a]	references
318	ν (C–S)	[10]
341	E (SO_3)	[10]
575	δ_{sym} (SO_3)	[10]
773	δ_{sym} (CF_3)	[10-12]
1070	ν_{sym} (SO_3)	[10-13]
1235	ν_{sym} (CF_3)	[10-12]
1288	ν_{asym} (SO_3)	[12] [13]

Table 4.1.6. *Observed Ramab bands of CF_3SO_3Li and their assignment. [a] δ_{sym}: symmetric deformation; ν_{sym}: symmetric stretching, ν_{asym}: asymmetric stretching.*

The Raman spectra of crystalline PMMA 15000 GPC, 120000 GPC and 996 GPC are shown in figures (4.1.11), (4.1.12) and (4.1.13) respectively. These spectra are quite similar. The only differences between the three spectra involve weak Raman bands in the range 1600 – 1650 cm^{-1} that could be attributed to combination bands of (C=C) and (C–COO) [14]. The observed Raman bands and their attribution are reported in table (4.1.7) together with references.

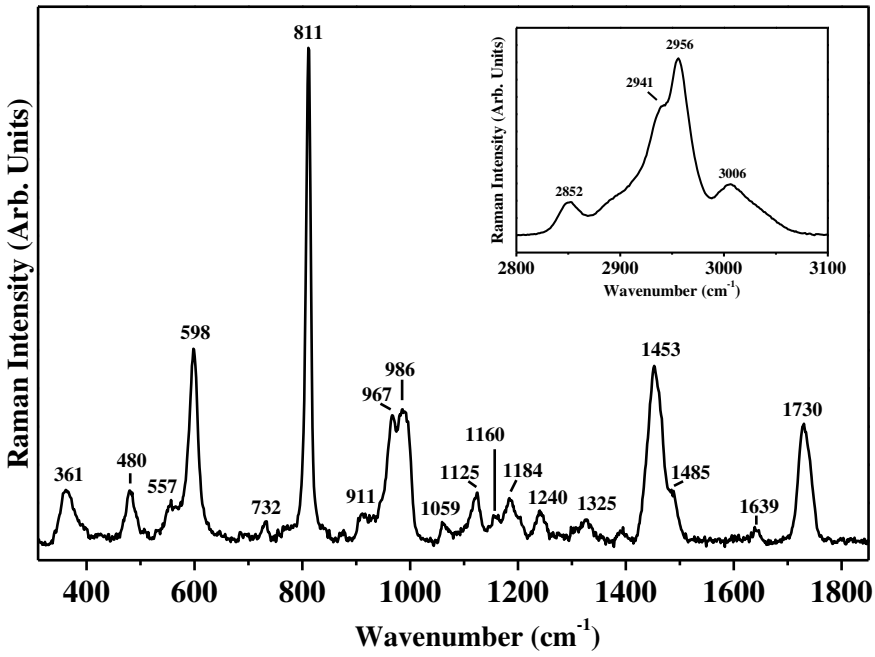

Figure 4.1.11. *Raman spectrum of crystalline PMMA 15000 GPC in the range 310 – 2000 cm^{-1} and 2800 – 3100 cm^{-1} in the inset.*

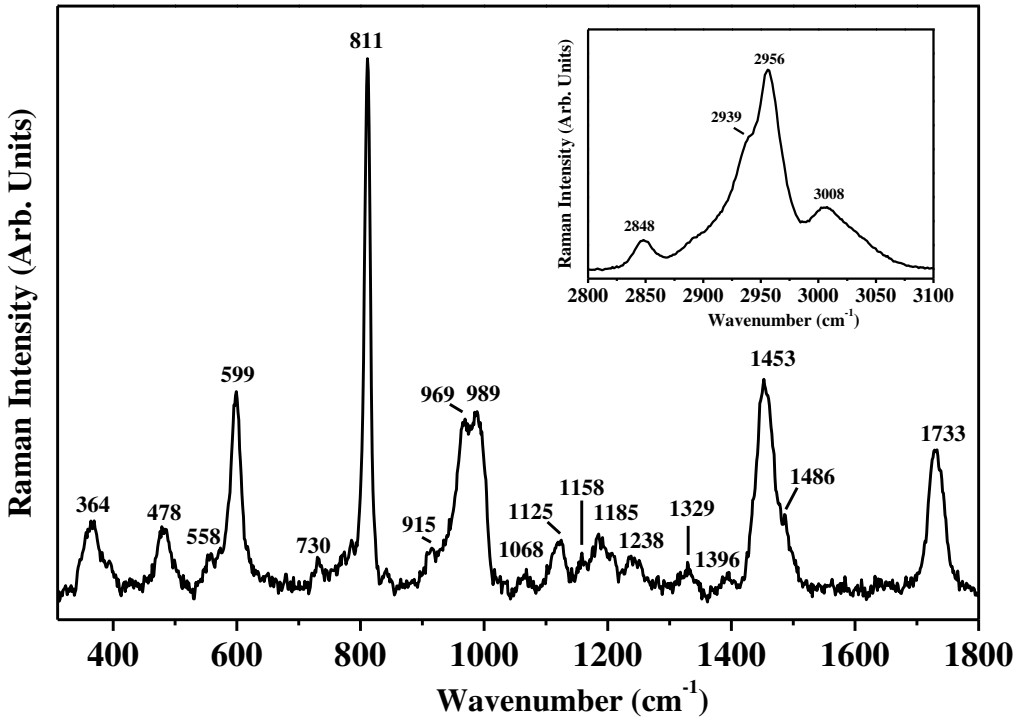

Figure 4.1.12. *Raman spectrum of crystalline PMMA 120000 GPC in the range 310 – 2000 cm^{-1} and 2800 – 3100 cm^{-1} in the inset.*

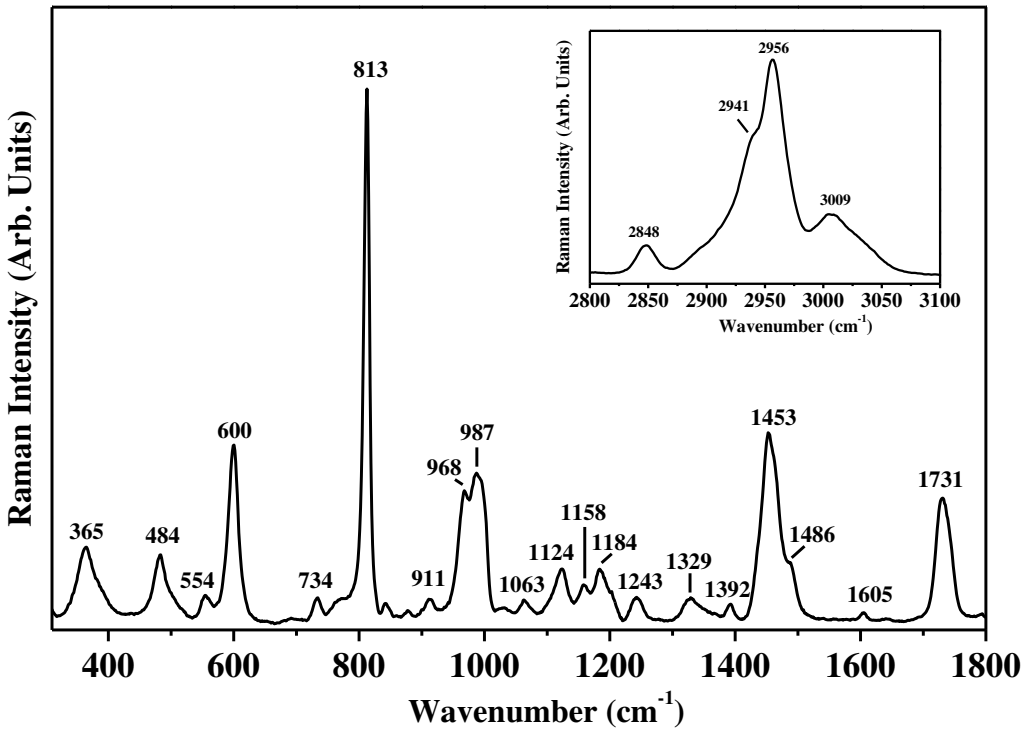

Figure 4.1.13. *Raman spectrum of crystalline PMMA 996000 GPC in the range 310 – 2000 cm^{-1} and 2800 – 3100 cm^{-1} in the inset.*

Frequency (cm^{-1})			Assignments [a]	references
PMMA15	**PMMA120**	**PMMA996**		
			δ_{sym} in plane 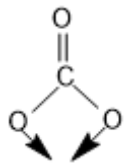	
361	364	365		[15][16]
			out-of-plane deformation 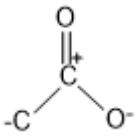	
480	478	484		[15][16]
557	558	554	δ(C–C–C) skeletal	[15]
			ν_{sym}(C–C–O) 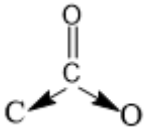	
598	599	600		[14-16]
732	730	734	ν(C–C) skeletal	[15]
811	811	813	ν_{sym}(C–O–C)	[15][16]
911	915	911		
967	969	968	α–CH_3 rock	[15]
986	989	987	O–CH_3 rock	[14-16]
1059	1068	1063	ν(C–C) skeletal	[14-16]
1125	1125	1124	ν(C–C) skeletal	[15]
1160	1158	1158	ν_{asym}(C–O–C–)	[15]
1184	1185	1184	ν(C–C) skeletal	[15]
			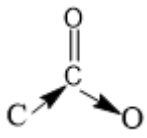 or C–O strech	
1240	1238	1243		[15]
1325	1329	1329		
	1396	1392	δ_{sym}(C–H) of α–CH_3	[15]
1453	1453	1453	δ_{asym}(C–H) of α–CH_3	[14][15]

Table 4.1.7. *Observed Raman bands of PMMA and their assignments. [a] ν: stretching, δ: bending, sym: symmetric, asym: antisymmetric.*

Frequency (cm^{-1})			Assignments [a]	references
PMMA15	**PMMA120**	**PMMA996**		
1485	1486	1486		
		1605		
1639			Combination band of (C–COO)	[14]
1730	1733	1731	C=O stretching	[15][16]
2852	2848	2848	Combination band of ($O–CH_3$)	[14][15]
2941	2939	2941		
2956	2956	2956	ν_{sym} (C–H) of ($O–CH_3$) and of ($\alpha–CH_3$) + ν_{asym} (CH_2)	[14][15]
3006	3008	3009	ν_{asym} (CH) of ($O–CH_3$) and of ($\alpha–CH_3$)	[14][15]

Table 4.1.7. (continued) *Observed Raman bands of PMMA and their assignments. [a] v: stretching, δ: bending, sym: symmetric, asym: antisymmetric.*

The last two components of the ES were analysed together because of the negligible concentration of Irgacure respect to the BPA. The figure (4.1.14) shows the Raman spectra acquired on BPA (a) and on BPA with 2% by weight of Irgacure (b). Considering the nature of Irgacure that is a photo initiator (indeed it is very sensible to sunlight), in spectrum (b) the phenomenon of luminescence has been very hight. As expected, the Raman spectra are very similar except for the shape of the bands in the region between 1230 – 1300 cm^{-1} and 1450 – 1515 cm^{-1}. In spectrum b) the band ascribable to skeletal vibration appear at 1001 cm^{-1}, the same band is not present in spectrum a). Raman bands are summarised in table (4.1.8).

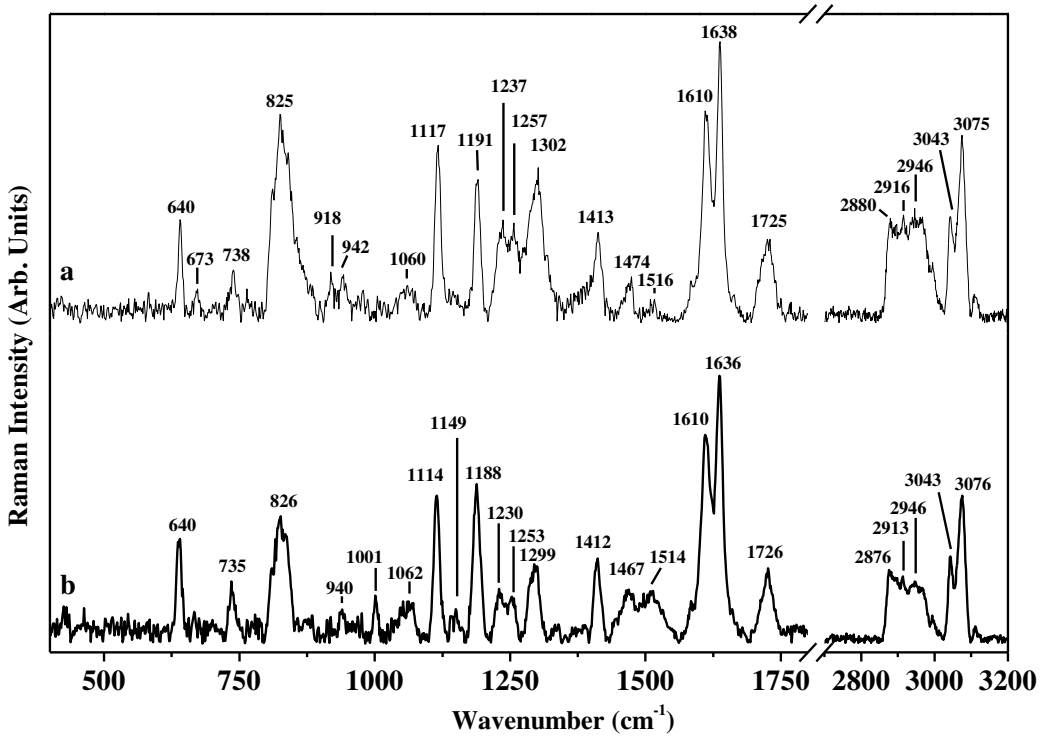

Figure 4.1.14. *Raman spectrum of BPA (a) and BPA + 2% by weigth of Irgacure (b) in the range 400 – 3200 cm^{-1}, the x-axis shows a break between 1800 and 2700 cm^{-1} because no Raman bands have been observed in this region.*

Frequency (cm^{-1})		Assignments [a]	reference
BPA	BPA + Irgacure		
640	640	Aromatic (C–H) out of plane def.	[12][17]
673		Aromatic (C–H) out of plane def.	[12][17]
738	735	(C–C) skeletal	[17]
825	825	Substituted aromatic out of plane def.	[12][17]
918			
942	940	($=CH_2$) wagging	[12]
	1001	skeletal vibration	[12]
1060	1062		
1114	1117	sym stretching (=C–O–C)	[12]
	1149		
1191	1188	(CH_3)/gem-dimethyl def. (C–C) stretching	[17]
1237	1230	(C–O) stretching and phenolic (C–O) stretching	[17]
1257	1253		
1302	1299	asym stretching (=C–O–C)	[12] [17]
1413	1412	($=CH_2$) def.	[12]
1474	1467	bending (C–H)	[12]
1516	1514		
1610	1610	Aromatic ring stretching vibration	[12][18-20]
1638	1636	Vinyl (C=C) stretching	[12][18-22]
1725	1726	(C=O) stretching	[12][20-22]
2880	2876	(CH_2) v_{sym}	[21]
2916	2913	(CH_2) v_{asym}	[12][21]
2946	2946	(CH_3) stretching	[12][21]
3043	3043	(=C–H) stretching	[12]
3075	3076	(=C–H) stretching	[12][22]

Table 4.1.8. *Observed Raman bands of BPA and Irgacure and their assignments. [a] sym: symmetric, asym: antisymmetric, def.: deformation.*

The Raman spectra acquired on the ES of figure (4.1.4) are shown in successive figures. Figure (4.1.15) shows the spectrum of ES made with PMMA 15, figures (4.1.16) and (4.1.17) show the spectra of ES made with PMMA 120 and PMMA 996 respectively.

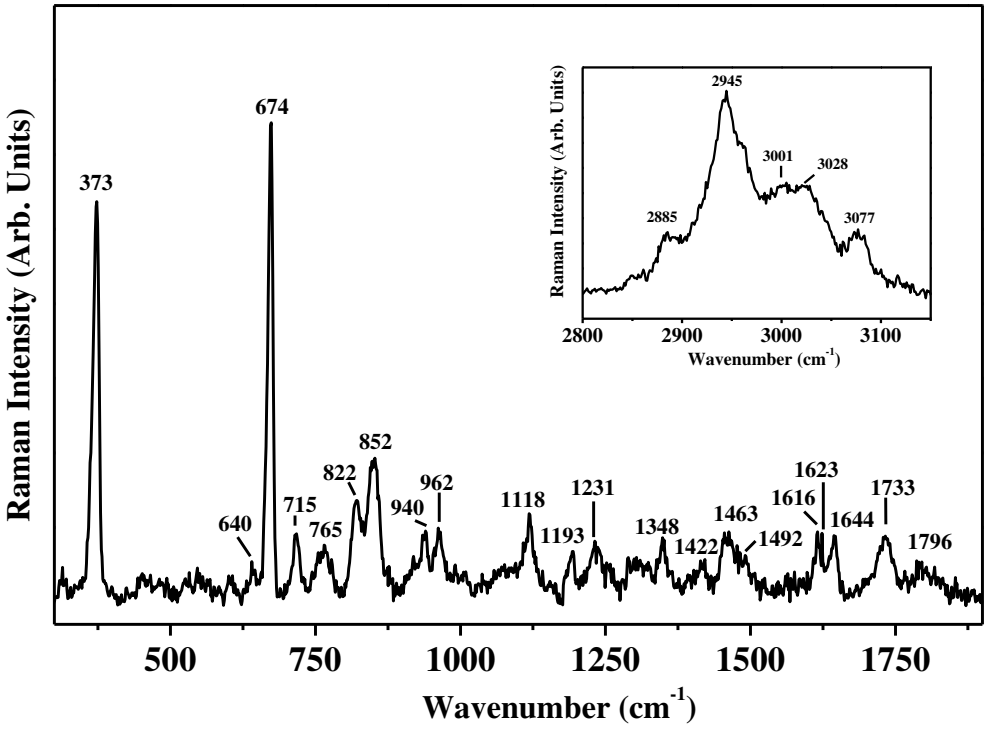

Figure 4.1.15. *Raman spectrum of ES made with PMMA 15 in the range 300 – 1900 cm^{-1} and 2800 – 3150 cm^{-1} in the inset.*

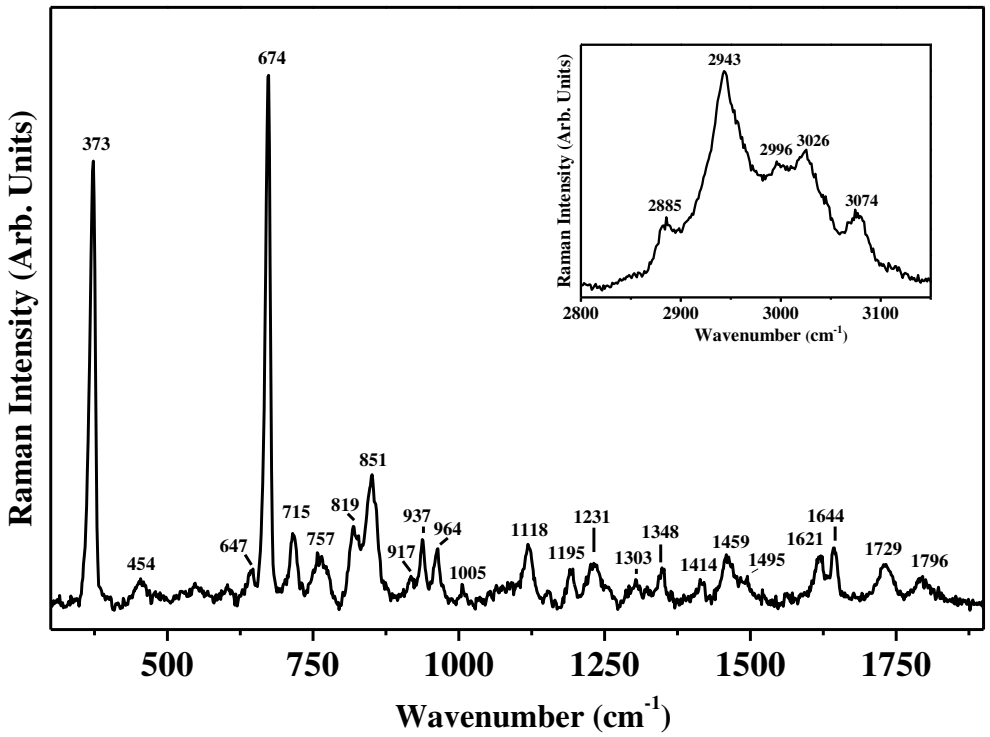

Figure 4.1.16. *Raman spectrum of ES made with PMMA 120 in the range 300 – 1900 cm^{-1} and 2800 – 3150 cm^{-1} in the inset.*

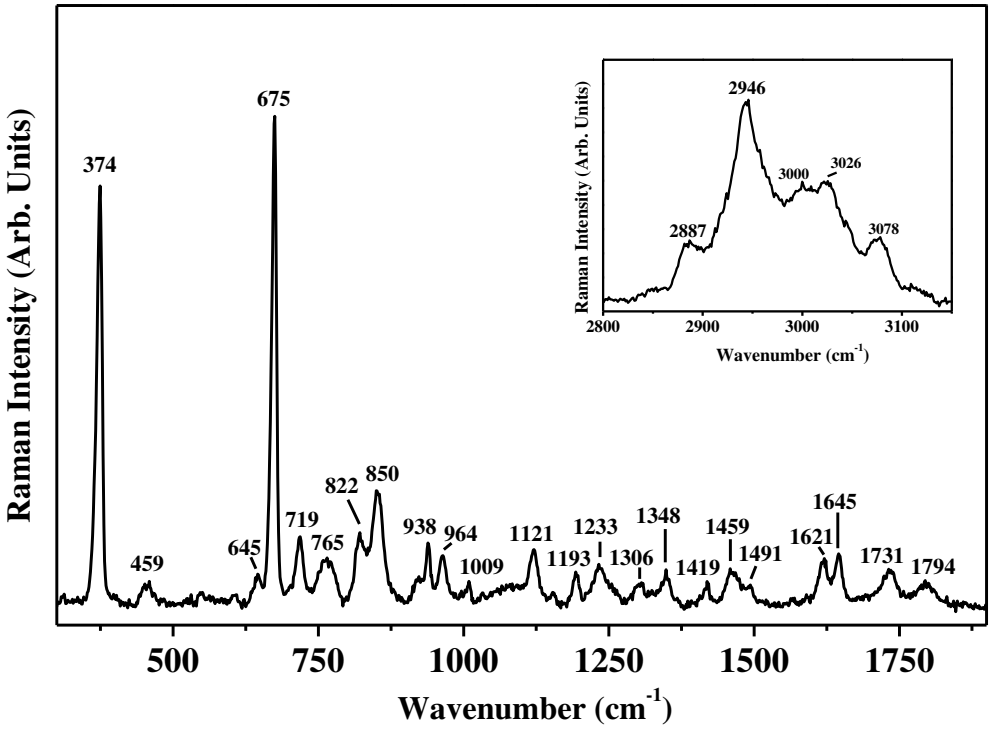

Figure 4.1.17. *Raman spectrum of ES made with PMMA 996 in the range 300 – 1900 cm^{-1} and 2800 – 3150 cm^{-1} in the inset.*

As mentioned above, the ES were used to fabricate the devices shown in figure (4.1.5). These were exposed to ultraviolet light to perform polymerization. The Raman spectra acquired on polymerised ES are shown in figure (4.1.18) (PMMA 15), (4.1.19) (PMMA 120) and (4.1.20) (PMMA 996).

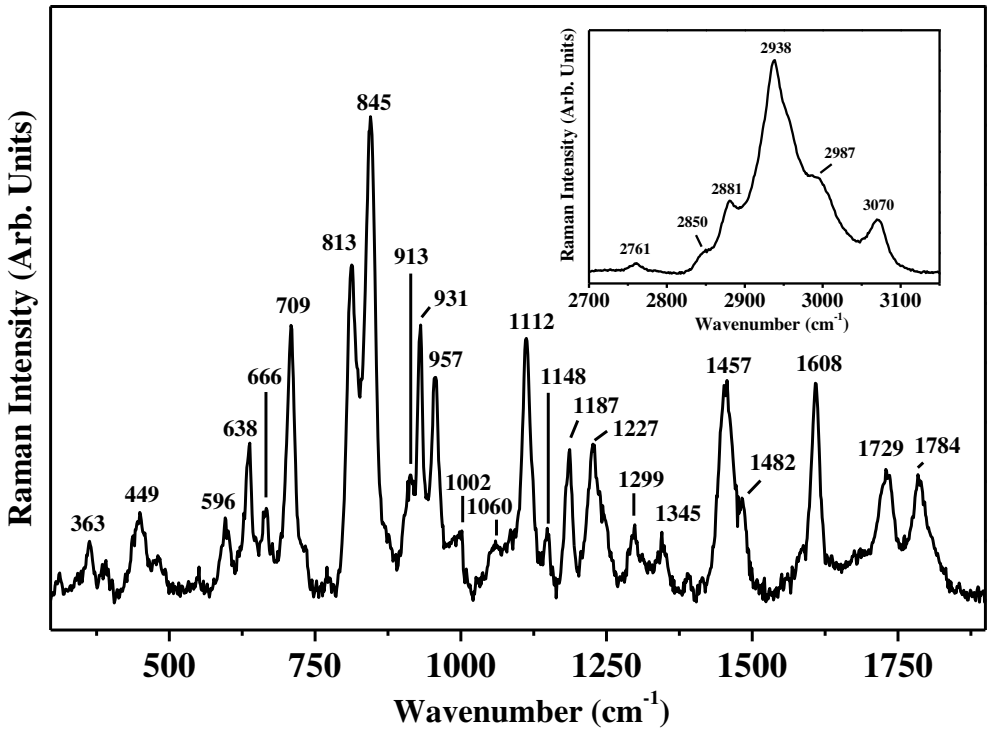

Figure 4.1.18. *Raman spectrum of polymerised ES made with PMMA 15 in the range 300 – 1900 cm^{-1} and 2700 – 3150 cm^{-1} in the inset.*

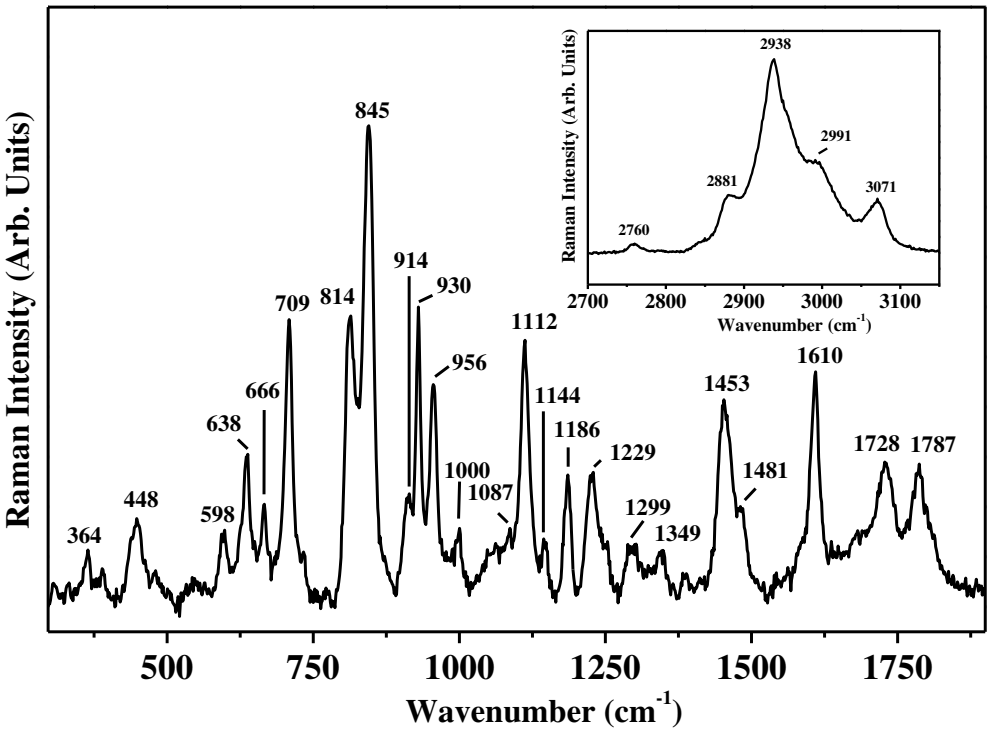

Figure 4.1.19. *Raman spectrum of polymerised ES made with PMMA 120 in the range 300 – 1900 cm^{-1} and 2700 – 3150 cm^{-1} in the inset.*

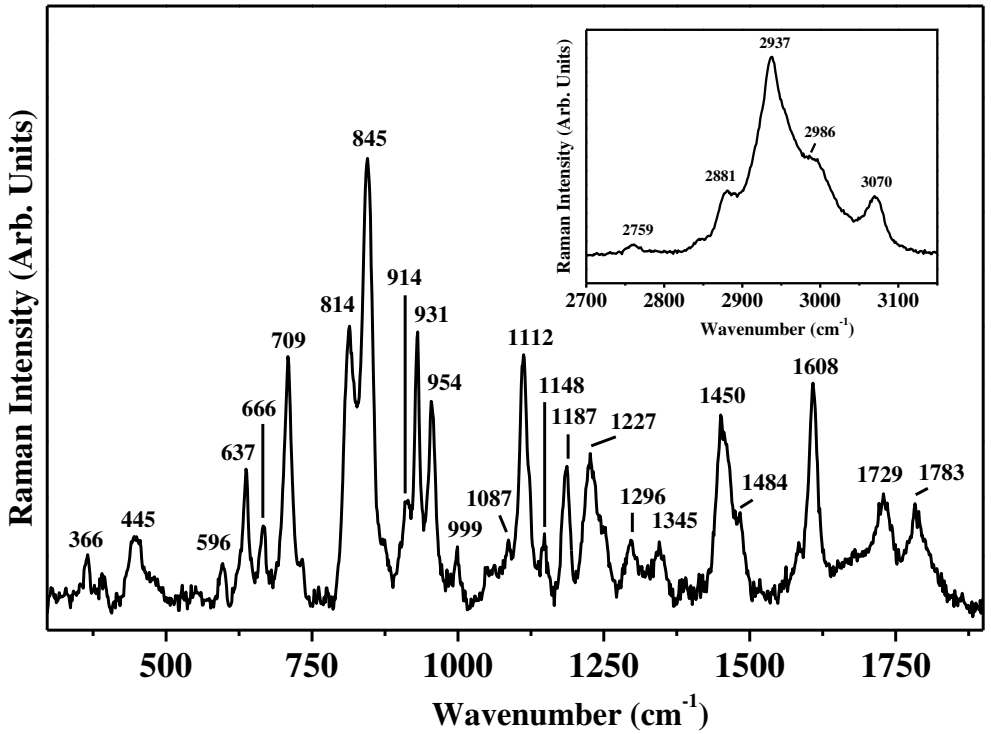

Figure 4.1.20. *Raman spectrum of polymerised ES made with PMMA 996 in the range 300 – 1900 cm^{-1} and 2700 – 3150 cm^{-1} in the inset.*

The spectra are divided in two regions, the first in the range between 300 cm^{-1} and 1900 cm^{-1}, the second, showed in an inset, in the range between 1800 cm^{-1} and 3150 cm^{-1} (in

the case of the polymerised ES the lower limit of the inset spectrum . The greatest peaks in the first region are the ones at ~373 and ~674 cm^{-1}. These signals, as well as the one at ~762 cm^{-1} are no longer present in the polymerised solution spectra shown below (only the first one is still observable but quite weak), making a great difference between the polymerised and the unpolymerized solution spectra. Assignments of these signals can be ascribed to the vibration modes of Chloroform [9], present in electrolyte solution since it's used as solvent for PMMA, and probably no longer present in the polymerised one, maybe due to its volatility and because of great temperature reached during curing. The other solvents used in making ES are PC and BPA, we can expect signals deriving from vibration modes related to these molecules. We observe signals ascribable to the (C=C) bond of both phenyls and acrylates groups of BPA at ~1619 cm^{-1} and ~1644 cm^{-1} respectively [12,18-22]. Acrylates groups are obviously also present in PMMA albeit we do not see any other signals (rather weak) attributable to combination bands in the acquired spectra of solid PMMA, see Fig. (4.1.11–4.1.13). It can be seen that the signal at ~1644 cm^{-1} due to the stretching mode of the (C=C) bond of acrylate groups present in the unpolymerized ES spectra is no longer present in those of polymerised ES and only the 1610 cm^{-1} signal remains. The decrease of the peak at 1645 cm^{-1} or its total disappearance due to curing by UV radiation has already been discussed in previous works [23]. The Raman band at ~644 cm^{-1} (~638 cm^{-1} in the polymerised ES spectra) is here attributed to the deformation out of plane of the aromatic (C–H) bonds of the BPA [12,17] but it should be kept in mind that a similar band is also present in the spectrum of the PC although there is not a precise attribution of the Raman mode observable at this wavenumber. Signal at ~1796 cm^{-1} is due to (C=O) stretching of PC [5,6] whereas the same stretching mode of BPA [12,20-22] and PMMA's [14-16] acrylate groups occurs at 1733 cm^{-1}. The signal at ~716 cm^{-1} also present in the spectrum of polymerised ES (although it is downshifted at ~709 cm^{-1}) is attributed to the symmetric ring deformation of PC [5-7]. The signals at ~821 – ~851 cm^{-1} in unpolymerized ES spectra and at ~813 – ~845 cm^{-1} in polymerised ES spectra are probably due to a combination of several signals. Indeed at the lower limit of the range fall the signals related to the stretching mode of (C−O−C) bond in PMMA [15][16] and to the out of plane deformation of the substituted aromatic ring of BPA [12][17] while at the upper limit fall the signals attributed to the rocking mode of (CH_3) group of PMMA [15] (not seen in our case in the solid PMMA's spectra) and to the symmetric stretching of the ring as well as the bending modes of (CH_3) and (O−C−C) bond of PC [5][6]. In the range between 900 cm^{-1} and 1000 cm^{-1} fall several

bands. The ones in the lower region of the range can be related to four species of the perchlorate ions dissolved in propylene carbonate: free perchlorate anion (ie ClO_4^-), solvent-shared ions, contact ion pairs and multiple ion aggregates [6]. The Raman bands in the upper limit of the range are ascribable to the rocking mode of ($\alpha-CH_3$) bond of PMMA [14-16] and to the symmetric stretching of (O−CO−O) in the ring of PC [5]. Signal at ~1119 cm^{-1} (~1112 cm^{-1} in the polymerised ES spectra) could be due to a combination of vibration modes of PC, BPA and PMMAs. We have already seen that wagging and bending modes of (CH_3) and (C−H) bond respectively of PC have been reported in this region [6] as well as the symmetric stretching of the (=C–O–C) of BPA [12] and stretching modes of (C−C) skeletal bonds of PMMAs [14-16]. The signal at ~1193 cm^{-1} (~1187 cm^{-1} in the polymerised ES spectra) could be attributed to the stretching mode of (C−O−C−) bonds of PMMAs [15]. But other assignments related to molecules very similar to BPA have also been reported in this range. Effectively, BPA is a basic molecule for synthesis of molecules that belong to the epoxy resin family and in a previous work signal at 1193 cm^{-1} was attributed to the stretching mode of C−C bond and to deformation mode of geminal methyl [17]. Signal at ~1231 cm^{-1} (~1227 cm^{-1} in the polymerised ES spectra) can be referred to the stretching mode of C−O bonds, and in this case, it could be assigned to ether bond of BPA [17], of propylene carbonate [5] and to the (C−O) of PMMA [15]. Attribution of signal at ~1348 cm^{-1} (~1346 cm^{-1} in the polymerised ES spectra) is referred to bending mode of CH_3 of PC [5,6]. The rather weak Raman band present in the ES spectra at ~1418 cm^{-1}, not observed in the Raman spectra of polymerised ES, is probably due to the ($=CH_2$) deformation of BPA [12]. This is in agreement with the aforementioned process of polymerization of acrylate groups. The last signals observed between 1400 cm^{-1} and 1500 cm^{-1} are attributed in general to deformation vibrations of (CH_3)and (CH_2) [12]. In this case they could be ascribed to (CH_2) bending and deformations of ($\alpha-CH_3$) and of ($O-CH_3$) bonds of PMMA [14-16] and to the asymmetric bending of (CH_3), the bending of ($–OCH_2$) and the umbrella modes of (CH_3) in PC [5,6]. The second region of the spectra (from 2700 cm^{-1} to 3150 cm^{-1}) is dominated by strong signals present at ~2884 cm^{-1}, ~2944 cm^{-1} and at ~3076 $cm^{-1}$and attributed to the stretching mode of (C−H) bonds in (CH) acyclic, (CH_2) acyclic and (CH_3) aliphatic groups presents in each molecule of the ES [5,6,9,12,14-16,18-22]. The difference spotted between ES spectra and polymerised ES spectra is on the hight frequency shoulder of the ~2944 cm^{-1} Raman band. The shoulder in the ES spectra shows two maxima at ~3000 cm^{-1} and ~3027 cm^{-1}. The second one is probably due to the

chloroform used to dissolve PMMA. Indeed, in the polymerised ES spectra, there is only a signal at lower frequency ~2988 cm^{-1}. The observed Raman bands together with their assignments are summarised in table (4.1.9).

Frequency (cm^{-1})						Assignments [a]	references
PMMA15		PMMA120		PMMA996			
ES	p-ES	ES	p-ES	ES	p-ES		
373	363	373	364	374	366	sym v_3 ($CHCl_3$)	[9]
						Bending	
	449	454	448	459	445	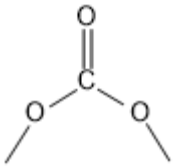	[5]
						Ring deformation (PC)	[6]
						ν_{sym}(C–C–O)	
	596		598		596	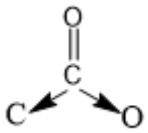	[14-16]
						(PMMA)	
640	638	647	638	645	637	Aromatic (C–H) out of plane def. (BPA)	[12][17]
674	666	674	666	675	666	sym v_2 ($CHCl_3$)	[9]
715	709	715	709	719	709	Symmetric ring deformation (PC)	[5] [6] [7]
765		757		765		deg v_5 ($CHCl_3$)	[9]
822	813	819	814	822	814	Stretching (C−O−C) (PMMA) + Substituted aromatic out of plane def (BPA)	[15][16] [12][17]

Table 4.1.9. *Observed Raman bands in ES and polymerised ES (p-ES) spectra and their assignments.* [a] *sym: symmetric; deg: degenerate.*

Frequency (cm^{-1})						Assignments [a]	references
PMMA15		PMMA120		PMMA996			
ES	p-ES	ES	p-ES	ES	p-ES		
						Rocking (CH_3) (PMMA) +	[15]
852	845	851	845	850	845	Ring breathing	[5]
						Bending (CH_3) and (O−C−C) (PC)	[6]
	913	917	914		914		
940	931	937	930	938	931	Perchlorate ions	[6][8]
						Symmetric stretching 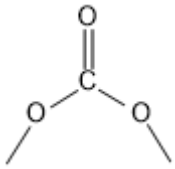 (PC) +	[5]
962	957	964	956	964	954	α–CH_3 rock (PMMA)	[15]
	1002	1005	1000	1009	999	skeletal vibration (BPA)	[12]
	1060 (sh)		1087 (sh)		1087 (sh)		
						(CH_3) wagging + (C–H) bending (PC) +	[6]
1118	1112	1118	1112	1121	1112	sym stretching (=C–O–C) (BPA) +	[12]
						ν(C–C) skeletal (PMMA)	[15]

Table 4.1.9. (continued) *Observed Raman bands in ES and polymerised ES (p-ES) spectra and their assignments.* [a] *sym: symmetric; asym: asymmetric deg: degenerate; (sh): shoulder.*

Frequency (cm^{-1})						Assignments [a]	references
PMMA15		PMMA120		PMMA996			
ES	p-ES	ES	p-ES	ES	p-ES		
	1148 (sh)		1144 (sh)		1148 (sh)	(C–C) + (C–O) stretching (PC)	[6]
1193	1187	1195	1186	1193	1187	ν_{asym}(C–O–C–) (PMMA) + (CH_3)/gem-dimethyl def. (C–C) stretching (BPA)	[15] [17]
1231	1227	1231	1229	1233	1227	Stretching (C–O) (BPA) and (PMMA) + stretching 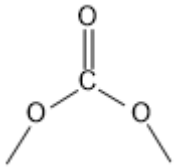 (PC)	[15][17] [5]
	1299	1303	1299	1306	1296	asym stretching (=C–O–C) (BPA)	[12][17]
1348	1345	1348	1349	1348	1345	Bending (CH_3) (PC)	[6]
1422		1414		1419		(=CH_2) def. (BPA)	[12]
1463	1457	1459	1453	1459	1450	Asymmetric bending (CH_3) (PC) + δ_{asym}(C–H) of α–CH_3 (PMMA)	[5] [14][15]
1492	1482	1495	1481	1491	1484	Bending (–OCH_2) (CH_3) umbrella (PC) + δ(CH_2) (PMMA)	[5][6] [14]

Table 4.1.9. (continued): *Observed Raman bands in ES and polymerised ES (p-ES) spectra and their assignments.* [a] *sym: symmetric; asym: asymmetric; gem: geminal; (sh): shoulder; def.: deformation.*

Frequency (cm^{-1})						Assignments [a]	references
PMMA15		**PMMA120**		**PMMA996**			
ES	**p-ES**	**ES**	**p-ES**	**ES**	**p-ES**		
1616	1608	1621	1610	1621	1608	Aromatic ring stretching vibration (BPA)	[12][18-20]
1623(sh)							
1644		1644		1645		Vinyl (C=C) stretching (BPA)	[12][18-22]
1733	1729	1729	1728	1731	1729	(C=O) stretching (BPA) and (PMMA)	[12][20-22] [14-16]
1796	1784	1796	1787	1794	1783	(C=O) stretching (PC)	[5][6][16]
2761		2760		2759		(C–H) stretching	[5][6][12] [14-16] [21,22]
2885	2881	2885	2881	2887	2881	(C–H_2) stretching	[5][6][12] [14-16][21,22]
2945	2938	2943	2938	2946	2937	(C–H_3) stretching	[5][6][12] [14-16][21,22]
3001	2987	2996	2991	3000	2986	(C–H_3) stretching	[5][6][12] [14-16][21,22]
3028		3026		3026		sym v_1 ($CHCl_3$) + (=C–H) stretching	[9] [12] [14-16][21,22]
3077	3070	3074	3071	3078	3070	(=C–H) stretching	[12] [14-16][21,22]

Table 4.1.9. (continued): *Observed Raman bands in ES and polymerised ES (p-ES) spectra and their assignments.* [a] *sym: symmetric; asym: asymmetric; deg: degenerate; (sh): shoulder.*

The acquired Raman spectra of the PMMA-based ES solutions with PC saline solutions of Lithium perchlorate and Lithium trifluoromethanesulfonate are shown in figure (4.1.21) and (4.1.22) in the range between 300 cm^{-1} – 2000 cm^{-1} and 2600 cm^{-1} – 3200 cm^{-1} respectively. The Raman spectra are quite similar to the previous ones. All the spectra show a band at ~632 cm^{-1} that is ascribable in this case to the PC but as said before, there is not a precise attribution of the Raman mode observable at this wavenumber for the propylene carbonate

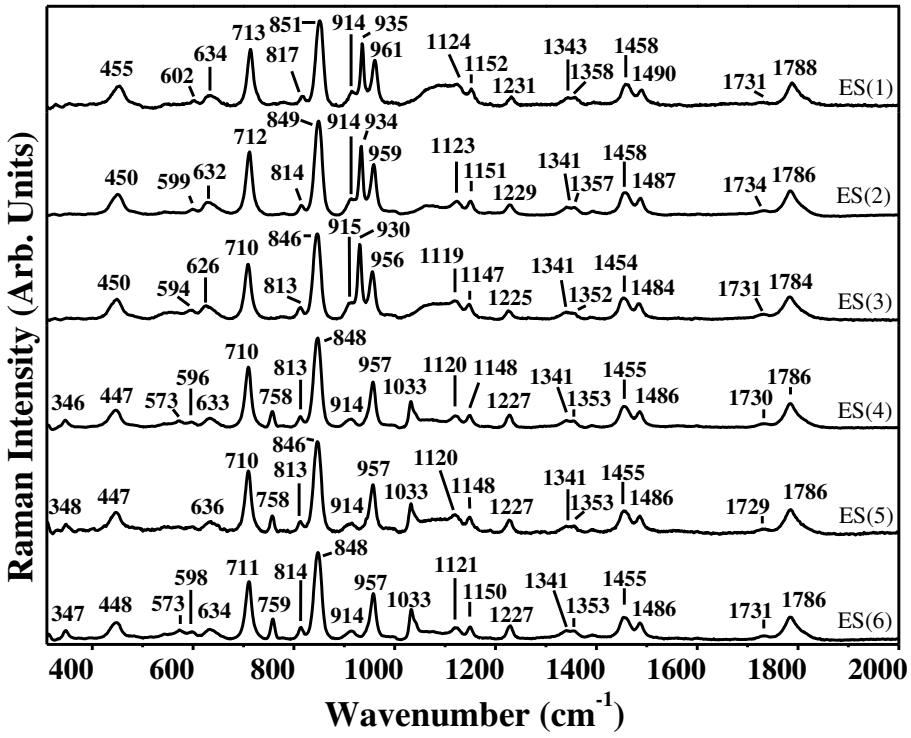

Figure 4.1.21. *Raman spectra of the PMMA based ES solutions made with $LiClO_4$ (ES 1-3) and with $LiCF_3SO_3CH_3$ (ES 4-6) in the range 300 cm^{-1} – 2000 cm^{-1}.*

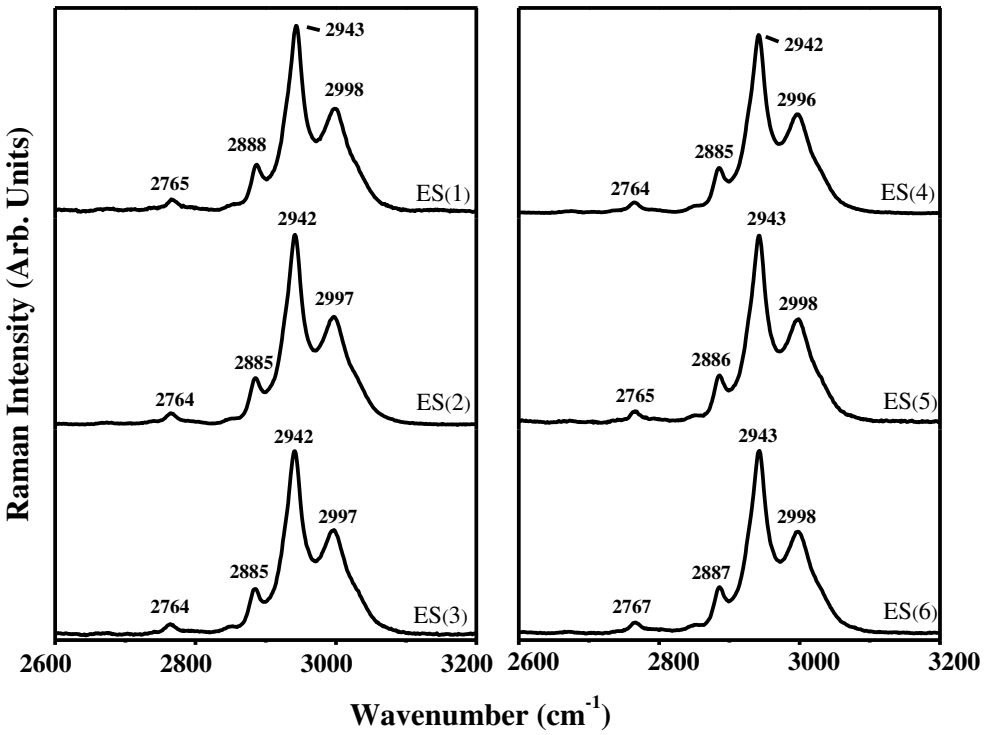

Figure 4.1.22. *Raman spectra of the PMMA based ES solutions made with $LiClO_4$ (ES 1-3) and with $LiCF_3SO_3CH_3$ (ES 4-6) in the range 2600 cm^{-1} – 3200 cm^{-1}.*

The observed Raman bands and assignments of vibrational modes are given in table (4.1.10).

Frequency (cm^{-1})						Assignments [a]	references
PMMA based solutions							
ES (1)	**ES (2)**	**ES (3)**	**ES (4)**	**ES (5)**	**ES (6)**		
			346	348	347	E (SO_3) (triflate) Bending	[10]
455	450	450	447	447	448	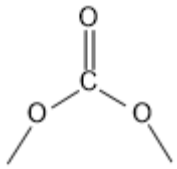	[5]
						Ring deformation (PC)	[6]
			573		573	δ_{sym} (SO_3) (triflate)	[10]
602	599	594	596		598	ν_{sym}(C–C–O) 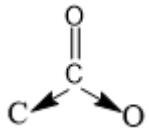 (PMMA)	[14-16]
634	632	626	633	636	634		
713	712	710	710	710	711	Symmetric ring deformation (PC)	[5-7]
			758	758	759	δ_{sym} (CF_3) (triflate)	[10-12]
817	814	813	813	813	814	ν_{sym}(C–O–C) (PMMA)	[15][16]
851	849	846	848	846	848	Rock. (CH_3) (PMMA) + Ring breathing Bending (CH_3) and (O−C−C) (PC)	[15] [5] [6]

Table 4.1.10. *Observed Raman bands and vibrational modes assignments of PMMA-based ES 1-6.* [a] *δ:bending; sym.: symmetric.*

Frequency (cm^{-1})						Assignments [a]	references
PMMA based solutions							
ES (1)	**ES (2)**	**ES (3)**	**ES (4)**	**ES (5)**	**ES (6)**		
914 (sh)	914(sh)	914(sh)	914	914	914		
935	934	930				Perchlorate Ions	[6][8]
961	959	956	957	957	957	Symmetric stretching 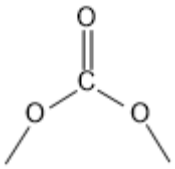 (PC) + α–CH_3 rock. (PMMA)	[5] [15]
			1033	1033	1033	ν_{sym} (SO_3) (triflate)	[10-13]
1124	1123	1119	1120	1120	1121	(CH_3) wag. + (C–H) bending (PC) + ν(C–C) skeletal (PMMA)	[6] [15]
1152	1151	1147	1148	1148	1150	(C–C) + (C–O) stretching (PC)	[6]
1231	1229	1225	1227	1227	1227	stretching 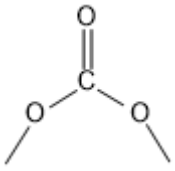 (PC)	[5]
1343	1341	1341	1341	1341	1341	Bending (CH_3) (PC)	[5][6]

Table 4.1.10. (continued): *Observed Raman bands and vibrational modes assignments of PMMA-based ES 1-6. [a] δ: bending; ν: stretching; rock.: rocking; wag.: wagging; sym.: symmetric; asym.: asymmetric; (sh): shoulder.*

Frequency (cm^{-1})						Assignments [a]	references
PMMA based solutions							
ES (1)	ES (2)	ES (3)	ES (4)	ES (5)	ES (6)		
1358	1357	1352	1353	1353	1353	Bending (CH_3) (PC)	[5] [6]
1458	1458	1454	1455	1455	1455	Asym. Bending (CH_3) (PC) + δ_{asym}(C–H) of α–CH_3 (PMMA)	[5] [14][15]
1490	1487	1484	1486	1486	1486	Bending (–OCH_2) (CH_3) umbrella (PC) + $\delta(CH_2)$ (PMMA)	[5][6] [14]
1731	1734	1731	1730	1729	1731	(C=O) stretching (PMMA)	[14-16]
1788	1786	1784	1786	1786	1786	(C=O) stretching (PC)	[5][6][16]
2765	2764	2764	2764	2765	2767	(C–H) stretching	[5][6][12] [14-16] [21,22]
2888	2885	2885	2885	2886	2887	(C–H_2) stretching	[5][6][12] [14-16]
2943	2942	2942	2942	2943	2943	(C–H_3) stretching	[5][6][12] [14-16]
2998	2997	2997	2996	2998	2998	(C–H_3) stretching	[5][6][12] [14-16]

Table 4.1.10. (continued) *Observed Raman bands and vibrational modes assignments of PMMA-based ES 1-6.* [a] *δ: bending; v: stretching; rock.: rocking; wag.: wagging; sym.: symmetric; asym.: asymmetric; (sh): shoulder.*

4.1.3 Conclusions

Electrolyte Solutions (ES) made with use of PMMA seems to be suitable in electrochromic technology because of good manageability of components without requirement of preparations before use. Further, the solutions reached seems to become like a film on ITO surface and polarization process acts on PMMAs as well as on the BPA. The Raman analysis conducted showed that the differences in the Raman spectra are related to the vinyl ($=CH_2$) of acrylate groups and to the Chloroform. The Raman bands ascribable acrylates or $CHCl_3$ are visible in the not polymerised ES spectra and not in the polymerised ES spectra. The different molecular weights of PMMA did not affect the Raman spectra. The only difference found is related rather to the viscosity of the solutions obtained and, therefore, to their easy or less manageability. This aspect can be easily solved by varying the percentage by weight of the components. The values of the electronic conductivities of the electrolytic solutions realized in the second part of the study have been calculated. These values are approximatively the same for all the dispositive and confirm the good conductivity of the lithium salt used.

4.2 Raman spectroscopic characterization of blend films of PMMA/PEO

The research on the best polymeric electrolyte for electrochromic use led to characterization of several blend solutions made with variable proportions of PMMA 120000 GPC and polyethylene oxide (PEO). The two polymers were mixed in variable proportions and dissolved in an ethylene carbonate (EC)/propylene carbonate (PC) solution. The solutions were characterized by Raman spectroscopy with a MicroRaman-LABRAM from Jobin Yvon Srl-Horiba.

4.2.1 Experimental

All chemicals were purchased from Sigma-Aldrich®. Five solutions of a 9 % by weight mixture of polymethylmethacrylate (PMMA, 120000 GPC) and polyethylene oxide (PEO) were prepared in a solvent consisting of ethylene carbonate (EC) and propylene carbonate (PC) with a molar ratio of 1:0,4. The percentages by weight of the PMMA/PEO ratio for the 5 solutions are summarized in table (4.2.1).

Solutions	Percentage Ratio (PMMA/PEO)
A	100/0
B	95/5
C	90/10
D	85/15
E	80/20

Table 4.2.1. *Percentage ratio PMMA/PEO of the solutions.*

The Raman spectra have been acquired with a NdYAG green laser, emission wavelength at 532 nm, modulable power at 50 mW. A long working distance objective 50x and an optical filter D03 were used. Every spectrum recorded is a result of 30 acquisitions.

4.2.2 Results and discussion

The acquired Raman spectra in the range between 550 cm^{-1}–1850 cm^{-1} and 2800 cm^{-1}–3100 cm^{-1} are shown in figure (4.2.1) and (4.2.2) respectively. The discussion about these spectra is done below.

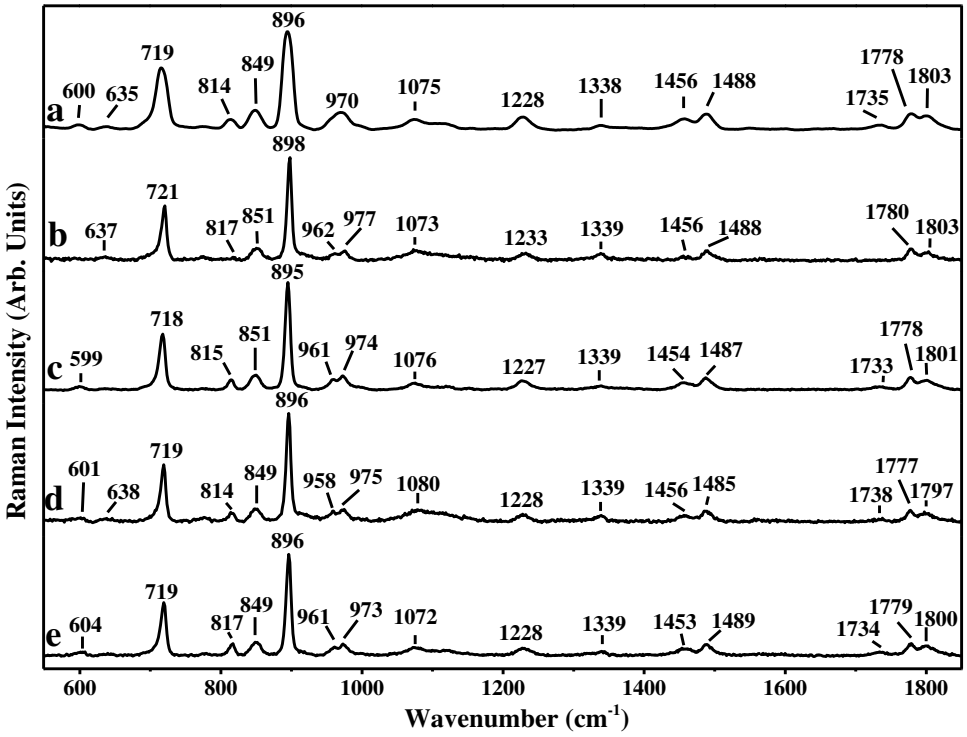

Figure 4.2.1. *Acquired Raman spectra in the range between 550 cm^{-1} and 1850 cm^{-1} of the 9% by weight solutions of PMMA/PEO in the molar ratios: a) 100/0; b) 95/5; c) 90/10; d) 85/15; e) 80/20.*

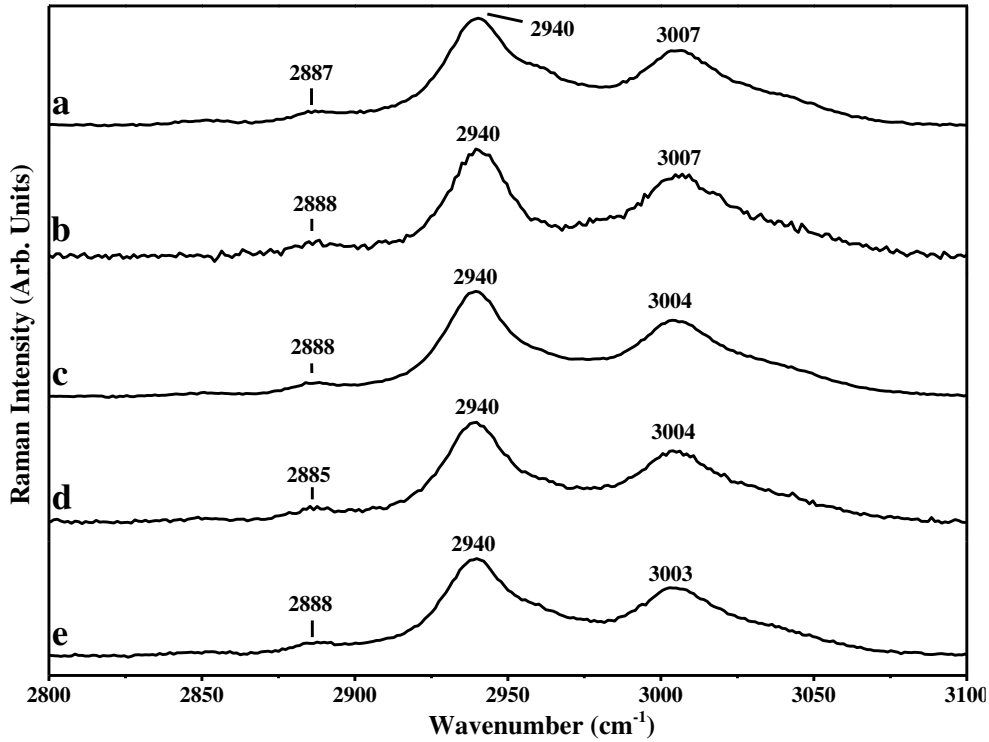

Figure 4.2.2. *Acquired Raman spectra in the range between 1800 cm^{-1} and 3100 cm^{-1} of the 9% by weight solutions of PMMA/PEO in the molar ratios: a) 100/0; b) 95/5; c) 90/10; d) 85/15; e) 80/20.*

All the acquired spectra show strong band at ~719 cm^{-1}, ~896 cm^{-1}, Fig. (4.2.1), and in the region of (C–H) stretching, Fig. (4.2.2). The former band is ascribable to the symmetric deformation of the solvents ring [5-7,16,23] and to the out of plane bending of the (C=O) bond of the EC ring [16,24]. The second band is the most intense in all the recorded spectra, it is attributable to the ring breathing of the solvents ring [16,23,24]. The region of (C–H) stretching is characterized by the bands ascribable to the symmetric and antisymmetric stretching of the methyl (CH_3) at 2940 cm^{-1} and at ~3005 cm^{-1} respectively and to the stretching of the methylene (CH_2) at ~2887 cm^{-1}. The frequency of these Raman bands are slightly higher compared to that of simple alkanes and alkenes and this indicates the presence of electronegative groups or atoms directly bonded to the (C–H) or the presence of little rings (non-aromatic) that due to the forces that come into play produce the slight increase in these frequencies [12]. These Raman modes are attributable to the solvents and to the PMMA [5,6,12,14-16,21,22]. The attribution of the Raman modes related to the PEO is somewhat more complicated due to the low percentage of the blend PMMA/PEO. The Raman band at ~1075 cm^{-1} can be ascribable to the EC solvent because of the stretching mode of the (C–O) bond reported here [24].

It is also remembered the presence of a similar band in the spectrum of PC, Fig. (4.1.7), however attribution of this band was not possible because of the absence of references in literature. The presence of PMMA is confirmed by the presence of characteristic Raman bands of relative low intensity at ~601 cm^{-1}, related to the symmetric stretching of (C–C–O) [14-16], and at ~815 cm^{-1}, related to the symmetric stretching of ethereal (C–O–C) [15,16]. Additional Raman mode ascribable to the PMMA is given by the broad band at 970 cm^{-1} in spectrum a of figure (4.2.1), that is a doublet in the other spectra located at ~961 cm^{-1} and ~975 cm^{-1}. The former of these bands is related to the rocking modes of (α–CH_3) [15] and the latter to the rocking of (O–CH_3) [14-16]. It should be born in mind that the 961 cm^{-1} band is ascribable as before also to the symmetric stretching of the (O−CO−O) in the ring of PC [5]. The stretching mode of the carbonyl (C=O) due to the PMMA is noticeable at ~1735 cm^{-1} but is very weak compared to the ones of the solvents visible at ~1778 cm^{-1} (PC) [5,6] and at ~1801 cm^{-1} (EC) [24]. The Raman bands in the range between 1200 cm^{-1} and 1500 cm^{-1} are related to the bending of the (C–H) bonds of methyl and methylene residues of the solvents and of the polymers [12]. Table (4.2.2) summarize the above discussion.

Frequency (cm^{-1})					**Assignments** [a]	**references**
PMMA/PEO						
100/0	**95/5**	**90/10**	**85/15**	**80/20**		
600		599	601	604	ν_{sym}(C–C–O) 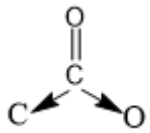 (PMMA)	[14-16]
635	637		638			
719	721	718	719	719	Symmetric ring deformation (PC) + Out of plane bending (C=O) (EC)	[5-7] [16,23]

Table 4.2.2. *Observed Raman bands of the PMMA/PEO solutions in EC/PC solvent.* [a] *v: stretching; sym: symmetric.*

Frequency (cm^{-1})					Assignments [a]	references
PMMA/PEO						
100/0	**95/5**	**90/10**	**85/15**	**80/20**		
814	817	815	814	817	ν_{sym}(C–O–C) (PMMA)	[15][16]
849	851	851	849	849	Rock. (CH_3) (PMMA) + Ring breathing + Bending (CH_3) and (O−C−C) (PC)	[15] [5] [6]
896	898	895	896	896	Ring breathing (EC)	[16][23][24]
	962	961	958	961	Symmetric stretching 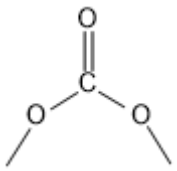 (PC) + α–CH_3 rock. (PMMA)	[5] [15]
970	977	974	975	973	O–CH_3 rock. (PMMA)	[14-16]
1075	1073	1076	1080	1072	Stretching (C–O) (EC)	[25]
1338	1339	1339	1339	1339	Bending (CH_3) (PC)	[5][6]
1456	1456	1454	1456	1453	Asym. Bending (CH_3) (PC) + δ_{asym}(C–H) of α–CH_3 (PMMA)	[5] [14][15]
1488	1488	1487	1485	1489	Bending (–OCH_2) (CH_3) umbrella (PC) + $\delta(CH_2)$ (PMMA)	[5][6] [14]

Table 4.2.2. (continued): *Observed Raman bands of the PMMA/PEO solutions in EC/PC solvent.* [a] *δ: bending; rock.: rocking; twist.: twisting; asym: antisymmetric.*

Frequency (cm^{-1})					Assignments [a]	references
PMMA/PEO						
100/0	**95/5**	**90/10**	**85/15**	**80/20**		
1735		1733	1738	1734	(C=O) stretching (PMMA)	[14-16]
1778	1780	1778	1777	1779	(C=O) stretching (PC)	[5][6][16]
1803	1803	1801	1797	1800	(C=O) stretching (EC)	[16][25]
2887	2888	2888	2885	2888	($C–H_2$) stretching	[5][6][12] [14-16]
2940	2940	2940	2940	2940	($C–H_3$) stretching	[5][6][12] [14-16]
3007	3007	3004	3004	3003	($C–H_3$) stretching	[5][6][12] [14-16]

Table 4.2.2. (continued): *Observed Raman bands of the PMMA/PEO solutions in EC/PC solvent.* [a] *δ: bending; rock.: rocking; twist.: twisting; asym: antisymmetric.*

4.2.3 Conclusions

Five 9% solutions by weight of a mixture of PMMA and PEO in different weight percentages by weight were prepared in a binary solvent consisting in propylene carbonate and ethylene carbonate in molar ratio 1/0.4. The samples were characterized by Raman spectroscopy demonstrating the presence of the two polymers in the PC/EC solutions. The attribution of the Raman modes attributable to the PEO has been more difficult because of the low percentages of polymer used compared to PMMA. The solutions at room temperature show two phase that seems attributable from literature to a solubility of polymers affected by the low percentages used [16].

4.3 Raman characterization of a blend consisting in folic acid and a polymer

The aim of the work has been the Raman characterization of a blend made by folic acid and a polymer consisting in methacrylic acid, ethylene glycol di-methacrylate and the precursors acetonitrile and 2,2′-azobis(2-methylpropionitrile). The Raman characterization of the blend follows the research of suitable polymeric electrolytes (in this case made of a natural polymer as folic acid) for electrochromic uses. The Raman characterization has been performed with a green laser at 532 nm of a Micro-Raman LABRAM. Raman spectra collected on single components and the blend show clear differences between the polymer and blend, sign of an interaction between the components of the latter.

4.3.1 Experimental

In figure (4.3.1) are shown the molecular structures of the folic acid and of the single components of a polymer consisting in methacrylic acid (MAA), ethylene glycol di-methacrylate (EGDMA), acetonitrile (CH_3CN) and 2,2'-azobis(2-methylpropionitrile) (AIBN), the latter two element probably used as initiators. The folic acid and the polymer have been used to realize a blend in order to make a polymeric film. Raman spectra have been collected with a confocal Micro-Raman–LABRAM by jobin Yvon Srl (now Horiba scientific) associate to an optical microscope highly stable with an objective long working distance. In this experiment a green laser with emission wavelength at 532 nm and 50 mW power has been used. Detector is a CCD device cooled with a Peltier module 1024x256, 16 bits dynamic range (pixel size 27 μm). Apparatus is equipped with a series of optical filters but in current analysis, OD1 was preferred. The spectral resolution is about 1 cm^{-1}.

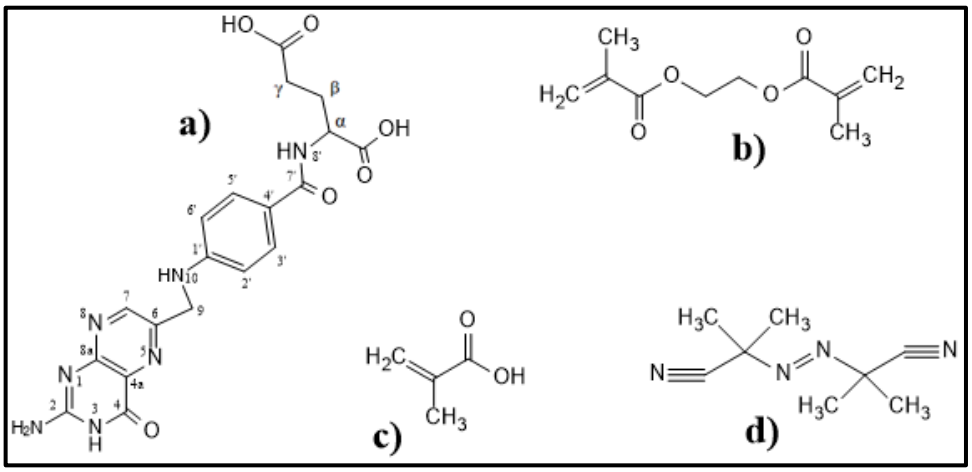

Figure 4.3.1. *Molecular structure of a) folic acid; b) EGDMA; c) MAA; d) AIBN.*

In figure (4.3.2) are shown the optical images acquired on the single components and on the blend.

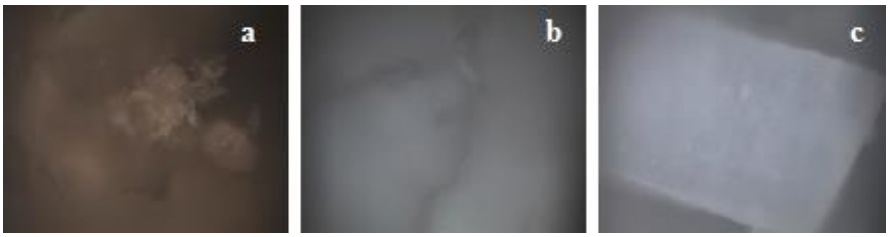

Figure 4.3.2. *Optical microscope images, magnification 50x, a) folic acid, b) polymer, c) blend.*

4.3.2 Results and discussion

Firstly, attention was directed to the individual elements of the blend, folic acid and polymer because of necessity to analyse any differences between the acquired Raman spectra. The samples were then deposited as received on a glass substrate and different acquisition times and optical filters were used. The Raman spectrum of folic acid deposited on glass is not shown here due to the large luminescence and lack of Raman signals, so no information could be deduced from the Raman spectra acquired in this way. Analysis were successively performed using a glass substrate on which a thin gold layer was previously deposited. Following several attempts, it has been decided to use an OD1 optical filter, best compromise because with smaller filters the folic acid sample was damaged after measurements while with larger filters the Raman signals were poorly resolved. The same conditions were maintained in the acquisition of the Raman spectra

of the polymer and of the blend. The Raman spectrum of folic acid is shown in figure (4.3.3), those of polymer and blend are shown in figure (4.3.4).

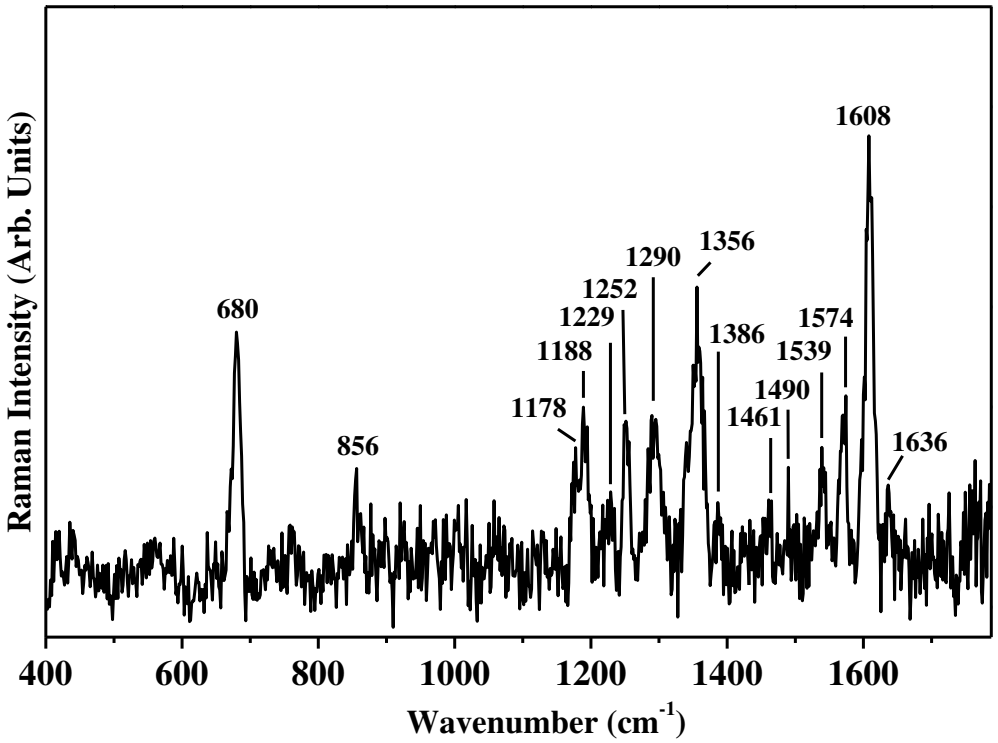

Figure 4.3.3. *Raman spectrum of folic acid acquired on gold substrate with 532 nm laser, OD1 optical filter, between 400 cm^{-1} and 1785 cm^{-1}.*

The discussion made below on the assignment of the Raman bands noticed in the folic acid spectrum follows that of some SERS (Surface-Enhanced Raman Spectroscopy) although the Raman spectra in our case have been acquired without sample preparation and on solid folic acid. The most intense signal of the spectrum is at 1608 cm^{-1} and is assigned to the symmetrical stretching of the aromatic ring of folic acid [25,26]. Signals at 1356 cm^{-1} and 680 cm^{-1}, seconds in relative intensity, are attributed respectively to the wagging of the aromatic (C–H) and C(β–γ)H_2 [25,26] and the out–of–plane deformation of the (OH) group [25]. The signal at 856 cm^{-1} is attributed to the deformation of the C(α)–H bond as well as the breathing of the aromatic ring [25]. The doublet at 1178–1188 cm^{-1} is a signal that can be traced back to the twisting of aliphatic CH_2 [25], the signal at 1252 cm^{-1} can be attributed to the C(9)H_2 wagging [25,26] as well as the in–plane deformation of C(7)–H [25]. The relatively very weak signal at 1386 cm^{-1} is attributed to the in–plane deformation of the C(7)–H bond and the rocking of the (NH_2) [25]. The relatively weak signal at 1461 cm^{-1} is attributed by Kokaislova et al. to the in–plane deformation of the N(10)–H bond and to the scissors of the C(β)H_2 [25]. In the same publication the band at 1490 cm^{-1} is attributed to the C(9)–H_2 scissoring and to the in–

plane deformation of the C(7)–H [25]. The 1539 cm^{-1} signal is assigned to the stretching of the aromatic ring and the in-plane stretching of the (N–H) [25,26]. The Raman signal at 1574 cm-1 is ascribable to the in–plane deformation of the N(3)–H bond [25,26]. Finally, a very weak signal can be found in the spectrum at 1636 cm^{-1} attributed in the literature to bending scissors of the (N–H) bond and stretching of the C(4)–O [25]. The results are summarized in table (4.3.1).

Frequency (cm^{-1})	**Assignment[a]**	**references**
680	out-of-plane def (OH)	[25]
856	def. C(α)–H + ring breathing	[25]
1178	twisting (CH_2)	[25]
1188	twisting (CH_2)	[25]
1229	wagging C(9)H_2	[25][26]
1252	+	
	in plane def. C(7)–H	[25]
1290		
1356	wagging aromatic (C–H) and C(β–γ)H_2	[25][26]
1386	In plane def. C(7)–H + Rocking (NH_2)	[25]
1461	in plane def. N(10)–H + scissoring C(β)H_2	[25]
1490	scissoring C(9)–H_2 + in plane def. C(7)–H	[25]
1539	ν aromatic ring + ν in plane (N–H)	[25][26]
1574	in plane def. N(3)–H	[25][26]
1608	ν_{sym} aromatic ring	[25][26]
1636	scissoring (N–H) + ν C(4)–O	[25]

Table 4.3.1. *Observed Raman bands of folic acid and relative assignments and references.* [a] *ν: stretching; def.: deformation; sym.: symmetric.*

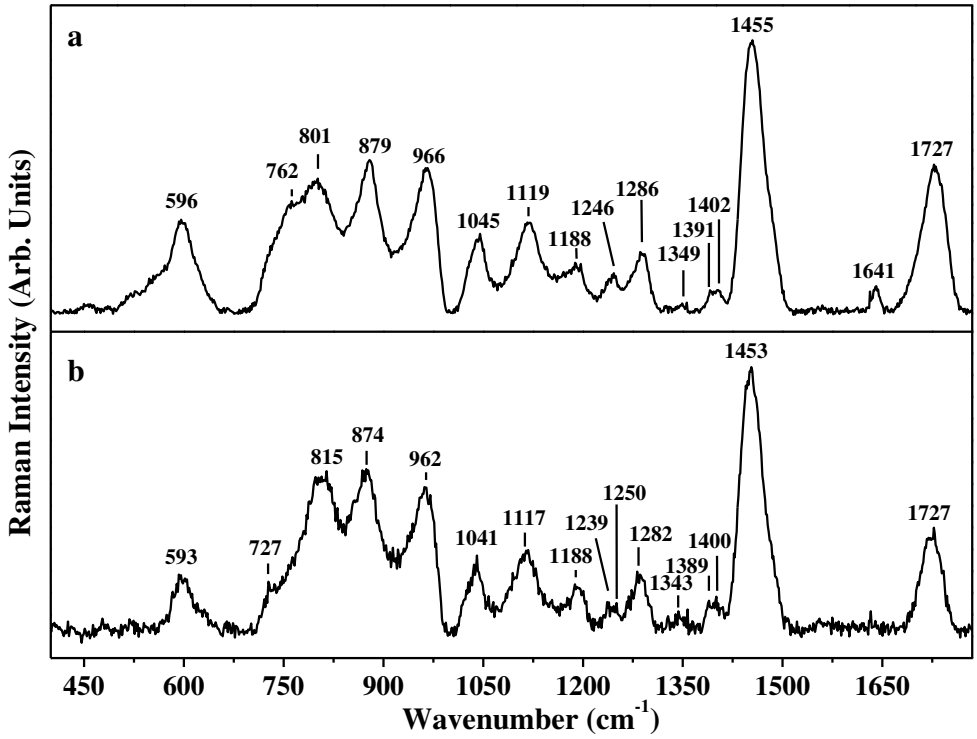

Figure 4.3.4. *Raman spectra acquired on gold substrate with 532 nm laser, OD1 optical filter, between 400 cm^{-1} and 1785 cm^{-1} of: a) polymer; b) blend of folic acid-polymer.*

Turning to the analysis of polymer, which should be a copolymer of MAA and EGDMA, with CH_3CN and AIBN as initiators of curing (for this reason perhaps present as minor components of the copolymer), and of blend copolymer–folic acid – related spectra, you can point out some differences that could be due to an interaction between the various components of the blend. At first glance, we notice the absence in the blend spectrum of the signal presents in the polymer spectrum at 1641 cm^{-1} as well as the different shape of the signal in the range at 700–850 cm^{-1}. The 1641 cm^{-1} signal is reported in the literature as stretching of the (C=C) bond in acrylates and methacrylates and is typically used as a cross-linking polymerization efficiency detector [12,18-22,27]. It is important to note that the signal is no longer present in the blend, which is likely index of the fact that there may have been a link between the terminal acrylate vinyl groups (responsible for the stretching signal (C=C) at that frequency in the polymer) and Folic Acid. The very intense band at 1727 cm^{-1}, reported in the literature as stretching of (C=O) of molecules having saturated carbon atoms adjacent to carboxyl group does not change frequency from polymer to blend [12,14,15,27]. It would therefore be reasonable to expect that even the signals relating to symmetric and asymmetric (C–O–C) stretching of the same carboxylic residues will not undergo changes in frequency from the polymer to the blend. In fact, in

the literature, such modes are reported around the frequencies of the signal detected at 1188 cm^{-1} for asymmetric stretching, while symmetrical stretching is reported around 816 cm^{-1} [14,15,27]. This brings us back to discuss the other big difference between the spectra of the polymer and the blend: the signals in the frequency range between 700 cm^{-1} and 820 cm^{-1}. If, indeed, as expected, the signal related to the asymmetric stretching of the (C–O–C) does not undergo frequency shifts from the polymer to the blend, the symmetrical stretching is instead absent in the polymer while it is found in the mixture at 815 cm^{-1}. Particularly, in the polymer, the signal closest to the symmetrical stretching frequency of the (C–O–C) is at 801 cm^{-1}. This signal is close to that detected at 762 cm^{-1} and associated with the symmetrical stretching of the (C–COOH) bond of the MAA monomer [28]. In the blend, the corresponding signals appear to be, as mentioned above, at 815 cm^{-1} and 727 cm^{-1} respectively. The attribution of the first signal has already been discussed, while the second could be attributed to skeleton (C–C) modes [15]. At this point it is good to discuss about the signal at 801 cm^{-1}, perhaps indicative of the fact that in the polymer the MAA turns out to be more in the monomeric component, or in the terminal positions of the copolymer. This signal is also attributed in the work of J. Bong et al. [29] to symmetrical stretching of the (C–COOH) binding of methacrylic acid; in this publication it is pointed out that the intensity of this signal wanes with the increase of a radiative dose that significantly improves the curing and therefore the disappearance of the vinyl portion adjacent to the bond [29]. The signals in the region of the spectrum between 700 cm^{-1} and 820 cm^{-1} are therefore attributable to methacrylic acid in the polymer while in the blend they are no longer. At this point, since the (C–O–C) bond is present only in the EGDMA monomer and also in the copolymer (result of polymerization) and given the presence of the signal at 1641 cm^{-1}, it is believed that the monomeric components within the polymer are important, or in terminal position of copolymer while the presence of folic acid in the mixture increases the degree of polymerization or lead to a link between Folic Acid and terminal monomer components of polymer. The signal in the polymer spectrum at 596 cm^{-1} is attributed in literature to the stretching of the (C–C–O) bond of the methacrylate ester groups, found in the spectrum of the mixture at 593 cm^{-1} [15]. At the same type of binding, but an opposite stretching in this case, is due to the signal at 1286 cm^{-1} in the polymer spectrum and shifted to 1282 cm^{-1} in the spectrum of the blend. By analysing the differences of the two spectra in more detail, we can see that the same type of signal displacement affects all bands attributable to the (C–H) and (C–C) bonds and that the displacement occurs at

lower frequencies in the blend than the polymer of an average shift of 3-4 cm^{-1}. Thus, the signal in the polymer at 1455 cm^{-1}, attributed to the asymmetric deformation of the (CH_3) is shifted at 1453 cm^{-1} in the blend [15,27]. Also in the polymer spectrum, the two rather weak bands at 1402 and 1391 cm^{-1} which are attributed to (CH_2) twisting or wagging modes and the symmetrical bending of the (C–H) bond in the (CH_3) groups respectively, are shifted in the spectrum of the blend to 1400 and 1389 cm^{-1} [15,27]. Finally, the signals in the polymer spectrum at 1119 cm^{-1}, 1045 cm^{-1}, 966 cm^{-1} and 879 cm^{-1}, attributed in literature to stretching of the skeleton (C–C) bonds, the first two and the rocking of the (CH_3) and (CH_2) the last two, are shifted to 1117 cm^{-1}, 1041 cm^{-1}, 962 cm^{-1} and 874 cm^{-1} in the blend spectrum [15,27]. In table (4.3.2) the observed Raman bands together with their assignments and the relative references are summarized.

Frequency (cm^{-1})		**Assignment[a]**	**references**
polymer	**Blend**		
596	593	ν(C–C–O) methacrylate esther	[15]
	727	skeleton (C–C)	[15]
762		ν_{sym} (C–COOH) (MAA)	[28]
815	801	ν_{sym} (C–O–C)	[14,15,27]
879	874	rocking (CH_2)	[15,27]
966	962	rocking (CH_3)	[15,27]
1045	1041		
1119	1117	ν(C–C)	[15,27]
1188	1188	ν_{asym} (C–O–C)	[14,15,27]
1246	1239 1250		
1286	1282	ν(C–C–O) methacrylate esther	[15]
1349	1343		
1391	1389	sym bending (C–H) of (CH_3)	[15,27]
1402	1400	(CH_2) twisting or wagging	[15,27]
1455	1453	asym def. (CH_3)	[15,27]
1641		stretching acrylate (C=C)	[12,18-22,27]
1727	1727	stretching (C=O)	[12,14,15,27]

Table 4.3.2. *Observed Raman bands in polymer and blend.* [a] *v: stretching; sym.: symmetric; asym.: asymmetric.*

4.4.3 Conclusions

In summary, some signals present in the polymer and not in the blend, can be traced back to the vinyl portions of the monomers that make up the polymer itself. It can be assumed that these monomeric units are located in terminal positions of polymer chains and that is at that level that a folic acid – polymer interaction occurs. Indeed, in the mixture, these signals are no longer present and noticing an overall shift at low frequencies of the vibrational modes of the C–H and C–C bonds, one can imagine a significant interaction between the two components of the blend.

4.4 Effect of combination of gold nanoparticles and polyelectrolyte layers applied on glass substrate on Raman spectra of a 10% volume aqueous solution of acetic acid.

In this work, polyelectrolyte layers (PE) are deposited on substrates made by glass covered by an array of gold nanoparticles (GNPs). Four types of substrates have been used, starting from a substrate without layers of PE (GGPE_0) and substrates that have got 3 layers of PE (GGPE_3), 11 layers of PE (GGPE_11) and 21 layers of PE (GGPE_21). The Raman analysis of an acetic acid solution (10 % v/v) was carried out in function of the different substrates. Focusing on the Raman bands of the acetic acid aqueous solution, it appears clear that an enhancement has been done. Theses Raman bands are much more intense with increasing the number of PE layers. The presence of Gnps layer is sufficient to obtain a small increase of the Raman signals related to acetic acid aqueous solution and the presence of PE layers further enhance the intensity of these bands.

SERS is nowadays well known and widely used in various studies such as: detection of low abundance molecules [30,31], monitoring environmental contaminants [32,33], food science [34], analysis of biomolecules, pharmaceutical and drugs research and many others [35,36].

SERS was observed for the first time in 1974 [37,38] and it is a technique that allows to promote the signals detected by Normal Raman spectroscopy. Briefly, SERS is due to electronic and chemical interactions between the sample, the substrate and the laser source. To explain the SERS effect, the mechanisms involved are two: the electromagnetic and the charge transfer. The first one occurs when the incident laser source excites the surface plasmons of the metal substrate and the second one is ascribed to a transfer of electrons between metal and sample [32].

Noble metal surfaces have been used as SERS substrates. Those have been used as flat surfaces or as nanoparticles [39]. Today, there are several methods to obtain SERS substrates: metal nanoparticles in suspension, metal nanoparticles immobilized on solid substrates and nanostructures fabricated directly on solid substrates [40-42].

4.4.1 Experimental

Acetic acid (99.0%, purity) was purchased by Fluka Analytical Company. Such solution has been diluted at the 10% in acid acetic by using double distilled water in order to be used as standard for the Raman analysis.

The substrates studied in this work are four samples composed of a GNPs array on glass substrate covered by: no PE layer, 3 PE layers, 11 PE layers and 21 PE layers labelled as GGPE_0, GGPE_3, GGPE_11 and GGPE_21, respectively. In figure (4.4.1) is reported a schematic view of the four samples studies.

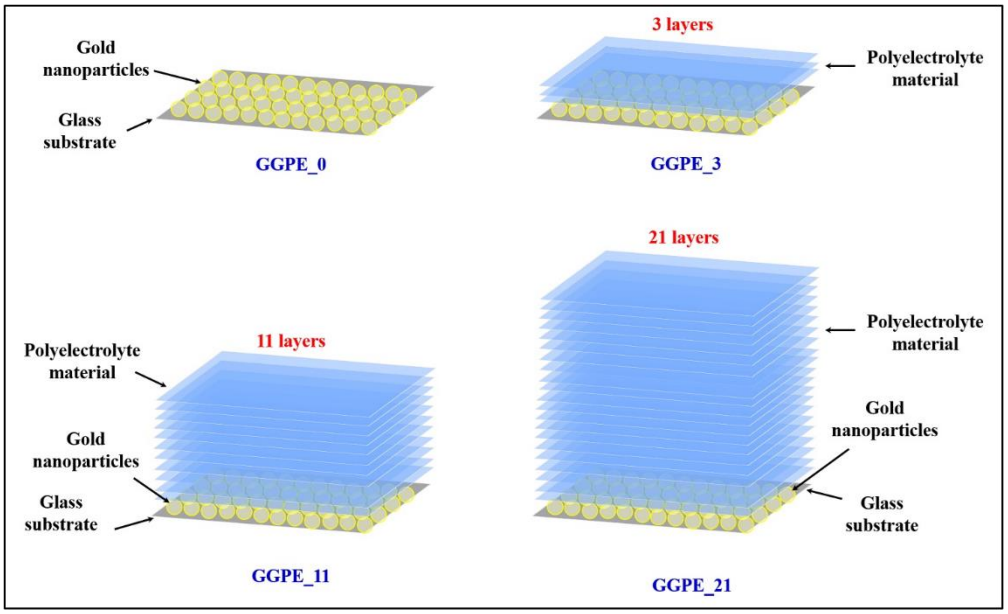

Figure 4.4.1. *Schematic view of the four samples: GGPE_0 (Glass substrate/Gold nanoparticles), GGPE_3 (Glass substrate/Gold nanoparticles/3 layers of Polyelectrolyte material), GGPE_11 (Glass substrate/Gold nanoparticles/11 layers of Polyelectrolyte material) and GGPE_21 (Glass substrate/Gold nanoparticles/21 layer of Polyelectrolyte material).*

The synthesis of gold nanoparticles, the functionalization of glass substrates and the gold nanoparticles array deposition have already been reported in a previous work [43]. Firstly, spherical gold nanoparticles have been synthesized following the Turkevich method [44]. In brief, 600 mL of an aqueous solution of tetrachloroauric (III) acid (0.25 mM) were brought to a boil in a round-bottomed flask under vigorous magnetic stirring. Subsequently, the gold has been reduced by pouring to the boiling solution 15 mL of aqueous sodium citrate solution (0.03 M). After 15 min, the full reduction of the gold salt into monodisperse gold nanoparticles with an average diameter of 20 nm was obtained, as demonstrated by the solution colour that turned from yellow to deep red.

The glass substrates were first cleaned and hydroxylated with piranha solution (3:1 mixture of sulphuric acid to hydrogen peroxide 30%) for 30 min. To modify the surface chemistry, the substrates were dipped in a 5% (v/v) solution of N-[3-(trimethoxysilyl)propyl] ethylenediamine in ethanol for 30 min and then rinsed with milli-Q water. Excess of water was removed using a stream of nitrogen followed by drying in a furnace at 120 °C for 30 min to assure good silanization.

The GNPs arrays were prepared by dipping the functionalized glass slides in the GNPs solution for two and a half hours. The samples were then washed with milli-Q water and dried under a stream of nitrogen.

The polyelectrolytes (PE) solutions of 5 mg/mL Poly(allylamine hydrochloride) (PAH, positively charged) and Poly(styrenesulfonate) (PSS, negatively charged) were prepared in 0.1 M of NaCl in water. Their opposite charge allows the fabrication of multilayers of PE layers via the layer-by-layer (LbL) deposition technique [45] by means of electrostatic interaction.

4.4.2 Results and discussion

Acetic acid has been chosen as test substance because its vibrational modes in liquid and gaseous forms are well-known and generally precisely assigned in literature [46-49]. In figure (4.4.2) are shown the representative Raman spectra collected on the 10% v/v acetic acid solution in a cuvette and on the top surfaces of the glass substrate that can be used as references.

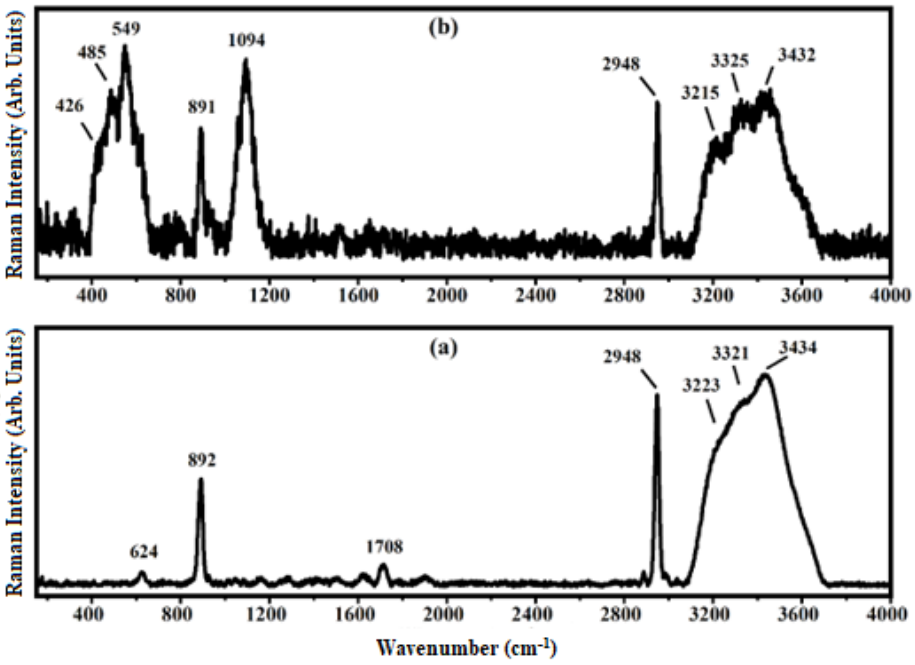

Figure 4.4.2. *Representative Raman spectra collected on the 10 % v/v acetic acid solution in a cuvette (a) and on the top surfaces of the glass substrate (b).*

The spectrum shown in figure (4.4.2.a) is due to acetic acid in volume: the whole laser spot is inside the liquid and the resulting Raman bands are very strong and well defined. The three bands at 892 cm^{-1}, 2948 cm^{-1} and the broad band at 3434 cm^{-1} have been assigned to the (C−C) stretching, (C−H) stretching of acetic acid molecules and to the (O−H) stretching of water molecules, respectively [46,47]. The bands at 3223 cm^{-1} and 3321 cm^{-1} have been assigned to the (O−H) stretching modes [46,47]. Others two weaker bands at 624 cm^{-1} and 1708 cm^{-1} are attributed to the (O=C−O) bending mode and (C=O) stretching, respectively [46,47]. The representative Raman spectrum collected on acetic acid deposited on the top of the glass substrate it is shown in figure (4.4.2.b). Besides the Raman bands described above, figure (4.4.2.a.) which are still detected, there are new bands, at 426 cm^{-1}, 485 cm^{-1}, 549 cm^{-1} and 1094 cm^{-1}, that have been ascribed to the glass substrate [50]. The bands at 624 cm^{-1} and 1708 cm^{-1} seen in the spectrum of figure (4.4.2.a). are not detected in the spectrum of figure (4.4.2.b).

In figure (4.4.3) are shown the Raman spectra of the 10 % v/v acetic acid solution deposited on the substrates with different numbers of polyelectrolyte, see Fig. (4.4.1).

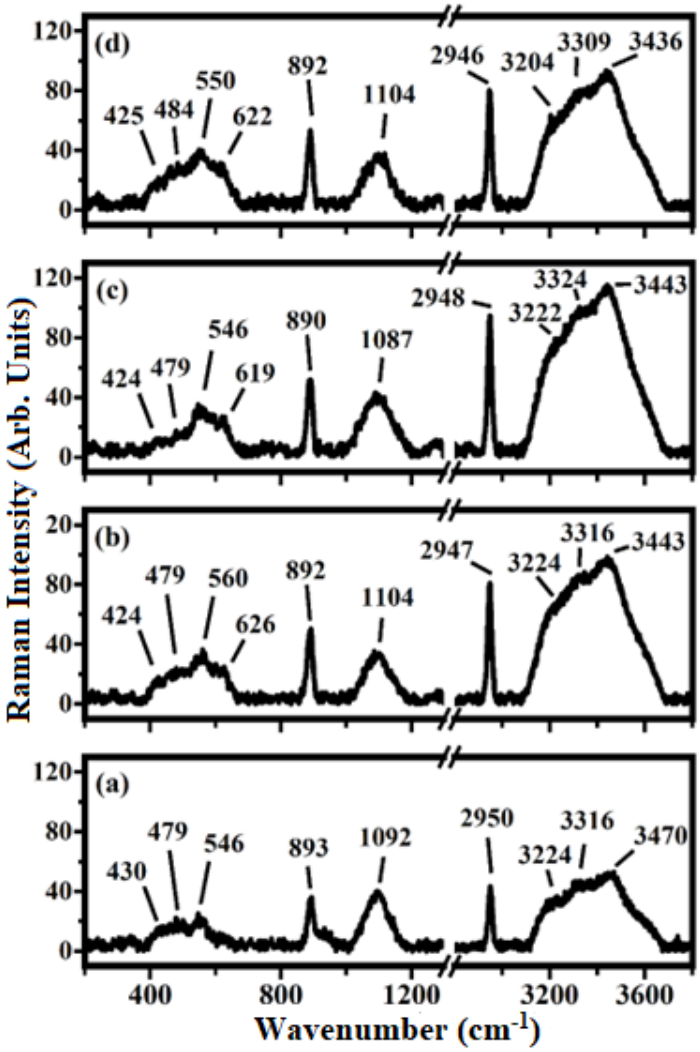

Figure 4.4.3. *Representative Raman spectra of 10 % v/v acetic acid solution in the ranges between 200 and 1300 cm^{-1} and between 2800 and 3800 cm^{-1} on GGPE_0 (Glass substrate/Gold nanoparticles) (a), GGPE_3 (Glass substrate/Gold nanoparticles/3 layers of Polyelectrolyte material) (b), GGPE_11 (Glass substrate/Gold nanoparticles/11 layers of Polyelectrolyte material) (c) and GGPE_21 (Glass substrate/Gold nanoparticles/21 layer of Polyelectrolyte material) (d).*

In the spectra of Figure (4.4.3) are present the bands that fall at 424 cm^{-1}, 430 cm^{-1}, 479 cm^{-1}, 484 cm^{-1}, 546 cm^{-1}, 550 cm^{-1}, 560 cm^{-1}, 1087 cm^{-1}, 1092 cm^{-1} and 1104 cm^{-1} and these are ascribed to the substrate; the bands at 619 cm^{-1}, 622 cm^{-1}, 626 cm^{-1}, 890 cm^{-1}, 892 cm^{-1}, 893 cm^{-1}, 2946 cm^{-1}, 2947 cm^{-1}, 294 cm^{-1}8 and 2950 cm^{-1} are ascribed to the acetic molecules and the others bands above the 3000 cm^{-1} are due to the (O-H) stretching of the water molecules.

Table (4.4.1) resume the observed Raman bands.

Frequency (cm^{-1})						Assignment	references
10% (V) acetic acid aqueous solution							
cuvette	**glass**	**GGPE_0**	**GGPE_3**	**GGPE_11**	**GGPE_21**		
	426	430	424	424	425	Delocalised modes (glass)	[50]
	485	479	479	479	484		
	549	546	560	546	550		
624			626	619	622	bending (O=C–O)	[46][47]
892	891	893	892	890	892	Stretching (C–C)	[46-49]
	1094	1092	1104	1087	1104	Stretching motion of silica tetrahedra (glass)	[50]
1708						Stretching (C=O)	[46][47]
2948	2948	2950	2947	2948	2946	Stretching (C–H)	[46-49]
3223	3215	3224	3224	3222	3204	Stretching (O–H)	[46-49]
3321	3325	3316	3316	3324	3309		
3434	3432	3470	3443	3443	3436		

Table 4.4.1. *Observed Raman bands of acetic acid aqueous solution on cuvette, glass, GGPE_0, GGPE_3, GGPE_11 and GGPE_21 substrates and their assignments.*

In figure (4.4.4) are shown some of the Raman bands of the spectra of figure (4.4.3) fitted in order to study what happen to the samples when the acetic acid is deposited on the different substrate used in this work where the number of polyelectrolyte layer changes as shown in figure (4.4.1).

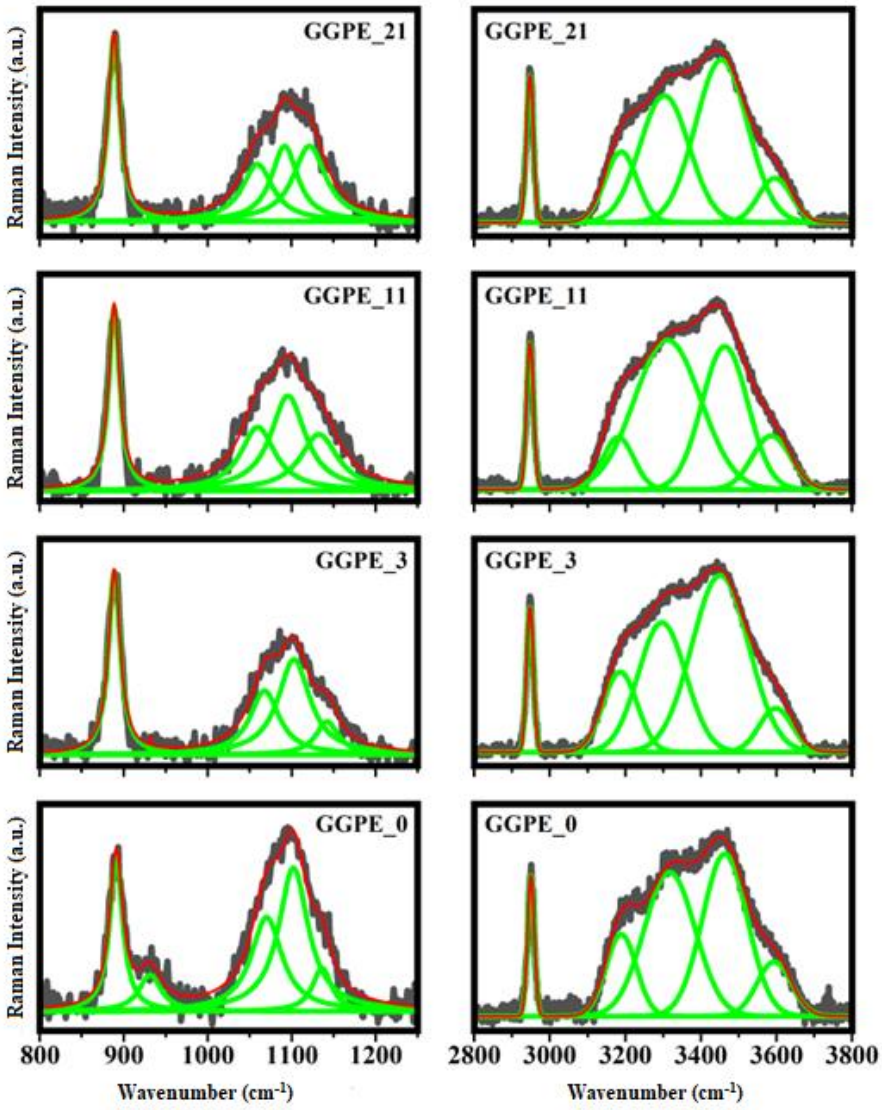

Figure 4.4.4. *Fitting procedure in the ranges between 800 and 1250 cm^{-1} (on the left) and between 2800 and 3800 cm^{-1} (on the right) of the Raman bands of 10 % v/v acetic acid solution deposited on GGPE_0 (Glass substrate/Gold nanoparticles), GGPE_3 (Glass substrate/Gold nanoparticles/3 layers of Polyelectrolyte material), GGPE_11 (Glass substrate/Gold nanoparticles/11 layers of Polyelectrolyte material) and GGPE_21 (Glass substrate/Gold nanoparticles/21 layer of Polyelectrolyte material). The grey line is the experimental spectra, the green lines are the single fitting curve and the red line is the total fitting curve.*

It is possible to see in figure (4.4.4) that the first band at 890 cm^{-1}, ascribed to the acetic acid, is fitted by a single Lorentzian function. (A second small band around 930 cm^{-1} is present in the sample without polyelectrolyte but becomes not detectable as well as the polyelectrolyte layer is deposited on the substrate). The other experimental band around at 1100 cm^{-1} has been fitted by three functions that fall at about: 1065 cm^{-1}, 1098 cm^{-1}

and 1130 cm^{-1}. The band in the middle seems to be the most representative of the Raman features of the substrates and it should be used as reference in order to monitor the effect of the polyelectrolyte layers on the scattering responses of the sample.

The other Raman band at about 2950 cm^{-1}, ascribed to the acetic acid has been fitted with just one single fitting function. The other band, ascribed to the (O-H) stretching in water, has been fitted with four functions that fall at 3186 cm^{-1}, 3307 cm^{-1}, 3458 cm^{-1} and 3593 cm^{-1}, in accordance with a previous study that has shown that the broad O–H band due to the water molecules was fitted with 4 Gaussian functions [49]. The first two bands, according to literature [48,49], are ascribable to the water molecules strongly associated (by hydrogen bonds). The other band at 3458 cm^{-1} is ascribed to the presence of the water molecules weakly associated (only one hydrogen atom involved in the hydrogen bond) and the last band at 3593 cm^{-1} is ascribed to completely free water molecules.

In order to evaluate the effects on the Raman features of the acetic acid solution performed by the increasing of the polyelectrolyte layer, the intensities of the bands ascribed to the acetic acid and of the water on the intensity of the band at 1098 cm^{-1} have been plotted as a function of the layer of polyelectrolyte. In particular, in figure (4.4.5) are shown the ratios I_{890} / I_{1098} (a), I_{2950} / I_{1098} (b), (I_{3186}+I_{3307}+I_{3458}+I_{3593}) / I_{1098} (c).

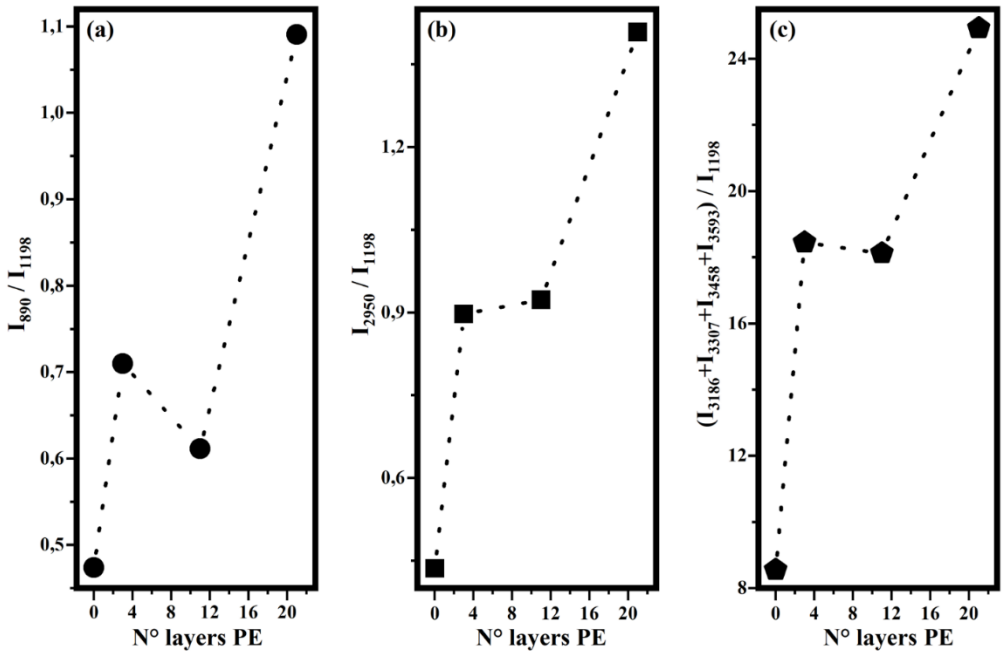

Figure 4.4.5 *Trends, as a function of the number of the layers of polyelectrolyte, of the ratios of the intensities bands that fall at the frequencies indicated as subscripts in the follow relationships:* I_{890} / I_{1098} *(a),* I_{2950} / I_{1098} *(b),* (I_{3186}+I_{3307}+I_{3458}+I_{3593}) / I_{1098} *(c) and that have been calculated by the fitting procedure shown above (see figure 4.4.4).*

The trends shown on figure (4.4.5) indicate that when the acetic acid solution is deposited on the substrates with higher number of layers of polyelectrolyte the Raman scattering results to be stronger then when it is deposited on the substrate without any polyelectrolyte layer. In particular, in the first two panels of figure (4.4.5.a and 4.4.5.b) it has been shown as the intensities of the bands ascribed to the acetic acid molecules are increased when are deposited on the sample GGPE_21 with respect to those collected on the sample GGPE_0. Similar behavior has been shown also for the intensities of the bands ascribed to the (O-H) stretching of the water molecules as it can be seen in figure (4.4.5.c), where the sum of the intensities of the four Raman bands increases as well as the number of the layers of polyelectrolyte that made the whole substrate increases. These results demonstrate that the polyelectrolyte layers behave as surfaces to enhance the Raman scattering.

4.4.3 Conclusions

In this work, sample made by a glass substrate, a layer of gold nanoparticles particles and different layers of polyelectrolyte (0, 3, 11 and 21) have been studied in order to analyse the effect of the number of polyelectrolyte layers on the Raman scattering. For this aim, an acetic acid solution 10 % v/v has been used as a test substance and characterized both in a cuvette and on the top of a glass substrate, and the relative Raman modes have been assigned. Subsequently, the acetic acid solution has been deposited on the four substrates and then the Raman spectra have been collected. In order to make a quantitative evaluation of the observed effects, all the Raman spectra collected on the different substrates have been fitted. The trends of the ratios of the intensities of the Raman bands of the acetic acid solution (acetic acid and water molecules) on the band at 1098 cm^{-1} ascribed to the substrates seem to indicate that there is a Surface Enhanced Raman Spectroscopy effect which is related to the number of the polyelectrolyte layers.

4.5 Raman analysis of chitosan complexed with inorganic complex

In the following section, Raman spectroscopy characterization has been performed on chitosan samples: chitosan films and blends obtained by chitosan films and zinc complex of both pyrazolone and methanol. The blends have been made with the following zinc complex / chitosan ratios: 1/80, 1/40, 1/20, 1/13 and 1/10 or in percentages 1.25%, 2.5%, 5.0%, 7.5% and 10.0%, respectively.

The chitosan polymer has been extensively used in many pharmaceutic and engineering technological applications because it is biocompatible and biodegradable [51]. The chitosan is obtained by deacetylation of chitin which is the primary structural element of shrimp shells and other sea crustaceans (Fig. 4.5.1).

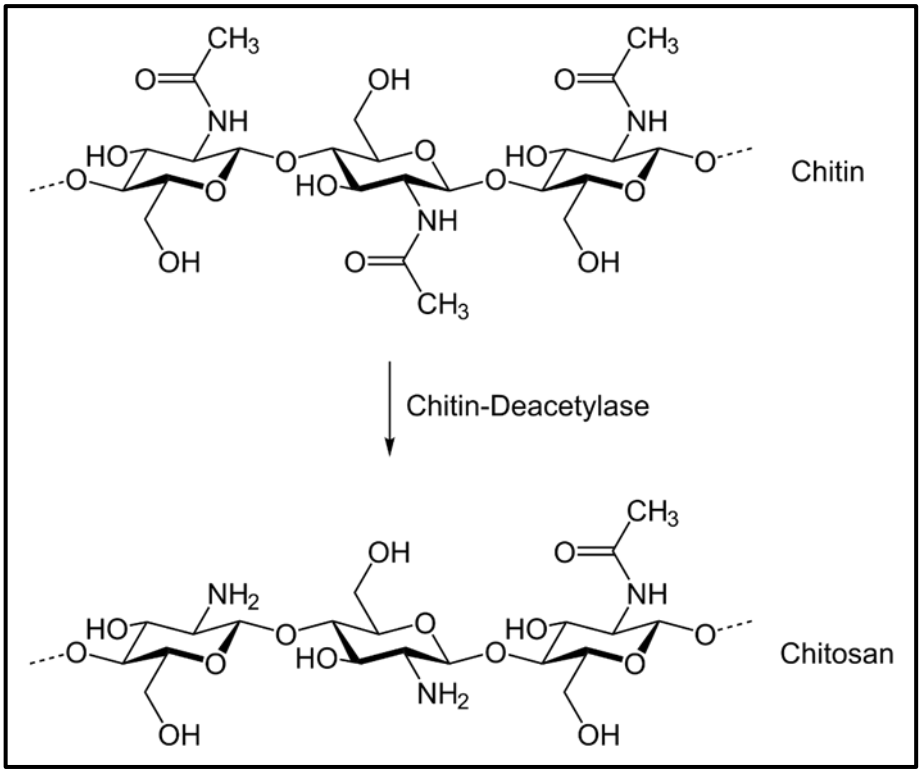

Figure 4.5.1. *Chitosan obtained by deacetylation of Chitin.*

As it can be seen in figure (4.6.1), Chitosan can be considered such as a linear polysaccharide made by two repetitive units: glucosamine and N-acetyl glucosamine. The glucosamine on N-acetyl glucosamine ratio value, called degree of deacetylation, can fall in the range between 30% and 95% [51]. When the degree of deacetylation is about 50%,

the chitosan polysaccharide becomes soluble in acidic aqueous solutions. The Chitosan polymeric structure could therefore be suitable for electrochromic purposes [52].
In the present work, the chitosan polymer has been used as host matrix for the zinc (Zn) complexes of both pyrazolone and methanol (Fig. 4.5.2).

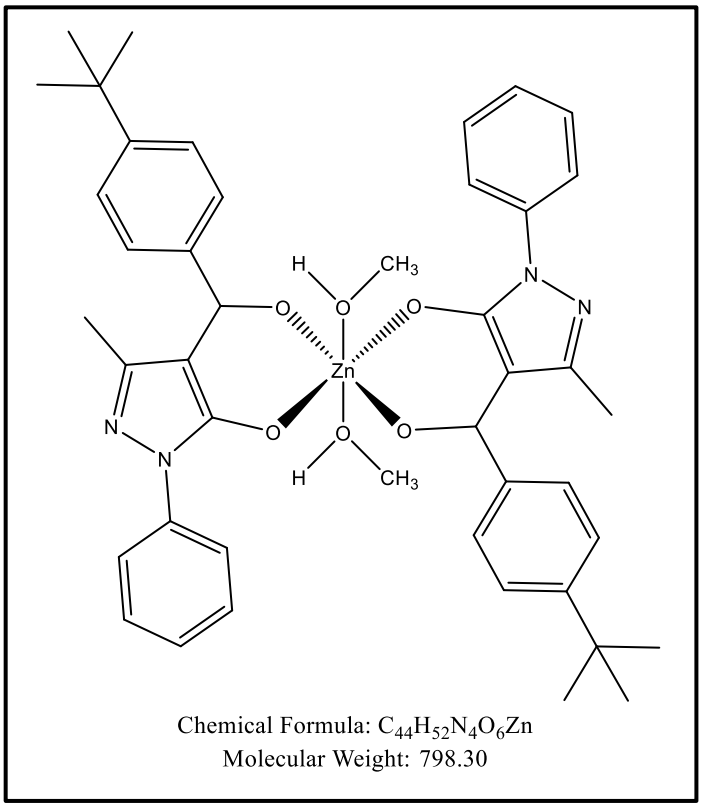

Figure 4.5.2. *Zinc complex of both pyrazolone and methanol.*

The interactions between the chitosan polymer and the Zn complex were studied by Raman spectroscopy, which allowed to better understand the mechanisms of the interactions involved in such systems [53].

This research is part of the paper "New Zinc-based active chitosan films: physicochemical characterization, antioxidant and antimicrobial properties" submitted on My Frontier Chemistry, Inorganic Chemistry.

4.5.1 Experimental

The studied samples are the pure chitosan film (labelled CS) and five other films made with different zinc complex /chitosan molar ratios: 1/80 (labelled CS@$ZNQ_{1,25}$), 1/40 (labelled CS@$ZNQ_{2,5}$), 1/20 (labelled CS@ZNQ_5), 1/13 (labelled CS@$ZNQ_{7,5}$) and 1/10 (labelled CS@ZNQ_{10}) (figure 4.5.3).

Raman spectra were collected by a micro-Raman LABRAM apparatus by Horiba Jobin – Yvon Srl equipped by a 632.8 nm laser sources (He:Ne laser), a 50x objective by Olympus lens with a focal length of 15 mm. The spectral resolutions can be esteemed in 2 cm^{-1}.

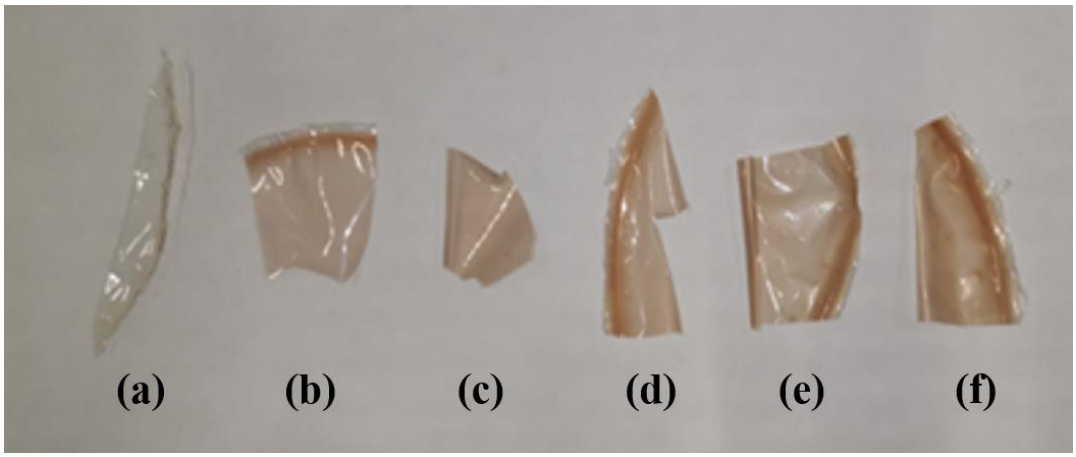

Figure 4.5.3. *Optical images of the studied samples with different zinc complex / chitosan molar ratios: (a) chitosan film labelled CS, (b) 1/80 (labelled CS@$ZNQ_{1,25}$), (c) 1/40 (labelled CS@$ZNQ_{2,5}$), (d) 1/20 (labelled CS@ZNQ_5), (e) 1/13 (labelled CS@$ZNQ_{7,5}$) and (f) 1/10 (labelled CS@ZNQ_{10}).*

4.6.2 Results and discussion

The representative Raman spectrum collected on solid crystalline Zinc complex is shown in figure (4.5.4).

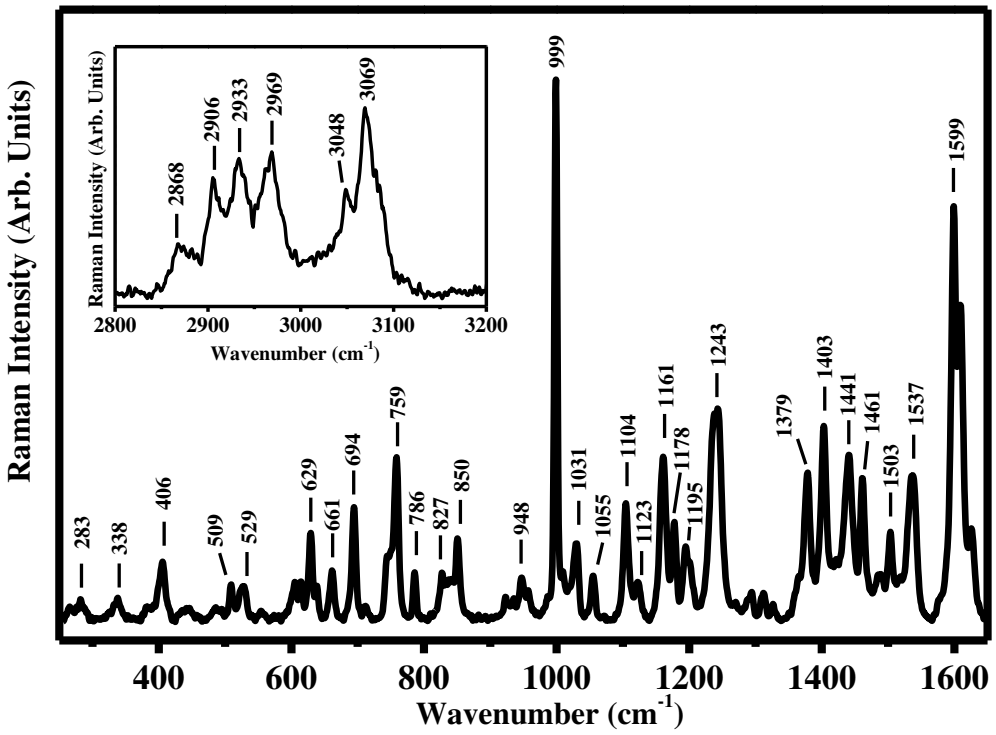

Figure 4.5.4. *Representative Raman spectra collected on the Zinc complex of both pyrazolone and methanol in the solid crystalline phase in the ranges between 250 cm^{-1} and 1650 cm^{-1} and 2800 cm^{-1} and 3200 cm^{-1} (in the inset).*

Among the different Raman features present in the spectra shown in figure (4.5.4) during this work the main attention has been given to the band at 999 cm^{-1}, ascribed to the aromatic ring breathing mode of the pyrazolone ligand. The other bands at 1599 cm^{-1}, 1609 cm^{-1} and 1626 cm^{-1} have been assigned to the C=O stretching of pyrazolone in the enolic forms [54,55]. The Raman bands visible in the inset of figure 4.5.4 are attributed to the (C–H) stretching of the pyrazolone ligand and of the substituent of the pyrazole ring [56,57].

In figure (4.5.5), it is shown the Raman spectra collected on the pure sample of Chitosan polysaccharide.

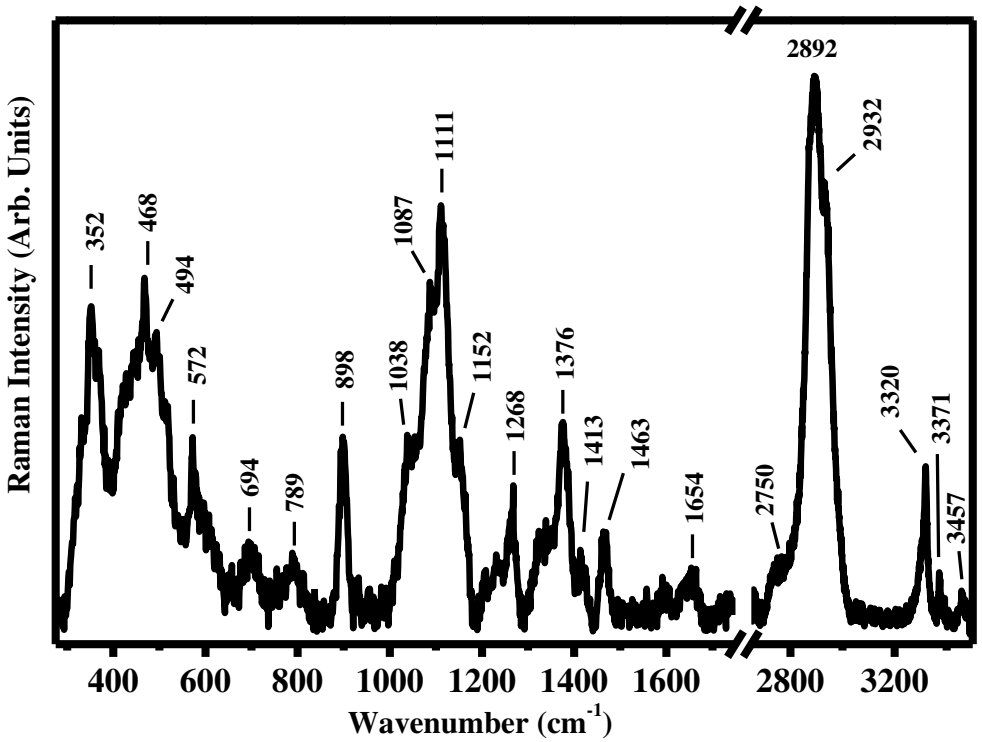

Figure 4.5.5. *Representative Raman spectra collected on the Chitosan polysaccharide pure sample in the ranges between 275 cm^{-1} and 1750 cm^{-1} and between 2650 cm^{-1} and 3500 cm^{-1}.*

The band at 352 cm^{-1} is attributed to the *out of plan bending mode (γ)* of (OH) and of the pyranoid ring (ϕ) while the two bands at 468 cm^{-1} and 494 cm^{-1} are assigned to the *in plane bending mode (δ)* of the glycosidic (C–O–C) and to the δ mode of (CO–NH) + (C–CH_3), respectively [58]. The band that falls at 572 cm^{-1} is due to the γ modes of (N-H) and (C=O) and to the *out of plan bending mode* (ω) of (CH_3) [58]. The Raman band centred at 1111 cm^{-1} is attributed to the overlapping of several peaks: two peaks that fall at 1038 cm^{-1} and 1087 cm^{-1}, assigned to the deformation mode (ρ) of (CH_3) and the (δ) modes of (CH) and (OH) and another peak, that falls at higher frequency 1152 cm^{-1}, is assigned to the stretching (ν) of *(C–O–C) + ν(ϕ) + ν(C–OH) + ν(C–CH_2) + δ(CH) + ρ(CH_2) + ρ(CH_3)* [58]. Other authors ascribed the last bands at 1087 cm^{-1} and at 1152 cm^{-1}, mainly, to the stretching modes of the glycosidic bond (C–O–C) and in particular: symmetric and antisymmetric of C–O–C, respectively [59-62].

The Raman peaks at 898 cm^{-1} is ascribed to the *ν(ϕ) ring breathing (pyd) + ρ(CH_2)* [58-62]. The other bands have been assigned to: the band at 1268 cm^{-1} is ascribed to δ(OH...O) hydrogen bond (HB) + ν(C–C) + ν(C–O) + δ(CH) + δ(CH_2), the band at 1376 cm^{-1} is due

to $\delta(CH_2)$-others deformation of the polysaccharide backbone and to the $\delta(OH)$ and $\nu(\phi)$ and the band at 1463 cm^{-1} is assigned to the $\delta(CH) + \omega(CH_2)$ modes [58-62].

The band at 1654 cm^{-1} is due to the double bond C=C. The other bands at 2750 cm^{-1}, 2892 cm^{-1} and 2932 cm^{-1} are assigned to the $\nu(CH)$, $\nu(CH_2)$ and $\nu(CH_3)$ modes, respectively [58-62].

The Raman band at 3320 cm^{-1} is assigned to the N-H stretching while the other two bands at 3371 cm^{-1} and 3457 cm^{-1} are assigned to the O-H stretching mode [63].

In figure (4.5.6) are shown the Raman spectra collected on the Chitosan sample mixed with different amount of the Zn complex.

The spectra of the $CS@Zn_n$ films show the main characteristics of both chitosan matrix and $[Zn(Q^{ph})_2(MeOH)_2]$ complex (figures 4.5.1 and 4.5.2 respectively). In fact, as it can be seen in figure (4.5.6), the band that falls at 1000 cm^{-1}, typical of the Zn complex, increases as well as the complex concentration in the blends increases. In the same way, the bands above 3300 cm^{-1}, totally ascribed to the chitosan polymer, seems to decrease as well as the Zn complex concentration in the blends increases.

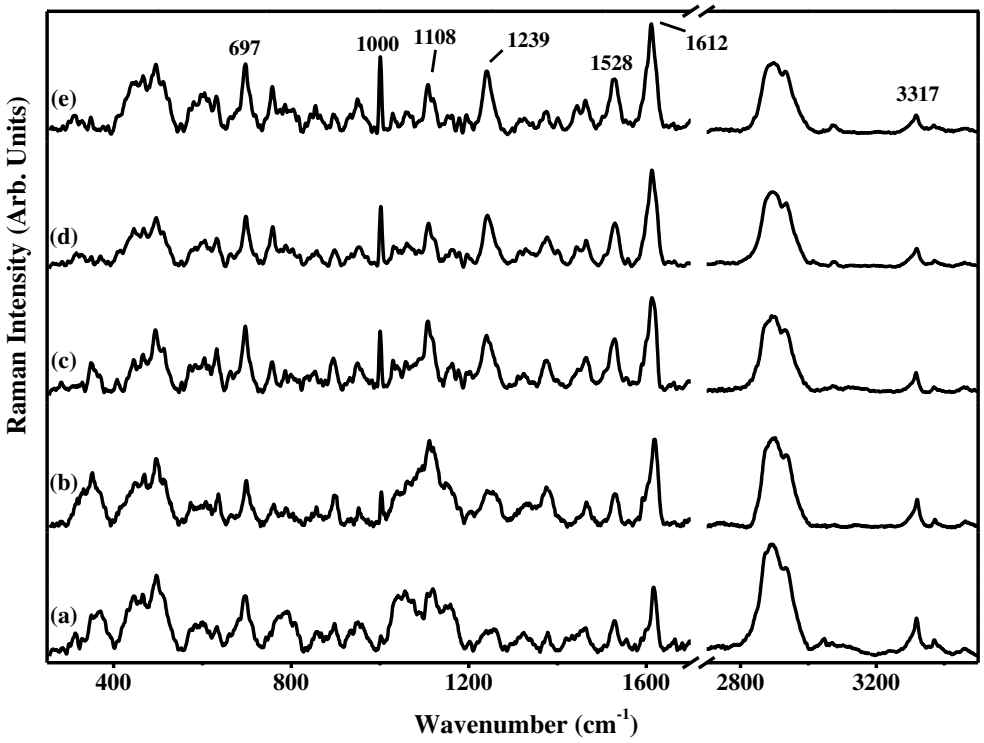

Figure 4.5.6. *Representative Raman spectra in the ranges between 250 cm^{-1} and 1700 cm^{-1} and between 2700 cm^{-1} and 3500 cm^{-1} of the samples obtained with different zinc complex /chitosan molar ratios: (a) 1/80 (labelled $CS@ZNQ_{1,25}$), (b) 1/40 (labelled $CS@ZNQ_{2,5}$), (c) 1/20 (labelled $CS@ZNQ_5$), (d) 1/13 (labelled $CS@ZNQ_{7,5}$) and (e) 1/10 (labelled $CS@ZNQ_{10}$).*

The Raman spectra of CS@Zn_n films show the main difference in the region of glycosidic bond. In fact, it is possible to see in figure (4.5.6) the progressive disappearing of the broad band typical of the pure chitosan band (around ~1108 cm^{-1}) as well as the Zn complex percentage increases. The same behavior can be observed for the Raman band ascribed to the γ(OH) (~350 cm^{-1}) and for the higher frequencies Raman bands due to the (NH) and (OH) stretching. At the same time, in the blend films, the Raman band of the complex ascribable to the (ϕ) ring breathing of the phenyl (ph) appears and grows in intensity (1000 cm^{-1}) [54,55] together with the Raman modes observed at ~1239 cm^{-1}, 1529 cm^{-1} and 1612 cm^{-1}. The strong band at 1612 cm^{-1} is ascribed to the C=O stretching in enolic form of pyrazole ligand which is different from the ketonic form which fall at about 1640 cm^{-1} [54,55]. This is confirmed in the work of *Patel et al.* [64] where this band and the one at 1529 cm^{-1} are related to the imine-ol tautomeric form of the pyrazole ring and to the (C=O) (the former) and the (C=N) (the latter) stretching.

Therefore, the Raman study confirms that the ligand is bonded to the Zn metal in a specific tautomeric form (the imine-ol one). In addition, as it can be seen in figure (4.5.6), the band occurring at 1000 cm^{-1}, typical of the Zn complex, increases as well as the complex concentration in the blends increases. In the same way, the bands above 3300 cm^{-1}, totally ascribed to the to the chitosan polymer, seems to decrease as well as the complex concentration in the blends increases. In order to study such behaviors quantitatively these bands have been fitted by using one single Lorentzian function for the band at 1000 cm^{-1} and two Lorentzian curves for the bands around 3300 cm^{-1}: in particular, one band falls at about 3300 cm^{-1} and the other band falls at about 3320 cm^{-1} (figure 4.5.7).

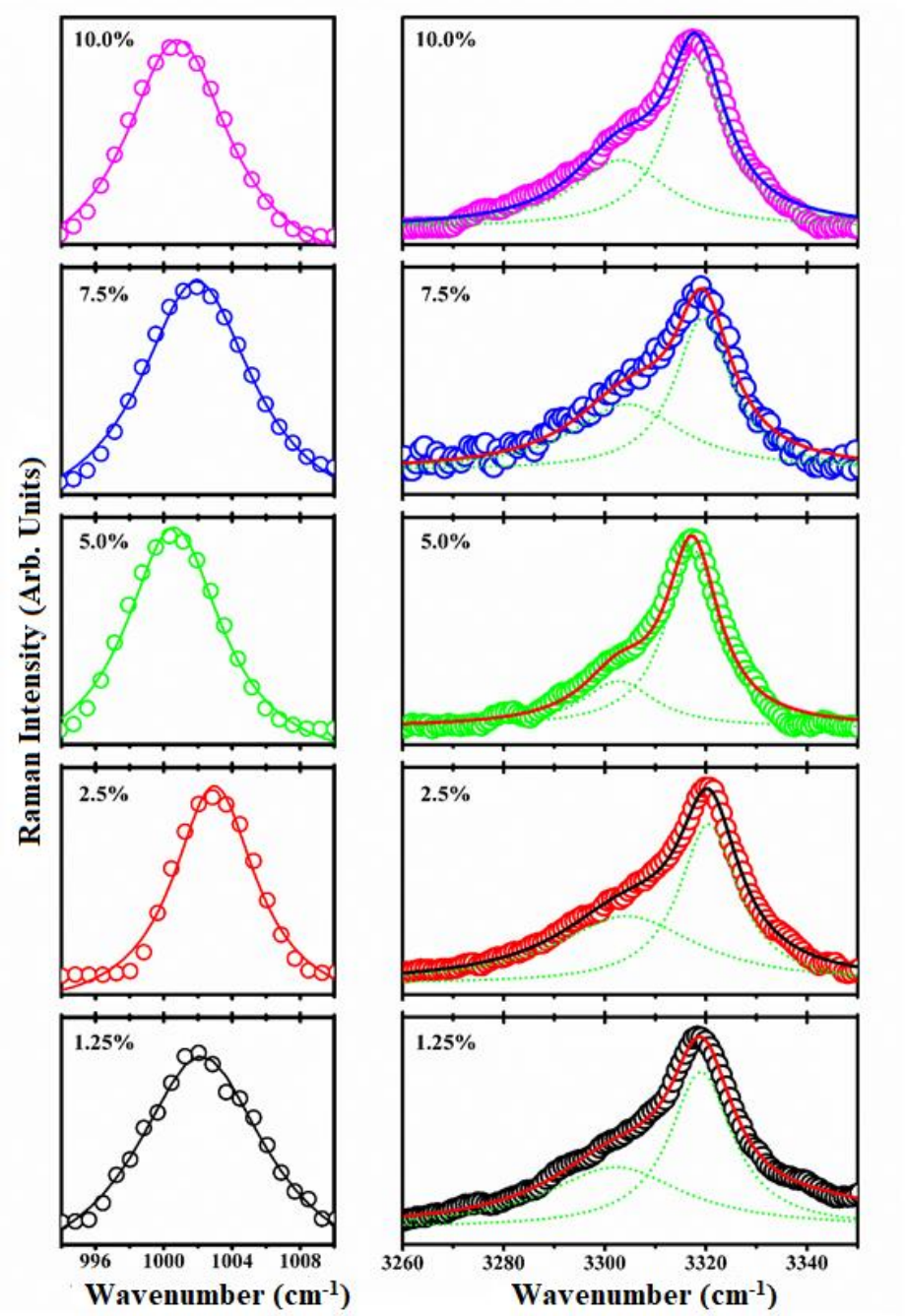

Figure 4.5.7. *Representative Raman spectra in the range between 994 cm^{-1} and 1010 cm^{-1} and between 3260 cm^{-1} and 3350 cm^{-1} of the blend film at different composition: 1.25%, 2.5%, 5.0%, 7.5% and 10%. The open circle are the experimental data, the short dot curves are the single Lorentzian bands and the solid line is the total fitting curves.*

In figure (4.5.8) is plotted the $R_{ZnComplex/Chitosan}$ ratio obtained by the ratio of the Intensity of the Zn complex band at 1000 cm^{-1} and the sum of the bands at 3300 cm^{-1} and 3320 cm^{-1} of the Chitosan, as a function of the blends composition in percentage:

$$R_{Zn\ complex/chitosan} = \frac{I_{(1000\ cm^{-1})}}{I_{(3300\ cm^{-1})} + I_{(3320\ cm^{-1})}} \quad (1)$$

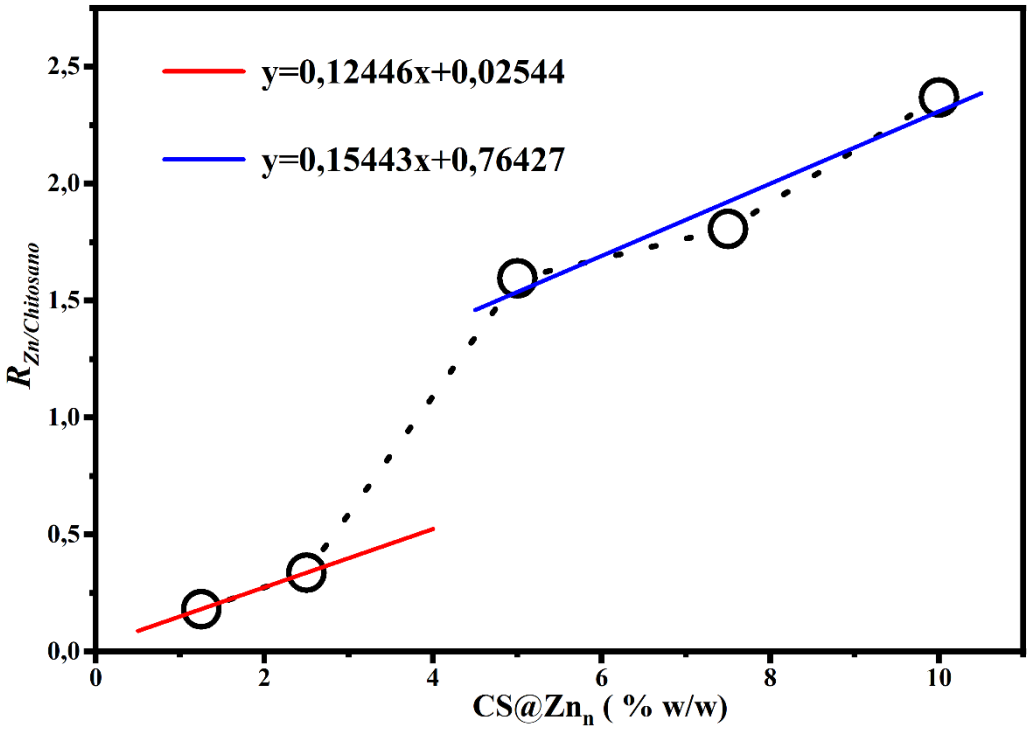

Figure 4.5.8. *Intensity Ratio of the Intensity of the Zn complex band at 1000 cm^{-1} and the sum of the bands at 3000 cm^{-1} and 3200 cm^{-1} as a function of the blends composition in percentage*.

As it can be seen in figure (4.5.8), the trend of such ratio is increasing vs Zn(II) complex composition in percentage. A jump in such trend can be observed for concentrations between 2.5% and 5.0% of the Zn(II) complex. For this reason, the first two points have been fitted with one linear fit (in red, in figure 4.5.8) whereas the last three points were fitted by another linear fit (in blue, in figure 4.5.8). The jump and the different slopes found in the linear fits may be due to a change of the structural order of the blends induced by the increase of the Zn complex percentage.

The intensity of the band at 3300 cm^{-1} band at 3320 cm^{-1} are assigned, as state above to the N-H stretching and therefore, in figure (4.5.8) it is also shown as the N-H bands decrease as well as the Zn complex percentage increases.

Similar trends have been observed for the bands assigned to the hydroxyl group (see Fig. 4.5.6), the intensity of the band around 352 cm^{-1}, attributed to the *out of plan bending mode (γ)* of (OH) and of the pyranoid ring (ϕ), decreases as well as the percentage of the Zn complex increases in the blend). In figure (4.5.9) it is shown the trend of the sum of

the intensities of the bands at 3371 cm^{-1} and 3457 cm^{-1} (assigned to the O-H stretching mode) and the Intensity of the Zn complex band at 1000 cm^{-1}, defined as $R_{(OH)}$:

$$R_{(OH)} = \frac{I_{(3371\ cm^{-1})} + I_{(3357\ cm^{-1})}}{I_{(1000\ cm^{-1})}} \qquad (2)$$

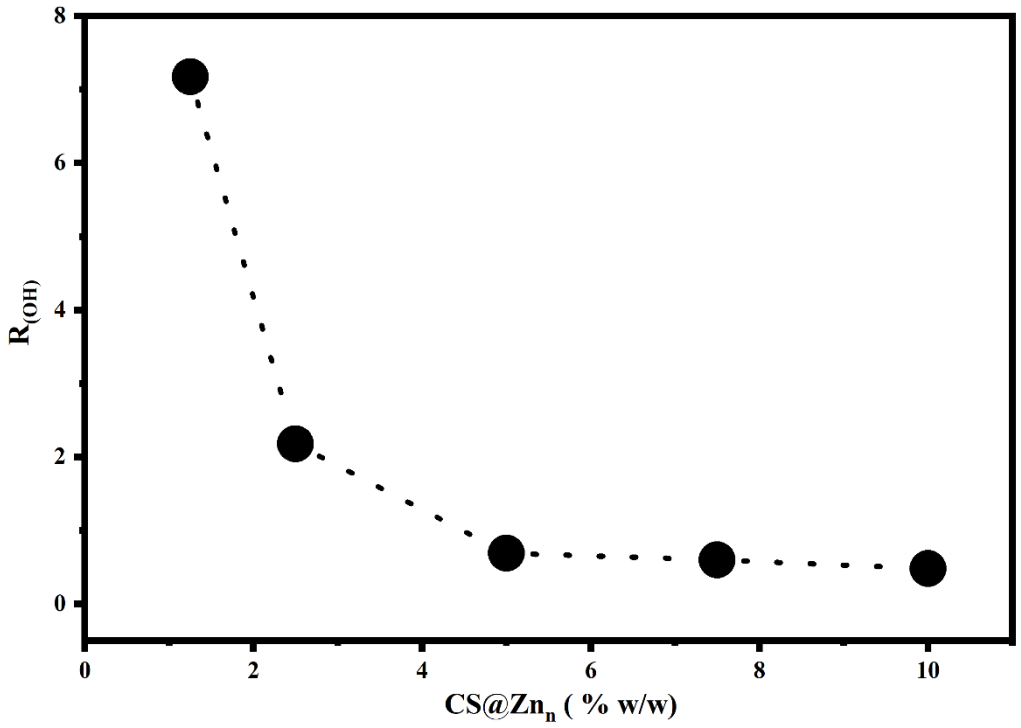

Figure 4.5.9. *Intensity Ratio, $R_{(OH)}$, of the sum of the bands at 3371 cm^{-1} and 3457 cm^{-1} and the Intensity of the Zn complex band at 1000 cm^{-1}, as a function of the blends composition in percentage*.

All the observed trends seem to indicate that the Zn complex affects simultaneously the hydrogen of both the amino and methanol groups, present on the chitosan structure. On the basis of such observations, it has been formulated on hypothesis that could explain the experimental data. It has been shown in figure (4.5.10).

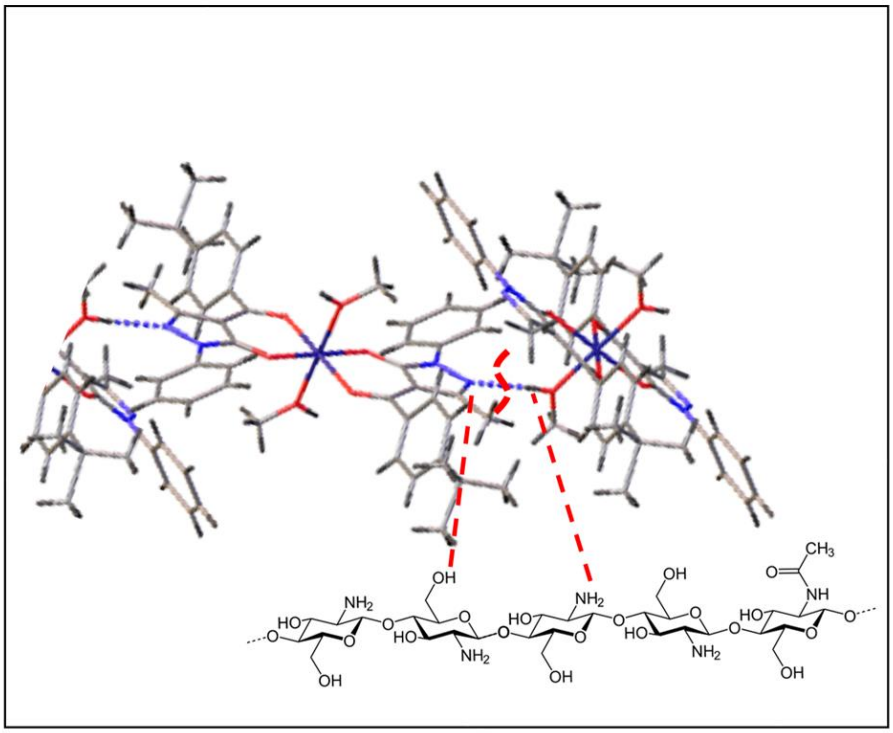

Figure 4.5.10. *Hypothesis of the interactions which occur between the chitosan polymer and the Zn complex: the different units of the complex bonded by hydrogen bonds are divided by the combined action of the –CH_2OH and –NH_2 of the chitosan.*

In the proposed model, Fig. (4.5.10), the different units of the Zn complex bonded each other by hydrogen bonds are divided by the combined actions of the –CH_2OH and –NH_2 of the chitosan chain which acts on the N(1) and O(3) sites of two units of the Zn complex adjacent, respectively.

Nevertheless, deeper quantitative investigations on the study of the interactions between the chitosan polymer and the Zn complex are on the way in order to better understand the mechanism involved.

4.6.3 Conclusions

Micro-Raman spectroscopy has been used in order to study blends made by using Zn-complex and chitosan polysaccharide with the ratios di Zn complex / Chitosan equal to: 1/80 (1.25%), 1/40 (2.5), 1/20 (5.0%), 1/13 (7.5%) and 1/10 (10%). The Raman spectra of the complex and of the polysaccharide and of all the blends samples have been shown and the main Raman features have

been assigned. The Raman study confirms that the ligand is bonded to the Zn metal in a specific tautomeric form (the imine-ol one).

In addition, the fitting procedure of some bands has been shown in order to following the ratio of the Raman band of the complex on the Raman band of the Chitosan. It has been shown that such ratio increases with the Zn complex composition in percentage, showing a jump above the Zn complex concentration of 2,5%. The points before and above the jump have been fitted by two lines with different slope and this aspect has been ascribed to a different change of the structural order of the blends induced by the increase of the Zn complex percentage.

It has been shown that, in the blends, the bands assigned to the N-H and O-H decrease as well as the Zn complex percentage increases. It has been assigned to the interactions between the complex and the N-H and O-H groups which interact with the ligands of the Zn complex. A model of the interactions has been purposed. Nevertheless, deeper quantitative investigations on the study of the interactions between the chitosan polymer and the Zn complex are on the way in order to better understand the mechanism involved.

4.6 Study of the SERS effect of gold plates on bipyridine samples

In this section, the Raman characterization of 5,5'-Bis(mercaptomethyl)-2,2′-bipyridine (BIPY-DT) sample has been performed with the help of gold plate (AuPl-BIPY-DT) to evaluate the SERS effect on the sample. This work is part of the Raman spectroscopic study as contribution to the paper "Luminescent Self-Assembled Monolayer on Gold Nanoparticles: Tuning of Emission According to the Surface Curvature".
The aim of the overall work has been the evaluation of the enhanced Raman response of several Bis(mercaptomethyl)-2,2′-bipyridine (BIPY-DT) due to the use of gold nanorods and gold plates.

4.6.1 Experimental

In figure (4.6.1) it is shown the structure formula of (BIPY-DT).

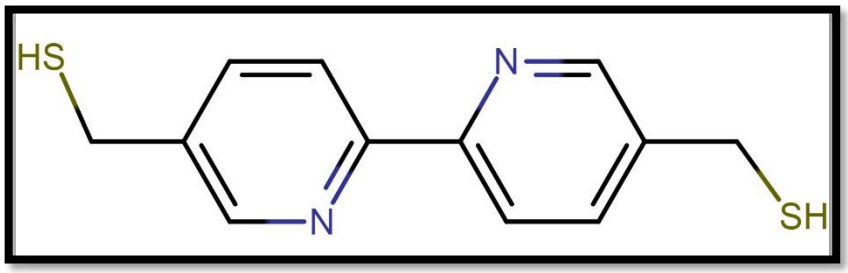

Figure 4.6.1. *Structure formula of 5,5'-Bis(mercaptomethyl)-2,2'-bipyridine (BIPY-DT).*

Micro-Raman spectra were collected using a Horiba-Jobin Yvon microprobe apparatus with spectral resolution ~2 cm-1), equipped with a CCD (256 x 1024 pixels) detector cooled at - 70°C. The spectrum was collected by using the line laser source at 633 nm of He-Ne laser with an emitted power of 17 mW power, equipped with edge filter. The film has been characterized by using the 50x Mplan Olympus objective, focusing a laser spot of about 1 μm of apparent diameter and the spectral resolution is below 2 cm-1. The Raman spectrum shown in the next section is the representative one collected on the sample and is shown only the range where the Raman features were detectable and are not shown the ranges where the Raman spectrum was made only by noise. The Micro-Raman study was carried out on the following sample, gold plate covered by the 5,5'-Bis(mercaptomethyl)-2,2′-bipyridine (AuPl-BIPY-DT).

4.6.2 Results and Discussion

An enhancement effect can be seen when the (BIPY-DT) is deposited on the gold plate (AuPl-BIPY-DT). In figure (4.6.2) and in figure (4.6.3) are shown the representative Raman spectra collected on the sample AuPl-BIPY-DT in the range between 400 and 1650 cm^{-1} (Fig. 4.6.2) and between 500 and 1100 cm^{-1}, 1170 and 1800 cm^{-1}, 2450 and 3000 cm^{-1} (Fig. 4.6.3).

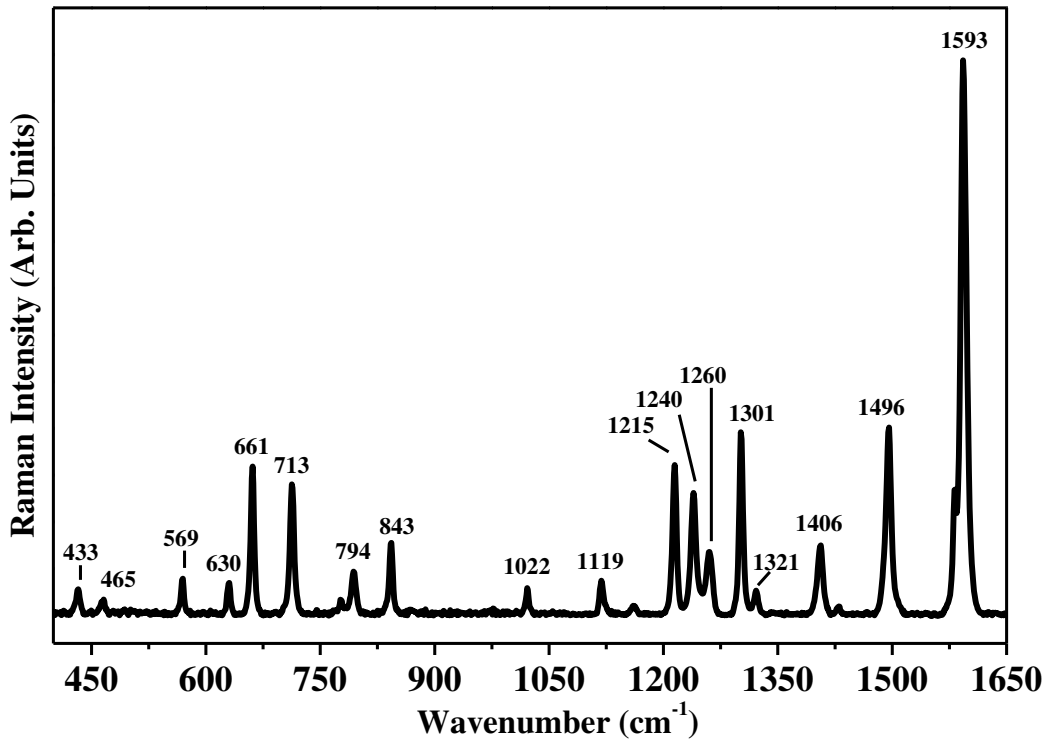

Figure 4.6.2. *Representative Raman spectrum collected, with laser source at 633 nm, on the sample AuPl-BIPY-DT in the range between 400 and 1650 cm^{-1}.*

The sharp Raman peaks of figure (4.6.2) that fall at 433 cm^{-1}, 465 cm^{-1}, 569 cm^{-1}, 630 cm^{-1}, 661 cm^{-1}, 713 cm^{-1}, 794 cm^{-1}, 843 cm^{-1}, 1022 cm^{-1}, 1119 cm^{-1}, 1215 cm^{-1}, 1240 cm^{-1}, 1260 cm^{-1}, 1301 cm^{-1}, 1321 cm^{-1}, 1406 cm^{-1}, 1496 cm^{-1} and 1593 cm^{-1} can be assigned by using the modes described in table (4.6.1). Such Raman peaks are due to the presence of the 5,5'-Bis(mercaptomethyl)-2,2′-bipyridine (BIPY-DT).

Frequency (cm^{-1})	Assignment[a]	references
433	τ(CCCC)16b' (Out of plane Vibration)	[65]
	Sym Ag – ν_{14} interring i.p. bend (In plane modes)	[66]
465	β(C'C)15' (In plane Vibration)	[65]
569	π(CC_{α})10a (Out of plane Vibration)	[65]
	Sym Bu - ν_6 ring o.p. def+interring o.p. bend + (CH) o.p. bend (out of plane modes)	[66]
630	β(CCC)6b' (In plane Vibration)	[65]
	Sym Ag - ν_{13} ring i.p. def (In plane modes) + Sym Bu - ν_{13} ring i.p. def (In plane modes)	[66]
661	Sym Bu - ν_{15} ring i.p. def (in plane modes)	[66]
	Ring i.p. def.	[67][68]
713	Ring breath.	[67][68]
794	Sym Au - ν_4 (CH) o.p. bend (out of plane modes)	[66]
843	β(CCC)12' (In plane Vibration)	[65]
	Sym Bg - ν_4 interring o.p. bend + (CH) o.p. bend (out of plane modes)	[66]
	CH o.p. bend	[67][68]

Table 4.6.1. *Observed Raman bands of AuPl-BIPY-DT and relative assignments and references. i.p., in-plane; o.p., out-of-plane; def, deformation; str, stretching*

Frequency (cm^{-1})	Assignment[a]	references
1022	Sym Bu - ν12 ring i.p. def + ring str (In plane modes)	[66]
1119	β(CH)18a' (In plane Vibration)	[65]
	Sym Bu - ν_8 (CH) i.p. bend (In plane modes)	[66]
	(CH) i.p. def. + ring str	[67][68]
1215	$(CH)_2$ Wagging	[68]
1240	ν(C-C)19a (In plane Vibration)	[65]
	Sym Ag - ν_7 ring str (In plane modes)	[66]
	Inter-ring stretch + ring str. + (CH) i.p. def	[67][68]
1260	Sym Bu – ν_5 + ν_7 ring str + (CH) i.p. bend (In plane modes)	[66]
1301	Sym Ag - ν_6 interring str+ring str+ring i.p. def (In plane modes)	[66]
1321	Sym Ag - ν_5 CH i.p. bend + interring i.p. bend (In plane modes)	[66]
	Inter-ring str. + ring str. + (CH) i.p. def	[67][68]
1406	Sym Bu - ν_4 CH i.p. bend + ring str (In plane modes)	[66]
	$(CH)_2$ Wagging	[67][68]

Table 4.6.1. (continued) *Observed Raman bands of AuPl-BIPY-DT and relative assignments and references. i.p., in-plane; o.p., out-of-plane; def, deformation; str, stretching.*

Frequency (cm^{-1})	Assignment[a]	references
1496	ν(C-C)19a (In plane Vibration)	[65]
	Sym Ag – ν_3 (CH) i.p. bend	[66]
	ring str (In plane modes)	
	(CH) i.p. def. + ring str	[67][68]
1593	ν(C-N)8b (In plane Vibration)	[65]
	Sym Ag - ν_1 ring str (In plane modes)	[66]
	Ring str.	[67][68]

Table 4.6.1. (continued) *Observed Raman bands of AuPl-BIPY-DT and relative assignments and references. i.p., in-plane; o.p., out-of-plane; def, deformation; str, stretching.*

Quite interesting are the Raman spectra shown in figure (4.6.3). In this case among the Raman bands at 567 cm^{-1}, 630 cm^{-1}, 661 cm^{-1}, 712 cm^{-1}, 747 cm^{-1}, 794 cm^{-1}, 843 cm^{-1}, 1023 cm^{-1}, 1216 cm^{-1}, 1241 cm^{-1}, 1262 cm^{-1}, 1302 cm^{-1}, 1407 cm^{-1}, 1495 cm^{-1}, 1541 cm^{-1} and 1593 cm^{-1} appears the Raman band at 2561 cm^{-1} which is assigned to the (S-H) stretching. The bands at 747 cm^{-1} and 1541 cm^{-1} are associated to the mode ν_5 ((CH) o.p. bend + ring o.p. def) and ν_2 (ring str.) of the BIPY-DT, respectively [77].

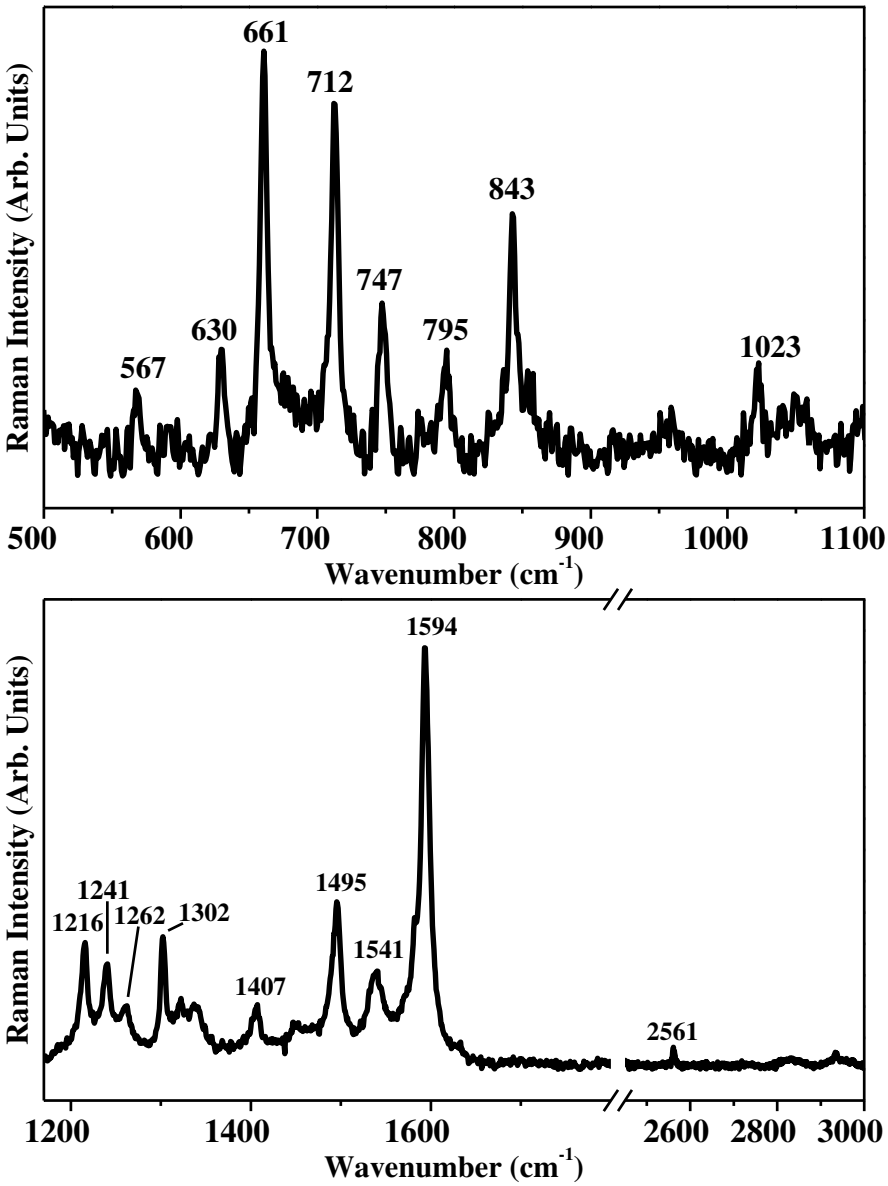

Figure 4.6.3. *Representative Raman spectra collected, with laser source at 633 nm, on the sample AuPl-BIPY-DT in the ranges between 500 and 1100 cm^{-1} (on the top) and between 1170 and 1800 cm^{-1} and between 2450 and 3000 cm^{-1} (on the bottom).*

The presence of the band associated to the (S-H) stretching means that the enhancement effect allows to see that the BIPY-DT layer on the gold plate in the AuPl-BIPY-DT samples is not homogenous: in some area there are not thiol groups free and in others are there is the presence of free S-H groups. The reason to explain such experimental evidence could be addressed to the orientation of the BIPY-DT molecules on the plate. When the (S-H) groups are detectable the molecules of BIPY-DT are

perpendicularly bonded to the gold surface and one of two thiols group of the BIPY-DT molecule remains free. It means that when the (S-H) stretching is not visible (Fig. 4.6.2) then the BIPY-DT molecules are parallel bonded to the gold surface. However, other studies are on the way with the aim to confirm such hypothesis.

4.6.3 Conclusions

Micro-Raman spectroscopy has been used to study 5,5'-Bis(mercaptomethyl)-2,2′-bipyridine deposited on gold nanoplate.

In this work, the attribution of the Raman spectra observed on the AUPl-BIPY-DT has been purposed.

In this work, an enhancement effect induced by gold plate has been shown on the BIPY-DT, with the characteristic ring stretching mode at about 1595 cm^{-1} seen in both the systems. Moreover, it has been shown that most probably the BIPY-DT molecules are bonded in two different ways: parallel to the gold surface (Fig. 4.6.2) and perpendicularly to the surface (Fig. 4.6.3). A deeper investigation on the orientation of such molecules, when bonded to the gold surfaces, is on the way.

4.7 Raman characterization of functionalised Graphite

In this section, the Raman spectroscopic study of graphite functionalised samples has been done. The samples have been functionalised with sulphur bridges and Raman investigation on the functionalised samples has been conducted in order to study the interaction between graphite and sulphur bridges. The typical Raman features of (S-S) and (S-H) bonds are not been appreciable in the functionalised graphite however a difference in the crystalline structure of the graphite has been detected between the functionalised samples and a reference.

Graphite is a natural molecule that possesses a polymeric crystalline lattice and has an intrinsic electronic conductance that can be used in optoelectronics. Uses of graphite in fabrication of electrodes for ED or as precursor to the formation of graphene films have already been reported [69-72]

4.7.1 Experimental

Raman analyses were performed by using a confocal micro-Raman LABRAM supplied by Horiba-Jobin-Yvon equipped with a Nd-YAG laser at 532 nm, a charge-coupled device (CCD) cooled with a Peltier module 1024x256, 16 bits dynamic range (pixel size 27 µm) and a long working distance objective 50x. (Some spectra have been collected by using He:Ne laser at 633 nm which do not show any remarkable differences and therefore not shown).

In figure (4.7.1) are shown the two samples which should be: graphite S-S and graphite S-H (Fig. 4.7.1a and 4.7.1b). In figure (4.7.1c) is shown the sample used as reference .

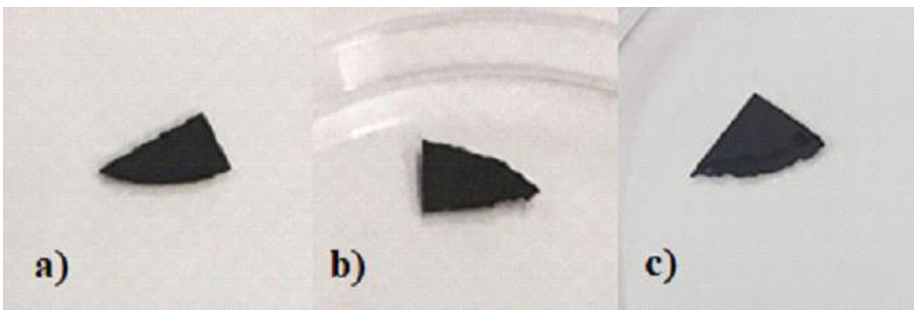

Figure (4.7.1): *Photographs of the graphite S-S (a), the graphite S-H (b) and the reference sample (c).*

As it can be seen in figure (4.7.1), all the samples result to be quite similar. In figure (4.7.2) are shown the relative optical images collected on these samples with the 50x objective of the microscope.

As it can be seen in figure (4.7.2), all the samples, together with the reference, show the same optical features typical of the graphite surfaces.

Figure 4.7.2. *Optical image collected with 50x objective of the graphite S-S (a), the graphite S-H (b) and the reference sample (c).*

4.7.2 Results and discussion

In figures (4.7.3-4.7.5) are shown the representative Raman spectra collected on the graphite S-S, the graphite S-H and the reference sample respectively.

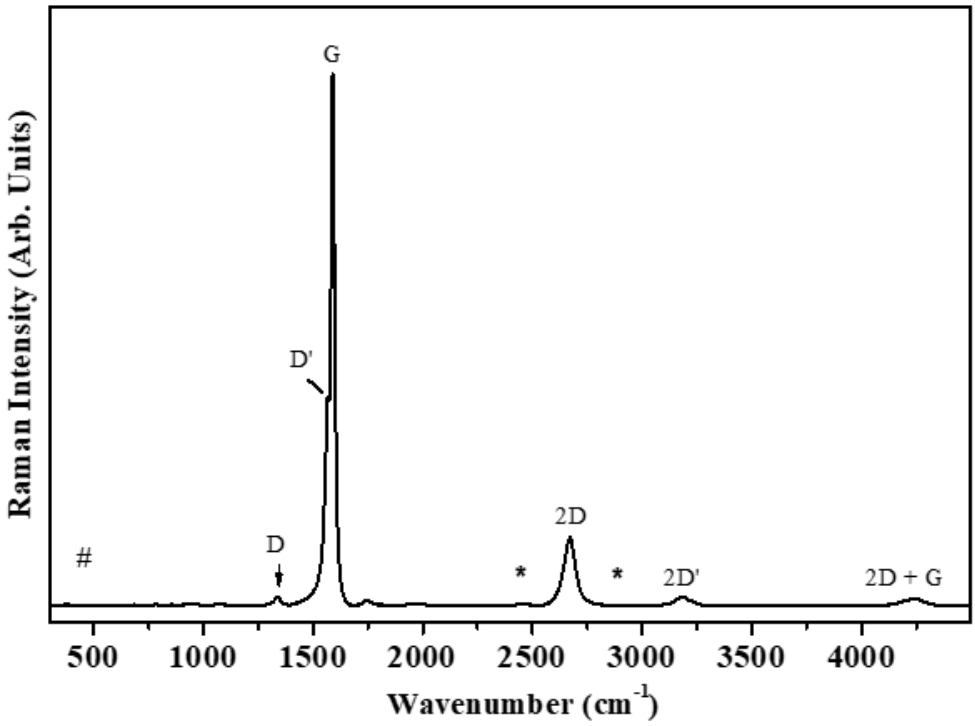

Figure 4.7.3. *Representative Raman spectrum of Graphite S-S. Hash symbol marks the position of S-S mode Raman band. Asterisk mark the position of combination bands.*

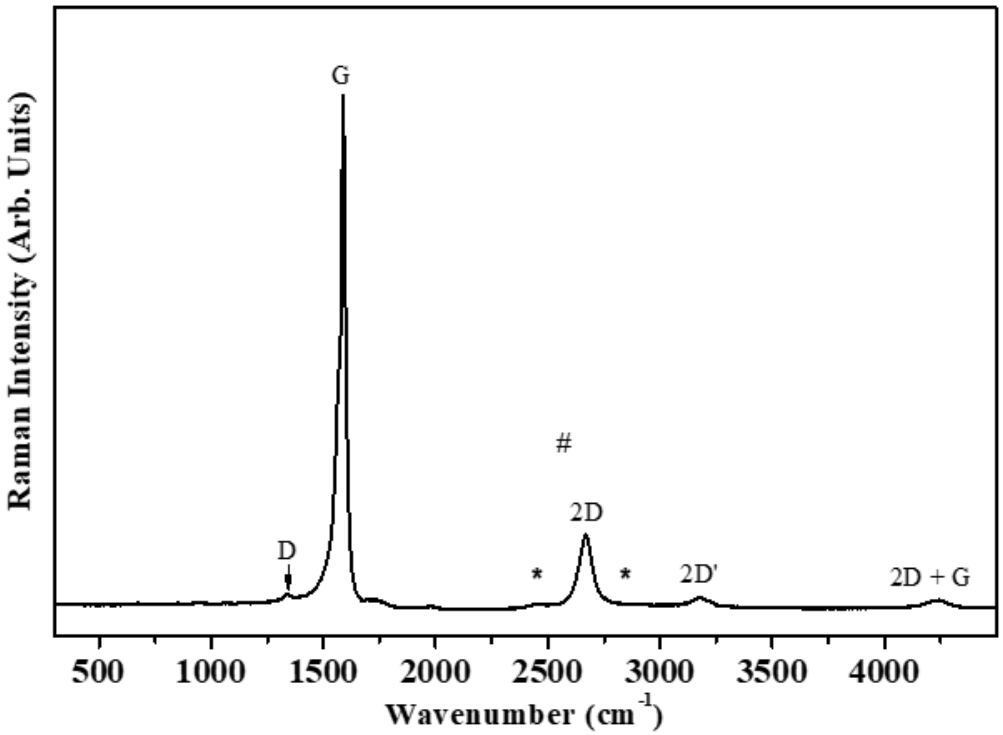

Figure 4.7.4. *Representative Raman spectrum of Graphite S-H. Hash symbol marks the position of S-H mode Raman band. Asterisk mark the position of combination bands.*

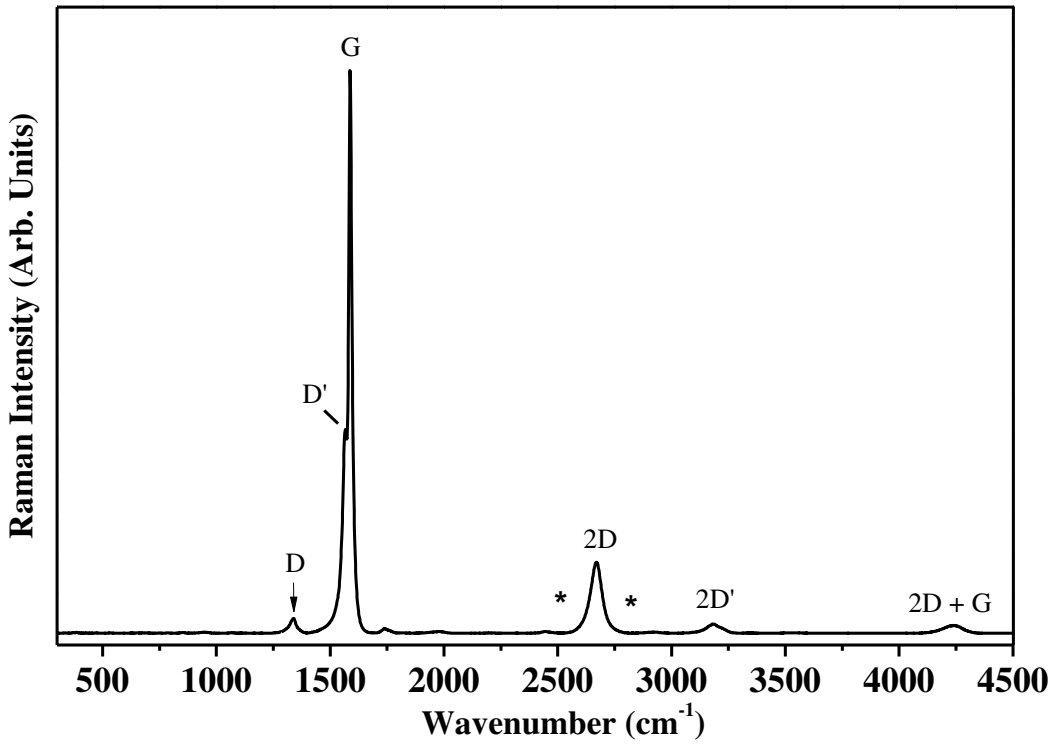

Figure 4.7.5. *Representative Raman spectrum of Graphite reference sample. Asterisk mark the position of combination bands.*

As it can be seen in the figures (4.7.3-4.7.5), all the spectra show the doubly degenerate phonon mode of graphite (E_{2g}) named G band which results to be quite sharp and intense band and falls at 1589 cm^{-1}. In the spectra shown in figures (4.7.3-4.7.5) is possible to notice the presence of a band indicated by D letter. The D band is connected to the "*disorder*" of the lattice. This band results to be quite weak in the studied samples. It falls at 1334 cm^{-1} for the graphite S-S, 1341 cm^{-1} for the graphite S-H and 1340 cm^{-1} for the reference sample.

Consequently, the overtones and combination bands of this band are very weak. Notably, the combination bands, for which the assignments are still difficult, at around ~2450 cm^{-1} (D + D") and ~2950 cm^{-1} (D +G) and marked with an asterisk in the spectra are here relatively absent.

Quite interesting are the bands 2D and 2D' at ~2669 cm^{-1} and ~3181 cm^{-1}, respectively. In the figures (4.7.3-4.7.5) the 2D + G combination band at ~4240 cm^{-1} can be detected [73-76].

The results of Raman characterization are summarised in table (4.7.1).

Frequency (cm^{-1})			**Assignments**	**References**
S-S	**S-H**	**reference**		
1336	1341	1340	D	[73-76]
1568		1567	D’	[73-76]
1589	1588	1587	G	[73-76]
2671	2669	2670	2D	[73-76]
3184	3184	3185	2D’	[73-76]
4242	4240	4245	2D+G	[73-76]

Table 4.7.1. *Observed Raman bands of graphite S-S, graphite S-H and graphite reference sample.*

In figure (4.7.6) are shown the bands obtained by the deconvolution procedures of the D band at ~1338 cm^{-1}, of the G band at ~1588 cm^{-1} and of the 2D band at ~2670 cm^{-1}.

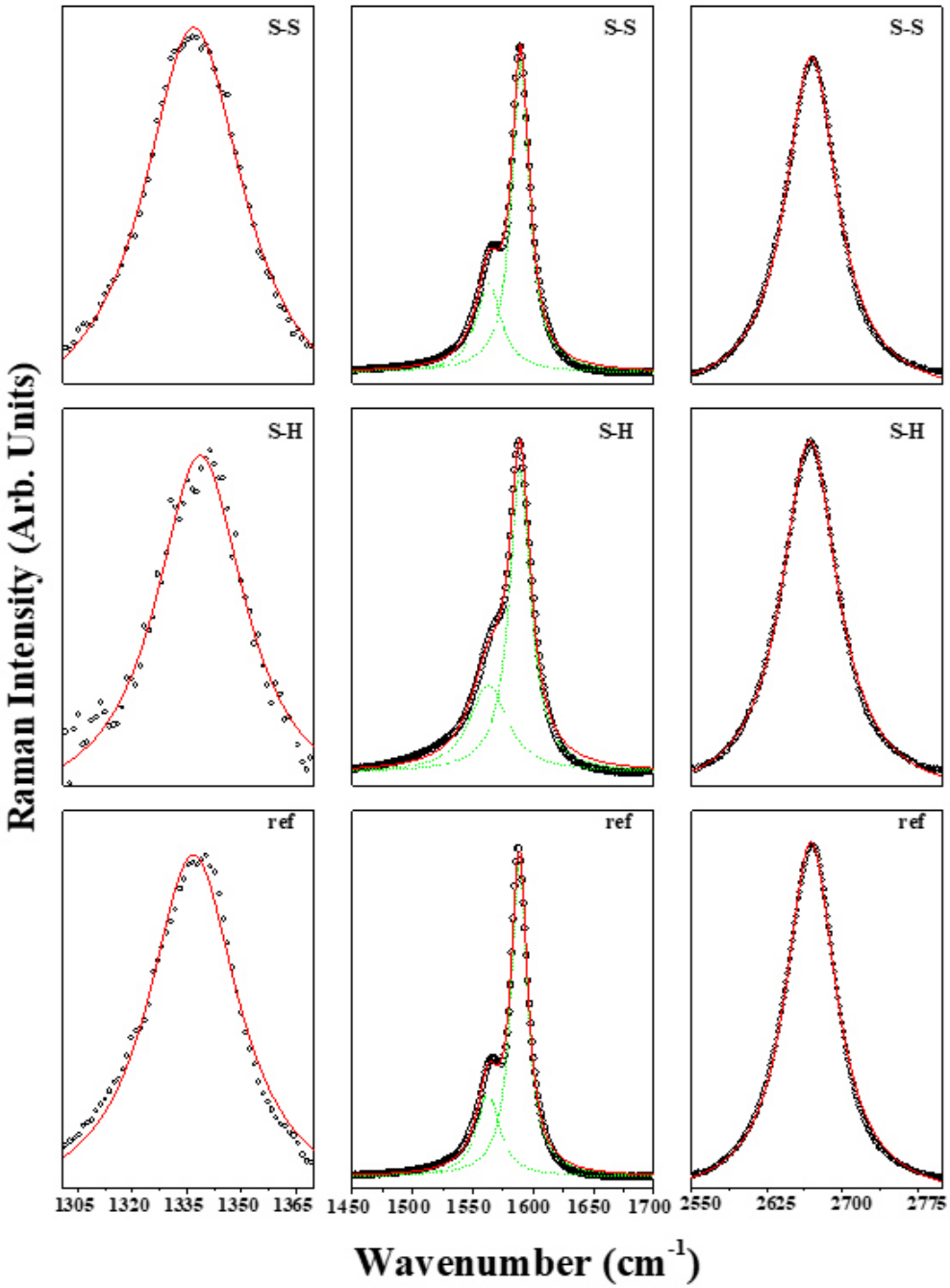

Figure 4.7.6. *Representative Raman spectra of Graphite in the range of the D band (~1338cm^{-1}), G band (~1588cm^{-1}) and 2D band (~2670 cm^{-1}) of the graphite S-S (top), graphite S-H (middle) and of the reference sample (bottom). The open circle are the experimental data (black line), the dot curves are the single Lorentzian functions (green lines) and the solid lines are the total fitting curves (red line).*

The S-S and S-H modes are not detected on the spectra shown in figures (4.7.3-4.7.5). In order to better investigate such samples the following ratios have been calculated: ratio between the intensities of the G and D bands labelled as $R_{G/D}$ (eq. 4.7.1), the ratio between the intensities of the G and D' bands labelled as $R_{G/D'}$ (eq. 4.7.2), the ratio of the intensities

of the G and 2D bands labelled as $R_{G/2D}$ (eq. 4.7.3), the ratio of the sum of the intensities of the G and D' bands on the intensity of the 2D band labelled as $R_{(G+D')/2D}$ (eq. 4.7.4) and the ratio of the intensities of the D' and 2D bands labelled as $R_{D'/2D}$ (eq. 4.7.5).

$$R_{G/D} = \frac{I_{(G\ band)}}{I_{(D\ band)}} \tag{4.7.1}$$

$$R_{G/D'} = \frac{I_{(G\ band)}}{I_{(D'\ band)}} \tag{4.7.2}$$

$$R_{G/2D} = \frac{I_{(G\ band)}}{I_{(2D\ band)}} \tag{4.7.3}$$

$$R_{G+D'/2D} = \frac{I_{(G\ band)} + I_{(D'\ band)}}{I_{(2D\ band)}} \tag{4.7.4}$$

$$R_{D'/2D} = \frac{I_{(D'\ band)}}{I_{(2D\ band)}} \tag{4.7.5}$$

In table (4.7.2) are reported the results of the ratios above listed.

	Intensity Ratios				
	$R_{G/D}$	$R_{G/D'}$	$R_{G/2D}$	$R_{G+D'/2D}$	$R_{D'/2D}$
graphite S-S	31	2.5	2	2.8	0.8
graphite S-H	68.5	1.9	2	3	1
Reference	21.2	2.8	1.9	2.6	0.7

Table 4.7.2. *Intensity ratio of eq. 1-5 between fitted bands obtained for graphite S-S, the graphite S-H and the reference sample.*

From the data shown in table (4.7.2) it is possible to state that the procedure used to obtain the graphite S-S does not affect the crystalline structure of the graphite lattice as well as the procedure used to obtain the graphite S-H does.

4.7.3 Conclusions

Raman spectroscopy has been used to characterize two samples of graphite functionalized: graphite S-S and graphite S-H. No Raman evidence of the S-S or S-H modes have been detected. From the deconvolution of some bands it has been possible to state that the procedure used to obtain the graphite S-S does not affect the crystalline structure of the graphite lattice as well as the procedure used to obtain the graphite S-H does.

4.8 Raman spectroscopic investigations of Graphene nano-plates on Silica support

Research on the use of graphene in optoelectronics is nowadays well-started. The performances of ED multilayer-based and the presence of interfacial layers of graphene have been already done [71, 77-79].

In the following section, graphene nano-plates (GNP) deposited on silica substrates have been studied by micro-Raman spectroscopy. GNP were made up by several sheets with overall thickness ranging from 1 to 15 nm [80].

It is known that graphene samples show the following Raman bands: G band (one phonon from Brillouin zone center), D band (one phonon due to the amorphous phase), the overtone 2D band and small bands due to the second/third order modes.

Raman analysis of these bands allows to investigate several properties of graphene systems, such as: the thickness, the degree of order of the lattice, the mechanical strain and, in some case, the chemical doping of the sample [81-84].

The Raman study is part of the paper "Spectroscopic and morphological study of graphene nanoplatelets thin films on Si/SiO2 substrates" published on Material Research Express in 2019.

4.8.1 Experimental

Raman spectroscopic investigation was performed by a micro-Raman LABRAM Jobin Yvon Srl, equipped with: 10X and 50X objectives, a Nd-YAG laser with 50 mW adjustable power, doubled 532 nm and with a CCD detector, cooled with a Peltier module 1024 x 256. The spectral resolution is ~2 cm^{-1}.

In figure (4.8.1) it is shown the photo representative of the samples. It can be seen in figure (4.8.1) a quite uniform black layer which covers the whole silica surface.

Figure 4.8.1. *Representative photograph of the samples.*

When the sample is observed under a microscope, it results to be as shown by the representative optical images of figure (4.8.2). The sample seems to be quite uniform with some "islands" thicker.

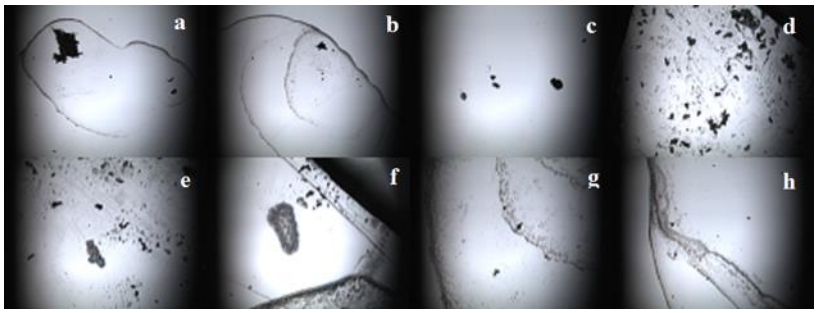

Figure 4.8.2. *Optical Images acquired on the top of the samples.*

4.8.2 Results and discussion

The representative Raman spectrum of the background it is shown in figure (4.8.3). As it is possible to see in figure (4.8.3), the background spectrum shows two Raman bands at 518 and 964 cm^{-1} assigned to the silica substrate, which will be present in all the spectra collected during this work. The Raman bands assigned to the "carbon-based material" used to cover the top surface of the substrate, are not detectable on the spectra collected on the background of the sample.

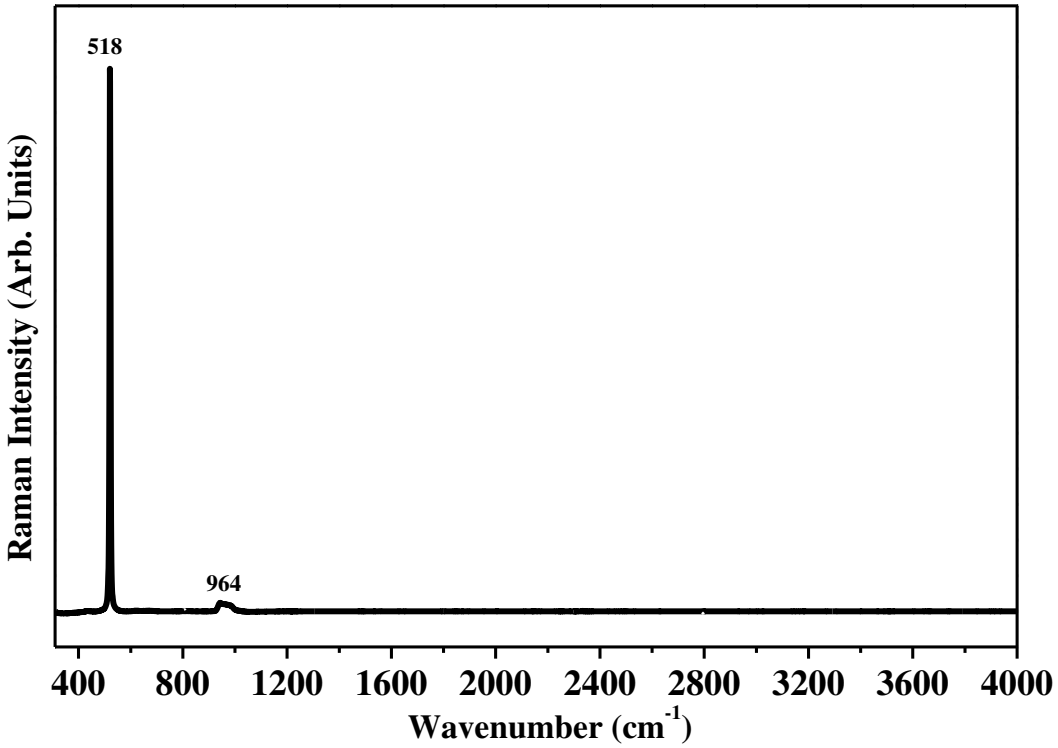

Figure 4.8.3. *Representative Raman spectra of the background of the sample*.

In figure (4.8.4) it is shown the representative Raman spectra collected on the "islands" saw in figure (4.8.2).

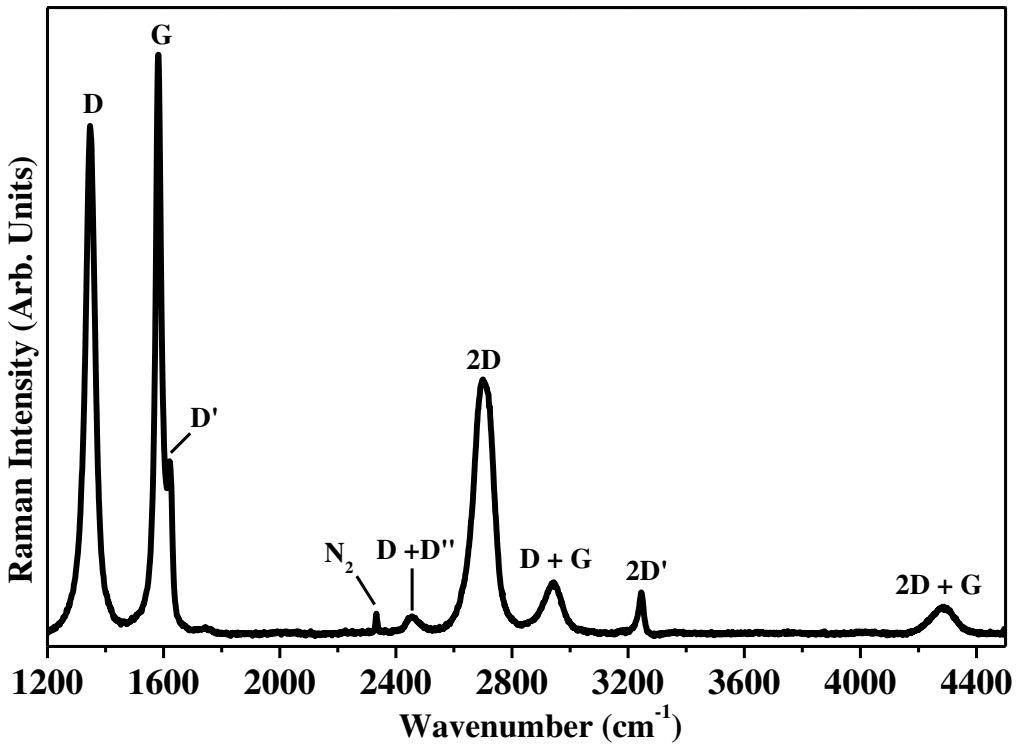

Figure 4.8.4. *Representative Raman spectra collected on the "islands" shown in figure 4.8.2 in the range 1200 - 4500 cm^{-1}*.

As it can be seen in figure (4.8.4), beyond the band assigned to the silica substrate (bands non shown in figure 4.8.4 since the spectral range goes from 1200 and 4500 cm^{-1}) are detectable bands which are assigned to the graphene. In fact, [80-84] there are the D, G and 2D bands which fall at 1346 cm^{-1}, 1582 cm^{-1} and 2719 cm^{-1}, respectively. At about 1620 cm^{-1} falls the D' band. Moreover, it is possible to see the others combination bands such as: D + D" (~2462 cm^{-1}), D + G (~2951 cm^{-1}), 2D +G (~4300 cm^{-1}) and the 2D' (~3249 cm^{-1}). These Raman bands are ascribed to the presence of disordered graphene [80-88].

4.8.3 Conclusions

In conclusion, during the present work silica substrates were covered by disorder graphene, also if it is not detectable of the background spectra. The presence of graphene it is confirmed by the spectra collected on the “island” which shows the typical Raman bands of disordered graphene.

4.9 Surface enhancement of Ag thin layer on Raman spectra of deposited Rhodamine 6G films by pseudo-cavity mode of the substrate

The Raman characterization of three samples made of spin coated Rhodamine 6g (R6g) directly on glass or Silver (Ag) thin layers have been performed. The characterization shows that a Surface Enhanced Raman Spectroscopy effect (SERS) has been reached. Focusing on the Xanthene Ring (XR) deformation band located at about 613 cm^{-1}, the fitting of the experimental Raman bands shows that the growth in the intensity is over 300% with respect to the reference sample. The reflectance spectrum of the enhanced sample shows a pseudo-cavity mode that falls exactly in the range of the excitation wavelength.

4.9.1 Experimental

Two deposited Rhodamine 6G (R6G) films on glass substrates by spin-coating technique (at 3000 rpm) were analysed by Micro-Raman spectroscopy.
The structural formula of Rhodamine 6G (R6G) is showed in figure (4.9.1).

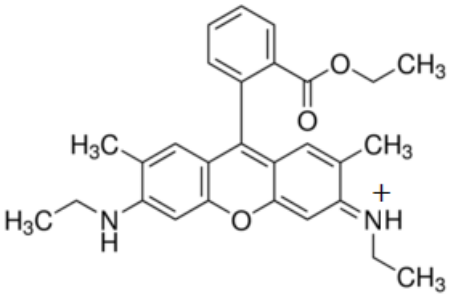

Figure 4.9.1. *Structural formula of Rhodamine 6G (R6G).*

In figure (4.9.2) there are shown the two samples based on R6G film deposited on glass substrate covered by a layer of silver (105nm) and the reference sample based on R6G film deposited directly on glass substrate indicated as S6, S7 and S_{REF1}, respectively.

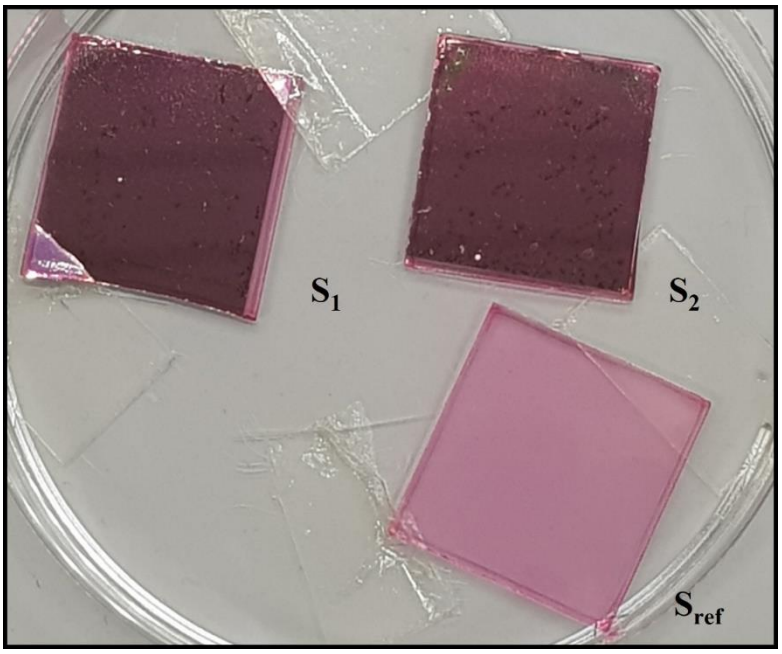

Figure 4.9.2. *The investigated reference sample R6G film deposited via spin coating directly on glass substrate (SRef) and the R6G films deposited on thin layer of silver (S1 and S2).*

Micro-Raman spectra were acquired with a Horiba – Jobin Yvon apparatus with spectral resolution of ~ 2 cm^{-1} equipped with a CCD (256 x 1024 pixels) detector cooled at -70°C. The spectra were collected by using He-Ne laser source (λ = 632.8 nm) with an emitted power of 17 mW. Analyses were performed using an Edge filter and a 50x Mplan Olympus objective of a coupled Microscope BX40. Several optical filters were used in order to reduce the luminescence.

The reflectance spectra were acquired with a spectroscopic ellipsometer M2000 by Woolam in the range from 300 to 700 nm.

4.9.2 Result and discussion

In figure (4.9.3) there are shown the Raman spectra acquired on samples S1 and S2 together with the Raman spectrum of the reference SRef in the spectral range between 255 cm^{-1} and 1800 cm^{-1}.

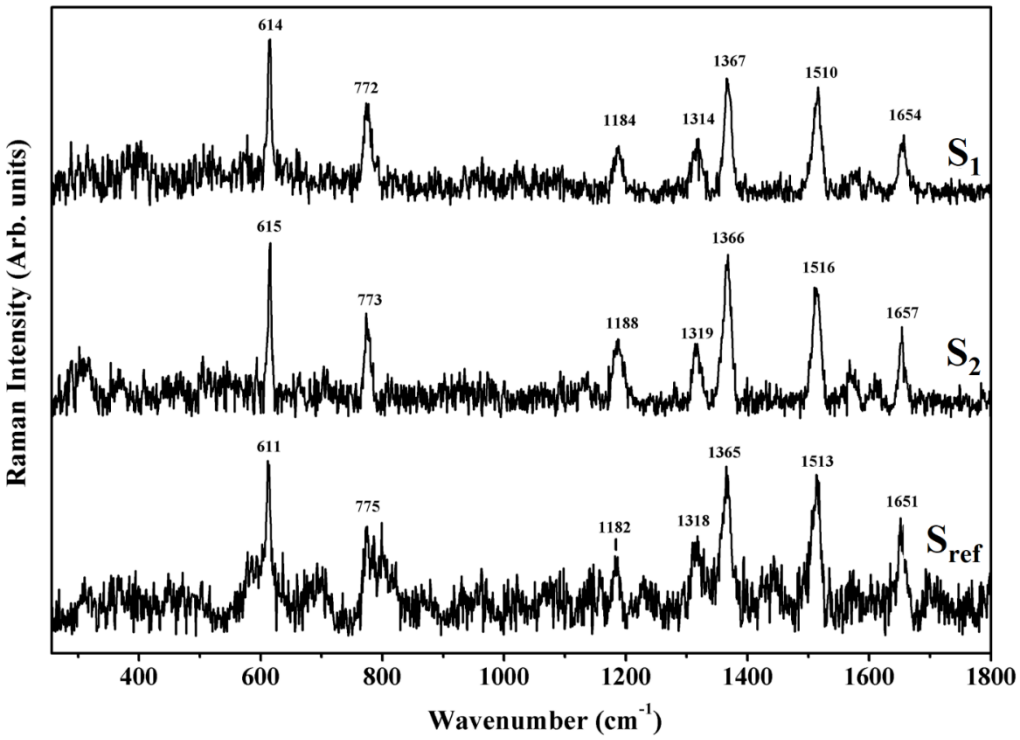

Figure 4.9.3. *Representative Raman spectra of the samples S1 and S2 and of the reference SRef acquired in the range between 255 cm^{-1} and 1800 cm^{-1}.*

In the acquired spectra, the Raman bands ascribable to the Rhodamine 6G are visible. Attribution of the bands made here follows the one in literature although there are some different points of view [30,89-93]. Raman band found at ~613 cm^{-1} is referred to the deformation of xanthene ring (XR) for all the authors cited here [89-93] except *Nie et al* [30] because the range of the discussed spectrum in this case is 1000 – 2000 cm^{-1}. In particular, for references [90-93] this band is due to the in plane bending of the XR while reference [90] also attributes the band to the out-of-plane bending of the ring. *Majombe et al*. [89] also attributes the Raman band found at ~773 cm^{-1} to the deformation of XR without going into detail. However, references [90,92,93] attribute it to the out-of-plane bending of (C–H) bonds. Raman band found at ~1184 is attributed by *Jensen et al.* [90] to the in-plane deformation of XR together with the bending of (C–H) and (N–H) bonds. References [30] and [91] seems to attribute it to the symmetric stretching modes of the aromatic moieties (in plane XR). The Raman band is present in the spectra of *Majoube et al.* [89], *Li et al.* [92] and *Hildebrandt et al.* [93] however these authors do not make any attribution of the band. All the Raman spectra, except the Raman spectra relative to the samples S8 and S9 in which there are multiple Raman bands in this region, show 4 Raman

bands in the upper region of the spectrum. The first band is found at ~1316 cm^{-1}, is visible in the spectra of reported literature [30,89,90,92,93] but in this case attribution of the band is difficult. *Majoube et al.* [89] attribute it to the (C–H) deformation while for *Jensen et al.* [90] it is due to the combination of the in plane breathing of XR + (N–H) bend and (CH_2) wagging and last, *Nie et al.* [30] attribute it to the symmetric modes of in plane (C–C) stretching. References [92] and [93] do not make any attribution of the band simply reporting it. Raman band found at ~1364 cm^{-1} is present in the spectra of reported literature. It is attributed by all the authors to the stretching of aromatic (C–C) of xanthene ring and its substituents. To the same vibration mode are attributed the last two Raman bands found at ~1514 cm^{-1} and ~1653 cm^{-1} [30,89-93]. Table (4.9.1) resumes the observed Raman bands of the investigated samples and their vibrational assignments.

Frequency (cm^{-1})				
S_{ref}	**S6**	**S7**	**Assignments**	**references**
611	614	615	δ XR in–plane δ XR out–of–plane δ XR	[89] [90-93] [90]
775	772	773	δ XR out–of–plane δ (C–H)	[89] [90,92,93]
1182	1184	1188	in–plane δ XR + δ (C–H) + δ (N–H) Stretching aromatic benzene ring	[90] [30] [91,93]
1318	1314	1319	(C–H) deformation breathing XR + δ (N–H) + (CH_2) wagging (C–C) aromatic stretching	[89] [90] [30]
1365	1367	1366	(C–C) XR aromatic stretching	[30] [89-93]
1514	1510	1516	(C–C) XR aromatic stretching	[30] [89-93]
1652	1654	1657	(C–C) XR aromatic stretching	[30] [89-93]

Table 4.9.1. *Frequencies of the observed Raman bands of R6G and their assignments and relative references; δ: bending, XR: xanthene ring*.

The Raman spectra acquired on the various samples show quite differences in the intensities and in some case in the shape of the Raman bands ascribed to the R6G. To evaluate the enhancing of the Raman bands related to R6G molecules, we have focus on the Xanthene Ring deformation band located at about 613 cm^{-1}. In figure (4.9.4) it is shown the comparison between the intensities of the fitted Raman bands relative to the Xanthene ring deformation mode situated at about 613 cm^{-1}. The experimental XR ring deformation Raman bands have been fitted with single Lorentzian functions.

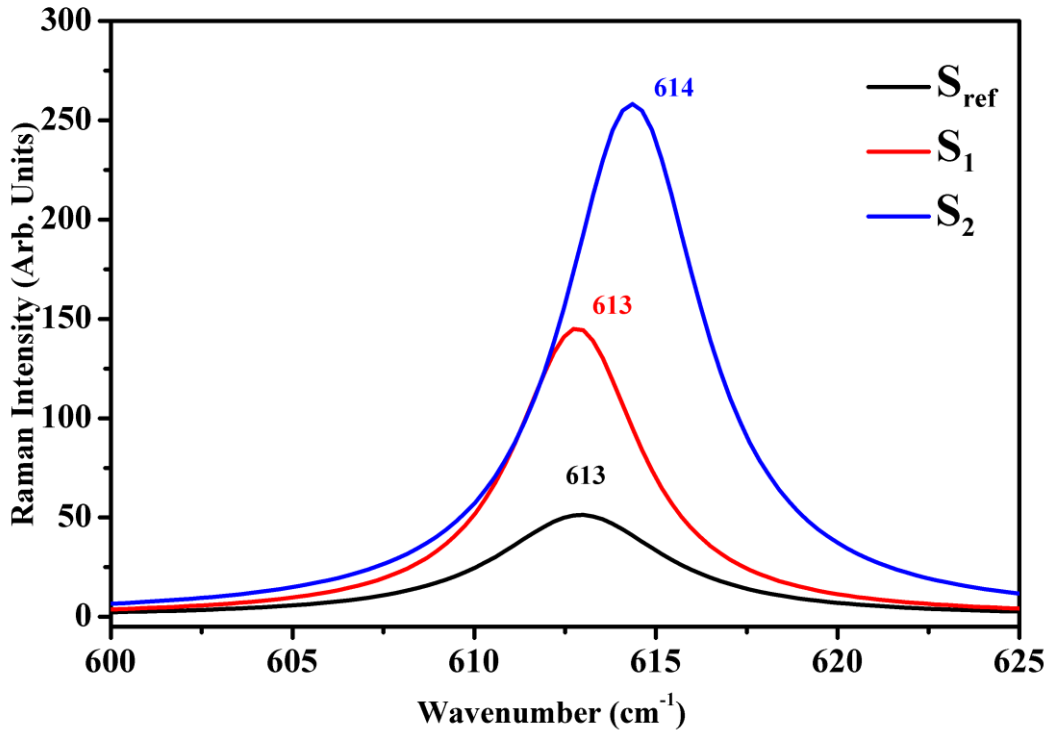

Figure 4.9.4. *Lorentzian functions of the XR ring deformation band located at about 613 cm^{-1}.*

The increase in the intensity between the reference sample S_{ref} and the samples is 111% in the case of sample S_1 and 314% in the case of sample S_2. The observed phenomenon is related to the substrate: in figure (4.9.5) it is shown the reflectance spectrum of the sample S_2 for different angles. In the upper quarter (angle at 25°) a mode of pseudo-cavity is observed for sample S_2 that is situated exactly in the range of excitation wavelength used during analysis (632.8 nm). In short, although the incident light is normal, the objective of the microscope focus the excitation light (laser) allowing to a series of low angle wave vectors (precisely up to 25°) to reach the sample (through the incident light). In this manner, at 25° sample S_2 exhibits the pseudo-cavity mode that enhances the available field by resonance mechanism [94]. The observed pseudo-cavity mode led to an important SERS effect on the Raman spectrum of sample S_2.

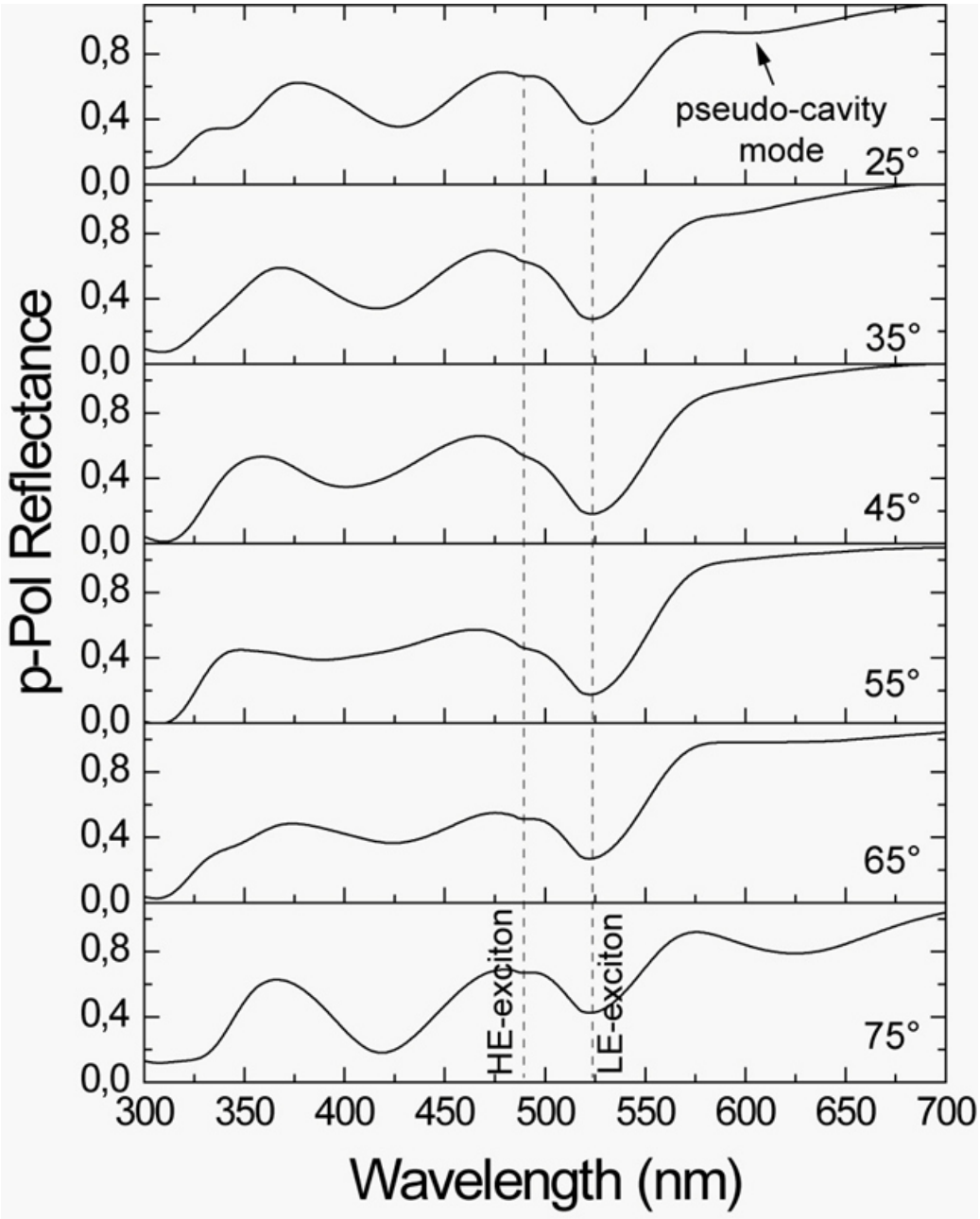

Figure 4.9.5. *Reflectance spectra for the sample S_2 taken at different angles in the range from 300 to 700 nm. In the 25° quarter the sample exhibits a pseudo-cavity mode (indicated by the narrow) in the range of excitation wavelength (that is 632.8 nm).*

4.9.3 Conclusions

Raman characterization of R6G various samples has been done. The spectra have been taken with 632.8 nm red laser because of the great luminescence registered during analysis with the 532 nm line. The acquired Raman spectra show the main Raman bands attributable to the Rhodamine molecule. A strong enhancement of the Raman features is observable (over 300% with respect to the reference sample for the sample S_2). The reflectance analysis on the S_2 sample shows that a pseudo-cavity mode is present at 25°, enhancing the field and producing the observed SERS for the sample. The sample S_1 does not present any similar mode on its reflectance spectra and so the SERS effect is not as relevant as for the sample S_2.

4.10 Raman characterization of TiO_2 films

Two samples of titanium dioxide (TiO_2) were obtained by sputtering on glass substrates with different deposition conditions. The samples have been characterized by Raman spectroscopy in order to determine the nature of the film and the used best deposition conditions.

4.10.1 Experimental

In figure (4.10.1) are shown the two TiO_2 samples obtained through use of sputtering technique. They have been obtained with two operating conditions of sputtering. Sample A has been obtained in Ar 30% and O_2 3%, while sample B is the result of a deposition in Ar 37% and O_2 12.5%. The two samples were raised to 400°C for one hour after deposition.

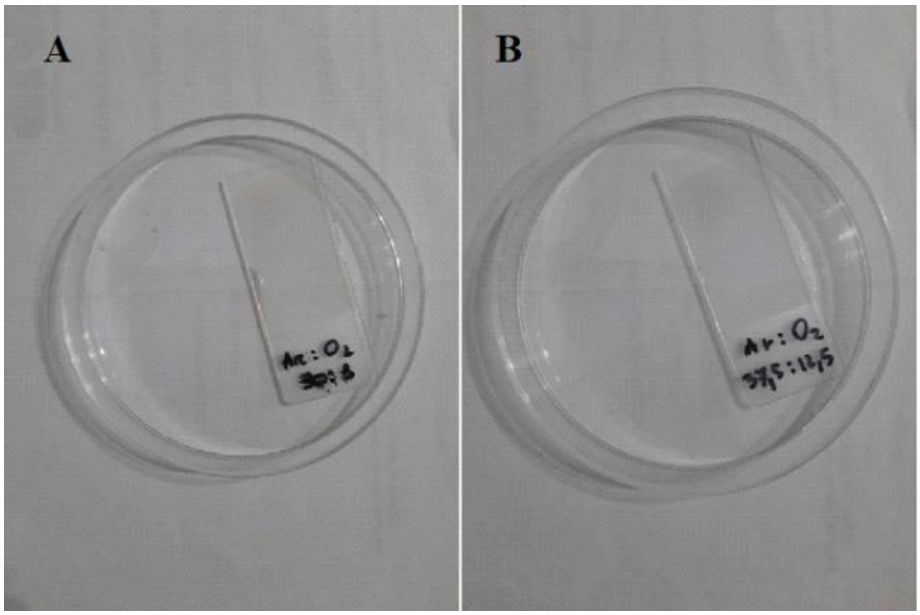

Figure 4.10.1. *TiO_2 samples A (left) and B (right).*

The Raman characterization of the film has been done with a microRaman LABRAM of Jobin-Yvon Horiba Srl with a red laser source at 633 nm and 17 mW power. A CCD detector has been used to register the spectra.

4.10.2 Results and discussion

In figure (4.10.2) are shown the optical images of the samples acquired with a 50x objective. In the case of sample A, micrometric accumulations of material has been detected on the overall surface of the sputtered glass, while sample B does not show any similar structure. The different morphology of surfaces A and B also emerged in the Raman study carried out.

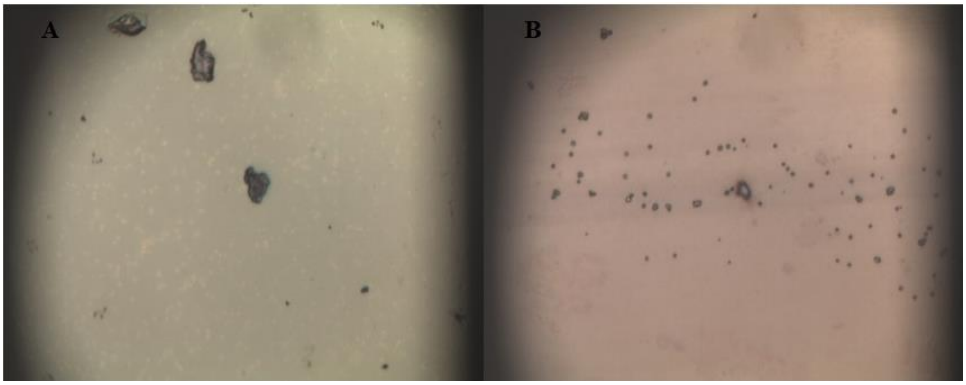

Figure 4.10.2. *Optical images of sample A (left) and sample B (right) acquired with a 50x objective.*

In figure (4.10.3) it is possible to see that while the process used for the preparation of sample A leads to the formation of TiO_2, the one used for obtaining sample B does not allow to obtain layers of materials that can be investigated by means of Raman analysis.

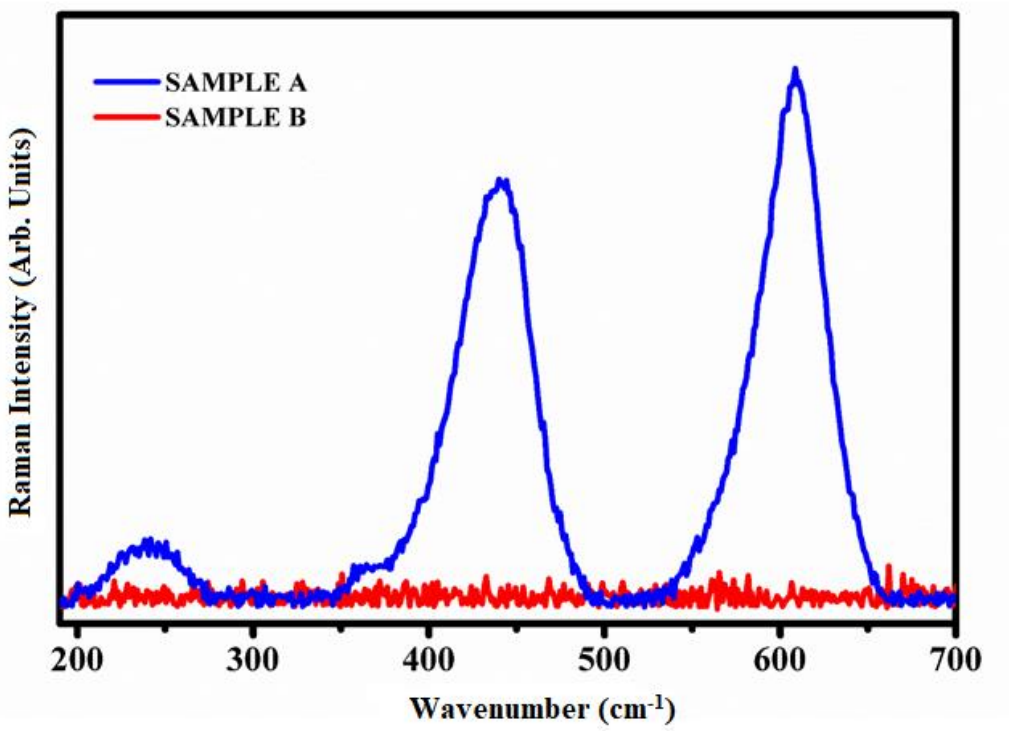

Figure 4.10.3. *Raman spectra acquired with 633 nm laser in the range 190 cm^{-1} 700 cm^{-1} of sample A (blue line), and sample B (red line).*

The spectrum of sample A shows two rather intense Raman bands at 440 cm^{-1} and 609 cm^{-1} and a broad and weaker band at 242 cm^{-1}. TiO_2 is found in nature both in the amorphous state and in different crystalline structures three of which are well known: rutile, anatase and brookite (the other two forms much less frequent are akaogiite and TiO_2II). The first two form are more widespread and are included in the tetragonal crystalline system. Brookite is instead part of the orthorhombic system. The bands observed in the spectrum of sample A are ascribable to the vibrational modes attributable to the irreducible representations of the space group D^{14}_{4h} - $P4_2/mnm$ of which the rutile is part [95-97]. The 15 vibrational modes of the space group are described by 8 irreducible representations of which 4 are allowed in Raman while the others are allowed in IR [95]. In particular, the 242 cm^{-1} band is attributed by Narayanan [95] and J. Zang et al. [97] to the B_{1g} mode. The modes E_g and A_{1g} can be attributed to the bands at 440 cm^{-1} and 609 cm^{-1} respectively [96,97]. Raman bands and their assignments are resumed in table 4.10.1.

Frequency (cm^{-1})		Assignment	references
Sample A	**Sample B**		
242	-	B_{1g}	[95][97]
440	-	E_g	[96][97]
609	-	A_1g	[96][97]

Table 4.10.1. *Observed Raman bands, assignments and references of sample A and B.*

4.10.3 Conclusions

The Raman analysis on two sample of TiO_2 films obtained through sputtering method has been done. The analysis has showed that sample A is a film of TiO_2 in the crystalline form of rutile while sample B does not present any Raman bands ascribable to the TiO_2.

4.11 Effect of UV-cured Bisphenol A glycerolate (1 glycerol/phenol) diacrylate on a Viologen solution-based electrochromic devices performances

In this work, electrochromic devices are made by using Diethyl Ferrocene and Ethyl Viologen Diperchlorate as a redox couple; Propylene Carbonate is used as an aprotic solvent to facilitate ions separation and diffusion inside the devices. Viologens are of great interest nowadays [98]. They can be defined as 1,1'-disubstituted-4.4'-bipyridinum salts and exist in dicationic form and can reduce two times: the most stable reduced form is the radical one. In this work Ethyl Viologen Diperchlorate has been used to realize electrochromic devices: it was plenty used in the past [99,100]. So, this Viologen can be involved in two reductions: the first one leads to the formation of a radical species, while the second one can fully reduce the Viologen leading to a neutral species. It is known that the radical species of a Viologen compound is very stable and has a very intense blue coloration because of the radical electron delocalization inside the π-system of the bipyridyl nucleus, while the neutral species has a less intense coloration and is less stable. The dicationic form of Viologens is colourless, the radical form shows a navy-blue coloration and the fully reduced form usually has less intense coloration [101]. Solution-based electrochromic devices are of great interest since they can lead to flexible electrochromic devices for several applications: since organic compounds can be processed in solution, Viologen-based electrochromic devices could be very adequate in order to obtain flexible electrochromic devices.

This work aims to underline the benefits of viologen-based electrochromic device performances due to the UV-cured Bisphenol A glycerolate (1 glycerol/phenol) diacrylate polymerization. To understand the differences in terms of performances between samples containing not polymerized Bisphenol A and samples containing polymerized Bisphenol A, such devices are characterized by different techniques, such as Cyclic Voltammetry, UV-vis-NIR, and Raman spectroscopies. Physically the devices show a light-yellow coloration in the bleached state and dark blue coloration in the colored state; furthermore, transmittance spectra show IR absorption in the devices ON-state and an optical contrast

(ΔT%) of ~ 40% at 432 nm, up to 88% at 580 nm and 78% at 1200 nm. This suggests that such devices should be used for energy-saving applications.

4.11.1 Experimental

Diethyl Ferrocene and a Viologen compound (Ethyl Viologen Diperchlorate, EV) were chosen as redox couple and mixed together with an aprotic solvent, Propylene Carbonate (PC, 99%) in order to facilitate ions separation inside the electrochromic device: the electrochromic couple is in solution phase (electrochromic solution, ES). Another solution of Bisphenol A glycerolate (1 glycerol/phenol) diacrylate and photoinitiator Irgacure (Dimethoxy-phenylacetophenon 99%) was prepared and added to the first solution.

The as-prepared electrochromic mix was inserted in a cell made with two ITO-coated glasses, in order to apply an electric potential to the mix. Different samples were prepared by filling the cells with the electrochromic mix by capillarity; this was possible by using glasses spheres spacers (diameter of 88 μm) between the two glasses. The solution used as glue was cured under a UV lamp (from Jelosil, HG 200 L model, optical power per unit area 0,043 W/cm^{-2}) light for 1 minute and 30 seconds, in order to maximize its strength between the two ITO-coated glasses.

Figure (4.11.1) shows the parts of an electrochromic device and the assembled device. In the disassembled device, the glue disposition used to attach the two ITO-coated glasses can be noticed on the lower ITO conductive layer: in the assembled device, the two glasses are staggered in order to apply a potential.

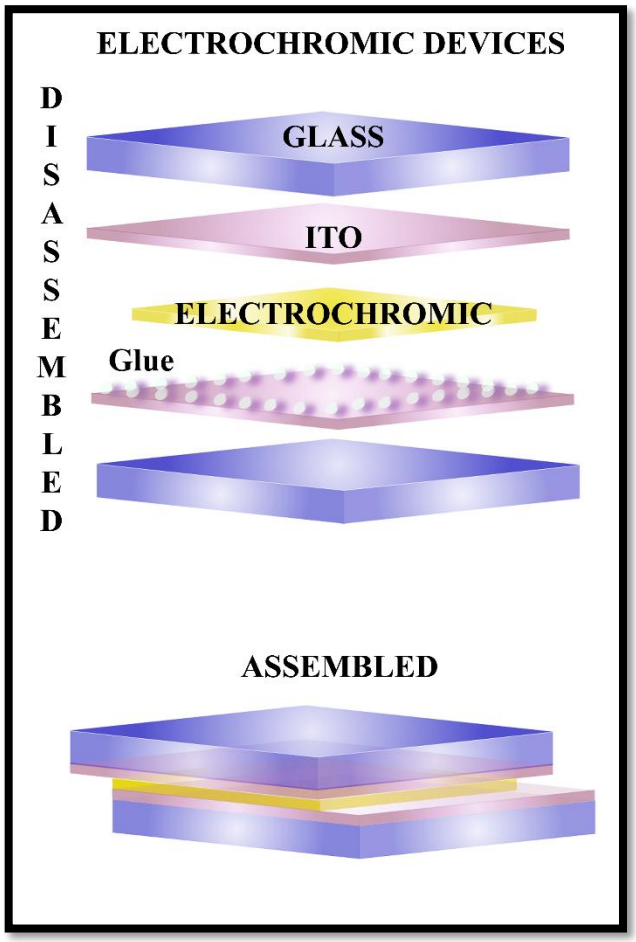

Figure 4.11.1. *Electrochromic device disassembled (on the top) and assembled (on the bottom).*

All chemicals, shown in figure (4.11.2), were purchased from Sigma Aldrich and used without any particular additional treatments, except for Bisphenol A glycerolate (1 glycerol/phenol) diacrylate: since this compound has too high density even at room temperature, a heat treatment was necessary to manipulate it.

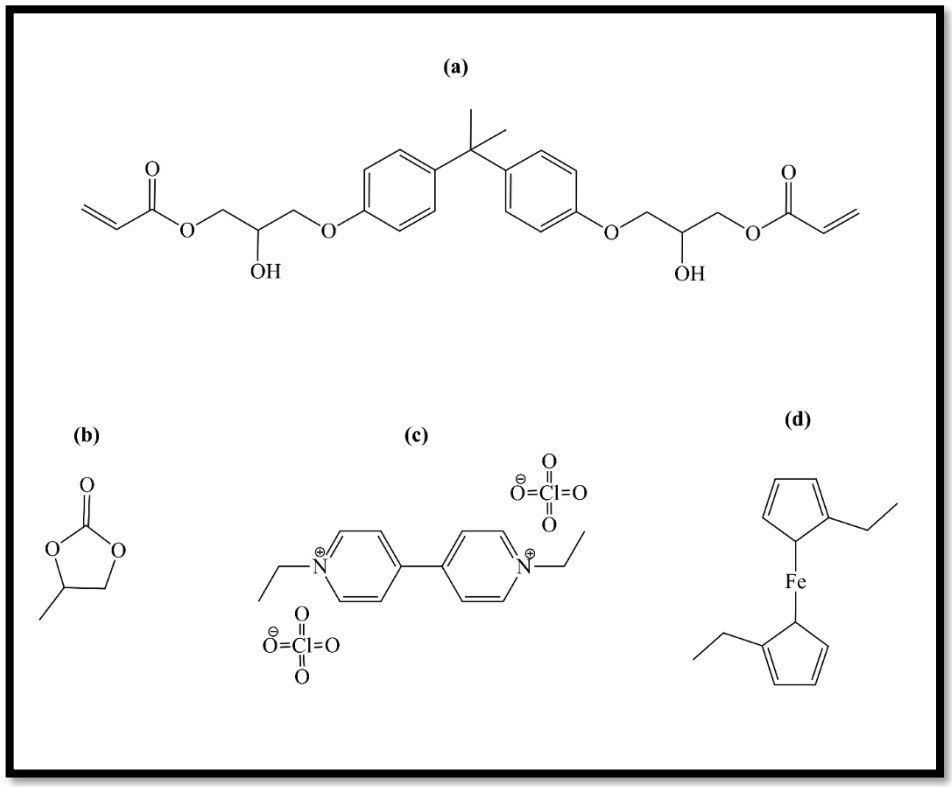

Figure 4.11.2. *Chemicals:* ***(a)*** *Bisphenol A glycerolate (1 glycerol/phenol) diacrylate,* ***(b)*** *Propylene Carbonate;* ***(c)*** *Ethyl Viologen Diperchlorate;* ***(d)*** *Diethyl Ferrocene.*

Systems with different EM compositions were prepared and studied; furthermore, systems with polymerized and not polymerized Bisphenol A inside the EM were studied in order to understand the differences. A Vortex mixer (from Velp Scientifica) was used to mix the two solutions. Bisphenol A inside the devices was polymerized by putting them under the UV lamp already described before for 1 minute and 30 seconds.

First of all, the study of this system was centered around the EM optimum composition: this was done by varying the ES wt% content inside the EM and systems with 20 wt%, 30 wt%, 40 wt%, 60 wt%, 70 wt% and 80 wt% ES were prepared. From a visual analysis, the best system was that containing 60 wt% ES content, so the study was focused on devices with three different compositions: 55 wt%, 60 wt% and 65 wt% ES content. (In the following, the three percentages of the electrochromic mix at 55%, 60% and 65%, studied in this work, are indicated by EM_{55}, EM_{60} and EM_{65}, respectively. Transmittance measurements were performed by using a Spectrophotometer (from AvaSpec), equipped with a halogen lamp, whose spectrum covers a wide range of wavelengths (from 180 nm, in the UV region, to 1310 nm, in the IR region): this range is wide enough to provide interesting informations about the devices.

Cyclic Voltammetry measurements were performed by using a potentiostat/galvanostat (model 2059 from Amel s.r.l.) equipped with the 7800 interface in order to manage measurements by Junior Assist software.

Raman spectroscopy measurements were performed by using a micro-Raman-LABRAM (from Jobin Yvon Srl), equipped with an optical microscope, in order to collect Raman spectra from small regions of the sample, such as 2-5µm. MicroRaman-LABRAM is equipped with a HeNe 17mW laser (633 nm), a NdYAG 50mW laser (doubled, 532 nm) and a CCD detector (Peltier cooled, 1024 x 256). Optical microscope is equipped with 10x NA 0.25, 50x NA 0.7 and 100x NA 0.9 objectives.

4.11.2 Results and discussion

4.11.2.a Cyclic Voltammetry measurements

Cyclic Voltammetry measurements have been performed in order to understand the response of the samples, from an electrochemical point of view, under the action of an electric potential. As stated in the experimental section, three electrochromic mixes at 55%, 60%, and 65 % weight ratios between the electrochromic solution and Bisphenol A glycerolate (1 glycerol/phenol) diacrylate have been studied and, here, are indicated by EM_{55}, EM_{60} and EM_{65}, respectively.

The cyclic voltammograms (CV) were collected on devices filled with the three mixes, but three kinds of devices were subjected to the polymerization process of the Bisphenol A whereas, others three kinds of devices were not subjected to the polymerization process of the polymer. In this way, the effect of the polymerization process on the electrochemical responses of the studied systems can be detected. All measurements were performed with a scanning speed of 50 mV/sec and vs open voltage circuit. Cyclic Voltammetry is fundamental to understanding the working voltages of the device and identifying the redox peaks; furthermore, Cyclic Voltammetry is a very important instrument to test the devices life after a certain number of cycles. Figure (4.11.3) represents an electrochromic device under different applied potentials and the species that are diffused to the two electrodes: the relative cyclic voltammograms show symmetric peaks at 1.2 Volt, -1.2 Volt, 0.4 Volt and -0.4 Volt and at these potentials coloration changes occur.

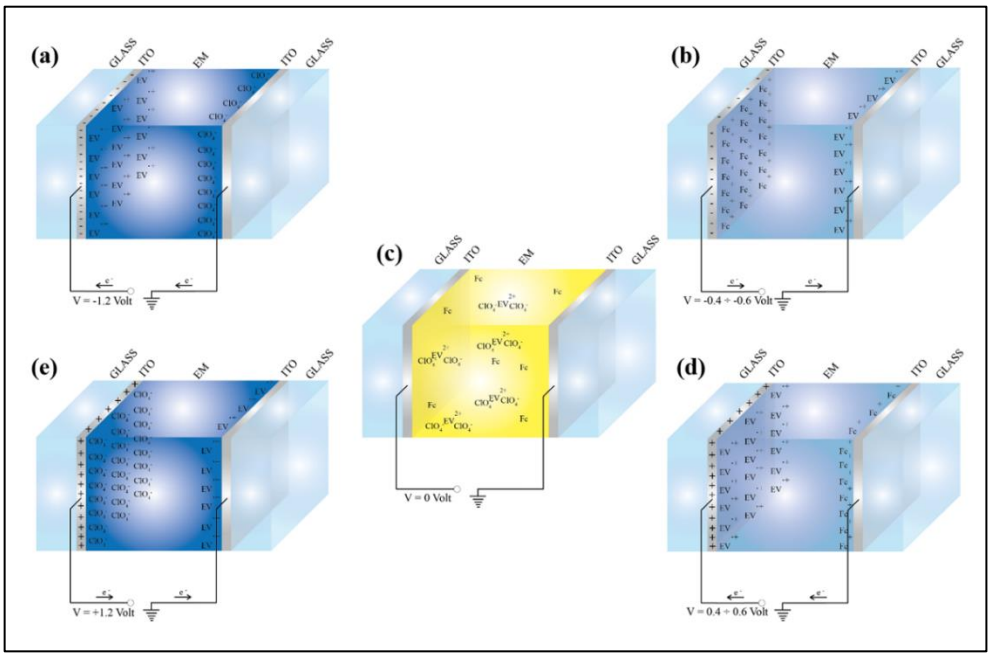

Figure 4.11.3. *Schematic representation of electrochromic device when voltages of -1.2 Volt (a), between -0.4 and -0.6 Volt (b), 0 Volt (c), between 0.4 and 0.6 Volt (d) and 1.2 Volt (e) are applied. Fc indicates Diethyl Ferrocene, EV is Ethyl Viologen.*

Figure (4.11.4) shows the voltammograms collected on the devices filled with the three percentages of the electrochromic mix at 55%, 60% and 65% indicated as EM_{55}, EM_{60} and EM_{65}, respectively with the Bisphenol A polymerized and not polymerized.

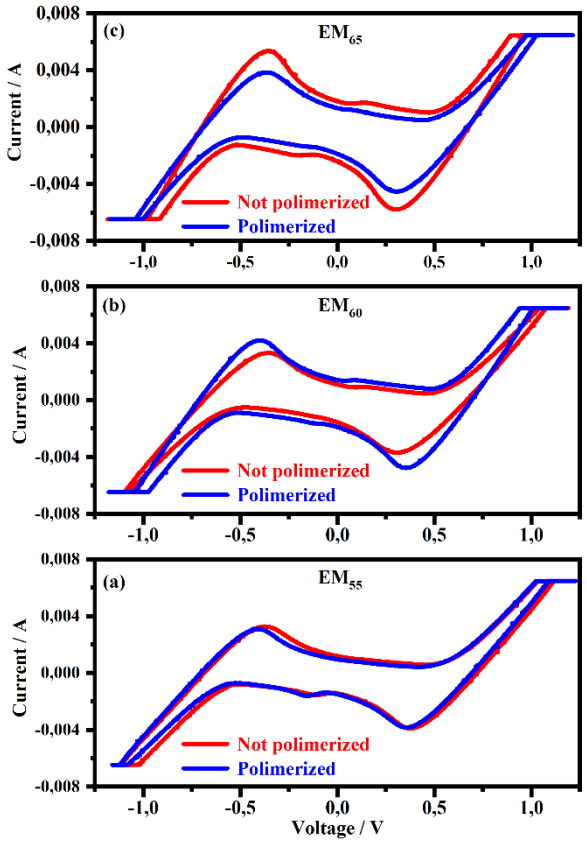

Figure 4.11.4. *Cyclic Voltammograms collected on the samples filled with the three percentages of the electrochromic mix at 55%, 60% and 65% indicated as EM_{55}, EM_{60} and EM_{65}, respectively. In particular in each frame are compared the voltammograms obtained with the Electrochromic mix polymerized (blue line) and not polymerized (red line).*

From a first fast analysis, cyclic voltammograms show a current maximum value (absolute value) at 6.5 x 10^{-3} Ampere inside the devices, while the switching potentials are comprised between 1.1 Volt and 1.2 Volt (in absolute value) for full coloration. Cyclic voltammograms show a noticeable symmetry when potential polarity is reversed, and a first noticeable redox peak occurs at 0.4 Volt (in absolute value). This one can be related to Diethyl Ferrocene oxidation [101] and to the Viologen reduction caused by redox reaction, while a peak comprised between 1.1 Volt and 1.2 Volt can be related to the Viologen compound charge separation. It was reported that at certain potentials the ionic bond between perchlorate ions and Viologen (in its oxidized form) can be broken, causing an accumulation of charges on the electrodes and the reduction of Viologen here [102]. Since Ferrocene-based compounds are blue [103] in the oxidized state and a radical form of a Viologen compound with short alkyl substituents (such as Ethyl) promotes a dark

blue form [103], the blue colour of the devices can be due to both the reactions: Diethyl Ferrocene oxidation and Viologen compound single reductio. The main redox reaction involved in the coloration process is the formation of a Viologen compound radical species and the oxidation of Diethyl Ferrocene. Since the coloration process starts at voltages between 0.4 Volt and 0.6 Volt and becomes more intense at voltages between 1.1 Volt and 1.2 Volt, one can believe that the process ends with the formation of radical species of the Viologen compound and not with the formation of its neutral species. Nevertheless, literature states that the double reduction reactions of Viologens are irreversibly [104] while the system described here shows reversibility and a dark blue, typical of a single reduced Viologen, occurs. A lower intense peak can be noted at 0.2 Volt potentials (in absolute value): it was reported a redox potential of 0.16 Volt for reactions involving Methyl Viologen Diperchlorate dimers, so that, in analogy, this peak can be related to a redox reaction involving Ethyl Viologen Diperchlorate dimers [105]. Voltammograms are symmetric since the electrochromic materials are in the solution and the devices have symmetrical electrodes. It means that by changing voltage polarity only the current direction is reversed, and the reaction involved is the same described above, together with the charge separation.

As can be seen in figure (4.11.4), the switching potentials seems to become lower as well as the composition in electrochromic solution pass from 55% to 65%. On the contrary, the current intensities present on the different devices become higher as well as the composition in electrochromic solution pass from 55% to 65%. The effect of the polymerization is negligible in the sample with EM_{55}. In the case of EM_{60}, the not polymerized samples show switching potentials higher than polymerized samples while in the case of EM_{65} the not polymerized samples show higher current with respect to the polymerized ones.

Figure (4.11.5) shows voltammograms collected on samples, polymerized and not polymerized, made with different Electrochromic mix compositions in terms of Electrochromic solution weight percentage: 55%, 60%, 65%, 70%, 80%.

The voltammograms of EM_{80} not polymerized its quite difficult from the others because in this case, the phase of the mix is almost liquid. Such trend changes a little bit when the systems is polymerized but still its form it is not the same of the other systems. It is possible to see in figure 3 that the voltammograms obtained on the polymerized samples show current peaks lower than respective samples not polymerized. The other systems shows similar characteristics with the samples at 60% polymerized that shows highest

current and with the lower applied voltage used to switch the displays which represent the best compromise between charge carries and voltage employed.

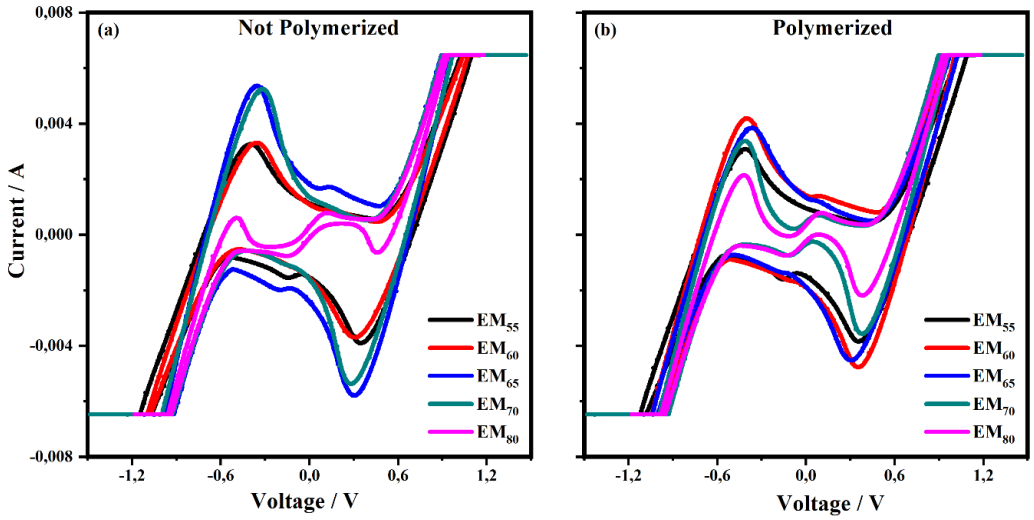

Figure 4.11.5. *Cyclic Voltammograms collected on the samples filled with five percentages of the electrochromic mix at 55%, 60% and 65%, 70% and 80% indicated as EM_{55}, EM_{60}, EM_{65}, EM_{70} and EM_{80}, respectively. In particular are shown the voltammograms obtained on the samples not polymerized (a) and polymerized (b).*

As can be seen in figure (4.11.6), the not polymerized sample is stable up to about 700 cycles, when the peaks of the voltammograms became lower with respect to those of the first cycles. The sample polymerized, indeed, remains stable up to 2000 cycles and the voltammograms taken in the last cycles are quite close to those of the first cycles (see figure 4.11.6.a). Of course, since each cycle corresponds to two switches On (transition from transparent to coloured states), the number of times that someone can turn On the devices is twice the number of the CV cycles performed (without any particular degradation of the systems): 1400 and 4000 switch On for the not polymerized and polymerized devices, respectively.

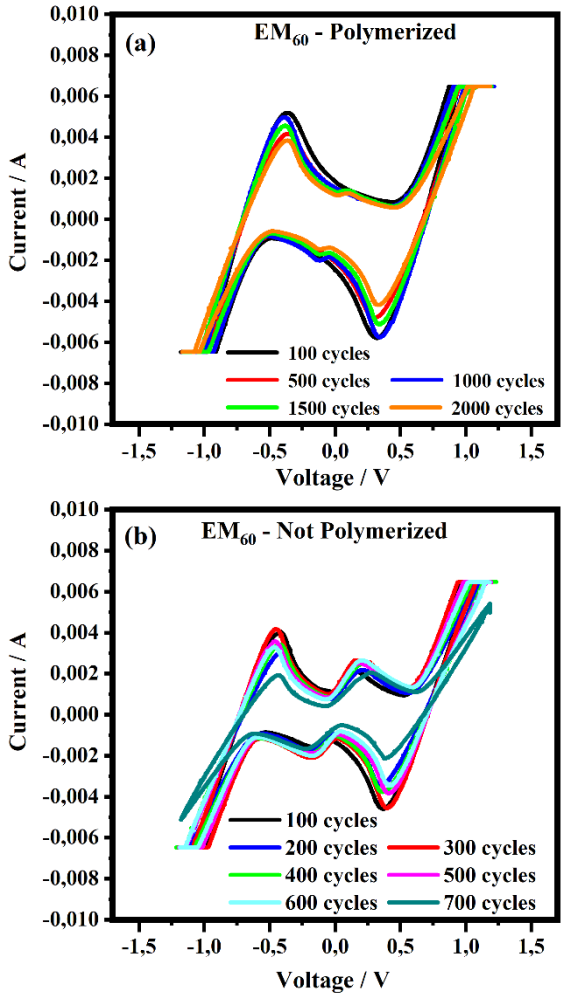

Figure 4.11.6. *Cyclic Voltammograms collected on the samples filled with five percentages of the electrochromic mix at 55%, 60% and 65%, 70% and 80% indicated as EM_{55}, EM_{60}, EM_{65}, EM_{70} and EM_{80}, respectively. In particular are shown the voltammograms obtained on the samples not polymerized (a) and polymerized (b).*

4.11.2.b UV-vis-NIR Spectroscopy

Dynamic transmittance measurements allowed us to determine the time employed by the devices during the complete switch Off-On and the time that the devices turn Off, spontaneously. Other measurements were performed to compare the transmittance spectra, of the devices, at a given constant applied potential: starting from 0.1 Volt to 1.2 Volt (steps of 0.1 Volt, each). It was possible to establish the potentials at which transmittance spectra change and to confirm them with the voltages of redox peaks,

discussed above (voltammograms). In addition, to monitor the degradation of the electrochromic systems, have been blotted also the transmittance spectra collected during the first cycle and after other cycles: if these spectra do not show any remarkable changing means that the active layer is still working well.

Figure (4.11.7) shows an example of the electrochromic device in the state Off and On.

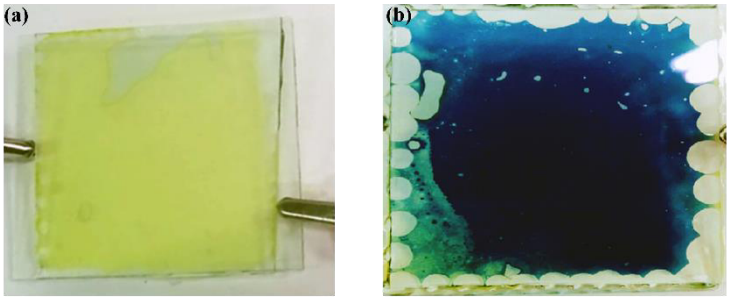

Figure 4.11.7. *Photographs of the devices in the state Off (a) and On (b).*

Figure (4.11.8) and figure (4.11.9) show the transmittance spectra collected on the devices filled with EM_{55}, EM_{60} and EM_{65} in the Off state and On state, respectively.

All spectra show characteristic absorption bands of viologens with short alkyl chain bond to nitrogen: in particular the two bands at 550 nm and 880 nm are related to the formation of ethylviologen radicals ($EV^{+\bullet}$) dimers, while the band at 600 nm is related to the presence of $EV^{+\bullet}$ species, indicating a strong concentration of the last one in the ON state [105]. The band at 400 nm can be related to the presence of Ethyl Viologen radicals too [103].

Since there is no evidence of characteristic oxidized Ferrocene compounds green coloration (when they are in a Ferrocene-based solution) [102], one can conclude that Diethyl Ferrocene oxidation and Ethyl Viologen Diperchlorate reduction occur at the same potential.

UV absorption can be related to glasses and to the Diethyl Ferrocene oxidized form [106], while the IR very broad band centered around 1200 nm can be assigned to reducted Ethyl Viologen since it can be noticed in the transmittance spectra (not reported) of a system that doesn't contain Diethyl Ferrocene as redox mediator.

First of all, transmittance spectra showing the differences between samples with polymerized and not polymerized Bisphenol A are reported.

Samples with polymerized Bisphenol-A have a higher transmittance compared to samples with not polymerized Bisphenol-A. This is due to the fact that this polymer is transparent and in the solid state it decreases the active area available for redox reactions.

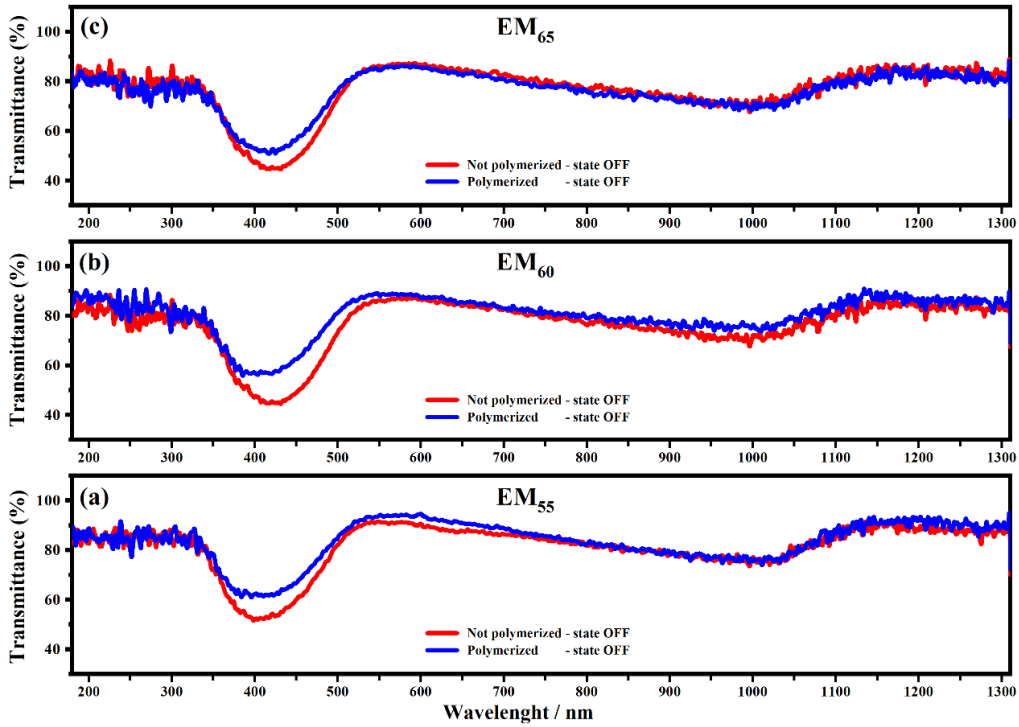

Figure 4.10.8. *Transmittance spectra collected on the devices filled with EM_{55}, EM_{60} and EM_{65} polymerized and not polymerized in the states OFF.*

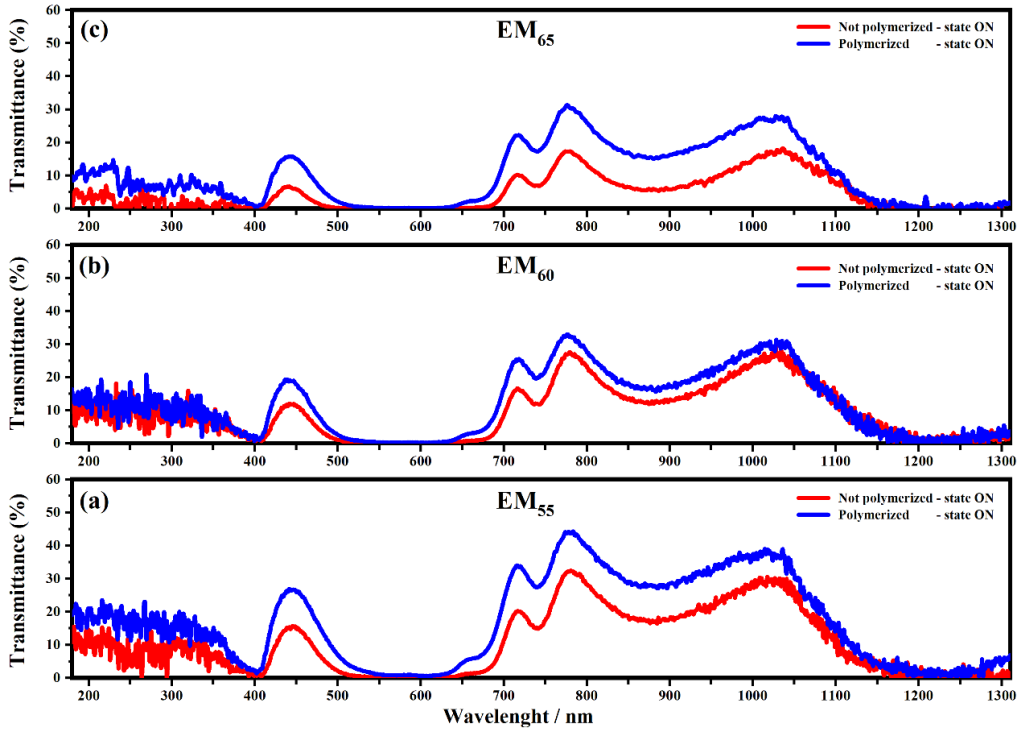

Figure 4.11.9. *Transmittance spectra collected on the devices filled with EM_{55}, EM_{60} and EM_{65} polymerized and not polymerized in the states ON.*

Figure (4.11.10) and figure (4.11.11) show the transmittance spectra at different applied voltages on the devices filled with EM_{55}, EM_{60}, and EM_{65} in polymerized and not polymerized states, respectively. A noticeable change of transmittance in the visible and in the IR regions can be seen for voltages comprised between 0.5 Volt and 0.6 Volt, when Diethyl Ferrocene exists in its oxidized form and the Viologen starts the reduction process.

When a voltage of 1.2 Volt is applied to the devices, the transmittance reaches its minimum value at each wavelength studied. This is in agreement with cyclic voltammetry measurements: the maximum in current is achieved at 1.2 Volt, when perchlorate ions and Viologen dications separate and diffuse to the electrodes.

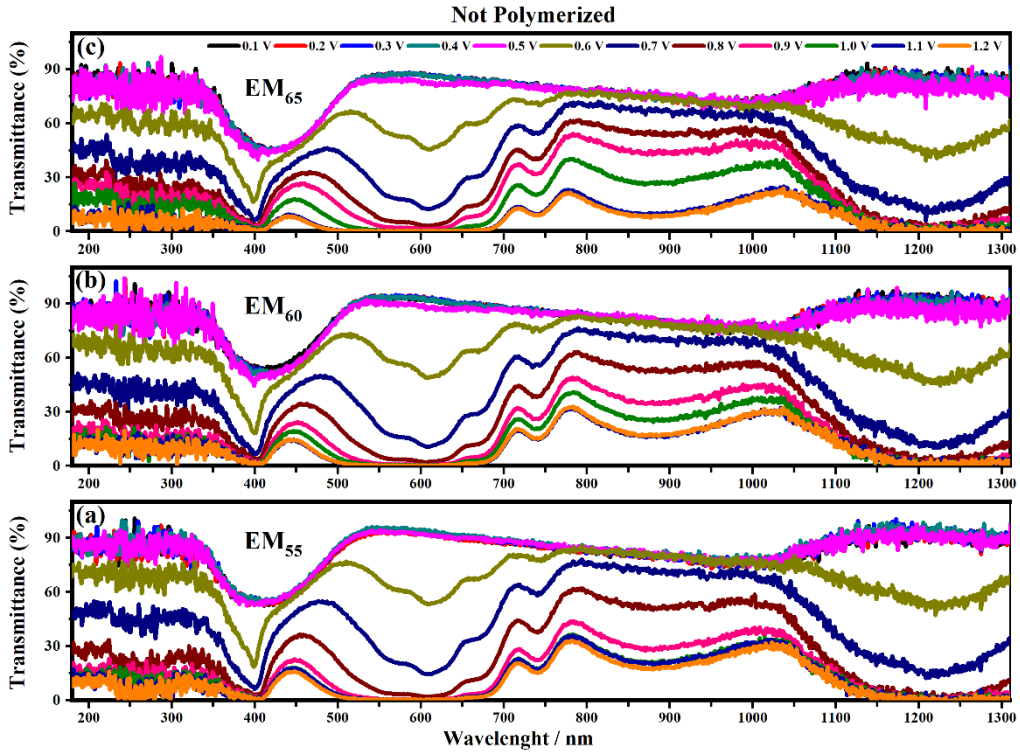

Figure 4.11.10. *Transmittance spectra collected on the devices filled with EM_{55}, EM_{60} and EM_{65} not polymerized at different applied voltages in the range between 0.1 V and 1.2 V with 0.1V step.*

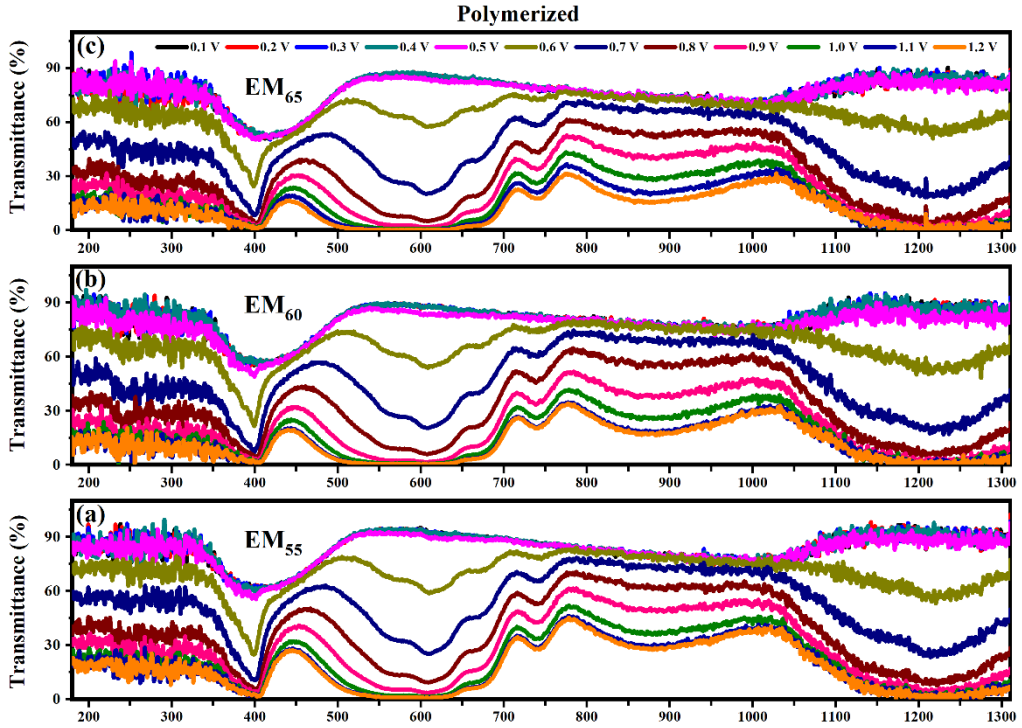

Figure 4.11.11. *Transmittance spectra collected on the devices filled with EM_{55}, EM_{60} and EM_{65} polymerized at different applied voltages in the range between 0.1 V and 1.2 V with 0.1V step.*

Figure (4.11.12) and figure (4.11.13) show transmittance spectra of the electrochromic devices, EM_{55}, EM_{60} and EM_{65} polymerized and not polymerized, at different times straight after the application of a voltage of 1.2 V in order to switch On the devices.

The figure (4.11.14) and (4.11.15) show the transmittance spectra of the electrochromic devices, EM_{55}, EM_{60} and EM_{65} polymerized and not polymerized, when the straight after the applied potential is switched Off once reached the minimum of transmittance, in order to estimate the memory times of the devices.

Samples with polymerized Bisphenol A are faster in switching On and in returning in the Off states after that the applied voltage is switched-OFF.

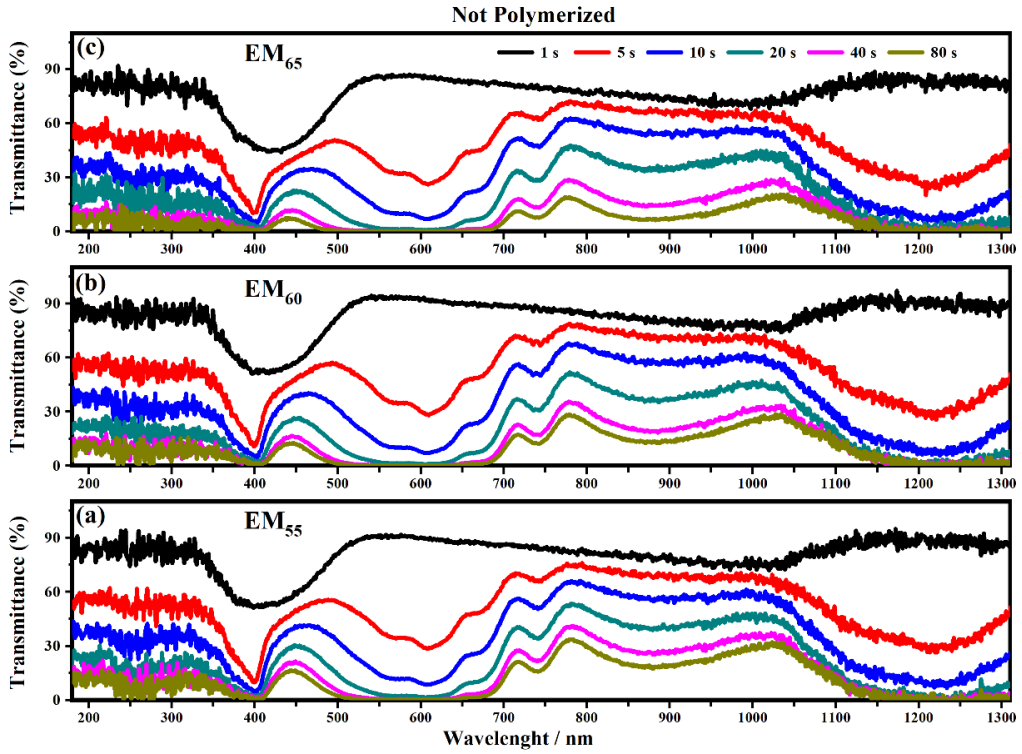

Figure 4.11.12. *Transmittance spectra collected on the devices filled with EM_{55}, EM_{60} and EM_{65} not polymerized at different times straight after the application of a voltage of 1.2 V in order to switch On the devices.*

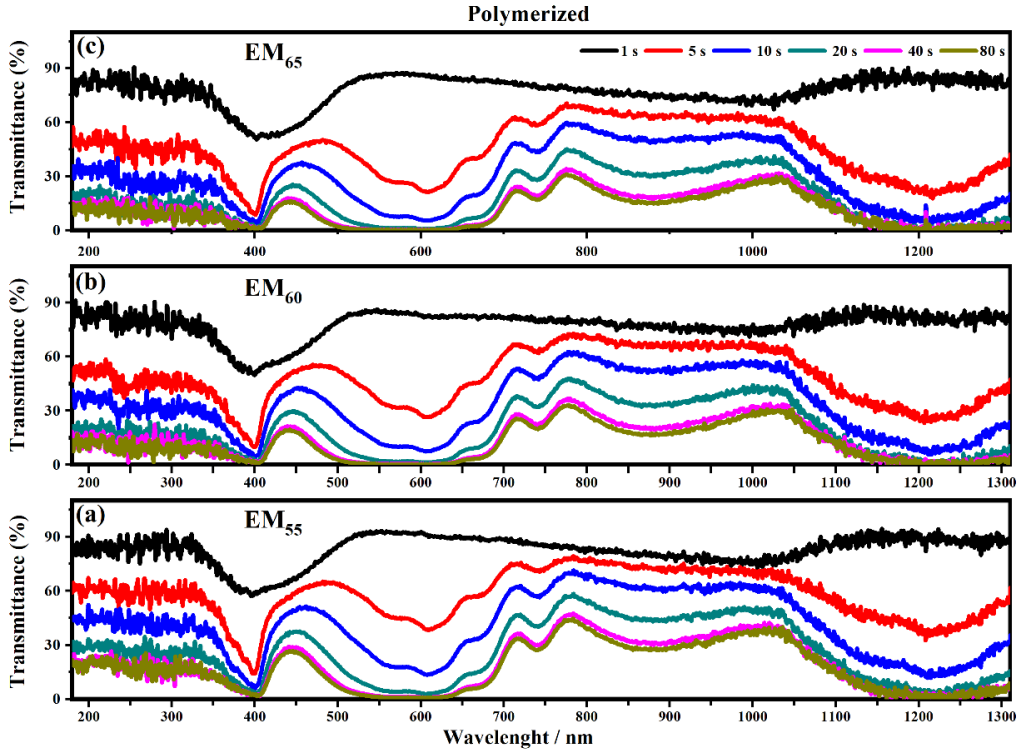

Figure 4.11.13. *Transmittance spectra collected on the devices filled with EM_{55}, EM_{60} and EM_{65} polymerized at different times straight after the application of a voltage of 1.2 V in order to switch On the devices.*

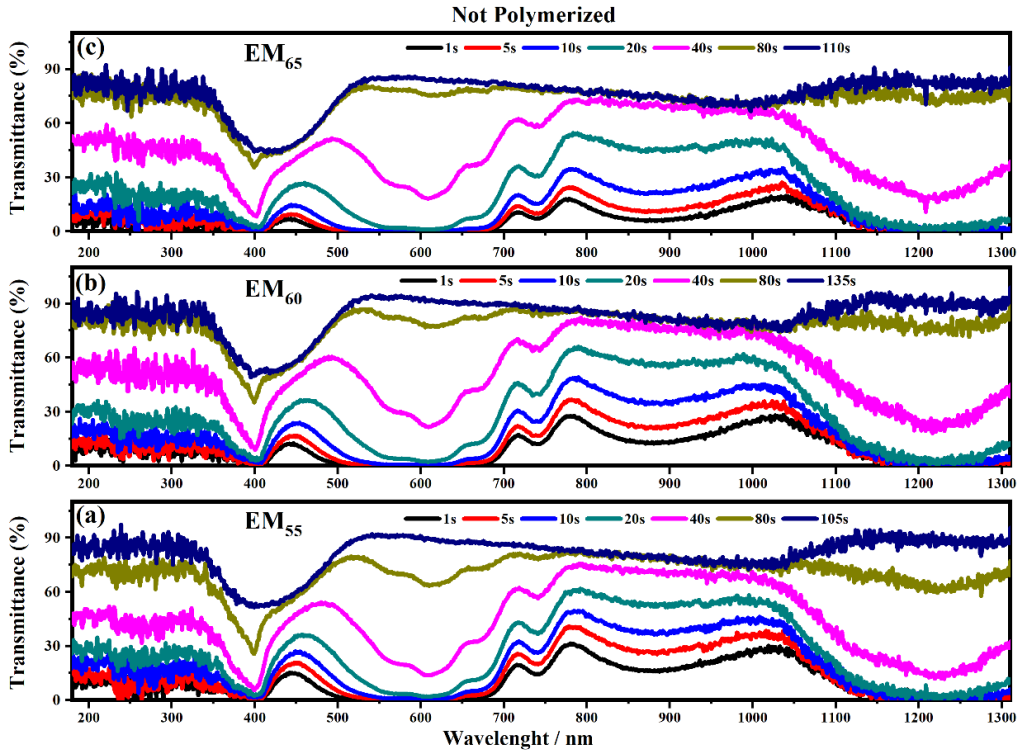

Figure 4.11.14. *Transmittance spectra collected on the devices filled with EM_{55}, EM_{60} and EM_{65} not polymerized straight after the applied potential is switched Off once reached the minimum of transmittance.*

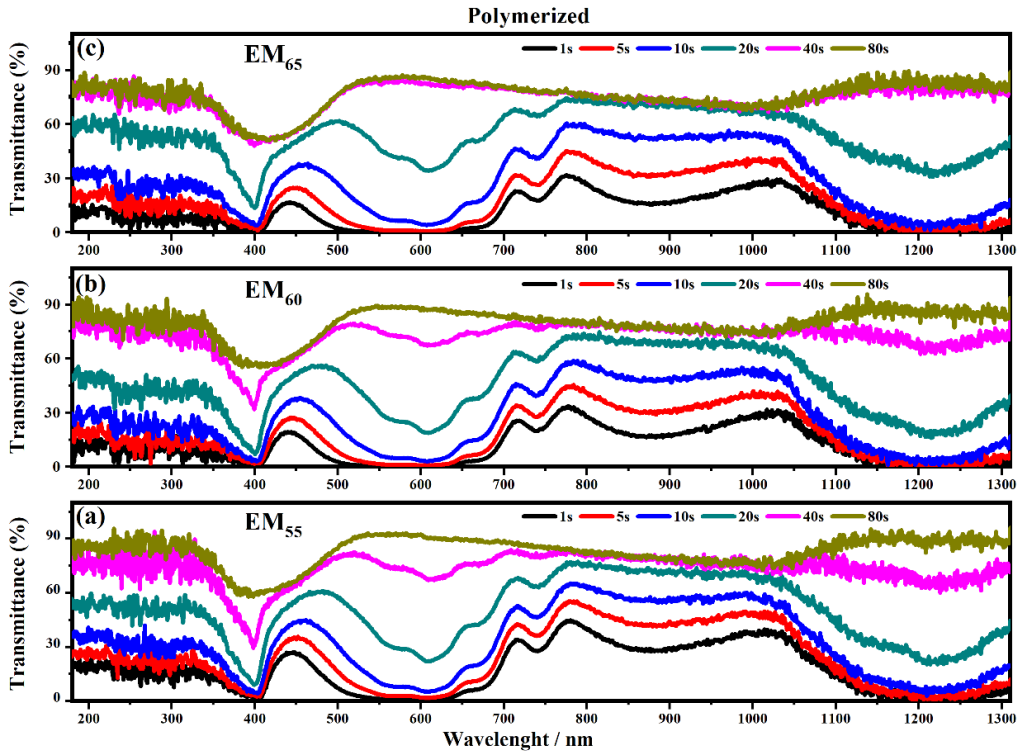

Figure 4.11.15. *Transmittance spectra collected on the devices filled with EM_{55}, EM_{60} and EM_{65} polymerized straight after the applied potential is switched Off once reached the minimum of transmittance.*

Figure (4.11.16) shows the switching time from the state Off to the state On and conversely measured for the Electrochromic devices filled with EM_{55}, EM_{60} and EM_{65} polymerized and not polymerized in order to compare the effect of the polymerization on such response times.

To reach full coloration, electrochromic devices filled with EM_{55}, EM_{60}, and EM_{65} polymerized are faster than the respective devices not polymerized (Fig. 4.11.16). Since the polymerization decreases the resistance to the ions diffusion inside the devices also the memory times are lower for polymerized systems with respect to those not polymerized.

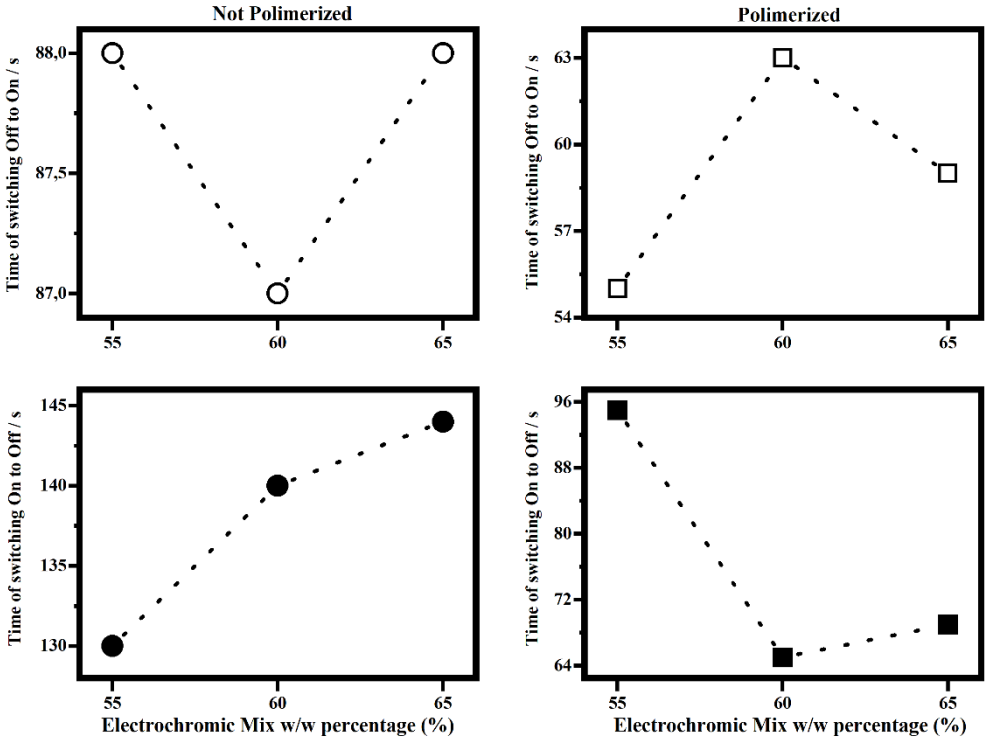

Figure 4.11.16. *Switching times Off-On (on the top) and On-Off (on the bottom) of the devices filled with EM_{55}, EM_{60} and EM_{65} not polymerized (circles symbols) and polymerized (square symbols).*

As it can be seen in figure (4.11.16), once applied a voltage of 1.2 V, the times for the switching Off-On of the electrochromic devices filled with EM_{55}, EM_{60} and EM_{65} not polymerized are about 88 s, while for the polymerized samples fall in the range between 55 s and 63 s. As stated above also the memory times in polymerized devices are lower than those polymerized . In fact, for the devices not-polymerized the memory times fall in the range between 130 s and 145 s while for the polymerized ones fall in the range between 64 s and 96 s.

In figure (4.11.17) are shown the transmittance spectra collected on the electrochromic devices filled with EM_{55}, EM_{60} and EM_{65} not polymerized and polymerized in the states On and Off.

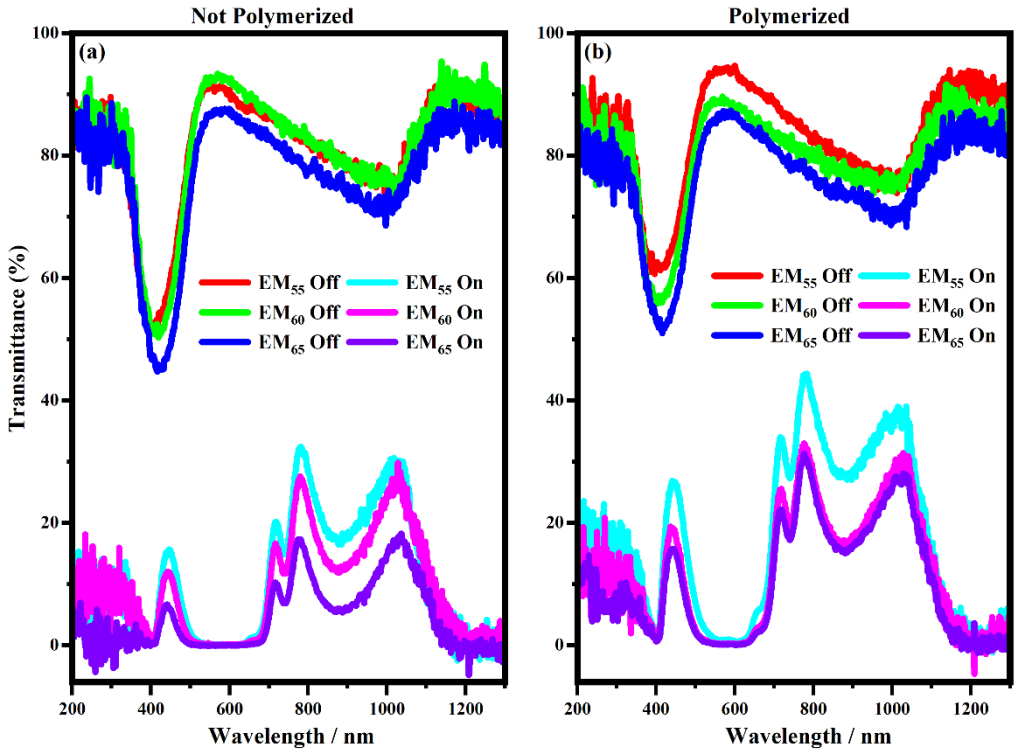

Figure 4.11.17. *Transmittance spectra, in the states Off and On, of the devices filled with EM_{55}, EM_{60} and EM_{65} not polymerized (a) and polymerized (b).*

In both the systems, polymerized and not polymerized, the spectra collected in the devices with the highest concentration of the electrochromic materials show a lower transmittance, at each wavelength, in both the states Off and On. Of course, it can be assigned to the number of the color centers that increases, as well as the concentration of the electrochromic materials, does.

Figure (4.11.18) and figure (4.11.19) show the comparison between transmittance spectra of the Off-state with respect to the On-state collected on the electrochromic devices filled with EM_{55}, EM_{60} and EM_{65} not polymerized and polymerized.

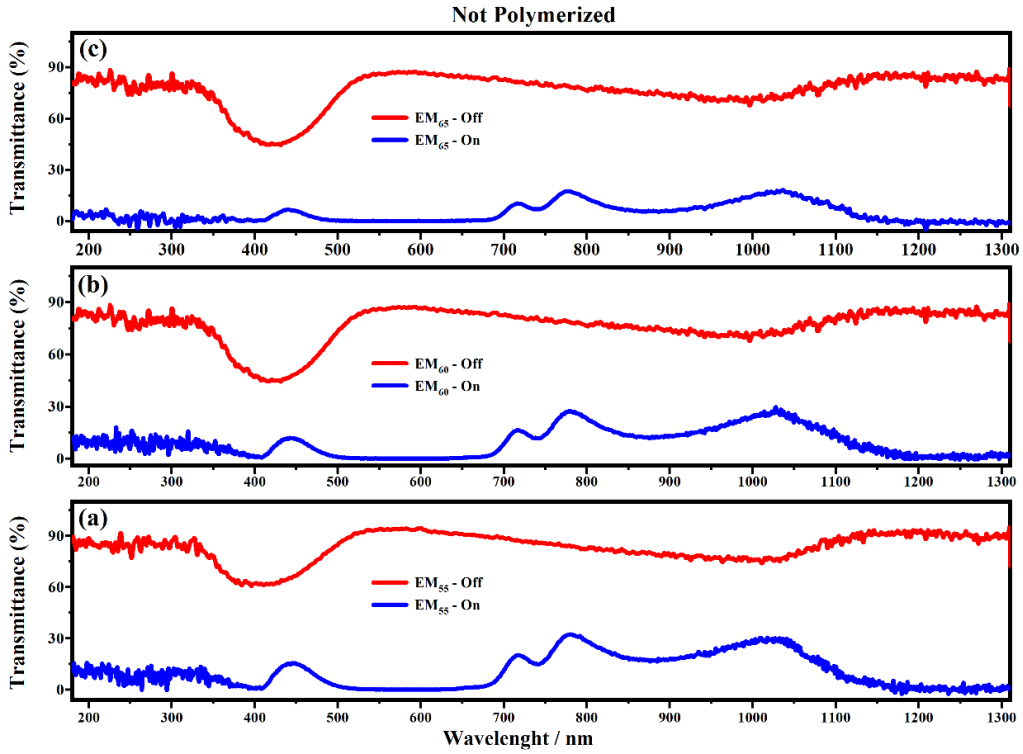

Figure 4.11.18. *Transmittance spectra, in the states Off and On, of the devices filled with EM_{55} (a), EM_{60} (b) and EM_{65} (c) not polymerized.*

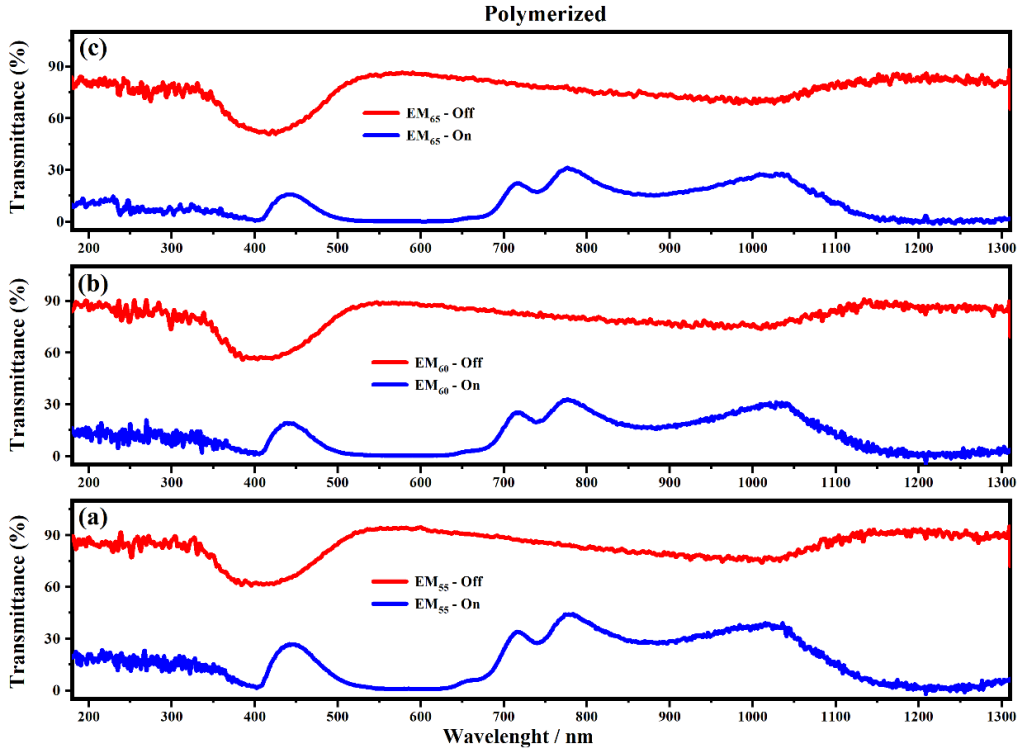

Figure 4.11.19. *Transmittance spectra, in the states Off and On, of the devices filled with EM_{55} (a), EM_{60} (b) and EM_{65} (c) not polymerized.*

Coloration Efficiency (CE) at a given wavelength is an important parameter to establish how good a device is:

$$CE = \frac{\Delta A}{Q}$$

In the previous formula, ΔA is the absorbance difference between ON and OFF states, and Q is the number of charges injected per unit area ([C]/[cm]^2). In the following table (4.11.1), CE at 580 nm and at 1200 nm for the devices filled with EM_{55}, EM_{60}, and EM_{65} polymerized and not polymerized are reported.

	Not polymerized		**Polymerized**	
Sample	**CE [C]/[cm]^2 (at 580 nm)**	**CE [C]/[cm]^2 (at 1200 nm)**	**CE [C]/[cm]^2 (at 580 nm)**	**CE [C]/[cm]^2 (at 1200 nm)**
EM_{55}	101,03	100,93	27,12	24,07
EM_{60}	93,61	65,03	92,82	80,38
EM_{65}	42,83	71,96	54,76	56,90

Table 4.11.1. *Coloration Efficiency at 580 nm and 1200 nm of the electrochromic devices filled with EM_{55} (a), EM_{60} (b) and EM_{65} (c) not polymerized.*

Figure (4.11.20) shows the transmittance spectra collected on the devices filled with EM_{60}, not polymerized after the first cycle and after 700 cycles (switch Off- On and switch On-Off).

By looking at the figure (4.11.20), it can be seen that the spectra collected after 700 cycles shows a lower transmittance with respect the spectra collected after one cycle and in particular ΔT% at 400nm, 600nm and 1205 nm is 3.3%, 6.6% and 6.3%, respectively. It means that the sample is becoming to degrade. On the contrary, as it can be seen in figure (4.11.21), when the EM_{60} is polymerized that system is still stable (without any forms of degradation) up to 2000 cycles. In the case of the polymerized samples (figure 4.11.21), the ΔT% is very low and does not shows any changes at each wavelength in the

considered range. It means that polymerization strongly enhances the life of the electrochromic devices.

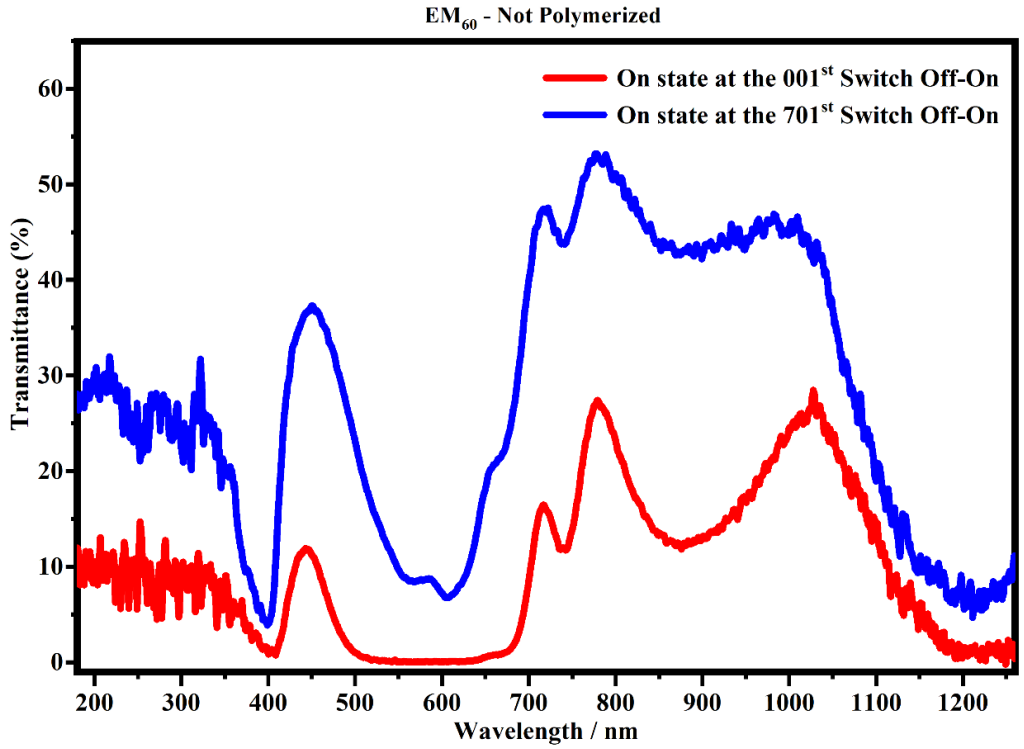

Figure 4.11.20. *Transmittance spectra, in the state On, of the devices filled with EM_{60} not polymerized at the 1st (red line) and 701st cycle (blue line).*

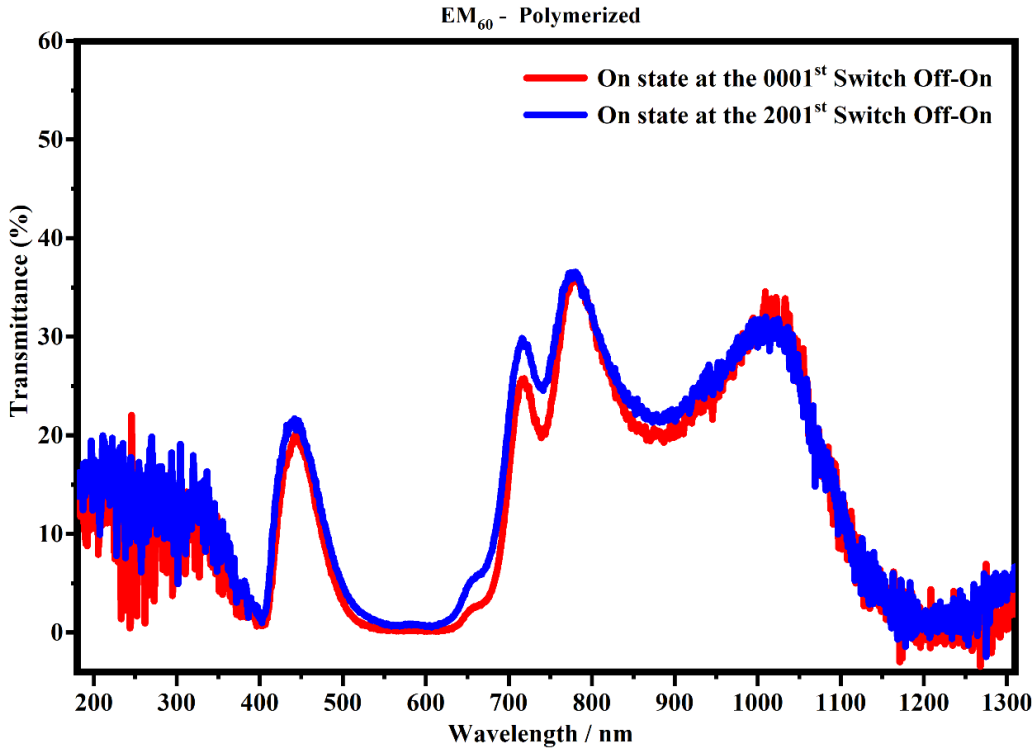

Figure 4.11.21. *Transmittance spectra, in the state On, of the devices filled with EM_{60} polymerized at the 1st (red line) and 2001st cycle (blue line).*

4.11.2.c Raman Spectroscopy

Raman spectroscopy was performed on the electrochromic devices filled with EM_{55}, $EM_{60,}$ and EM_{65} polymerized and not polymerized.

Raman spectra have been shown in two ranges: from 310 cm^{-1} to 2000 cm^{-1} and 2000 cm^{-1}-3510 cm^{-1}. In Figures (4.11.22-4.11.27) are shown the Raman spectra of the electrochromic devices filled with EM_{55}, $EM_{60,}$ and EM_{65} polymerized and not polymerized. All the Raman spectra show similar peaks. A triplet centred around 935 cm^{-1}, that is related to the (Cl−O) stretching in the perchlorate ions when they are free, interacts with propylene carbonate or with each other [6,102]. Peaks comprised between 822 cm^{-1} and 826 cm^{-1} correspond to the rings breathing mode of the viologen. In the 2000 cm^{-1} − 3500 cm^{-1} region, a change in the Raman spectra can be noticed between those collected on not polymerized spectra with respect to those collected on the polymerized spectra. The signal at about 3043 cm^{-1} in the spectra of the polymerized samples is very weak or totally absent compared to the spectra of not polymerized samples. Such behaviour is similar to the peak at 1640 cm^{-1} because both are related to the (C=C) stretching of the acrylate group of Bisphenol A. The Bisphenol A polymerization occurs at the terminal (C=C) double bond; studies of the intensity variation of the 1640 cm^{-1} bands during polymerization have already been reported [23]. Peaks at 1726 cm^{-1} and 1787 cm^{-1} can be assigned to (C=O) groups: the first one to the acrylate carbonyl group, the second one to the propylene Carbonate carbonyl group). Several signals in the spectra can be assigned to Propylene Carbonate [6]: the band at ~455 cm^{-1} can be assigned to the propylene carbonate ring deformation, while the strong band at ~712 cm^{-1} can be assigned to its symmetric ring deformation. The strong band at ~849 cm^{-1} can be assigned to the (C−H) methyl group and to (O−C−C) (not comprising Carbon bond to the methyl group) bending of Propylene Carbonate. The band at ~1119 cm^{-1} is assigned to the (C-H) methyl group and to the (C-H) stretching of Carbon of the methyl group of Propylene Carbonate. A very low signal can be identified at ~1147 cm^{-1}, corresponding to a (C−C) stretching (Carbon to the methyl group and the immediately one bound in the ring) and to an (O−C−O) (comprising the Carbon in the (C=O) group) bending of the Propylene Carbonate. Signals with very low intensity can be identified between 1336 cm^{-1} and 1391 cm^{-1}, related to the (C−H) methyl group bending of Propylene Carbonate. Signal centred around 1460 cm^{-1} can be assigned to the (C−H)

methyl group umbrella mode of Propylene Carbonate. Signals at ~2882 cm^{-1}, ~2940 cm^{-1} and ~2990 cm^{-1} can be assigned to the various (CH_2) and (CH_3) stretching modes of species in solution. Very low Raman peaks below 455 cm^{-1} can be assigned to Diethyl Ferrocene rings modes. Signal at 3073 cm^{-1} cans be assigned to the (C-H) stretching of aromatic rings. Since no signals can be observed in the 3200 cm^{-1} – 3500 cm^{-1} range, condensation between different polymeric chains can be excluded (i.e. no water can be identified in the spectra).

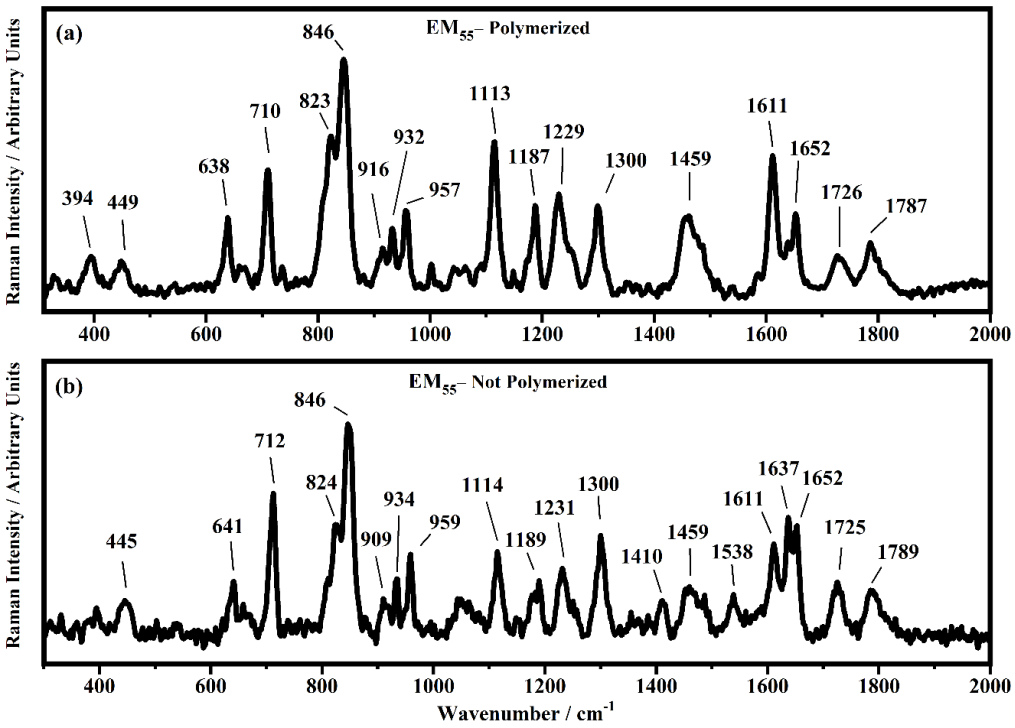

Figure 4.11.22. *Raman Spectra collected in the range between 310 and 2000 cm^{-1} on the samples EM_{55} polymerized (a) and not polymerized (b).*

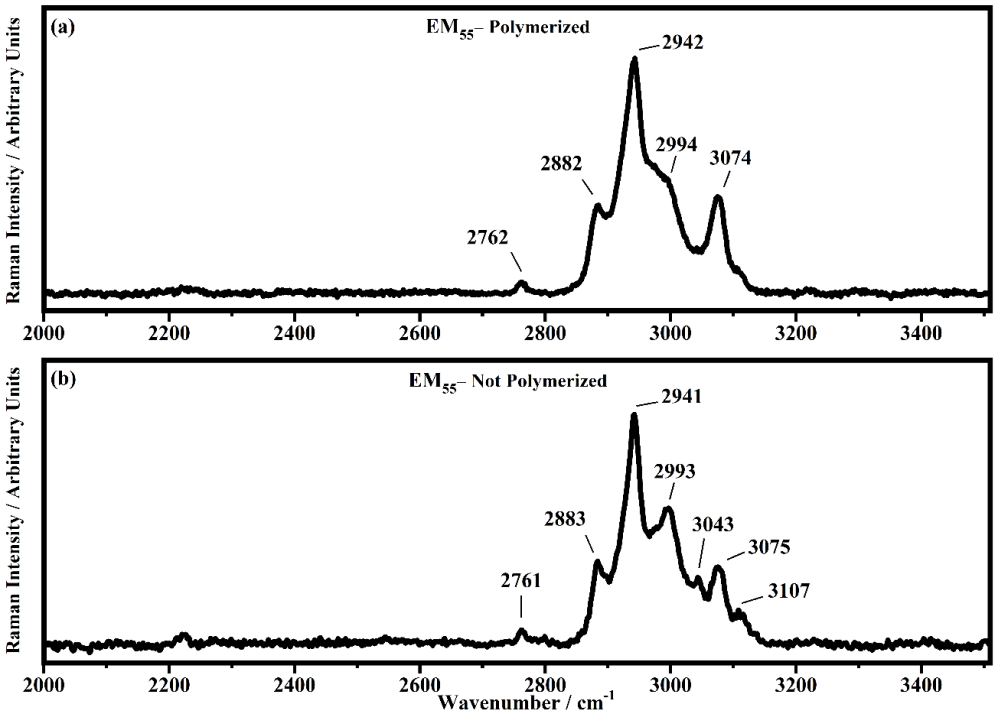

Figure 4.11.23. *Raman Spectra collected in the range between 2000 and 3510 cm^{-1} on the samples EM$_{55}$ polymerized (a) and not polymerized (b).*

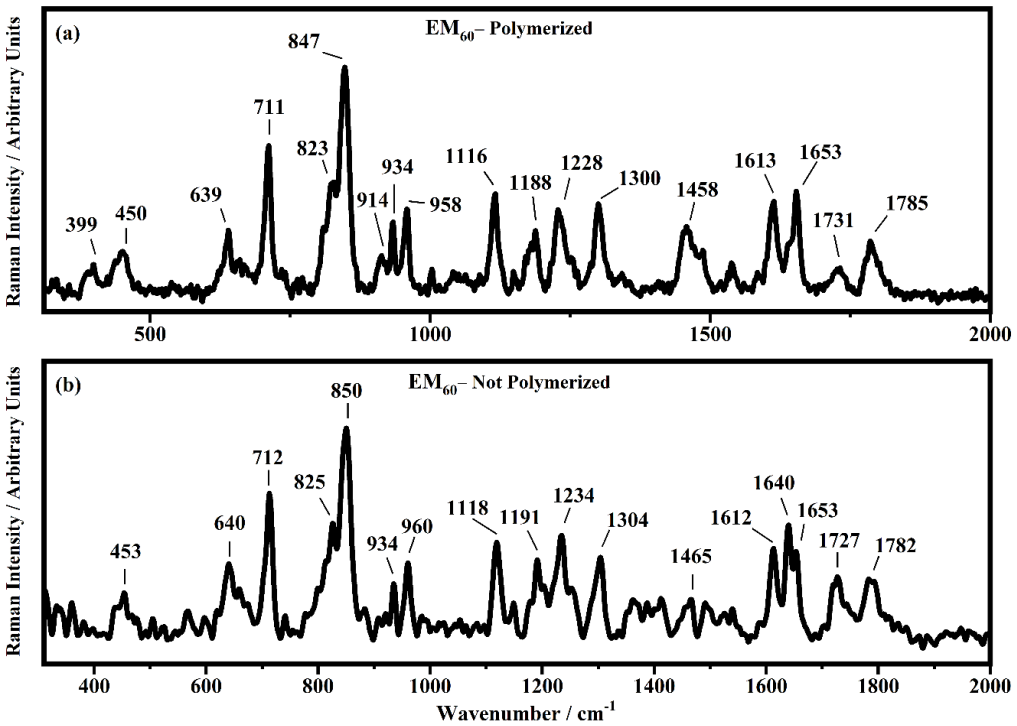

Figure 4.11.24. *Raman Spectra collected in the range between 310 and 2000 cm^{-1} on the samples EM$_{60}$ polymerized (a) and not polymerized (b).*

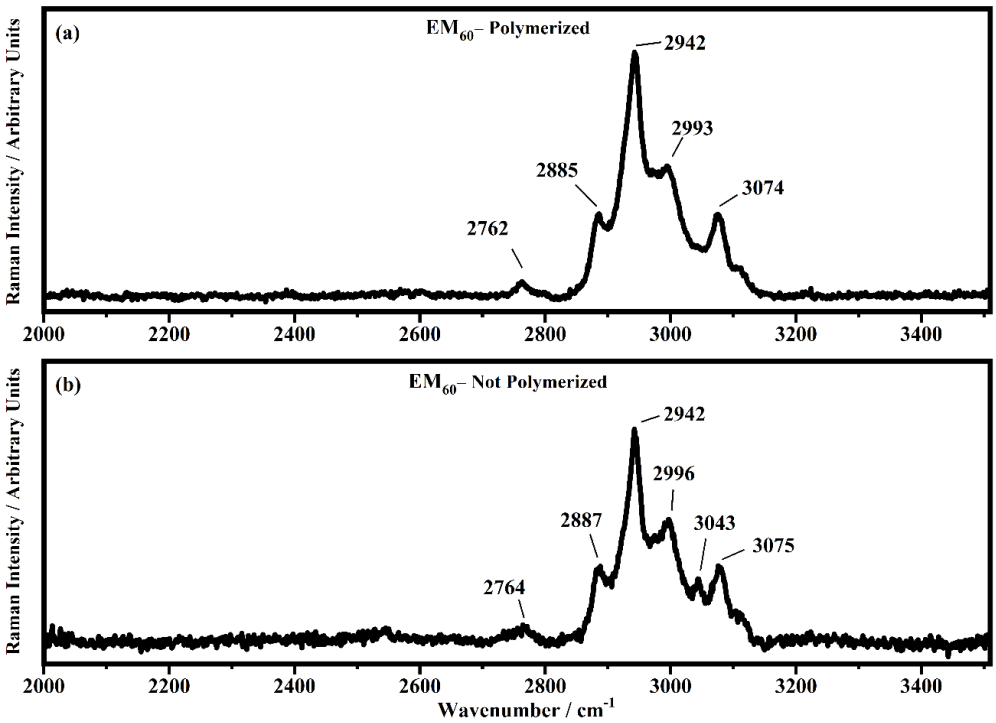

Figure 4.11.25. *Raman Spectra collected in the range between 2000 and 3510 cm^{-1} on the samples EM_{60} polymerized (a) and not polymerized (b).*

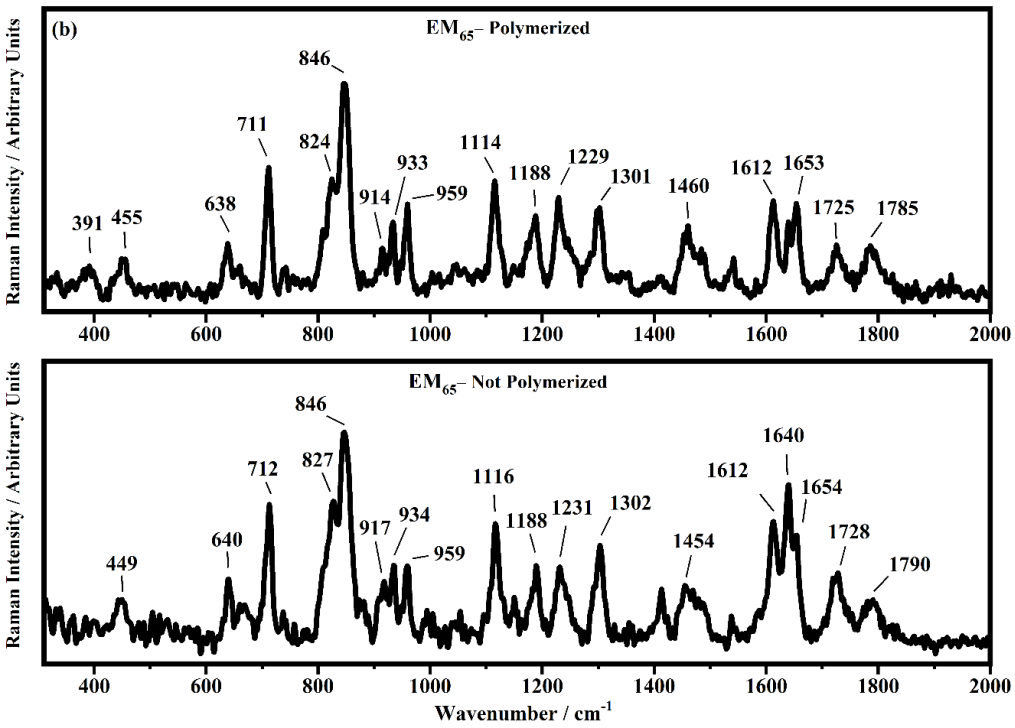

Figure 4.11.26. *Raman Spectra collected in the range between 310 and 2000 cm^{-1} on the samples EM_{65} polymerized (a) and not polymerized (b).*

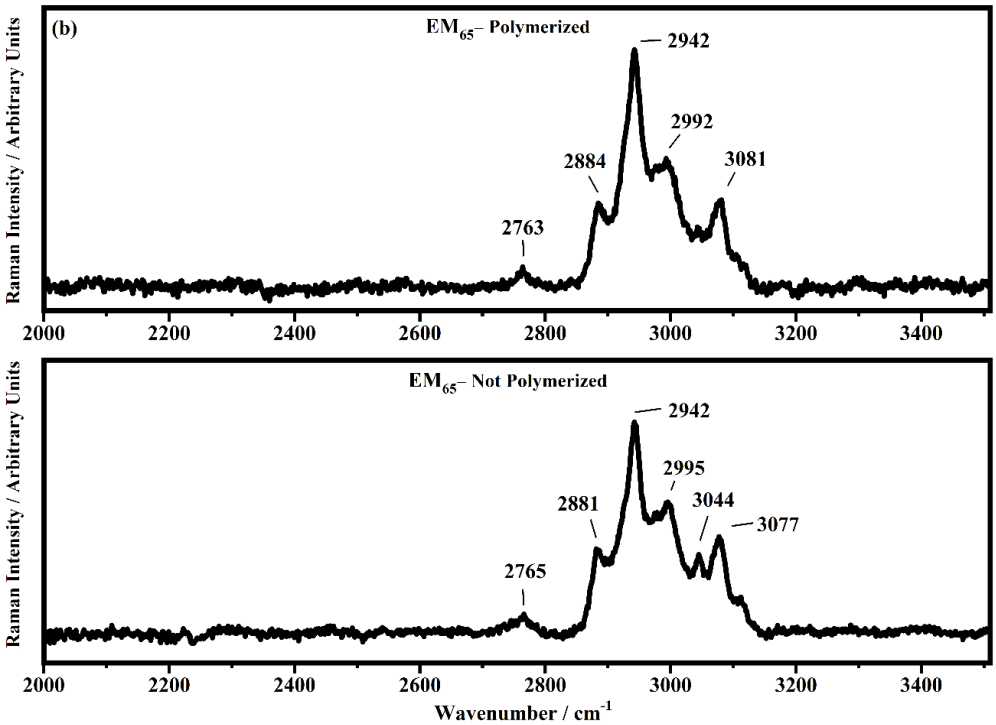

Figure 4.11.27. *Raman Spectra collected in the range between 2000 and 3510 cm^{-1} on the samples EM_{65} polymerized (a) and not polymerized (b).*

Table (4.11.2-4.11.4) summarize the above discussion.

Frequency (cm^{-1})		Assignments	references
EM_{55}			
polymerized	**Not polymerized**		
394			
449	445	PC ring deformation	[6]
638	641	Aromatic (C–H) out of plane def. (BPA)	[12][17]
710	712	Sym. ring deformation (PC)	[6]
823	824	Ring breathing viologen	
846	846	Sym. ring vibration (PC) + (CH_3) and (O–C–C) bending of PC	[5] [6]
916	909	(Cl−O) stretching	[6][102]
932	934	(Cl−O) stretching	[6][102]
957	959	(Cl−O) stretching	[6][102]
1113	1114	(CH_3) wagging + (C–H) bending (PC)	[6]
1187	1185	(CH_3)/gem-dimethyl def. (C–C) stretching (BPA)	[17]
1229	1231	Asymmetric stretching (PC) 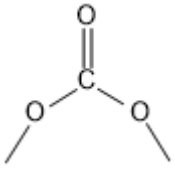	[5]
1300	1300	asym stretching (=C–O–C) (BPA)	[12] [17]
	1410		
1459	1459	Asymmetric bending (CH_3) (PC)	[5]
	1538		
1611	1611	Aromatic ring stretching vibration (BPA)	[12][18-20]
	1637	Vinyl (C=C) stretching (BPA)	[12][18-22]
1652	1652		

Table 4.11.2. *Observed Raman bands of the EM_{55} device.*

Frequency (cm^{-1})		Assignments	references
EM_{55}			
polymerized	**Not polymerized**		
1726	1725	(C=O) stretching acrylates	[12][20-22]
1787	1789	(C=O) stretching PC	[5][6]
2762	2761	(C–H) stretching	[5] [6]
2882	2883	($C–H_2$) stretching	[5] [6][21]
2942	2941	($C–H_3$) stretching	[5][6][12][21]
2994	2993	($C–H_3$) stretching	[5] [6]
	3043	BPA (=C–H) stretching	[12]
3074	3075	BPA (=C–H) stretching	[12][22]
	3107		

Table 4.11.2. (continued) *Observed Raman bands of the EM_{55} device.*

Frequency (cm^{-1})		Assignments	references
EM_{60}			
polymerized	**Not polymerized**		
399			
450	453	PC ring deformation	[6]
639	640	Aromatic (C–H) out of plane def. (BPA)	[12][17]
711	712	Sym. ring deformation (PC)	[6]
823	825	Ring breathing viologen	
847	850	Sym. ring vibration (PC) + (CH_3) and (O–C–C) bending of PC	[5] [6]
914		(Cl−O) stretching	[6][102]
934	934	(Cl−O) stretching	[6][102]
958	960	(Cl−O) stretching	[6][102]
1116	1118	(CH_3) wagging + (C–H) bending (PC)	[6]
1188	1191	(CH_3)/gem-dimethyl def. (C–C) stretching (BPA)	[17]

Table 4.11.3. *Observed Raman bands of the EM_{60} device.*

Frequency (cm^{-1})		Assignments	references
EM_{60}			
polymerized	Not polymerized		
		Asymmetric stretching (PC)	
1228	1234	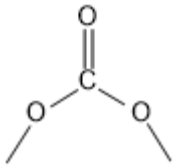	[5]
1300	1304	asym stretching (=C–O–C) (BPA)	[12] [17]
1458	1465	Asymmetric bending (CH_3) (PC)	[5]
1613	1612	Aromatic ring stretching vibration (BPA)	[12][18-20]
	1640	Vinyl (C=C) stretching (BPA)	[12][18-22]
1653	1653		
1731	1727	(C=O) stretching acrylates	[12][20-22]
1785	1782	(C=O) stretching PC	[5][6]
2762	2764	(C–H) stretching	[5] [6]
2885	2887	($C–H_2$) stretching	[5] [6][21]
2942	2942	($C–H_3$) stretching	[5][6][12][21]
2993	2996	($C–H_3$) stretching	[5] [6]
	3043	BPA (=C–H) stretching	[12]
3074	3075	BPA (=C–H) stretching	[12][22]

Table 4.11.3. (continued) *Observed Raman bands of the EM_{60} device.*

Frequency (cm^{-1})		Assignments	references
EM_{65}			
polymerized	Not polymerized		
391			
455	445	PC ring deformation	[6]
638	640	Aromatic (C–H) out of plane def. (BPA)	[12][17]
711	712	Sym. ring deformation (PC)	[6]
824	827	Ring breathing viologen	
846	846	Sym. ring vibration (PC) + (CH_3) and (O–C–C) bending of PC	[5] [6]

Table 4.11.4. *Observed Raman bands of the EM_{65} device.*

Frequency (cm^{-1})		Assignments	references
EM_{65}			
polymerized	**Not polymerized**		
914	917	(Cl−O) stretching	[6][102]
933	934	(Cl−O) stretching	[6][102]
959	959	(Cl−O) stretching	[6][102]
1114	1116	(CH_3) wagging + (C–H) bending (PC)	[6]
1188	1188	(CH_3)/gem-dimethyl def. (C–C) stretching (BPA)	[17]
1229	1231	Asymmetric stretching (PC) 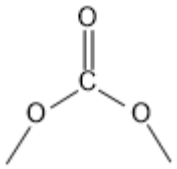	[5]
1301	1302	asym stretching (=C–O–C) (BPA)	[12] [17]
1460	1454	Asymmetric bending (CH_3) (PC)	[5]
1612	1612	Aromatic ring stretching vibration (BPA)	[12][18-20]
	1640	Vinyl (C=C) stretching (BPA)	[12][18-22]
1653	1654		
1725	1728	(C=O) stretching acrylates	[12][20-22]
1785	1790	(C=O) stretching PC	[5][6]
2763	2765	(C–H) stretching	[5] [6]
2884	2881	(C–H_2) stretching	[5] [6][21]
2942	2942	(C–H_3) stretching	[5][6][12][21]
2992	2995	(C–H_3) stretching	[5] [6]
	3044	BPA (=C–H) stretching	[12]
3081	3077	BPA (=C–H) stretching	[12][22]

Table 4.11.4. (continued) *Observed Raman bands of the EM_{65} device.*

4.11.3 Conclusions

Several samples containing an electrochromic mix were prepared: electrochromic solution contained electrochromic materials, with a redox couple (Ethyl Viologen Diperchlorate and Diethyl Ferrocene) and an aprotic solvent (Propylene Carbonate). Electrochromic solution was mixed together with a solution of Bisphenol A glycerolate (1 glycerol/phenol) diacrylate with photinitiator Irgacure, in different proportions, in order to verify the electrochromic performances of devices by varying EM compositions. The best composition was that with 60 wt% of electrochromic solution. Differences in terms of performance were noticed between samples not polymerized and samples polymerized. The last ones show shorter switching times and were able to have a longer cycle life (more than 2000 cycles vs 700 and, since cycles were symmetrical when polarity was reversed during cyclic voltammetry, one can take into account a doubled number of cycles, so (4000 vs 1400). Degradation occurs inside samples not polymerized. Transmittance spectra revealed typical absorbance peaks at 585, 600 and 880 nm of Ethyl Viologen radical and dimer forms: the sample's dark blue color is related to Diethyl Ferrocene oxidation, Ethyl Viologen single reduction, and charge separation inside the solution due to the applied potential.

Samples show exceptional optical contrast ($\Delta T\%$) of ~ 40% at 432 nm, up to 88% at 580 nm and 78% at 1200 nm, making the Electrochromic devices studied during this work as good candidates to make smart windows.

A sample with not polymerized Bisphenol A at its 1^{st} and 701^{st} cycle shows at 1205 nm a difference in terms of $\Delta T\%$ (between a new and a degraded sample in the ON state) of 6.3%, 6,63% at 605 nm and 3.27% at 400 nm; this difference is almost zero in a sample with polymerized Bisphenol A inside between its 1^{st} and 2001^{st} cycle (in the ON state).

It has been seen that the spectra collected after 700 cycles shows a lower transmittance with respect the spectra collected after one cycle and in particular $\Delta T\%$ at 400nm, 600nm and 1205 nm is 3.3%, 6.6% and 6.3%, respectively. It means that the sample is becoming to degrade.

On the contrary, the relative Electrochromic device polymerized are stables up to 2000 cycles.

4.12 References

[1] G. Cai, J. Wang, P.S. Lee, *Next-Generation Multifunctional Electrochromic Devices*, **Acc. Chem. Res.**, **49** (2016), 1469 – 1476.

[2] V.K. Thakur, G. Ding, J. Ma, P.S. Lee, X. Lu, *Hybrid Materials and Polymer Electrolytes for Electrochromic Device Applications*, **Adv. Mater.**, **24** (2012), 4071 – 4096.

[3] A.L.S. Eh, A.W.M. Tan, X. Cheng, S. Magdassi, P.S. Lee, *Recent Advances in Flexible Electrochromic Devices: Prerequisites, Challenges, and Prospects*, **Energy Technol.**, **6** (2018), 33 – 45.

[4] V. Rai, R.S. Singh, D.J. Blackwood, D. Zhili, *A Review on Recent Advances in Electrochromic Devices: A Material Approach*, **Adv. Eng. Mater.**, **22** (2020).

[5] G.J. Janz, J. Ambrose, J.W. Coutts, J.R. Downey, *Raman spectrum of propylene carbonate*, **spectrochimica Acta**, **35A** (1979), 175 – 179.

[6] D. Battisti, G.A. Nazri, B. Klassen, R. Aroca, *Vibrational Studies of Lithium Perchlorate in Propylene Carbonate Solutions*, **J. Phys. Chem.**, **97** (1993), 5826 – 5830.

[7] I. Nicotera, L. Coppola, C. Oliviero, M. Castriota, E. Cazzanelli, *Investigation of ionic conduction and mechanical properties of PMMA – PVdF blend based polymer electrolytes*, **Solid State Ionics**, **177** (2006), 581 – 588.

[8] J. Grondin, D. Talaga, J.C. Lassègues, W.A. Henderson, *Raman study of crystalline solvates between glymes CH3(OCH2CH2)nOCH3 (n = 1, 2 and 3) and LiClO4*, **Phys. Chem. Chem. Phys.**, **6** (2004), 938 – 944.

[9] H. Graener, R. Zürl, M. Hofmann, *Vibrational relaxation of liquid chloroform*, **J. Phys. Chem. B**, **101** (1997), 1745 – 1749.

[10] B. Sandner, J. Tübke S. Wartewig, S. Shashkov, *Ionic association in oligo(ethylene glycol)-lithium triflat solutions as studied by FT Raman spectroscopy*, **Solid State Ionics, 83** (1996), 87 – 97.

[11] B. Sandner, J. Tübke, A. Werther, R. Sandner, S. Wartewig, S. Shashkov, *Ionic association in gel electrolytes of varied polarity as studied by FT Raman spectroscopy*, **Electrochimica Acta**, **43** (1998), 1563 – 1567.

[12] G. Socrates, *Infrared and Raman characteristic group frequencies*, **Wiley** (2001).

[13] A. Ferry, *Ionic Interactions and Transport Properties in Methyl Terminated Poly(propylene glycol)(4000) Complexed with $LiCF_3SO_3$*, **J. Phys. Chem. B**, **101** (1997), 150 – 157.

[14] K. J. Thomas, M. Sheeba, V. P. N. Nampoori, C. P. G. Vallabhan, P. Radhakrishnan, *Raman spectra of polymethyl methacrylate optical fibres excited by a 532 nm diode pumped solid state laser*, **J. Opt. A: Pure Appl. Opt.**, (2008).

[15] H. A. Willis, Mrs. V.J.I. Zichy, P.J. Hendra, *The Laser-Raman and Infra-red Spectra of Poly(Methyl Methacrylate)*, **Polymer Volume 10**, (1969).

[16] E. Cazzanelli, G. Mariotto, G.B. Apetecchi, F. Croce, *Raman Study of Ion-Molecules Interaction in Poly(Methylmetacrylate)-Based Gel Electrolytes*, **Ionics 2** (1996).

[17] K.E. Chike, M.L. Myrick, R.E. Lyon, S.M. Angel, *Raman and Near-Infrared Studies of an Epoxy Resin*, **Applied Spectroscopy**, **47** (1993).

[18] K. Bukovinszky, M. Szalóki, I. Csarnovics, I. Szabó, S. Kéki, M. Nagy , C. Hegedüs, *Green LED as an Effective Light Source for Curing Acrylate-Based Dental Resins in Combination with Irgacure 784*, **Advances in Condensed Matter Physics**, (2018).

[19] A. Lungu, N.M. Florea, G. Voicu, H. Iovu, *Comparison between octa - or monofunctional poss interactions with dimethacrylate monomers*, **U.P.B. Sci. Bull., Series B**, **73** (2011).

[20] X. Guo, P. Spencer, Y. Wang, Q. Ye, X. Yao, K. Williams, *Effects of a solubility enhancer on penetration of hydrophobic component in model adhesives into wet demineralized dentin*, **dental materials 23**, (2007).

[21] N.M. Sulca, A. Lungu, R. Popescu, S.A. Garea, H. Iovu, *New Polymeric Nanocomposites Based on Polyhedral Oligomeric Silsesquioxanes*, **Materiale Plastice**, **46** (2009).

[22] L. Hodásová, J. Sans, B.G. Molina, C. Alemán, L. Llanes, G. Fargas, E. Armelin, *Polymer infiltrated ceramic networks with biocompatible adhesive and 3D-printed highly porous scaffolds*, **Additive Manufacturing**, **39** (2021).

[23] D. Ostrovskii, .LM. Torell, G.B. Appetecchi, B. Scrosati, *An electrochemical and Raman spectroscopical study of gel polymer electrolytes for lithium batteries*, **Solid State Ionics**, **106** (1998), 19 – 24.

[24] B. Klassen, R. Aroca, M. Nazri, G.A. Nazri, *Raman spectra and transport properties of lithium perchlorate in ethylene carbonate based binary solvent systems for lithium batteries*, **J. Phys. Chem. B**, **102** (1998), 4795 – 4801.

[25] A. Kokaislová, T. Helešicová, M. Ončák, P. Matějka, *Spectroscopic studies of folic acid adsorbed on various metal substrates: does the type of substrate play an essential role in temperature dependence of spectral features?*, **J. Raman Spectrosc.**, **45** (2014), 750 – 757.

[26] J.J. Castillo, T. Rindzevicius, C.E. Rozo, A. Boisen, *Adsorption and Vibrational Study of Folic Acid on Gold Nanopillar Structures Using Surface-enhanced Raman Scattering Spectroscopy*, **Nanomater Nanotechnol**, (2015).

[27] M.B. Moran, G.C. Martin, *The Laser Raman Spectrum of Poly(ethylene Glycol Dimethacrylate)*, **J. Macromol. Sci.**, **Part A-Chem.** (1983), 611 – 618.

[28] J.L. Koenig, A.C. Angood, J. Semen, J.B. Lando, *Laser-Excited Raman Studies of the Conformational Transition of Syndiotactic Polymethacrylic Acid in Water*, **J. of the Amer. Chem. Soc.**, (1969).

[29] J. Bong, K. Choi, S.C. Yu, S.I. Kwon, Y. Cho, C. Park, H.W. Park, *Raman Spectroscopy of Irradiated Normoxic Polymethacrylic Acid Gel Dosimeter*, **Bull. Korean Chem. Soc.**, **32** (2011).

[30] S. Nie, S.R. Emory, *Probing Single Molecules and Single Nanoparticles by Surface-Enhanced Raman Scattering*, **Science, 275** (1997), 1102 – 1106.

[31] E.C. Le Ru, M. Meyer, P.G. Etchegoin, *Proof of Single-Molecule Sensitivity in Surface Enhanced Raman Scattering (SERS) by Means of a Two-Analyte Technique*, **J. Phys. Chem. B, 110** (2006), 1944 – 1948.

[32] R.A. Halvorson, P.J. Vikesland, *Surface-Enhanced Raman Spectroscopy (SERS) for Environmental Analyses*, **Environ. Sci. Technol., 44** (2010), 7749 – 7755.

[33] R.A. Álvarez-Puebla, L.M. Liz-Marzán*, Environmental Applications of Plasmon Assisted Raman Scattering*, **Energy Environ. Sci., 3** (2010).

[34] C. Andreou, R. Mirsafavi, M. Moskovits, C.D. Meinhart, *Detection of Low Concentrations of Ampicillin in Milk*, **The Analyst, 140** (2015), 5003 – 5005.

[35] A. Pallaoro, M.R. Hoonejani, G.B. Braun, C.D. Meinhart, M. Moskovits, *Rapid Identification by Surface-Enhanced Raman Spectroscopy of Cancer Cells at Low Concentrations Flowing in a Microfluidic Channel*, **ACS Nano, 9** (2015), 4328 – 4336.

[36] J. Yang, M. Palla, F. G. Bosco, T. Rindzevicius, T.S. Alstrøm, M.S. Schmidt, A. Boisen, J. Ju, Q. Lin, *Surface-Enhanced Raman Spectroscopy Based Quantitative Bioassay on Aptamer-Functionalized Nanopillars Using Large-Area Raman Mapping*, **ACS Nano, 7** (2013), 5350 – 5359.

[37] R. Pilot, R. Signorini, C. Durante, L. Orian, M. Bhamidipati, L. Fabris, *A Review on Surface-Enhanced Raman Scattering*, **Biosensors, 9** (2019), 57.

[38] M. Fleischmann, P.J. Hendra, A.J. McQuillan, *Raman Spectra of Pyridine Adsorbed at a Silver Electrode*, **Chem. Phys. Lett., 26** (1974), 163 – 166.

[39] M. Castriota, T. Caruso, A. Policicchio, S. La Rosa, R.G. Agostino, E. Cazzanelli, *Anomalous Enhancement of Raman Scattering of Metal Oxide Film Deposited on Thermally Treated ITO-Coated Glass Substrates*. **Chem. Phys. Lett., 478** (2009), 195 – 199.

[40] P. Mosier-Boss*, Review of SERS Substrates for Chemical Sensing*, **Nanomaterials, 7** (2017), 142.

[41] D. Policastro, E. Giorno, F. Scarpelli, N. Godbert, L. Ricciardi, A. Crispini, A. Candreva, F. Marchetti, S. Xhafa, R. De Rose, A. Nucera, R.C. Barberi, M. Castriota, L. De Bartolo, I. Aiello, New Zinc-Based Active Chitosan Films: Physicochemical Characterization, Antioxidant, and Antimicrobial Properties. **Front. Chem., 10** (2022), 884059.

[42] A. Candreva, G. Di Maio, F. Parisi, F. Scarpelli, A. Crispini, N. Godbert, L. Ricciardi, A. Nucera, C. Rizzuto, R.C. Barberi, M. Castriota, M. La Deda, *Luminescent*

Self-Assembled Monolayer on Gold Nanoparticles: Tuning of Emission According to the Surface Curvature, **Chemosensors, 10** (2022), 176.

[43] G. Palermo, R. Grillo, L. Pezzi, T. Bürgi, N. Tabiryan, L. De Sio, C. Umeton, Photo-Aligned Nematic Liquid Crystals Enable the Modulation of Thermoplasmonic Heating. **Appl. Sci., 11** (2021), 6272.

[44] J. Kimling, M.Maier, B. Okenve, V. Kotaidis,; H. Ballot, A. Plech, *Turkevich Method for Gold Nanoparticle Synthesis Revisited*, **J. Phys. Chem. B110** (2006), 15700 – 15707.

[45] G. Decher, Fuzzy Nanoassemblies: Toward Layered Polymeric Multicomposites. **Science, 277** (1997), 1232 – 1237.

[46] X. Shen, K. Han, L. Ma, M. Gao, X. Xu, J. Luo, *Nano-Ag-forest based surface enhanced Raman spectroscopy (SERS) of confined acetic acid*, **Colloids and Surfaces A, 547** (2018), 126 – 133.

[47] J.E. Bertie, K.H. Michaelian, *The Raman spectrum of gaseous acetic acid at 21 °C*, **The J. of Chem. Phys., 77** (1982), 5267 – 5271.

[48] B. Yang, Y. Li, N. Gong, X. Cao, S. Wang, C. Sun, *Study of molecular association in acetic acid-water binary solution by Raman spectroscopy*, **Spectrochimica Acta Part A: Molec. and Biomol. Spec., 213** (2019), 463 – 466.

[49] N. Nishi, T. Nakabayashi, K. Kosugi, *Raman Spectroscopic Study on Acetic Acid Clusters in Aqueous Solutions: Dominance of Acid-Acid Association Producing Microphase*, **J. of Phys. Chem. A, 103** (1999), 10851 – 10858.

[50] W. B. White, D. G. Minser, *Raman spectra and structure of natural glasses*, **J. of Non-Cryst. Solids, 67** (1984), 45 – 59.

[51] X.F. Liu, Y.L. Guan, D.Z. Yang, Z. Li, K.D. Yao, *Antibacterial Action of Chitosan and Carboxymethylated Chitosan*, **J. of Appl. Poly. Science, 79** (2001), 1324 – 1335.

[52] R. Alves, F. Sentanin, R.C. Sabadini, A. Pawlicka, M.M. Silva, *Solid polymer electrolytes based on chitosan and Dy(CF3SO3)3 for electrochromic devices***, Solid State Ionics, 310** (2017), 112 – 120.

[53] R.S. Das, Y.K. Agrawal, *Raman spectroscopy: Recent advancements, techniques and applications*, **Vibrational Spectroscopy, 57** (2011), 165.

[54] Y. Akama, A. Tong, N. Matsumoto, T. Ikeda, S. Tanaka, *Raman spectroscopic study on keto–enol tautomers of 1–phenyl–3–methyl–4–benzoyl–5–pyrazolone*, **Vibrational Spectroscopy, 13** (1996), 113 – 115.

[55] T. Ueda, Y. Akama, *Spectroscopic proof for intermolecular or intramolecular hydrogen bonds in keto-enol tautomers of 1 -phenyl-3-methyl-4-benzoyl-5-pyrazolone*, **Chemical Physics Letters, 222** (1994), 559 – 562.

[56] T. Chithambarathanu, V. Umayorubaghan, V. Krishnakumar, *Vibrational analysis of some pyrazole derivatives*, **Ind. J. of Pure & Appl. Phys., 41** (2003), 844 – 848.

[57] K. Baghat, T. El-Emary, *Infrared Raman and NMR spectra conformational stability normal coordinate analysis and B3LYP calculations of 5-Amino-3-methyl-1-phenyl-1H-pyrazole-4-carbaldehyde*, **J. of Mol. Struc., 1034** (2013), 325 – 335.

[58] A. Zajac, J. Hanuza, M. Wandas, L. Dyminska, *Determination of N–acetylation degree in chitosan using Raman spectroscopy*, **Spectro. Acta Part A: Mole. and Biomol. Spect., 134** (2015), 114 – 120.

[59] K. Zhang, A. Geissler, S. Fischer, E. Brendler, E. Baucker, *Solid-State Spectroscopic Characterization of α-Chitins Deacetylated in Homogeneous Solutions*, **J. of Phys. Chem. B, 116** (2012), 4584 – 4592.

[60] G. P. Mikhailova, S. V. Tuchkova, V. V. Lazareva, E. I. Kulish, *Complexation of Chitosan with Acetic Acid According to Fourier Transform Raman Spectroscopy Data*, **Russian Journal of Physical Chemistry A, 88** (2014).

[61] S. Kumar, J. Koh, Synthesis, *physiochemical and optical properties of chitosan-based dye containing naphthalimide group*, **Carbohydrate Polymers, 94** (2013), 221 – 228.

[62] M. Escamilla–García, G. Calderón–Domínguez, J.J. Chanona–Pérez, R.R. Farrera–Rebollo, J.A. Andraca–Adame, I. Arzate–Vázquez, J.V. Mendez–Mendez, L.A. Moreno–Ruiz, *Physical and structural characterisation of zein and chitosan edible films using nanotechnology tools*, **Intern. J. of Biol. Macro., 61** (2013), 196-203.

[63] J.E.S.A. Menezes, H.S. dos Santos, M.K.A. Ferreira, F.E.A. Magalhães, D.S. da Silva, P.N. Bandeira, G.D. Saraiva, O.D.L. Pessoa, N.M.P.S. Ricardo, B.G. Cruz, A.M.R. Teixeira, *Preparation, structural and spectroscopic characterization of chitosan membranes containing allantoin*, **J. of Mol. Stru., 1199** (2020), 126968.

[64] M. Patel, M. Travadi, R.N. Jadeja, *Synthesis, crystal structure and spectral characterization of Co(II) complexes with acylpyrazolone ligands*, **J. of the Ind. Chem. Soc., 98** (2021), 100 − 168

[65] L. Ravindranath, B.V. Reddy, *Theoretical and experimental study of torsional potentials, molecular structure (monomer and dimer), vibrational analysis and molecular characteristics of some dimethyl bipyridines*, **Journal of Molecular Structure, 1200** (2020), 127089.

[66] L. Ould-Moussa, M. Castella-Ventura, E. Kassab, O. Poizat, D.P. Strommen, J.R. Kincaid, *Ab initio and density functional study of the geometrical, electronic and vibrational properties of 2,2'−bipyridine*, **J. Raman Spectrosc., 31** (2000), 377 – 390.

[67] J. Kumar, R. Thomas, R.S. Swathi, K.G. Thomas, *Au nanorod quartets and Raman signal enhancement: towards the design of plasmonic platforms*, **Nanoscale, 6** (2014), 10454.

[68] J. Kumar, K.G. Thomas, *Surface-Enhanced Raman Spectroscopy: Investigations at the Nanorod Edges and Dimer Junctions*, **J. Phys. Chem. Lett., 2** (2011), 610 – 615.

[69] K. Yamanaka, *New Counter-Electrodes Made of Iron Compound Graphite Mixtures for WO3 Liquid Electrolyte Electrochromic Devices*, **Jpn. J. Appl. Phys., 21** (1982), 926 – 929.

[70] H. Kim, Y. Park, D. Choi, W.S. Chu, S.H. Ahn, D.-M. Chun, C.S. Lee, *Kinetic spraying of silver nanowire blended graphite powder to fabricate transparent conductive electrode and their application in electrochromic device*, **Applied Surface Science, 456** (2018), 19 – 24

[71] S. Mishra, R. Kumar, *Graphene nanoflakes: Foundation for improving solid state electrochemistry based electrochromic devices*, **Sol. Ener. Mater. and Sol. Cells, 200** (2019), 110041

[72] S. Soylemez, H.Z. Kaya, Y.A. Udum, L. Toppare, *A multipurpose conjugated polymer: Electrochromic device and biosensor construction for glucose detection*, **Orga. Electro., 65** (2019), 327 – 333.

[73] F. Tuinstra, J.L. Koenig, *Raman Spectrum of Graphite*, **journ. of chem. physics 53, n° 3** (1970).

[74] S. Reich, C. Thomsen, *Raman spectroscopy of graphite*, **Phil. Trans. R. Soc. Lond. A,** (2004).

[75] M. A. Pimenta, G. Dresselhaus, M.S. Dresselhaus, L.G. Cançado, A. Jorio, R. Saito, *Studying disorder in graphite-based systems by Raman spectroscopy***, Phys. Chem. Chem. Phys**. 9, (2007) 1276–1291.

[76] A.C. Ferrari, D.M. Basko, *Raman spectroscopy as a versatile tool for studying the properties of graphene*, **nature nanotechnology 8**,(2013).

[77] E.O. Polat, O. Balci, C. Kocabas, Graphene based flexible electrochromic devices, **Scientific Reports, 4** (2014), 6484.

[78] F. Lin, J.B. Bult, S. Nanayakkara, A.C. Dillon, R.M. Richards, J.L. Blackburn, C. Engtrakul, Graphene as an Efficient Interfacial Layer for Electrochromic Devices, **ACS Appl. Mater. Interfaces, 7** (2015), 11330 – 11336.

[79] Lu Zhao, L. Zhao, Y. Xu, T. Qiu, L. Zhi, G. Shi, *Polyaniline electrochromic devices with transparent graphene electrodes*, **Electroc. Acta, 55** (2009), 491 – 497.

[80] L. Kavan, J.H. Yum, M. Graetzel, *Application of graphene-based nanostructures in dye-sensitized solar cells*, **Phys. Status Solidi, 12** (2013), 2643 – 2648.

[81] M. Castriota, E. Cazzanelli, D. Pacilè, L. Papagno, Ç.O. Girit, J.C. Meyer, A. Zettl, M. Giarola, G. Mariotto, *Spatial dependence of Raman frequencies in ordered and disordered monolayer graphene*, **Diamond & Rel. Mat., 19** (2010), 608 – 613.

[82] M. Castriota, G.G. Politano, C. Vena, M. P. De Santo, G. Desiderio, M. Davoli, E. Cazzanelli, C. Versace, *Variable Angle Spectroscopic Ellipsometry investigation of CVD-grown monolayer graphene*, **Applied Sur. Sci, 467-468** (2019), 213 – 220.

[83] G.G. Politano, C. Versace, C. Vena, M. Castriota, F. Ciuchi, A. Fasanella, G. Desiderio, E. Cazzanelli, *Physical investigation of electrophoretically deposited*

graphene oxide and reduced graphene oxide thin films, **Journal of app. phy., 120** (2016), 195307.

[84] G.G. Politano, E. Cazzanelli, C. Versace, C. Vena, M. P. De Santo, M. Castriota, F. Ciuchi, R. Bartolino, *Graphene oxide on magnetron sputtered silver thin films for SERS and metamaterial applications*, **Applied Sur. Sci., 427** (2018), 927 – 933.

[85] D. Graf, F. Molitor, K. Ensslin, C. Stampfer, A. Jungen, C. Hierold, L. Wirtz, *Spatially Resolved Raman Spectroscopy of Single- and Few-Layer Graphene*, **Nano Lett., 7** (2007), 238 – 242.

[86] A.C. Ferrari, J.C. Meyer, V. Scardaci, C. Casiraghi, M. Lazzeri, F. Mauri, S. Piscanec, D. Jiang, K.S. Novoselov, S. Roth, A.K. Geim, *Raman Spectrum of Graphene and Graphene Layers*, **Phys. Rev. Lett., 97** (2006), 187401.

[87] A. Gupta, G. Chen, P. Joshi, S. Tadigadapa, P.C. Eklund, *Raman Scattering from High-Frequency Phonons in Supported n-Graphene Layer Films*, **Nano Lett., 6** (2006) 2667.

[88] L.M. Malard, M.A. Pimenta, G. Dresselhaus, M.S. Dresselhaus, *Raman spectroscopy in graphene*, **Phys. Reports, 473** (2009), 51 – 87.

[89] M. Majoube, M. Henry, *Fourier transform Raman and infrared and surface-enhanced Raman spectra for rhodamine 6G*, **Spectrochimica Acta 47A, 9/10** (1991), 1459 – 1466

[90] L. Jensen, G.C. Schatz, *Resonance Raman Scattering of Rhodamine 6G as Calculated Using Time-Dependent Density Functional Theory*, **J. Phys. Chem. A 110, 18** (2006), 5973 – 5977.

[91] S. Shim, C.M. Stuart, R.A. Mathies, *Resonance Raman Cross-Sections and Vibronic Analysis of Rhodamine 6G from Broadband Stimulated Raman Spectroscopy*, Chem. Phys. Chem. 9, (2008), 697 – 699

[92] G. Li, H. Li, Y. Mo, X. Huang, L. Chen, *Surface enhanced resonance Raman spectroscopy of rhodamine 6G adsorbed on silver electrode in lithium batteries*, Chemical Physics Letters, 330 (2000) 249 – 254.

[93] P. Hildebrandt, M. Stockburger, *Surface-Enhanced Resonance Raman Spectroscopy of Rhodamine 6G Adsorbed on Colloidal Silver*, J. Phys. Chem., 88 (1984), 5935 – 5944.

[94] A. Patra, V. Caligiuri, R. Krahne, A. De Luca, *Strong Light–Matter Interaction and Spontaneous Emission Reshaping via Pseudo-Cavity Modes*, **Adv. Optical Mater.**, (2021), 2101076.

[95] P.S. Narayanan, *Raman spectrum of rutile (TiO2)*, **Proc. Indian Acad. Sci. (Math. Sci.), 32** (1950), 279 – 283.

[96] O. Frank, M. Zukalova, B. Laskova, J. Kürti, J. Koltai, L. Kavan, *Raman spectra of titanium dioxide (anatase, rutile) with identified oxygen isotopes (16, 17, 18)*, **Phys. Chem. Chem. Phys., 14** (2012), 14567 – 14572.

[97] J. Zhang, M. Li, Z. Feng, J. Chen, C. Li, *UV Raman Spectroscopic Study on TiO2. I. Phase Transformation at the Surface and in the Bulk*, **J. Phys. Chem. B, 110** (2006), 927 – 935.

[98] T.-H. Chang, H.-C. Lu, M.-H. Lee, S.-Y. Kao, K.-C. Ho, *Multi-color electrochromic devices based on phenyl and heptyl viologens immobilized with UV-cured polymer electrolyte*, **Solar Energy Materials and Solar Cells**, **177** (2018), 75 – 81.

[99] S. Mishra, H. Pandey, P. Yogi, S. K. Saxena, S. Roy, P. R. Sagdeo, R. Kumar, *Live spectroscopy to observe electrochromism in viologen based solid state Device*, ***Solid State Communications***, ***261*** (2017), 17 – 20.

[100] A. Danine, L.M. Manceriu, A. Fargues, A. Rougier, *Eco-friendly redox mediator gelatin-electrolyte for simplified TiO2-viologen based electrochromic devices*, ***Electrochimica Acta, 258*** (2017), 200 – 207.

[101] K. A. Groat, S. E. Creager, *Self-Assembled Monolayers in Organic Solvents: Electrochemistry at Alkanethiolate-Coated Gold in Propylene Carbonate*, ***Langmuir, 9*** (1993), 3668 – 3675.

[102] S. Mishra, H. Pandey, P. Yogi, S. K. Saxena, S. Roy, P. R. Sagdeo, R. Kumar, *Interfacial redox centers as origin of color switching in organic electrochromic device*, **Optical Materials, 66** (2017), 65 – 71.

[103] G.N. Kamau, T.M. Saccucci, G.Gounili, A.E. Nassar, J.F. Rusling, *Films Formed by Oxidation of Ferrocene at Platinum Electrodes*, **Anal. Chem., 66** (1994), 994 – 1001.

[104] H.-C. Lu, S.-Y. Kao, H.-F. Yu, T.-H. Chang, C.-W. Kung, K.-C. Ho, *Achieving Low-Energy Driven Viologens-Based Electrochromic Devices Utilizing Polymeric Ionic Liquids*, **ACS Appl. Mater. Interfaces, 8** (2016), 30351 – 30361.

[105] R. Raghavan, R.T. Iwamoto, *Chemical-Electrochemical Method for the Determination of the Positions of Coupling in the Dimeric one-Electron Reduction Products of Ring-Substituted 1-Alkylpyridinium Ions*, **Journal of Electroanalytical Chemistry and Interfacial Electrochemistry, 102** (1979), 85 – 92.

[106] H. Tahara, R. Baba, K. Iwanaga, T. Sagara, H. Murakami, *Electrochromism of a bipolar reversible redox-active ferrocene–viologen linked ionic liquid*, **Chem. Commun., 53** (2017), 2455 – 2458.

[107] S. Haymond, J.K. Zak, Y. Show, J.E. Butler, G.T. Babcock, G.M. Swain, *Spectroelectrochemical responsiveness of a freestanding, boron-doped diamond, optically transparent electrode toward ferrocene*, **Analytica Chimica Acta, 500** (2003), 137.

Chapter 5

Conclusions and Future Outlooks

In this thesis work, materials with different technological properties have been studied in order to their own potential use in the electrochromic technology. Such materials have been characterized with different techniques. In particular, the main technique has been the Raman spectroscopy which allowed to obtain numerous information about the physical chemistry.

Following the preliminary studies on the different materials, an electrochromic demonstrator has been successfully produced using the following components:

- the redox couple has been made with ethyl viologen diperchlorate and diethyl ferrocene dissolved in a solution of Propylene Carbonate.
- the electrolyte layer has been realised with the use of bisphenol A glycerolate directly added to the solution in a precise percentage.

The final electrochromic solution has been inserted by capillarity into a cell made with two ITO coated glass. The application of a voltage between 1.5 and 3.5 Volts allows the device to switch from a phase substantially transparent (characterized by a pale-yellow colour) to a coloured one.

A complete characterization of the demonstrator in the states ON and OFF has been made by Cyclic voltammetry, UV-vis Spectroscopy and Raman spectroscopy techniques.
At the time, the research on electrochromic device technologies is focused on the use of polymeric materials that can enhance the performances of the device both from a structural point of view, are currently studying the realization of flexible devices, and from the point of view of the environmental sustainability of the device production chain.

Another critical point is the scale up of the electrochromic devices fabrication. In fact, the realization of large electrochromic devices is subject to several complications such as ohmic fall and differences in thickness at different points of the device. Further analyses are therefore currently under consideration to resolve these impediments.